Title
Experimental and Analytical Studies on Old Reinforced Concrete Buildings with Seismically Vulnerable Beam-Column Joints

Author
PARK, SANGJOON

Publication Date
2010

Peer reviewed|Thesis/dissertation

Experimental and Analytical Studies on Old Reinforced Concrete Buildings with Seismically Vulnerable Beam-Column Joints

by

Sangjoon Park

A dissertation submitted in partial satisfaction of the

requirements for the degree of

Doctor of Philosophy

in

Engineering – Civil and Environmental Engineering

in the

Graduate Division

of the

University of California, Berkeley

Committee in charge:

Professor Khalid M. Mosalam, Chair
Professor Jack P. Moehle
Professor Haiyan Huang

Fall 2010

Experimental and Analytical Studies on Old Reinforced Concrete Buildings with Seismically Vulnerable Beam-Column Joints

by

Sangjoon Park

Abstract

Experimental and Analytical Studies on Old Reinforced Concrete Buildings with Seismically Vulnerable Beam-Column Joints

by

Sangjoon Park

Doctor of Philosophy in Engineering – Civil and Environmental Engineering

University of California, Berkeley

Professor Khalid M. Mosalam, Chair

Existing reinforced concrete (RC) buildings designed prior to 1970s are vulnerable to shear failure in beam-column joints under earthquake loads because of insufficient transverse reinforcement in the joint region. To assess the seismic risk of old RC buildings, the accurate prediction of shear strength and deformability for these unreinforced beam-column joints is essential. Several joint shear strength models are available in the literature but they have been originally developed to predict the shear strength of reinforced beam-column joints. Due to the different shear force transfer mechanism between reinforced and unreinforced beam-column joints, the existing models have little success to assess the shear strength of unreinforced beam-column joints. The ASCE/SEI 41-06 provisions specify shear strengths and backbone curves for unreinforced beam-column joints but the predictions using these provisions are usually conservative compared with many experimental test data collected from the literature. This study is focusing on developing accurate shear strength models and backbone relationships for unreinforced exterior and corner beam-column joints.

This study proposes two shear strength models, semi-empirical and analytical, for unreinforced exterior and corner beam-column joints to reflect the influence of two key parameters: (1) joint aspect ratio which is defined as the ratio of beam to column cross-section heights, and (2) beam reinforcement index which is related to the amount of beam longitudinal reinforcement in tension. These key parameters are determined from a parametric study using a large experimental data set of unreinforced exterior and corner beam-column joints from the published literature. The proposed models are validated by accurate predictions of the shear

strength for the database specimens. Besides the accuracy of the proposed models, the semi-empirical model has the advantage of straightforward extension to other types of beam-column joints. An important advantage of the analytical model is that for the case of beam yielding followed by joint failure, the analytical model can predict the reduced shear strength without the need for the complexity of ductility consideration.

The experimental phase of this study includes testing four full-scale unreinforced corner beam-column joint specimens. These four specimens are designed to investigate the effect of the joint aspect ratio and the beam longitudinal reinforcement ratio. The test results show that the joint shear strengths are reduced with increase of the joint aspect ratio and for each of the joint aspect ratio, the joint shear strengths are proportional to the beam longitudinal reinforcement ratio within the range provided in the test specimens. The shear strengths of the four specimens are accurately predicted by the two proposed models, while the ASCE/SEI 41-06 provisions for shear strength produce conservative estimates of the strengths for the test specimens.

Based on the measured joint shear stress-rotation and visual observation of the tested corner beam-column joint specimens, a multi-linear backbone relationship is proposed in this study to reflect the following beam-column joint responses: (1) initial joint cracking, (2) either beam reinforcement yielding or significant opening of existing joint cracks, (3) either existing joint cracks further propagation or additional joint cracks opening at the peak load, and (4) residual joint shear stress and rotation after severe damage in the joint. Corresponding parameters in the backbone relationship are defined from the comparison with test results. The proposed backbone relationship is verified by the simulations for beam-column subassemblies of the tested four specimens and other four planar exterior beam-column joint specimens from the literature. To investigate the effect of beam-column joint flexibility on the lateral response in a structural system level, nonlinear static and dynamic simulations are performed. These simulations indicate that beam-column joint flexibility is essential for older-type RC buildings characterized by having unreinforced beam-column joints. As an extension of this study, progressive collapse analysis for older-type RC buildings will be pursued with the proposed beam-column joint backbone relationships.

To my wife Soojung, our everything Aidan, and our dedicated parents

TABLE OF CONTENTS

LIST OF FIGURES

LIST OF TABLES

ACKNOWLEDGMENTS

I would like to express my deepest gratitude to my advisor, Professor Khalid Mosalam for his invaluable guidance, support throughout my graduate studies. His knowledge and keen eyes made me realize lack of my knowledge and consideration. His suggestion gave me a different aspect to find a breakthrough when my research confronted problems. Besides his academic distinction, his kindness was a big stress relief to me. He is definitely a role model who I want to be.

I also want to express many thanks to all SEMM faculty members. Special thanks to Professor Jack Moehle for serving as a member of my qualifying examination and dissertation committee. His sound advice and guidance were a big contribution to my research. I wish to thank Professor Shaofan Li, a member of my qualifying examination committee, for making me have interest in mechanics, Professor Haiyan Huang, a member of my qualifying examination and dissertation committee, for her excellent teaching of statistics, and Professor Marios Panagiotou, a member of my qualifying examination committee.

Successful experimental tests could not have been possible without the assistance from *nees@berkeley* and the Pacific Earthquake Engineering Research Center (PEER) laboratory staff at Richmond Field Station. I am especially grateful to Dr. Shakhzod Takhirov for his great advice and to Mr. Robert Cerney for his extensive assistance. I also want to thank Mr. Don Clyde, Mr. Donald Patterson, Mr. David McLam, Mr. Jose Robles, and Mr. Nathaniel Knight for their excellent support. I would like to thank Webcor builders and special thanks to the carpenter Mr. Wassim Lazkani for his dedication to build my tested specimens.

I was very happy to have many outstanding friends in Berkeley. Special thanks to my best friend, Matias Hube, for his help and friendship. I also want to thank my friends, Chui-Hsin Chen, Vesna Terzic, Hong Kim, Selim Günay, and Shinji Kishida. I would like to mention two my undergraduate helpers, Will Nguyen and Steven Liu who are now graduate students in Berkeley.

I also want to mention my former advisor from the Seoul National University, Professor Emeritus Sungmok Hong who encouraged me to study at the University of California at Berkeley.

Last, I would like to thank my wonderful wife Soojung and our lovely son Aidan. All my achievement must have been made due to her sacrifice, patience, and unconditional love for me and our family. I could not find relevant words in any dictionary to express my love and gratitude to her. I would also like to thank my parents and my parents-in-law for their love, support and understanding.

The research conducted in this dissertation was supported by the National Science Foundation award number 0618804 through the Pacific Earthquake Engineering Research Center. I am grateful for the support that I received.

I Introduction

I-1 Motivation

Numerous reinforced concrete (RC) buildings designed prior to 1970s still exist in the western US and in other seismically active regions worldwide. These old RC buildings were usually designed for gravity load only or little consideration of seismic forces and detailing. Consequently, insufficient shear reinforcements were provided in columns and beam-column joint regions. To assess the risk of such seismically vulnerable RC buildings, there have been significant experimental and analytical research activities conducted to investigate the capacity of shear-critical columns and to predict their axial failure (Lynn, 2001; Sezen, 2002; Elwood, 2003; Ghannoum, 2007; Shin, 2007). Meanwhile, most studies on beam-column joints (hereafter beam-column joints are denoted as joints) have been dealing with improving requirements for new joint seismic designs so that they have adequate strength and ductility. Relatively fewer studies have focused on seismic performance of older-type joints without transverse reinforcement in the joint region (referred to hereafter as "unreinforced"). An exception is the study conducted at Cornell University in the early 1990s (Pesski et al., 1990; El-Attar et al., 1992; Beres et al., 1992). However, the specimens tested in the Cornell University included unreinforced joints as well as other beam and column details typically found in non-seismic zone such as the eastern US. Therefore, the results of this study may not be understood as solely the behavior of unreinforced joints.

Earthquake reconnaissance reports (Uang et al, 1999; Sezen et al., 2000; Li et al., 2008; Günay and Mosalam, 2010) indicate that the older-type RC buildings are prone to collapse due to failure of unreinforced joints, especially corner joints, as shown in Figure I.1. Currently, ASCE/SEI 41-06 (2006), referred to hereafter as ASCE 41, specifies the shear strength and drift capacity for unreinforced interior and exterior joints. The ASCE 41 provisions, however, are found to be conservative compared with the strengths determined from laboratory tests on unreinforced exterior joints in the literature. Several shear strength models for unreinforced joints are also available in the literature. These models have little success to predict the shear strength of unreinforced joints since they have been originally developed to reflect the behavior of reinforced joints. Therefore, an accurate and predictive shear strength model for unreinforced joints to be used in progressive collapse simulation is still lacking.

Laboratory test data for unreinforced joints are available in the published literature. The majority of tests were, however, conducted with planar exterior joints (Figure I.2) under constant column axial load during testing. The planar exterior joints rarely occur in real buildings which have slabs and transverse beams. Moreover, under earthquake loads, column axial loads are varying due to the overturning moment of the building. In some tests, test results from small-scale of specimens are arguable because of size effect as well as small size of aggregate and rarely used reinforcing bar size. Therefore, data from tests on full-scale unreinforced joints with

floor slabs and transverse beams are needed.

For convenience, most of conventional analysis for RC buildings is modeling the joints as rigid connections where beams and columns are intersecting. Joint deformation may make a significant difference in the lateral response of RC buildings, particularly if the buildings contain unreinforced joints. To account for joint deformation, several types of joint macro-models have been proposed by other researchers, such as separating joint shear deformation from slip rotation (named as explicit modeling) and combining the two types of deformations into a single variable (named as implicit modeling). Implicit modeling is a more practical option for simulating a building having a large number of degrees of freedom in terms of numerical efficiency. For implicit modeling and for simulating old RC buildings accounting for joint flexibility, representative backbone relationships for unreinforced joints are necessary.

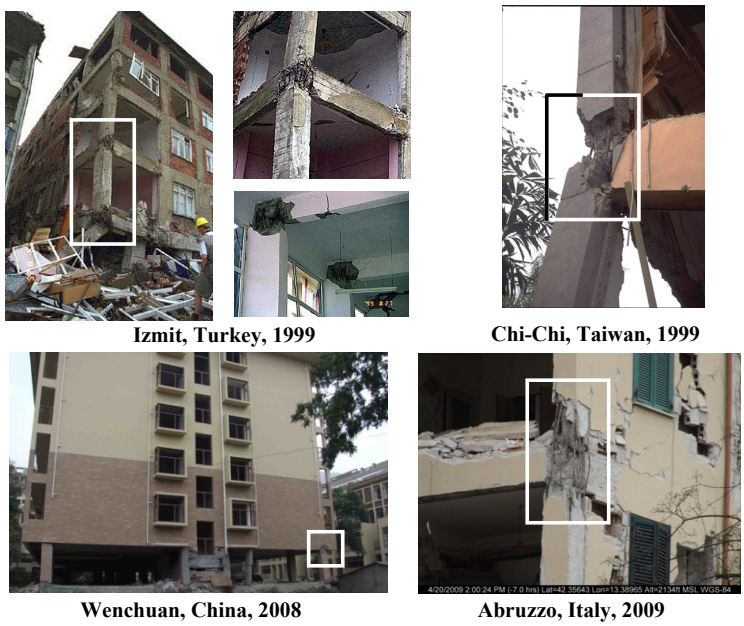

Figure I.1 Failure of corner joints in past earthquakes.

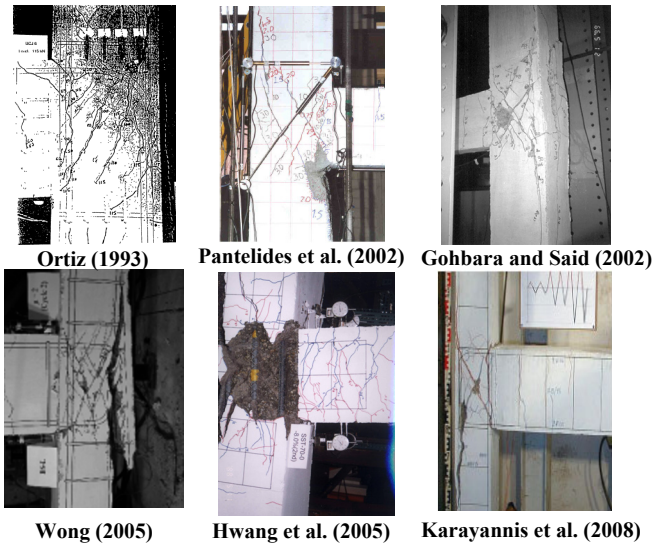

Figure I.2 Tests on planar exterior joints in the literature.

I-2 Research Overview

This study is initiated as a key part of a collaborative project (NEES-Grand Challenge) aiming at assessing collapse risk and developing mitigation strategy for older-type RC buildings. The overview of the project is shown in Figure I.3. Among several topics in the project, the behavior of unreinforced exterior and corner joints under earthquake loads is of interest in this study as indicated by the gray colored boxes in Figure I.3. In this study, extensive experimental and analytical investigations have been conducted to ultimately simulate the progressive collapse of older-type RC buildings and generate collapse fragility curves.

This dissertation presents development of shear strength models, experimental program, and finally simulations of beam-column subassemblies and two dimensional building frames using the developed backbone relationships for unreinforced exterior and corner joints. For shear strength prediction, two shear strength models have developed by semi-empirical and analytical approaches to reflect the effect of two governing parameters, i.e. joint aspect ratio and beam longitudinal reinforcement ratio. Four full-scale unreinforced corner joint tests have been conducted to verify the proposed shear strength models and to provide key information for developing backbone relationships of unreinforced exterior and corner joints. The developed backbone relationships are validated by accurately reproducing the load-displacement responses of the tested four corner joint specimens and other four planar exterior joint specimens from the literature. As a prelude of progressive collapse analysis for older-type RC buildings, nonlinear static and dynamic analyses for two dimensional building frames are performed including joint flexibility.

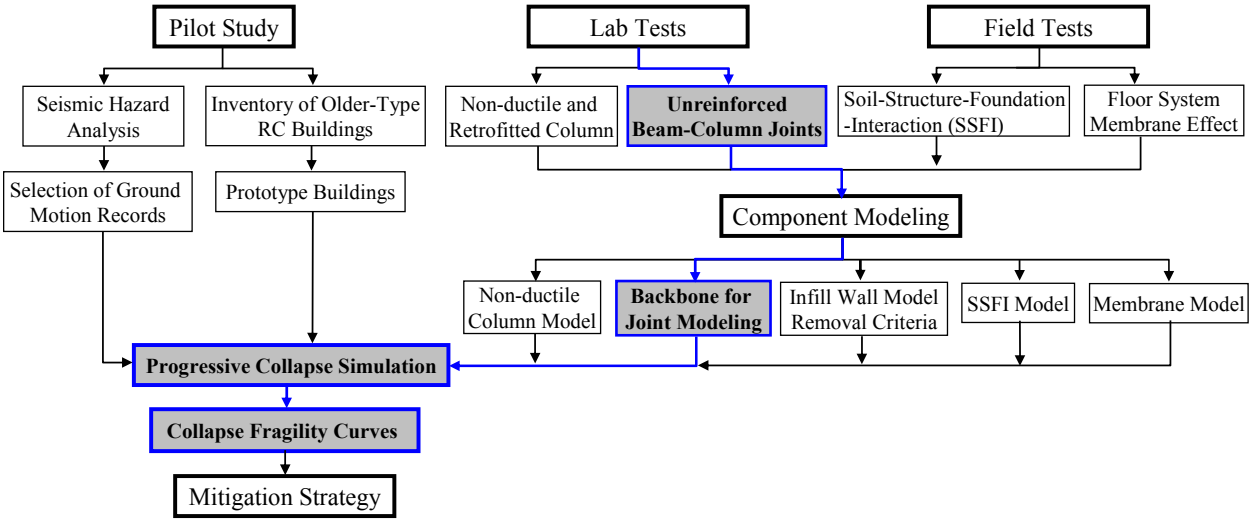

Figure I.3 Overview of the research on older-type RC buildings (NEES-Grand Challenge).

I-3 Objectives, Scope, and Definitions

The ultimate goal of the NEES-Grand Challenge Project is to perform a progressive collapse analysis of older-type RC buildings under earthquake loads. As a part of this collaborative project, this study focuses on understanding the behavior and modeling of RC exterior and corner joints without transverse reinforcement.

The first primary objective of this study is the development and validation of shear strength models for unreinforced exterior and corner joints. The developed shear strength models consider the following objectives:

1. To include the main parameters, i.e. joint aspect ratio and beam reinforcement index, affecting the shear strength of unreinforced exterior and corner joints;
2. To propose a semi-empirical model that is expressed as a simple equation but capable of predicting the shear strength with high accuracy;
3. To propose an analytical model to be able to predict two joint failure modes, namely, joint shear failure without beam reinforcement yielding (J failure mode) and joint shear failure with beam reinforcement yielding (BJ failure mode); and
4. To practically extend the models to other types of unreinforced joints, such as interior and knee joints.

As an experimental part of this study, four full-scale unreinforced corner joint tests are conducted. The objectives of the tests are as follows:

5. To investigate the effect of the joint aspect ratio and the beam reinforcement index obtained from a parametric study using collected data set of unreinforced exterior and corner joint tests;
6. To verify the developed shear strength models; and
7. To provide benchmark data for developing backbone relationship of unreinforced exterior and corner joints.

For practicality, an implicit joint macro-modeling is selected in this study and the corresponding backbone relationships are developed. Considering the developed backbone relationships, simulations are performed for beam-column subassemblies and prototype buildings. The simulations are intended to assess the importance of the joint flexibility on the lateral response of RC buildings having unreinforced joints.

For clarity, the terminologies used in this dissertation are defined in this section. The definitions and terms are consistently referred to throughout this dissertation.

1. Beam-column joints are referred to as joints;
2. Unreinforced joints are defined as joints without transverse reinforcement in the joint region;
3. Longitudinal beam is the one that frames into the joint in the direction of loading for which the joint shear is being considered;
4. Transverse beam is the one that frames into the joint in a direction perpendicular to the longitudinal beam;

5. Exterior joint is defined as a joint with columns above and below and one longitudinal beam framing into the joint without transverse beam;
6. Corner joint is an exterior joint but with one transverse beam framing into one face of the exterior joint;
7. Interior joint is defined as a joint with columns above and below and two longitudinal beams framing into the joint without or with one transverse beam;
8. Joint aspect ratio is defined as the ratio of the total beam height, h_b, to column cross-sectional height, h_c, i.e. h_b/h_c;
9. Joint shear stress and strength are used to refer to horizontal joint shear stress and strength;
10. Negative bending for beam is defined as the flexural loading to cause tension in top reinforcement of the beam or tension in slab in case of the beam having floor slab; and
11. Positive bending for beam is defined as the flexural loading to cause tension in bottom reinforcement of the beam or compression in slab in case of the beam having floor slab.

I-4 Outline

This dissertation consists of eight chapters and two appendices. Chapter I presents the motivation, overview and contribution of this research to the collaborative NEES-Grand Challenge project, and the objectives that this research pursues. The following main chapters are categorized into three parts: (1) development of shear strength models for unreinforced exterior and corner joints, (2) experimental tests on unreinforced corner joints, and (3) structural simulation using developed shear strength models and backbone relationships, as presented in Figure I.4.

For developing shear strength models suitable for unreinforced exterior and corner joints, Chapter II presents an extensive literature study. A large experimental data set of unreinforced exterior and corner joints are collected from the published literature with consistent selection criteria, and parametric studies are performed using this database. The parametric study provides main parameters to affect the shear strength of unreinforced exterior and corner joints and these parameters are directly adopted for developing shear strength models and designing the specimens in the subsequent experimental program. The basic idea for the new shear strength models is obtained from a review of existing joint shear strength models. Based on the observation from Chapter II, shear strength models for unreinforced exterior joints are newly developed in Chapter III. Two shear strength models are derived using semi-empirical and analytical approaches. Accuracy and advantages of each of the two models are discussed.

Experimental study and discussion of the test results are presented in Chapter IV through VI. Chapter IV describes the experimental program of four full-scale corner joint specimens including the details of specimen design, loading protocol, test setup, and instrumentation plans. The evaluation of the test results and observations are followed in Chapter V. The evaluated test results are discussed in Chapter VI. Key information of joint shear stress-rotation responses is presented to develop a backbone relationship in the subsequent simulation part.

Structural simulations are performed including joint flexibility in Chapter VII. First, backbone relationships are developed based on the evaluated joint shear stress-rotation responses

and visual observation of joint damage propagation from the tested four corner joint specimens. For verification of the proposed backbone relationships, simulations are performed for the beam-column subassemblies of the specimens tested in the experimental part of this study and others specimens from the literature. To investigate the effect of joint flexibility on the lateral response of a structural system, nonlinear static and dynamic simulations are performed for prototype buildings considered in this study.

As a concluding remark of this study, Chapter VIII presents a summary of the main findings and conclusions of this research. Several future research topics are listed to extend this research to progressive collapse analysis of older-type RC buildings.

Finally, two appendices are included in this dissertation. Appendix A presents the detailed design drawings of the four test specimens and test setup. Appendix B presents the concrete and reinforcing steel material properties obtained from their sample tests.

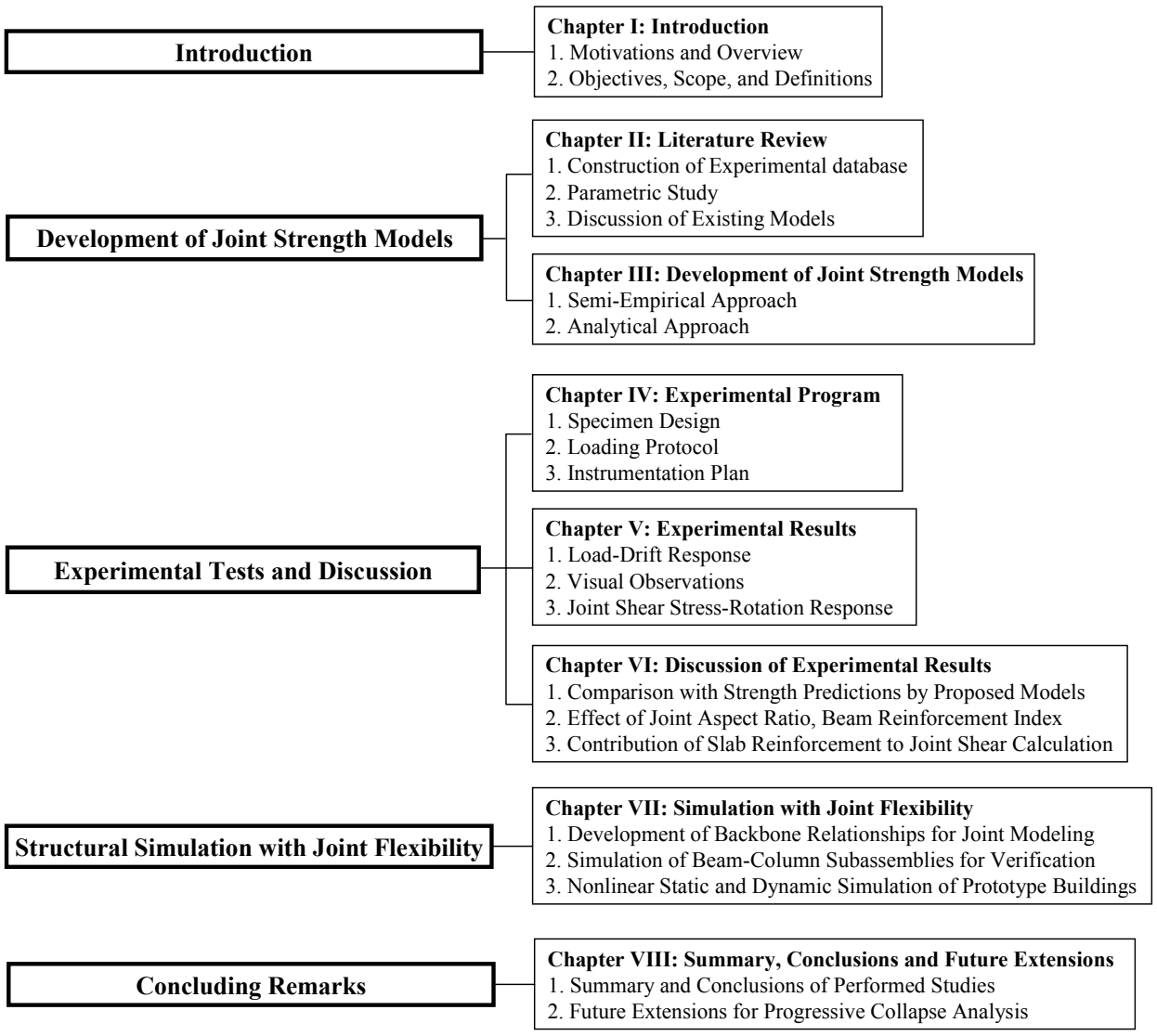

Figure I.4 Classification of dissertation chapters.

II Literature Study

This chapter provides a parametric study with a large number of laboratory test data collected from the literature. The parametric study is intended to find key parameters affecting shear strength of unreinforced exterior joints and also to develop joint shear strength models in the subsequent chapters. This chapter also presents an overview of existing shear strength equations and joint macro-models used in simulation of RC buildings.

II-1 Database and Parametric Study

II-1.1 Database of Unreinforced Exterior and Corner Joints

A large data set of unreinforced joint tests are collected from the published literature and analyzed in this section. To focus on the joints vulnerable to shear failure, only exterior (Figure II.1(a)) and corner joints (Figure II.1(b)) are included in this database, while interior joints of exterior frames (Figure II.1(c)) and exterior joints having two transverse beams on both sides of joint (Figure II.1(d)) are excluded. It is reported that crushing along the joint diagonal occurred in the joints without transverse beams or with a transverse beam on one side only, and the shear capacity of joints with transverse beams on two sides increased significantly compared with the two other cases (Zhang and Jirsa, 1982; Ohwada, 1977). In addition, the anchorage details of the beam longitudinal reinforcement into the joint region are also considered as one of the criteria for limiting the database candidates. There are several types of these anchorage details in the joint region, which were used in gravity-load-designed RC buildings. Figure II.2 shows the selected anchorage details for collecting database candidates where at least one strut mechanism can develop under lateral loading. Among the shown four types, Type B is most common in older gravity-load-designed RC buildings, followed by Type A. Types C and D are less common and impractical from a constructability point of view. It is to be noted that the tests designed with a wide beam, i.e., with beam width greater than column width, are not included in the database due to different confinement conditions of the joint region.

Based on the discussion above, 62 tests for unreinforced beam-column joints satisfying the selection requirements of the database are identified and summarized in Table II.1. The information of each test is extracted from the published literature and consistent assumptions are made when available data are incomplete. For instance, the joint shear strength specified in the corresponding literature is used in the database, while the joint shear strength is calculated by the constant moment arm assumption if only applied beam or column shear force is reported. The constant moment arm is assumed to be $0.9d_b$ (Wong, 2005) for the case of joint shear failure with beam longitudinal reinforcement yielding, and it is reduced to be $0.875d_b$ for the case of joint shear failure without beam longitudinal reinforcement yielding because of the relatively short distance from the neutral axis to the center of compressive block in the beam cross-section. Note

that d_b is the effective depth of beam cross-section. The joint shear strength is normalized by the square root of the concrete standard compressive strength, $\sqrt{f_c'}$, i.e., $\gamma = V_{jh} \big/ b_j h_c \sqrt{f_c'}$, to be compared with the criteria of the current U.S. code provisions. The effective joint width, b_j, is taken as $(b_c + b_b)/2$ which gives a reasonable equivalent strut (Zhang and Jirsa, 1982). Note that V_{jh} is the joint shear strength which is defined as the maximum horizontal shear force in the joint, h_c is the total height of column cross-section in the loading direction, and b_c and b_b are the width of the column and beam cross-section, respectively. It is worth mentioning that the possible size effect on the experimental results is not taken into consideration in the analysis of this database. The specimen failure obtained from tests is categorized into six modes: (1) joint shear failure without beam longitudinal reinforcement yielding (J mode), (2) joint shear failure with beam longitudinal reinforcement yielding (BJ mode), (3) beam flexural failure (BF mode), (4) column flexural failure (CF mode), (5) beam reinforcement pull-out failure (P mode), and (6) anchorage failure (A mode).

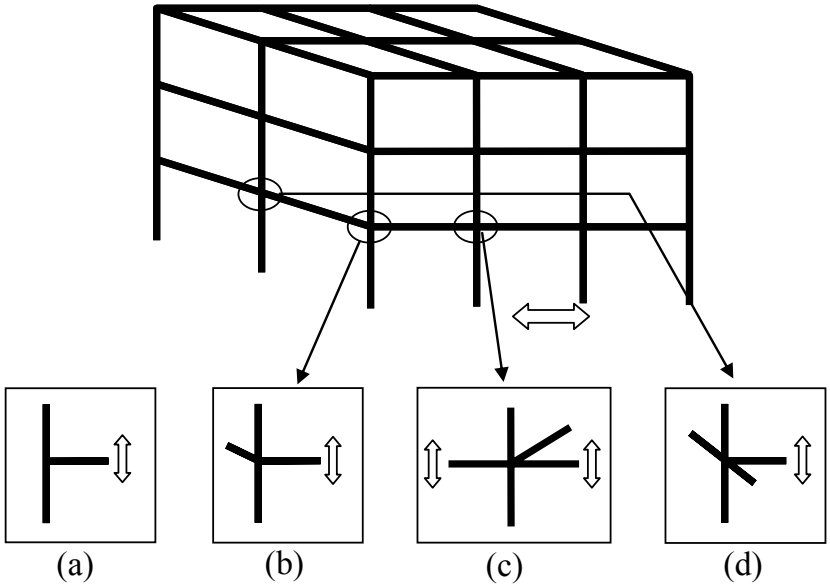

Figure II.1 Beam-column joint types: (a) exterior joint, (b) corner joint, (c) interior joint, and (d) exterior joint with two transverse beams.

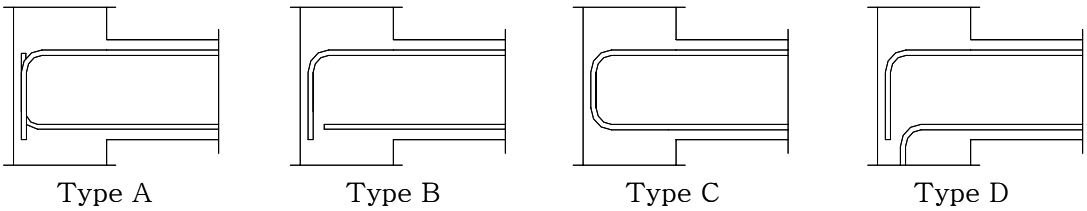

Figure II.2 Selected anchorage types for exterior beam-column joints.

Table II.1 Database of unreinforced exterior beam-column joint tests.

Reference	Specimen	f'_c (ksi)	$f_{y,beam}$ (ksi)	A_s [*1] ($in.^2$)	b_j (in.)	h_c (in.)	h_b (in.)	P/f'_cA_g	V_{jh} (kip)	γ ($psi^{0.5}$)	Failure Mode [*2]
Antonopoulos & Triantafillou	C-1	84.8	84.8	0.72	7.9	7.9	11.8	0.06	24.4	7.4	J
	C-2	84.8	84.8	0.72	7.9	7.9	11.8	0.05	24.2	6.7	J
	T-C	84.8	84.8	0.72	7.9	7.9	11.8	0.05	28.1	7.6	J
Clyde et al.	02	65.9	65.9	4.0	12.0	18.0	16.0	0.10	213.9	12.1	J
	06	65.9	65.9	4.0	12.0	18.0	16.0	0.10	211.4	12.7	J
	04	65.9	65.9	4.0	12.0	18.0	16.0	0.25	208.9	13.2	J
	05	65.9	65.9	4.0	12.0	18.0	16.0	0.25	220.8	13.4	J
El-Amoury & Ghobara	T0	61.6	61.6	1.95	9.8	15.7	15.7	0.20	91.3	8.8	BJ
Engindeniz	SP1-NS	45.7	45.7	2.64	13.0	14.0	20	0.02	81.4	7.3	CF
	SP1-EW	45.7	45.7	2.64	13.0	14.0	20	0.02	90.4	8.1	CF
	SP2-NS	45.7	45.7	2.64	13.0	14.0	20	0.02	91.7	7.1	J
	SP2-EW	45.7	45.7	2.64	13.0	14.0	20	0.02	96.9	7.5	J
Gencoğlu & Eren	RCNH1	76.1	76.1	0.22	4.9	7.9	11.8	0.13	10.9	4.3	BF
Ghobara & Said	T-1	61.6	61.6	1.85	9.8	15.7	15.7	0.19	124.5	12.0	BJ
	T-2	61.6	61.6	1.85	9.8	15.7	15.7	0.10	117.0	11.3	BJ
Hanson & Connor	V	51.0	51.0	4.0	13.5	15.0	20	0.86	138.4	11.9	J
	7	51.0	51.0	4.0	13.5	15.0	20	0.50	189.7	12.4	BJ
Hwang et al.	0T0	63.1	63.1	3.16	14.6	16.5	17.7	0.02	224.1	9.4	BJ
Karayannis et al.	A0	84.1	84.1	0.22	7.9	7.9	11.8	0.05	18.2	4.3	BJ
	B0	84.1	84.1	0.66	7.9	11.8	11.8	0.05	44.4	7.1	BJ
	C0	84.1	84.1	0.70	7.9	11.8	11.8	0.05	45.9	7.3	BJ
Liu	RC-1	46.9	46.9	0.66	8.5	9.1	13.0	0	29.3	7.2	BJ
Ortiz	BCJ1	104.4	104.4	1.24	7.9	11.8	15.7	0	68.8	10.5	J
	BCJ3	104.4	104.4	1.24	7.9	11.8	15.7	0	72.4	11.3	J
	BCJ5	104.4	104.4	1.24	7.9	11.8	15.7	0.08	70.6	10.2	J
	BCJ6	104.4	104.4	1.24	7.9	11.8	15.7	0.09	70.8	10.7	J
Parker & Bullman	4a	82.7	82.7	1.52	10.8	11.8	19.7	0	43.0	4.5	CF
	4b	82.7	82.7	1.52	10.8	11.8	19.7	0.09	50.3	5.2	J
	4c	82.7	82.7	1.52	10.8	11.8	19.7	0.16	62.0	6.4	J
	4d	82.7	82.7	1.52	10.8	11.8	19.7	0	54.7	5.7	J
	4e	82.7	82.7	1.52	10.8	11.8	19.7	0.09	58.4	6.1	J
	4f	82.7	82.7	1.52	10.8	11.8	19.7	0.17	66.7	6.9	J
Pantelides et al.	01	66.5	66.5	4.0	16.0	16.0	16.0	0.10	193.2	10.9	J
	02	66.5	66.5	4.0	16.0	16.0	16.0	0.25	179.6	10.6	J
	03	66.5	66.5	4.0	16.0	16.0	16.0	0.10	183.4	10.2	J
	04	66.5	66.5	4.0	16.0	16.0	16.0	0.25	202.7	11.7	J
	05	66.5	66.5	4.0	16.0	16.0	16.0	0.10	192.6	11.1	J
	06	66.5	66.5	4.0	16.0	16.0	16.0	0.25	193.9	11.3	J
Sagbas	ED1	50.6	50.6	3.0	13.5	15	20	0	134.1	9.9	BJ
Sarsam & Phipps	EX-2	75.4	75.4	0.88	6.1	10.7	12.0	0.13	39.6	7.0	BJ
Scott & Hamil	C4ALN0	75.7	75.7	0.62	5.1	5.9	8.3	0.05	24.8	10.5	P
	C4ALH0	75.7	75.7	0.62	5.1	5.9	8.3	0.02	42.3	11.4	P
	C6LN0	75.7	75.7	0.62	5.1	5.9	8.3	0.04	23.4	9.0	J
	C6LH0	75.7	75.7	0.62	5.1	5.9	8.3	0.02	35.4	9.7	J
Uzumeri	SP1	50.3	50.3	3.0	13.5	15.0	20	0.41	140.9	10.4	BJ
	SP2	50.6	50.6	3.0	13.5	15.0	20	0.41	136.9	10.1	BJ
	SP5	50.4	50.4	3.0	15.0	15.0	20	0.43	136.7	8.9	BJ
Wilson	J1	75.4	75.4	1.04	6.1	11.8	11.8	0.30	57.1	11.7	J

Table II.1 Database of unreinforced exterior beam-column joint tests-*continued*.

Reference	Specimen	f_c' (ksi)	$f_{y,beam}$ (ksi)	A_s[*1] (in.^{2})	b_j (in.)	h_c (in.)	h_b (in.)	$P/f_c'A_g$	V_{jh} (kip)	γ (psi$^{0.5}$)	Failure Mode[*2]
Wong	BS-L	75.4	75.4	1.46	11.0	11.8	17.7	0.15	70.9	8.1	J
	BS-U	75.4	75.4	1.46	11.0	11.8	17.7	0.15	76.7	8.8	J
	BS-L-LS	75.4	75.4	1.46	11.0	11.8	17.7	0.15	77.5	8.8	J
	BS-L-300	75.4	75.4	1.46	11.0	11.8	11.8	0.15	113.5	12.4	BJ
	BS-L-600	75.4	75.4	1.46	11.0	11.8	23.6	0.15	63.8	6.7	J
	BS-L-V2T10	75.4	75.4	1.46	11.0	11.8	17.7	0.15	89.7	10.0	J
	BS-L-V4T10	75.4	75.4	1.46	11.0	11.8	17.7	0.15	90.6	10.9	J
	JA-NN03	75.4	75.4	0.97	11.0	11.8	15.7	0.03	68.9	5.3	BJ
	JA-NN15	75.4	75.4	0.97	11.0	11.8	15.7	0.15	69.9	6.6	BJ
	JB-NN03	75.4	75.4	0.97	11.0	11.8	11.8	0.03	70.4	6.5	BJ
Woo	Model 5	55.8	55.8	0.44	6.6	6.6	7.9	0	16.8	6.3	BJ

[*1] A_s is total area of beam reinforcement in tension;

[*2] Failure mode: J = joint shear failure without beam reinforcement yielding, BJ = joint shear failure with beam reinforcement yielding, BF = beam flexural failure, CF = column flexural failure, P = pull-out failure, A = anchorage failure.

Notes: 1ksi = 6.90 MPa; 1 in. = 25.4 mm; 1kip = 4.45 kN; $1.0\sqrt{f_c'}$ psi$^{0.5}$ = $0.083\sqrt{f_c'}$ MPa$^{0.5}$.

II-1.2 Parametric Study

In this section, a parametric study is performed using the database constructed in the previous section. For the parametric study, three parameters are selected because of their importance in the behavior of unreinforced exterior joints considered in the literature: joint aspect ratio, beam longitudinal reinforcement, and column axial load.

II-1.2.1 Effect of Joint Aspect Ratio

The effect of the joint aspect ratio has been investigated experimentally by other researchers. For the case of reinforced joints, Kim and LaFave (2007) reported that the joint aspect ratio from 1.0 to 1.6 for exterior joints had little influence on the joint shear stresses and strains in the case of J failure mode but slightly reduced the joint shear strength in the case of BJ failure mode. Wong (2005) tested unreinforced exterior joints having the three joint aspect ratios 1.0, 1.5, and 2.0. These test results showed that the normalized joint strength, γ, is inversely proportional to the joint aspect ratio, where $\gamma = 6.7$ psi$^{0.5}$ (0.56 MPa$^{0.5}$) for the high aspect ratio ($h_b/h_c = 2.0$), $\gamma = 8.6$ psi$^{0.5}$ (0.71 MPa$^{0.5}$) for the intermediate aspect ratio ($h_b/h_c = 1.5$), and $\gamma = 12.4$ psi$^{0.5}$ (1.03 MPa$^{0.5}$) for the low aspect ratio ($h_b/h_c = 1.0$), as indicated in Figure II.3. Vollum (1998) and Bakir and Bouroğlu (2002) made the same observations from a large data sets of literature test results. Each of these studies developed a separate joint strength model including the adverse effect of the joint aspect ratio.

The effect of joint aspect ratio on joint shear strength can be understood by the following concept. In the sense of the strut-and-tie (SAT) approach, a steeper single diagonal strut is to be developed in the high aspect ratio of a joint region due to the absence of ties if there is no transverse reinforcement in this region. Consequently, the steeper diagonal strut is less effective in providing shear resistance to equilibrate the horizontal joint shear force. Hence, the shear strength of unreinforced exterior joints is inversely proportional to its aspect ratio. This fact is supported by the plot of the database as shown in Figure II.3. In particular, the effect of the joint aspect ratio is more evident by selecting the cases of J failure mode. Furthermore, it is found that the joint shear strengths corresponding to other failure modes do not exceed that for the J failure mode except for the pull-out failure and column high axial load specimens.

II-1.2.2 Effect of Beam Longitudinal Reinforcement

According to the ACI Code provisions for beam-column joints (ACI 352R-02, 2002), joint shear capacity can be determined by the joint type, dimensions, and concrete strength for joint details satisfying minimum requirements of confinement. However, tests on unreinforced interior joints (Walker, 2001; and Alire, 2002) showed that joints failed in shear at different levels of shear stress demand represented by the factor γ: from 10.9 to 15.7 psi$^{0.5}$ (0.90 to 1.30 MPa$^{0.5}$) in Walker (2001), and 8.5 to 25.0 psi$^{0.5}$ (0.71 to 2.08 MPa$^{0.5}$) in Alire (2002). It is to be noted that all these tests were conducted with the same dimensions and column axial load. From this

observation, Anderson et al. (2008) claimed that strength and failure mode for the unreinforced joints are influenced by the shear stress demand determined by the amount of beam longitudinal reinforcement rather than the constant shear capacity of the joints. A similar observation was made in unreinforced exterior joint tests by Wong (2005). Two different reinforcement ratios were considered in the beam cross-section. Test results showed that the specimens having high beam longitudinal reinforcement ratio experienced joint shear failure without beam reinforcement yielding, while the specimens having low beam longitudinal reinforcement ratio experienced ductile behavior followed by joint shear failure. Bakir and Bouroğlu (2002) arrived to the conclusion that the normalized joint strength is related to the beam longitudinal reinforcement ratio after investigating the results of tests by Scott (1992) which had three different beam reinforcement ratios. Similarly, the shear strength equation of RC beams without stirrups, proposed by Bažant and Yu (2005), includes reinforcement ratio parameter as follows,

$$v_c = \mu \rho_w^{3/8} \left(1 + \frac{d_b}{a}\right) \sqrt{\frac{f_c'}{1 + d_b / d_o}} \tag{II.1}$$

where μ is a constant defined by regression, ρ_w is the beam longitudinal reinforcement ratio, a is the shear span, and d_o is the size effect parameter.

In the unreinforced joints, the improvement of joint shear strength due to increasing the beam longitudinal reinforcement ratio can be explained as follows: an increase of the beam longitudinal reinforcement ratio induces a larger compressive force in the diagonal strut because there is no truss mechanism to transmit horizontal joint shear, while the bond resistance between the beam longitudinal bars and surrounding concrete is maintained if joint failure occurs before beam reinforcement yielding. This more stable bond resistance induces a wider diagonal strut which can carry more horizontal joint shear stress. From the analysis of the database, it is shown that the joint shear strength is approximately linearly proportional to the amount of beam longitudinal reinforcement if joints are designed with the same material and geometry, refer to Figure II.4. Note that the beam reinforcement index on the horizontal axis of Figure II.4 is related to the amount of beam longitudinal reinforcement and the derivation of beam reinforcement index is presented in the subsequent Chapter III. For better understanding of the influence of the beam longitudinal reinforcement on the joint shear strength, these data of low joint aspect ratio ($0.89 \le h_b / h_c \le 1.33$) and high joint aspect ratio ($1.4 \le h_b / h_c \le 2.0$) are plotted with different symbols in Figure II.4. It is noted that the following test data marked with open circles in Figure II.4 can be excluded from the data for the high joint aspect ratio: (1) six tests by Parker and Bullman (1997) whose test results are questionable due to low joint shear strength as discussed by Vollum (1998), (2) two tests (C4ALH0 and C6LH0) by Scott and Hamil (1998) due to high joint shear strength by using high strength concrete, 15.1 ksi and 14.6 ksi (104 MPa and 101 MPa), and (3) two tests (BS-L-V2T10 and BS-L-V4T10) by Wong (2005) due to high joint shear strength by using unusual details of column intermediate bars.

For the data corresponding to the low joint aspect ratio, the increase of the normalized joint shear strength (vertical axis in Figure II.4) due to beam longitudinal reinforcement (horizontal axis in Figure II.4) is evident within a range of 4 $psi^{0.5}$ (0.33 $MPa^{0.5}$) to 12 $psi^{0.5}$ (1.0 $MPa^{0.5}$) of the horizontal axis in Figure II.4. This range corresponds to where the cases of joint shear failure with beam reinforcement yielding (BJ mode) are located. Beyond the beam

reinforcement index value of 12 psi$^{0.5}$ (1.0 MPa$^{0.5}$), the joint shear strength does not clearly increase.

On the other hand, for the data corresponding to the high joint aspect ratio case, fewer experimental data points are available compared with the low joint aspect ratio case. From these limited data points, the joint shear strengths of five specimens having the same aspect ratio, $h_b/h_c = 1.5$, are compared. The minimum normalized joint shear strength are 4.3 psi$^{0.5}$ (0.36 MPa$^{0.5}$) from specimen A0 (Karayannis et al., 2007) and specimen RCNH1 (Gencoğlu and Eren, 2002) whose beam reinforcement indices are equal to 3.6 psi$^{0.5}$ (0.30 MPa$^{0.5}$) and 5.4 psi$^{0.5}$ (0.45 MPa$^{0.5}$), respectively. It is reported in the literature that specimen RCNH1 (Gencoğlu and Eren, 2002) failed due to the widening of beam flexural cracks. On the other hand, the maximum normalized joint shear strength is obtained as 8.6 psi$^{0.5}$ (0.72 MPa$^{0.5}$) by averaging the shear strengths of the specimens BS-L, BS-U, and BS-L-LS (Wong, 2005) where beam reinforcements did not yield. Accordingly, their beam reinforcement index of 11.0 psi$^{0.5}$ (0.91 MPa$^{0.5}$) based on the yield strength, f_y, is an overestimation. As a result, the maximum joint shear strength for high aspect ratio appears to be bounded by the value of 9.0 psi$^{0.5}$ (0.75 MPa$^{0.5}$) rounding off the value of 8.6 psi$^{0.5}$ (0.72 MPa$^{0.5}$). Based on this comparison, the similar assumption can be made for the high joint aspect ratio that the joint normalized shear strengths are linearly proportional to the beam reinforcement index within a range of 4 psi$^{0.5}$ (0.33 MPa$^{0.5}$) to 9 psi$^{0.5}$ (0.75 MPa$^{0.5}$) as observed in the low joint aspect ratio data, refer to Figure II.4,. This assumption will be clarified by the ongoing tests having a larger beam longitudinal reinforcement ratio.

The non-dimensional parameter reflecting the effect of beam longitudinal reinforcement is selected as $\left(A_s f_y / b_j h_c \sqrt{f_c'}\right)\left(1 - 0.85 h_b / H\right)$ based on the global equilibrium and the joint strength normalization, as discussed in the subsequent Chapter III. This parameter reflects the joint shear demand at the onset of beam reinforcement yielding as well as beyond yielding if the beam reinforcement is assumed elastic-perfectly-plastic (EPP) material. From Figure II.4, it can be postulated that joint shear strength (vertical axis) is close to joint shear demand (horizontal axis) within the aforementioned ranges for each low and high joint aspect ratio. This observation is similar to that for unreinforced interior joints (Anderson et al., 2008). The three approximate values, 12 psi$^{0.5}$ (1.0 MPa$^{0.5}$), 9 psi$^{0.5}$ (0.75 MPa$^{0.5}$), and 4 psi$^{0.5}$ (0.33 MPa$^{0.5}$), shown in Figure II.4 are explained as follows: (1) the values of 12 psi$^{0.5}$ (1.0 MPa$^{0.5}$) and 9 psi$^{0.5}$ (0.75 MPa$^{0.5}$) are close to the maximum normalized joint shear strength having joint aspect ratio 1.0 and 1.5, respectively, as shown in Figure II.3, and (2) the value of 4 psi$^{0.5}$ (0.33 MPa$^{0.5}$) is coincident with the minimum normalized joint shear strength of unreinforced exterior joints suggested by Moehle (2008) based on the tests of Hakuto et al. (2000).

II-1.2.3 Effect of Column Axial Load

The effect of column axial load on the shear strength for reinforced and unreinforced joints is not completely understood. Some researches concluded that the joint strength is influenced little by the column axial load (Meinheit and Jirsa, 1977; Kurose et al., 1988; Kitayama et al., 1991; Pantazopoulou and Bonacci, 1992; and Vollum, 1998). Other researchers reported that the high axial load on column increased the joint strength in their tests (Beres et al., 1992; Clyde et al., 2000; Pantelides et al., 2002). In the case of weak column and strong beam design, increasing the

column axial load up to the column cross-section balanced point improves the joint shear strength because the column moment capacity is improved by the axial load. In the case of strong column and weak beam design, which is the case of most tests, high column axial load is expected to cause both beneficial and detrimental effects to the joint shear strength, as explained in the next paragraph. From the plot of experimental database shown in Figure II.5, little and unclear influence of column axial load on the joint shear strength is observed for the column axial load less than $0.2f_c'A_g$. Note that $A_g = h_c b_c$ is the gross area of the column cross-section. More test data for higher column axial load are needed to clarify the effect of column axial load.

The principal tensile strain in Equation (II.2), derived by Pantazopoulou and Bonacci (1992) has been used to explain the detrimental effect of the high column axial load by other researchers.

$$\varepsilon_1 = \frac{\varepsilon_x - \varepsilon_y \tan^2 \beta}{1 - \tan^2 \beta} \tag{II.2}$$

where ε_x and ε_y are the average joint transverse (horizontal) and longitudinal (vertical) strains, respectively, and β is the angle of inclination (from the horizontal axis) of the joint principal tensile strain. Note that the positive sign represents the tensile strain in this study. Pantazopoulou and Bonacci (1992) concluded that the principal tensile strain, ε_1, increases as the compressive column axial load increases the average compressive (negative) longitudinal strain, ε_y. This conclusion is based on the assumption that the principal tensile strain direction, i.e. the angle β, is fixed while the column axial load increases. However, the shear strain has to significantly increase to keep the principal tensile strain direction fixed which is unacceptable, Figure II.6(a). Equation (II.3a) shows that the principal tensile strain is not significantly affected by the change of the average compressive (negative) longitudinal strain if the shear strain, γ_{xy}, does not significantly change. This is more apparent if the average transverse strain is assumed to be zero, as shown in Equation (II.3b), refer to Figure II.6(b).

$$\varepsilon_1 = \frac{\varepsilon_x + \varepsilon_y}{2} + \frac{1}{2}\sqrt{\left(\varepsilon_x - \varepsilon_y\right)^2 + \gamma_{xy}^2} \tag{II.3a}$$

Letting $\varepsilon_x = 0$,

$$\varepsilon_1 = \frac{\varepsilon_y}{2} + \frac{1}{2}\sqrt{\varepsilon_y^2 + \gamma_{xy}^2} \tag{II.3b}$$

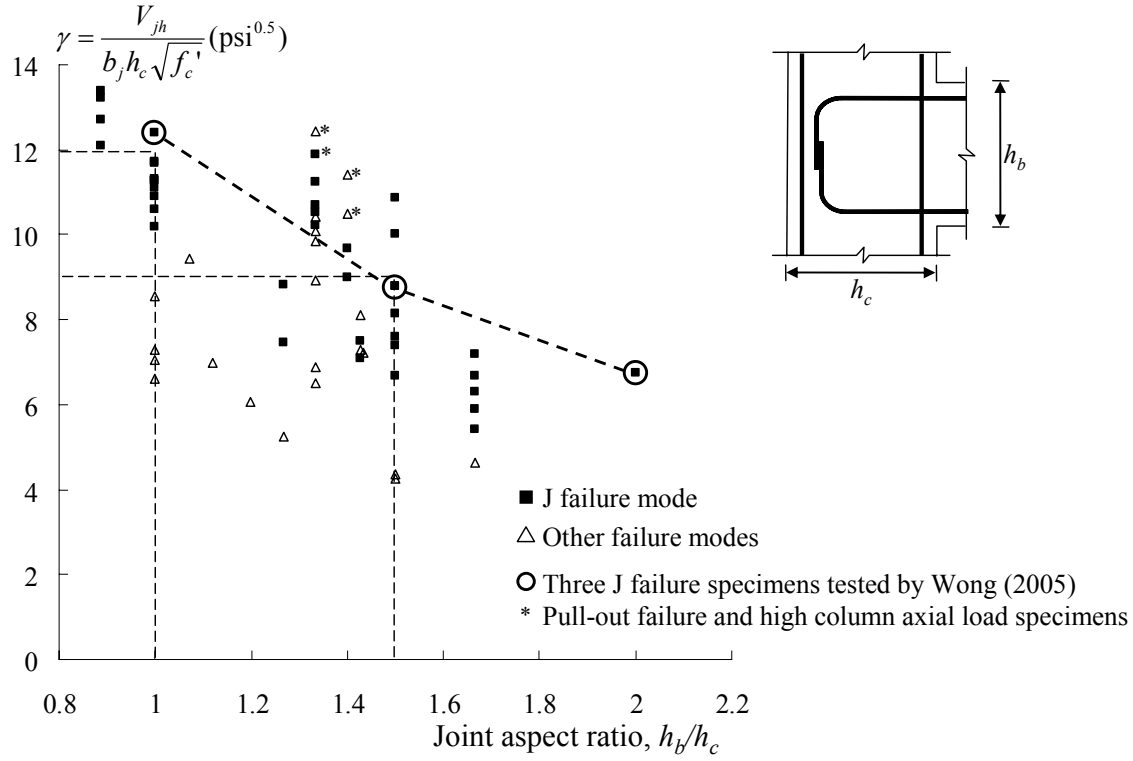

Note: $1.0\sqrt{f_c'}$ psi$^{0.5}$ = $0.083\sqrt{f_c'}$ MPa$^{0.5}$

Figure II.3 Effect of joint aspect ratio.

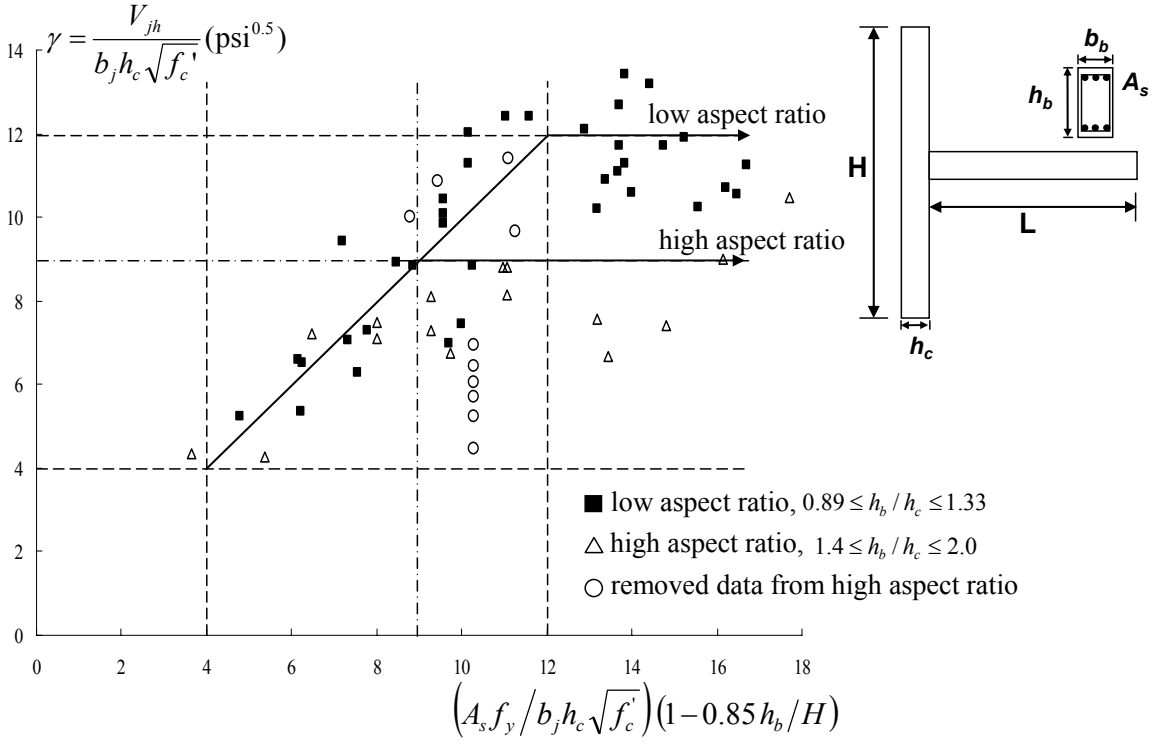

Note: $1.0\sqrt{f_c'}$ psi$^{0.5}$ = $0.083\sqrt{f_c'}$ MPa$^{0.5}$

Figure II.4 Effect of beam longitudinal reinforcement.

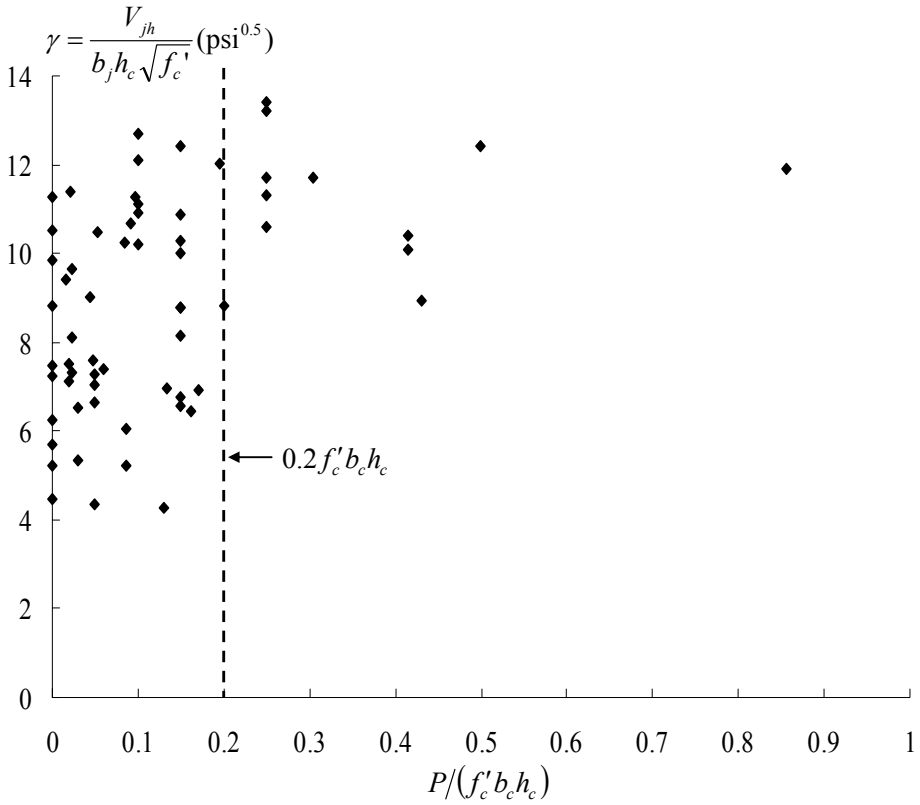

Note: $1.0\sqrt{f_c'}$ psi$^{0.5}$ = $0.083\sqrt{f_c'}$ MPa$^{0.5}$

Figure II.5 Complex effect of column axial load ratio.

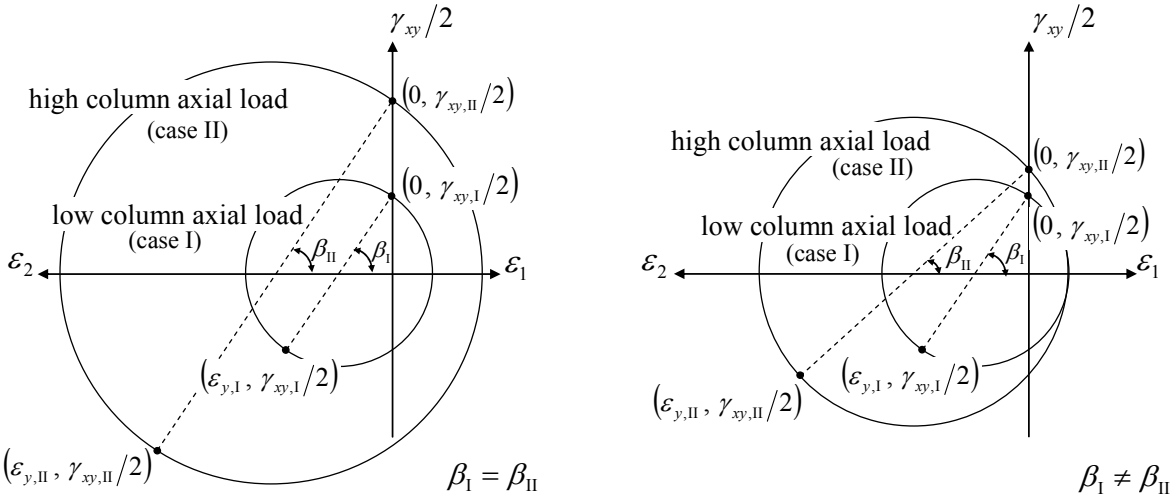

(a) constant principal directional angle (b) varying principal directional angle

Figure II.6 Change of principal strain due to column axial load ratio.

II-2 Joint Shear Strength Models

In this section, existing shear strength models are briefly introduced based on the category of underlying basic concepts, such as average plane stress and strain, strut-and-tie mechanism, single strut mechanism, and empirical model. This section also presents the methods to accommodate the variation of joint shear strength for different joint failure modes.

II-2.1 Database of Unreinforced Exterior and Corner Joints

II-2.1.1 Pantazopoulou and Bonacci Model

Pantazopoulou and Bonacci (1992) developed a shear strength model of reinforced interior joints based on mechanical considerations, i.e., kinematics, equilibrium, and material constitutive relationships, under the assumption that the joint is well confined such that average stress and strain values are applicable, refer to Figure II.7. Pantazopoulou and Bonacci (1992) defined two types of joint failure without yielding of joint reinforcement: (1) column reinforcement yielding and (2) concrete crushing in the principal compressive stress direction. The joint shear stress (v_{jh}) at each failure type is calculated as follows:
For joint failure by column reinforcement yielding,

$$v_{jh} = \sqrt{\left(\rho_x f_y + \frac{P_x}{b_c h_b}\right)\left(\rho_y f_y + \frac{P}{b_c h_c}\right)} \tag{II.4}$$

where ρ_x and ρ_y are the area ratio of joint transverse reinforcement including beam longitudinal reinforcement, and column longitudinal reinforcement, respectively, f_y is the yield strength of both beam and column reinforcement, and P_x and P are the axial load in the beam and column, respectively.
For joint failure by concrete crushing,

$$v_{jh} = \sqrt{\left(f^c_{\max} - \rho_x f_y - \frac{P_x}{b_c h_b}\right)\left(\rho_x f_y + \frac{P_x}{b_c h_b}\right)} \tag{II.5}$$

where $f_c^{\max} = \lambda f_c'$ and $\lambda = \dfrac{1 + \rho_s f_y / f_c'}{0.8 - 0.34\varepsilon_1 / \varepsilon_0}$, ε_1 is the principal tensile (positive) strain, and ε_0 is the concrete compressive (negative) strain at the peak compressive stress.

II-2.1.2 Principal Tensile Stress Model

One approach to assess the shear strength of unreinforced joints is to compare the average principal tensile stress of the joint panel with some critical values representing diagonal cracking and shear failure. This approach has been traditionally used by many researchers to estimate the

concrete shear strength of column with different limits on the principal tensile stress. Under the assumption of no axial force in the beam, the principal tensile stress (σ_1) is calculated as follows,

$$\sigma_1 = -\frac{1}{2}\left(\frac{P}{A_g}\right) + \sqrt{\frac{1}{4}\left(\frac{P}{A_g}\right)^2 + \left(\frac{V_{jh}}{A_g}\right)^2} \tag{II.6}$$

where P is the column axial load (positive for compression in this case), V_{jh} is the horizontal joint shear force, and A_g is the gross area of the column cross-section, i.e. $A_g = b_c\ h_c$.

As shown in Figure II.8, Priestley (1997) suggested the lower limit of $\sigma_1 = 3.5\sqrt{f_c'}$ psi ($0.29\sqrt{f_c'}$ MPa) for joint shear cracking, and $\sigma_1 = 5.0\sqrt{f_c'}$ psi ($0.42\sqrt{f_c'}$ MPa) for maximum shear strength of an unreinforced exterior and corner joints. Kim and LaFave (2007) collected a large number of test data and observed that the first diagonal crack in the joint occurred generally at $\sigma_1 = 4.0\sqrt{f_c'}$ psi ($0.33\sqrt{f_c'}$ MPa). However, the principal tensile stress approach may be too conservative because more joint shear can be carried by the diagonal compression strut mechanism even after onset of diagonal cracking (Hakuto et al. 2000). Moreover, a high column axial load on the joint improves the joint shear strength based on Equation (II.6), which is not clearly concluded as discussed in Section II-1.2.3.

II-2.1.3 Tsonos Model

Tsonos (2007) proposed a new formulation to predict beam-column joint ultimate shear strength by adopting the biaxial concrete strength curve as a fifth-degree polynomial. In the case of unreinforced joints, joint shear strength is determined by the follow equation,

$$\left[\frac{\alpha\gamma}{2\sqrt{f_c}}\left(1+\sqrt{1+\frac{4}{\alpha^2}}\right)\right]^5 + 5\frac{\alpha\gamma}{\sqrt{f_c}}\left(\sqrt{1+\frac{4}{\alpha^2}}-1\right) = 1 \tag{II.7}$$

where γ is the horizontal joint shear stress normalized by $\sqrt{f_c'}$ and α is the joint aspect ratio, h_b/h_c.

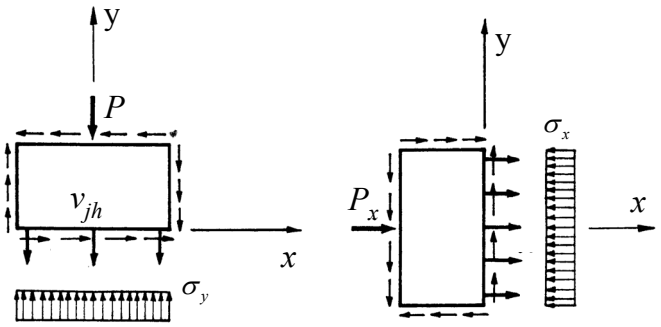

(a) Stress equilibrium

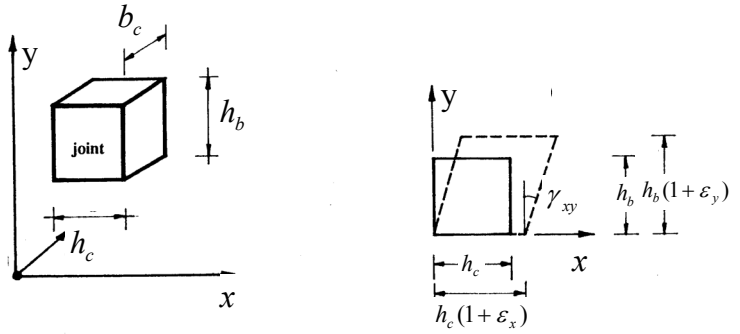

(b) Kinematics of joint

Figure II.7 Average stress and strain in joint (Pantazopoulou and Bonacci, 1992).

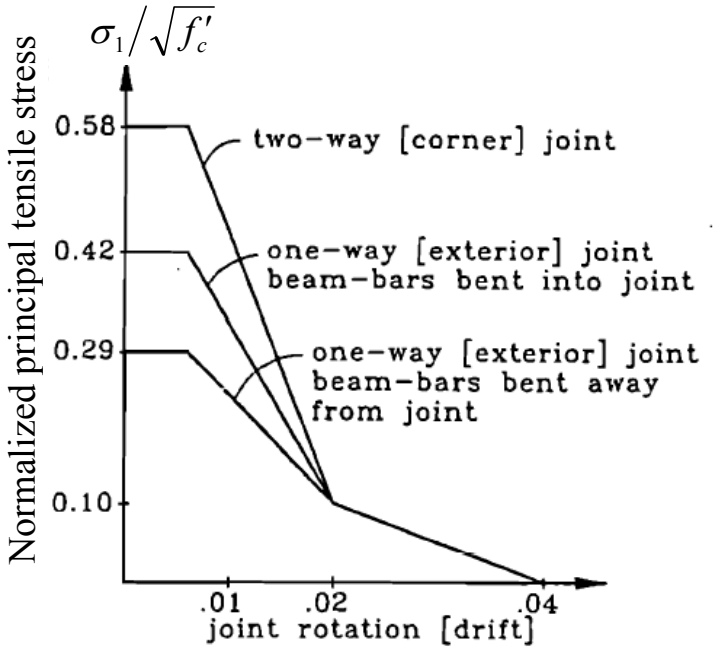

Figure II.8 Principal tensile stress limits in $MPa^{0.5}$ (Priestley, 1997).

II-2.2 Strut-and-Tie Mechanism

II-2.2.1 Ortiz Model

Ortiz (1993) used the SAT concept to predict the shear strength of exterior joints with and without transverse reinforcement. The concrete strength of the diagonal strut is taken as the design strength for cracked concrete proposed by the CEB Model Code (1990). Assuming the forces are identical in the column cross-section above and below the joint, the formulation is as follows,

$$D\ \sin\theta = F_v,\ \ D\cos\theta = V_{jh} \tag{II.8a}$$

$$F_v = T_c + C_c,\ \ V_{jh} = T_b - V_c \tag{II.8b}$$

$$D/(w_i b_c) = \sigma_d = 0.6 f_c'(1 - f_c'/250) \tag{II.8c}$$

where T_c is the tension of the column longitudinal bars, and T_b is the tension of the beam longitudinal bars in tension, as shown in Figure II.9(a). A strut depth is simply assumed to be

$$w_i = 0.45W \tag{II.9}$$

where $W = h_c \sin\theta + s\cos\theta$, $\theta = \tan^{-1}\left(\dfrac{F_v}{V_{jh}}\right)$, and s is the depth to the neutral axis of the beam from the extreme compression fiber at the intersection with the column. To determine the joint shear strength, V_{jh}, an iterative solution procedure is needed because W is a function of both s and θ which are dependent on the applied loading.

II-2.2.2 Vollum Model

Vollum (1998) constructed a SAT model for exterior joints with and without transverse reinforcement (Figure II.9(b)). The geometry of the top and bottom nodes is defined by the section analysis of beam and column under the Bernoulli assumption of a plane section remaining plane after bending. From the stress state and experimental observation, this model defines the joint shear failure when the maximum diagonal stress at the top node reaches the cracked concrete strength. The maximum stress and tensile strain are determined by

$$\sigma_d = \lambda f_c'\left[2\left(\frac{\varepsilon_2}{\varepsilon_o}\right) - \left(\frac{\varepsilon_2}{\varepsilon_o}\right)^2\right],\ \ \lambda = \frac{1}{0.8 - 0.34\dfrac{\varepsilon_1}{\varepsilon_o}} \tag{II.10a}$$

$$\varepsilon_1 = \varepsilon_h + (\varepsilon_h - \varepsilon_o)\cot^2\theta \tag{II.10b}$$

where ε_1 and ε_2 are principal tensile and compressive strain, respectively, ε_0 is the maximum compressive (negative) strain in the diagonal strut and assumed to be -0.002, and ε_h is tensile strain in the transverse direction.

Vollum (1998) introduced a coefficient k as shown in Figure II.9(b) for different levels of column axial load using one of Ortiz (1993) test results that failed in joint shear. The value of k is calibrated to be 0.4 under zero axial load. Then, two approaches were made to simplify the analytical model as follows,

Approach A

Two assumptions are made: (1) the column axial load is zero, which means ignoring the column load effect, and (2) the strut width is taken as $0.4h_c/\sin\theta$ where θ can be determined by the joint aspect ratio or the ratio of horizontal to vertical shear force. Then, the joint failure load is estimated by the following procedures:

1. Assume the joint failure load;
2. Calculate the corresponding forces in the column and beam cross-section;
3. Find the factor by which the tensile force in the column internal longitudinal bars, T_{si}, should multiplied to give the specified strut width of $0.4h_c/\sin\theta$; and
4. Calculate the stress in the inclined strut at the top node. If this is greater (or less) than the cracked concrete strength, increase (or reduce) the estimated failure load and repeat the analysis until the stresses are equal.

Approach B

The same procedures above are followed in this approach but all of the forces in the column and beam cross-section are calculated with accounting for the actual column axial load. This approach adjusts T_{si} until the minimum strut width is obtained, but it should be kept equal to or greater than $0.4h_c/\sin\theta$.

Vollum (1998) indicated that *Approach B* underestimates the joint shear strength at low to medium column loads for prediction of the reference test (Ortiz, 1993). Therefore, *Approach A* was selected due to its simplicity and accuracy for estimating the joint failure load.

II-2.2.3 Hwang and Lee Model

Hwang and Lee (1999) developed a joint shear strength model named as Softened Strut-and-Tie (SST) model by satisfying equilibrium, compatibility, and constitutive laws of cracked reinforced concrete. The SST model assumes that the joint shear resisting mechanisms consist of three mechanisms: (1) diagonal strut mechanism, (2) horizontal mechanism, and (3) vertical mechanism, as shown in Figure II.10.

Equilibrium

$$V_{jh} = D\cos\theta + F_h + F_v\cot\theta \tag{II.11}$$

where D is the compression force in the diagonal strut, F_h is the tension force in the horizontal tie, and F_v is the tension force in the vertical tie, and diagonal angle $\theta = \tan^{-1}\left(h_b''/h_c''\right)$ where h_b'' is the distance between the top and bottom beam reinforcement and h_c'' is the distance between the tail of the beam longitudinal reinforcement anchorage hook and the inner side of column longitudinal reinforcement as shown in Figure II.10. The fraction of each mechanism is

determined by the diagonal strut angle. The maximum compressive stress acting on the nodal zone of the diagonal strut is formulated as

$$\sigma_{d,\max} = \frac{1}{A_{str}}\left\{ D + \frac{\cos\left(\theta - \tan^{-1}\left(\frac{h_b''}{2h_c''}\right)\right)}{\cos\left(\tan^{-1}\left(\frac{h_b''}{2h_c''}\right)\right)} F_h + \frac{\cos\left(\tan^{-1}\left(\frac{2h_b''}{h_c''}\right) - \theta\right)}{\sin\left(\tan^{-1}\left(\frac{2h_b''}{h_c''}\right)\right)} F_v \right\} \tag{II.12}$$

where A_{str} is the effective area of the diagonal strut, $A_{str} = h_s b_j$, and

$$h_s = \left(0.25 + 0.85\frac{P}{A_g f_c'}\right) h_c \tag{II.13}$$

and b_j is defined following ACI 318-95 (1995).

Constitutive Law

The concrete strength in the diagonal strut follows the softening concrete model by Belarbi and Hsu (1995) as follows,

$$\sigma_d = \zeta f_c' \left[2\left(\frac{\varepsilon_2}{\zeta \varepsilon_0}\right) - \left(\frac{\varepsilon_2}{\zeta \varepsilon_0}\right)^2 \right] \quad \text{for} \quad \frac{\varepsilon_2}{\zeta \varepsilon_0} \le 1 \tag{II.14}$$

where the softening coefficient $\zeta = \frac{5.8}{\sqrt{f_c'}} \frac{1}{\sqrt{1+400\varepsilon_1}} \le \frac{0.9}{\sqrt{1+400\varepsilon_1}}$ and $\varepsilon_0 = -0.002 - 0.001\left(\frac{f_c' - 20}{80}\right)$ for $20 \le f_c' \le 100$ (MPa). The joint shear strength is defined when the compressive stress and strain of the diagonal strut reach their peaks as

$$\sigma_d = \zeta f_c' \quad \text{and} \quad \varepsilon_d = \zeta \varepsilon_0 \tag{II.15}$$

The behavior of the reinforcing steel is assumed to be elastic-perfectly-plastic.

$$f_s = E_s \varepsilon_s \quad \text{for} \quad \varepsilon_s < \varepsilon_y \tag{II.16a}$$

$$f_s = f_y \quad \text{for} \quad \varepsilon_s \ge \varepsilon_y \tag{II.16b}$$

where E_s and f_y are the elastic modulus and yield strength of reinforcing steel, respectively. From the above constitutive relationships, the horizontal and vertical tension tie forces are determined by

$$F_h = A_{th} E_s \varepsilon_h \le F_{yh} \quad \text{and} \quad F_{yh} = A_{th} f_y \tag{II.17a}$$

$$F_v = A_{tv} E_s \varepsilon_v \le F_{yv} \quad \text{and} \quad F_{yv} = A_{tv} f_y \tag{II.17b}$$

where A_{th} and A_{tv} are the areas of reinforcement in the horizontal and vertical directions, respectively, and ε_h and ε_v are the average strains in the horizontal and vertical directions, respectively.

Compatibility

The two-dimensional compatibility condition is constructed considering the average strains in the joint panel as follows,

$$\varepsilon_1 = \varepsilon_h + (\varepsilon_h - \varepsilon_2)^2 \cot^2 \theta \quad \text{(II.18a)}$$

$$\varepsilon_1 = \varepsilon_v + (\varepsilon_v - \varepsilon_2)^2 \tan^2 \theta \quad \text{(II.18b)}$$

where ε_1 and ε_2 are the average principal tensile and compressive strains, respectively.

To calculate the joint shear strength by SST model, an iterative solver is needed. The iterative solver controls the softening coefficient ζ such that this coefficient satisfies both equilibrium and compatibility. For unreinforced joints, the strain of the beam reinforcement is considered as the horizontal strain ε_h in Equation (II.18a). Similarly, the strain of the column reinforcement in tension is taken as the vertical strain ε_v in Equation (II.18b) if there is no column intermediate longitudinal bar(s) between inner and outer side of the joint. Since the horizontal and vertical strains are taken as the yield strains of beam and column longitudinal bars for unreinforced joints, this model is not able to predict the joint shear failure before beam and column longitudinal reinforcement yielding.

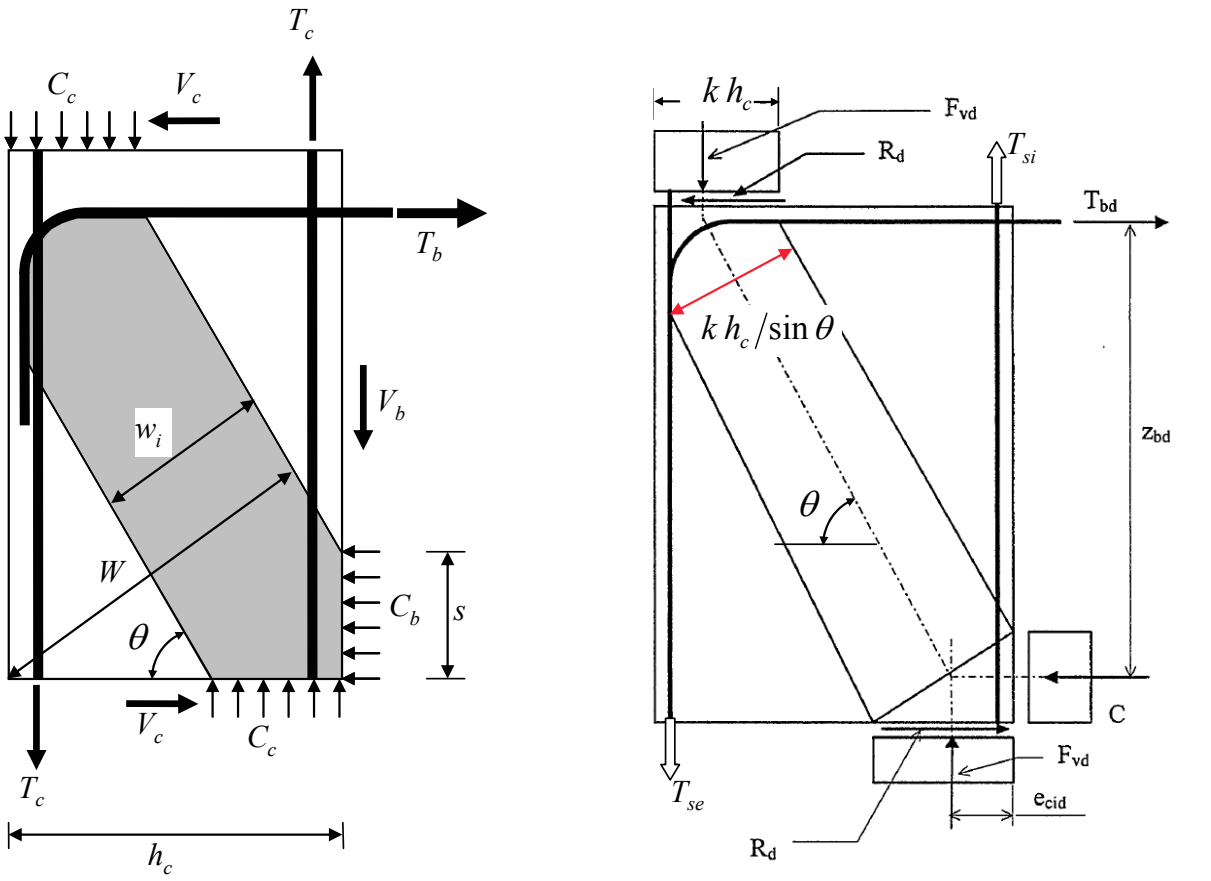

(a) Ortiz Model (b) Vollum Model

Figure II.9 Single Strut-and-Tie Models.

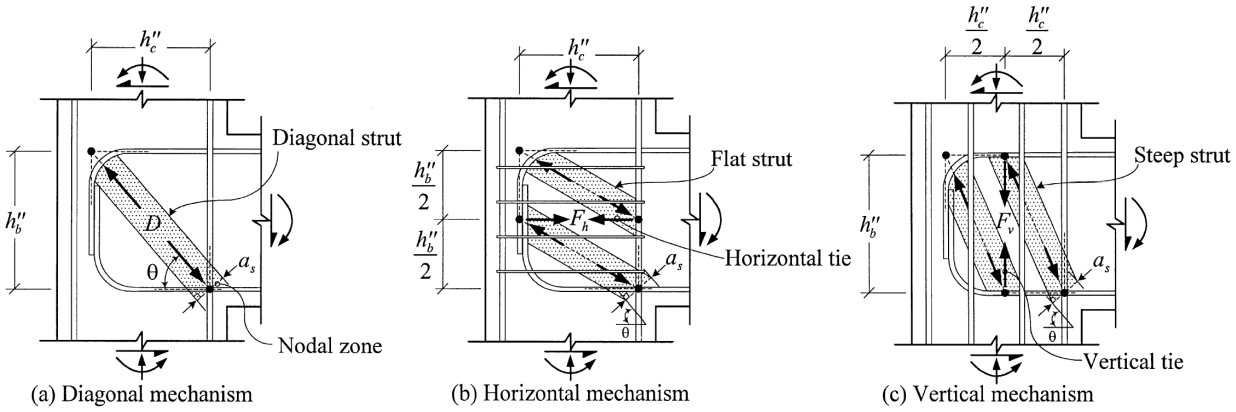

Figure II.10 Joint shear resisting mechanisms of SST model (Hwang and Lee, 1999).

II-2.3 Single Strut Mechanism

II-2.3.1 Zhang and Jirsa Model

Zhang and Jirsa (1982) developed an approach to determine the shear strength and behavior of beam-column joints under monotonic and cyclic loading from a large number of published test data. This model assumes that the joint shear strength is determined by the failure of a single diagonal strut whose strength is affected by several parameters: the concrete strength, the hinge mechanism, the column axial load, the transverse reinforcement ratio, the joint aspect ratio, and the existence of lateral beams. The effects of these parameters were derived by a statistical approach. The different joint strength equations for monotonic loading are given depending on the formation of plastic hinges in the beams adjacent to the joint.

For joint failure without beam hinge, $Q_m = K\zeta\eta f_c' b_c \sqrt{a_c^2 + a_b^2}\cos\theta$ (II.19a)

For joint failure with beam hinge, $Q_m = K\zeta\eta f_c' b_c a_c \cos\theta$ (II.19b)

where K represents the effect of concrete strength such that $K = 1.20 - 0.1 f_c'$, f_c' in ksi, ζ represents the effect of the volumetric transverse reinforcement ratio, ρ_s, as follows,

$$\zeta = 0.95 + 4.5\rho_s \le 1.20,\ 0.01 \le \rho_s \le 0.06 \tag{II.20}$$

η represents the effect of the lateral beams as

$$\eta = 0.85 + 0.30\frac{W_L}{h_c},\quad 0.5 \le \frac{W_L}{h_c} \le 1.0 \tag{II.21}$$

where W_L is the width of the lateral beam. a_c and a_b are the depth of the compression zone in column and beam, respectively, which are determined considering the effect of column axial load, θ represents the angle of inclination of the strut obtained as follows,

For joint failure without beam hinge, $\theta = \tan^{-1}\left[\left(h_b - \frac{2}{3}a_b\right)\Big/\left(h_c - \frac{2}{3}a_c\right)\right]$ (II.22a)

For joint failure with beam hinge, $\theta = \tan^{-1}\left[h_b\Big/\left(h_c - \frac{2}{3}a_c\right)\right]$ (II.22a)

The joint strength under cyclic loading was modified from the monotonic loading case by adding one parameter ξ as follows,

$$Q_c = \xi Q_m,\quad \xi = \begin{cases} 1.0 - 4.0R & \text{as an average value} \\ 0.83 - 4.0R & \text{for design purpose} \end{cases} \tag{II.23}$$

where R is defined as a rotation index, $R = \Delta/L$, Δ is total beam end deflection, and L is the length from the beam inflection point to the column face. The average value is determined by a statistical analysis of literature test data and the design value is the lower limit of those data.

II-2.3.2 ASCE/SEI 41-06

ASCE/SEI 41-06 (2006) suggests recommendations of shear strengths for unreinforced joints with referring to FEMA 356. According to ASCE/SEI 41-06, the nominal joint shear strength is defined as follows,

$$V_n = \gamma \sqrt{f_c'} b_j h_c \tag{II.24}$$

where γ is a coefficient to represent the joint geometry (that is, whether it is of exterior, interior, or knee configuration, and whether there is a beam framing into the joint in the orthogonal direction). For unreinforced exterior joints, the coefficient γ is equal to 6.0. The effective joint width b_j is defined by either ACI 318-08 or ACI 352R-02. According to ACI 318-08 and ACI 352R-02, the effective joint width b_j is defined as follows,

$$\text{ACI 318-08: } b_j = \text{the smallest of} \begin{cases} b_b + 2x \\ b_b + h_c \\ b_c \end{cases} \tag{II.25a}$$

$$\text{ACI 352-02: } b_j = \text{the smallest of} \begin{cases} \dfrac{b_c + b_b}{2} \\ b_b + \sum \dfrac{m b_c}{2} \\ b_c \end{cases} \tag{II.25b}$$

where x is the smaller distance between the beam and column edges, and $m = 0.3$ for joints where the eccentricity between the beam centerline and the column centerline exceeds $b_c/8$ and $m = 0.5$ for all other cases. Other terms follow the same definition made earlier in this study. Note that the summation term in Equation (II.25b) should be applied on each side of the joint where the edge of the column extends beyond the edge of the beam.

II-2.4 Empirical Models

II-2.4.1 Vollum Model

Vollum (1998) developed an empirical strength model based on SI units for exterior joints with and without transverse reinforcement. Vollum and Newman (1999) insisted that it is not feasible to develop a realistic SAT model due to the complexity of joint shear resisting mechanism. The following equation was developed and calibrated from published test data for unreinforced exterior joints,

$$V_{jh} = 0.642\,\beta\left[1 + 0.552\left(2 - h_b/h_c\right)\right] b_j\, h_c \sqrt{f_c'} \tag{II.26}$$

where β is a capacity reduction factor of not less than 0.8, and the effective joint width b_j is defined in this model as the smaller of $\left(b_b + b_c\right)/2$ and $b_b + b_c/2$ if $b_b < b_c$, and the smaller of $b_c + h_c/2$ and b_b if $b_b > b_c$.

II-2.4.2 Hegger et al. Model

Hegger et al. (2003) developed an empirical model based on SI units including the parameters of column reinforcement ratio and joint aspect ratio. The model is formulated as follows,

$$V_{jh} = \alpha_1\, A B C b_j\, h_c \tag{II.27}$$

where α_1 represents the effect of anchorage detail: $\alpha_1 = 0.95$ for a 90° degree hook and $\alpha_1 = 0.85$ for a 180° degree hook, A represents the effect of aspect ratio: $A = 1.2 - 0.3\,h_b/h_c, 0.75 \le h_b/h_c \le 2$, B represents the effect of column reinforcement ratio: $B = 1.0 + \left(\rho_{col} - 0.5\right)/7.5$ where ρ_{col} is the ratio of column longitudinal reinforcement in tension, and C represents the effect of concrete strength: $C = 2\sqrt[3]{f_c'},\ 20 \le f_c' \le 100$ MPa. Note that the effective joint width b_j is defined as the same as ACI 352R-02.

II-2.4.3 Bakir and Boduroğlu Model

Bakir and Boduroğlu (2002) developed an empirical model by regression of published test data. This model includes the parameters of the beam reinforcement ratio, $\rho = 100\,A_s/b_b d_b$, and the joint aspect ratio, h_b/h_c. The shear strength of unreinforced joints is calculated as follows,

$$V_{jh} = \frac{0.71\beta\,\rho^{0.43}}{\left(h_b/h_c\right)^{0.61}}\left(\frac{b_c + b_b}{2}\right) h_c \sqrt{f_c'} \tag{II.28}$$

where β represents the effect of anchorage detail: $\beta = 1.0$ for a 90° degree hook and $\beta = 0.85$ for a 180° degree hook. Note that Equation (II.28) is based on SI units. It is noted that the exponent value of 0.43 is actually 0.4289 in the published literature of this model.

II-2.5 Shear Strength Degradation

Joint shear failure modes are mainly divided into two cases: (1) joint shear failure without beam reinforcement yielding (J) and (2) joint shear failure with beam reinforcement yielding (BJ). The joint shear strength of the BJ failure mode is less than that of the J failure mode due to relatively lower beam longitudinal reinforcement ratio. To obtain the reduced shear strength of the BJ failure mode, two modification methods are adopted in the existing models.

II-2.5.1 Modification of Shear Strength

The simple method is to reduce joint shear strength as the ductility increases. Park (1997) proposed the simple linear degradation model of joint shear strength in terms of curvature ductility of the beam plastic hinges at the column faces (Figure II.11). The joint shear strength remains to be $\gamma = 12.0$ psi$^{0.5}$ (1.0 MPa$^{0.5}$) up to a ductility of 2 and thereafter decreases linearly to be $\gamma = 3.6$ psi$^{0.5}$ (0.3 MPa$^{0.5}$) at a ductility of 9. Similarly, Hakuto et al. (2000) suggested the degradation curve of joint shear strength in terms of the displacement ductility for unreinforced exterior joints. The maximum horizontal joint shear stress ratio, v_{jh}, is 0.17 f_c' at a displacement ductility factor $\mu \le 1$ and the minimum horizontal shear stress is 0.05 f_c' at $\mu = 8$ (Figure II.12). The joints having shear demand less than the minimum value do not experience shear failure, and beam flexural hinges are developed.

II-2.5.2 Modification of Diagonal Strut Width

Zhang and Jirsa (1982) used two different diagonal strut width equations, Equations (II.19a) and (II.19b), depending on the occurrence of a beam hinge mechanism. The diagonal strut width is less in case of joint failure with a beam hinge than that without a beam hinge and consequently the joint shear strength of the former case becomes less. However, it is not simple to predict the occurrence of a beam hinge mechanism in advance.

Hwang (2001) modified his SST model to add a ductility parameter in the equation to determine the strut width, a_s, as follows,

$$a_s = \sqrt{a_b^2 + a_c^2} - \left(\sqrt{a_b^2 + a_c^2} - a_c\right) \times \sqrt{\frac{\mu - 1}{3}} \qquad \text{(II.29)}$$

where a_b is the compression block in the beam section at the column joint face, assuming $a_b = 0.2\,h_b$, a_c is the compression block in the column section at the beam joint face, assuming $a_c = \left(0.25 + 0.85\,P / f_c' A_g\right) h_c$, and μ is the displacement ductility factor. As the ductility increases, the width of the diagonal strut decreases and thus the joint shear strength decreases.

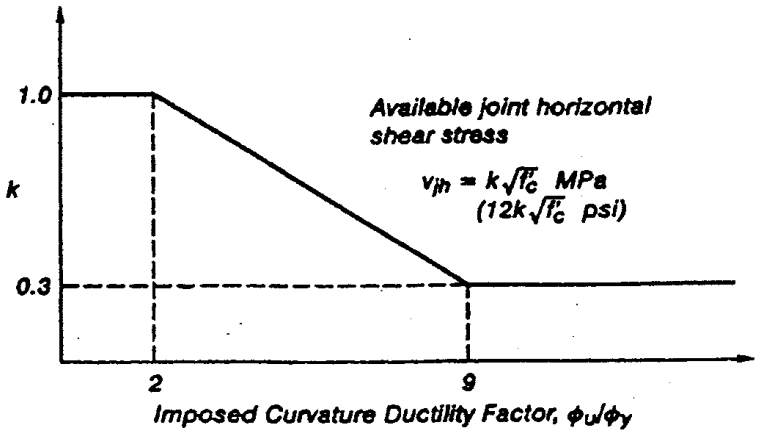

Figure II.11 Shear strength degradation by curvature ductility (Park, 1997).

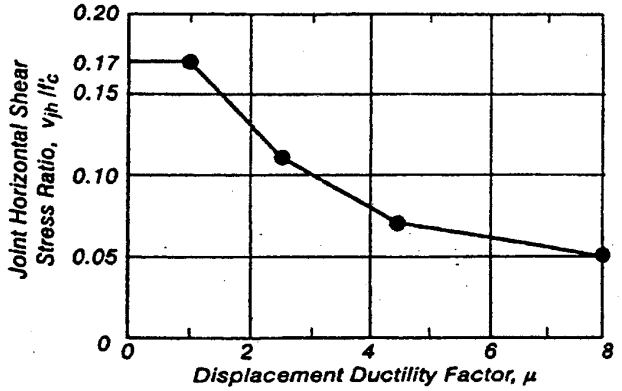

Figure II.12 Shear strength degradation by displacement ductility (Hakuto et al., 2000).

II-3 Macro-Models for Beam-Column Joints

There have been several attempts to simulate RC frames including the flexibility of beam-column joints. Due to the inherent complex behavior of RC beam-column joints, rotational spring elements have been used to reflect the shear deformation of the joint panel and the rotation due to bar slip. This section refers to Theiss (2005), and Celik and Ellingwood (2008) for the summary of the published macro-models for beam-column joints as shown in Figure II.13. The main features for each of the different macro-models are listed below.

***Alath and Kunnath* (1995), Figure II.13(a)**

- Zero length rotational spring and rigid links to represent joint panel geometry;
- Flexibility of rotational spring is determined using empirical joint shear stress-strain relationship;
- Including hysteretic degradation.

***Biddah and Ghobarah* (1999), Figure II.13(b)**

- Zero length rotational springs to consider separately joint shear deformation and bond-slip deformations;
- In an interior joint, two rotational springs for bond-slip deformation and one spring for joint shear deformation;
- In an exterior joint, one rotational spring for bond-slip deformation and one spring for joint shear deformation;
- Joint shear stress-strain relationship for rotational spring is defined as a trilinear idealization based on the softening truss model (Hsu 1988);
- The cyclic behavior includes hysteretic degradation without pinching effect;
- The bond-slip relationship is idealized with a bilinear model and cyclic pinching effect.

***Youssef and Ghobarah* (2001), Figure II.13(c)**

- Twelve translational zero length springs located at four beam-joint and column-joint interfaces to simulate inelastic behaviors (e.g., bond slip and concrete crushing);
- Two elastic diagonal springs to simulate joint shear deformation.

***Lowes and Altoontash* (2003) and *Mitra and Lowes* (2007), Figure II.13(d)**

- In each side, two springs for bar slip and one spring for shear at the interface, totaling twelve springs between external nodes and internal nodes in the interior joint;
- One rotational spring for joint shear distortion;
- Thirteen springs are needed for an internal joint, while ten springs are needed for an external joint;
- Lowes and Altoontash (2003) model used the modified compression field theory (MCFT) (Vecchio and Collins 1986) to derive the constitutive relationship of the joint panel;
- Mitra and Lowes (2007) model derived empirically diagonal concrete strut strength with the concept of confinement effect of transverse hoop suggested by Mander et al. (1988);

- "*beamColumnJoint*" element object in OpenSees represents the model by Mitra and Lowes (2007).

***Altoontash and Deierlein* (2003), Figure II.13(e)**

- Neglecting the component of shear at the interface from the model by Lowes and Altoontash (2003);
- one rotational spring per each side for beam and column end rotation due to bar slip;
- One rotational spring for joint panel distortion;
- Constitutive relationship of joint panel is still using MCFT (Vecchio and Collins 1986);
- "*Joint2D*" element object in OpenSees.

***Shin and LaFave* (2004), Figure II.13(f)**

- Assemble four rigid elements by hinge to represent the joint panel, and one rotational spring is located on one of four hinges;
- Two rotational springs (in series) are located between the beam and the joint to represent beam end rotations due to bar slip and plastic hinge rotation.

Multi-spring models in the above, except for Alath and Kunnath (1995), are intended to simulate more realistic behavior of beam-column joints but to need significant calibration per each spring based on test data. Even though the springs are calibrated from some test data, these springs do not ensure the accuracy of the analysis for other test results. Multi-spring models also have a high possibility of causing numerical divergence during frame analysis. Thus, a single rotational spring with a rigid panel to represent the joint geometry was adopted by Pampanin et al. (2003), Theiss (2005), and Celik and Elingwood (2008). Note that Pampanin et al. (2003) adopted the principal tensile stress model to predict the shear strength for joints but it did not account for the effect of varying column axial load to the joint strength which is an important factor of the principal tensile stress model. To include varying column axial load, Hertanto (2005) split the joint rotational spring into two springs. The properties of the two springs were identical and each spring had half of the joint strength and stiffness.

Backbone relationships of the joint rotational springs are expressed as joint moment-rotation relationships which can be obtained from joint shear stress-strain relationships once the dimensions of the frame and the joint are known, Figure II.14.

$$M_j = v_{jh} b_j h_c / \lambda \ , \ \lambda = \frac{2L}{(2L + h_c) j d_b} - \frac{1}{H} \tag{II.30a}$$

$$\theta_j = \gamma_{xy} \tag{II.30b}$$

where M_j is the moment, L is the length from the beam inflection point to the column face, H is the height between upper and lower column inflection points, d_b is the effective depth of the beam, jd_b indicates the internal moment arm of the beam cross-section at the beam-joint interface, θ_j is the joint rotation, and γ_{xy} is the shear strain of the joint.

To define the backbone curves for the joint shear stress-strain relationships, Celik and Elingwood (2008) adopted the *Pinching4* material object available in OpenSees (2010) as shown in Figure II.15(a). The key points of the envelope were defined based on the available test data in

the literature. Hertanto (2005) used the hysteresis model including the pinching behavior proposed by Pampanin et al. (2003) as shown in Figure II.15(b). The yielding point of the envelope is determined by the principal tensile stress limit proposed by Priestley (1997).

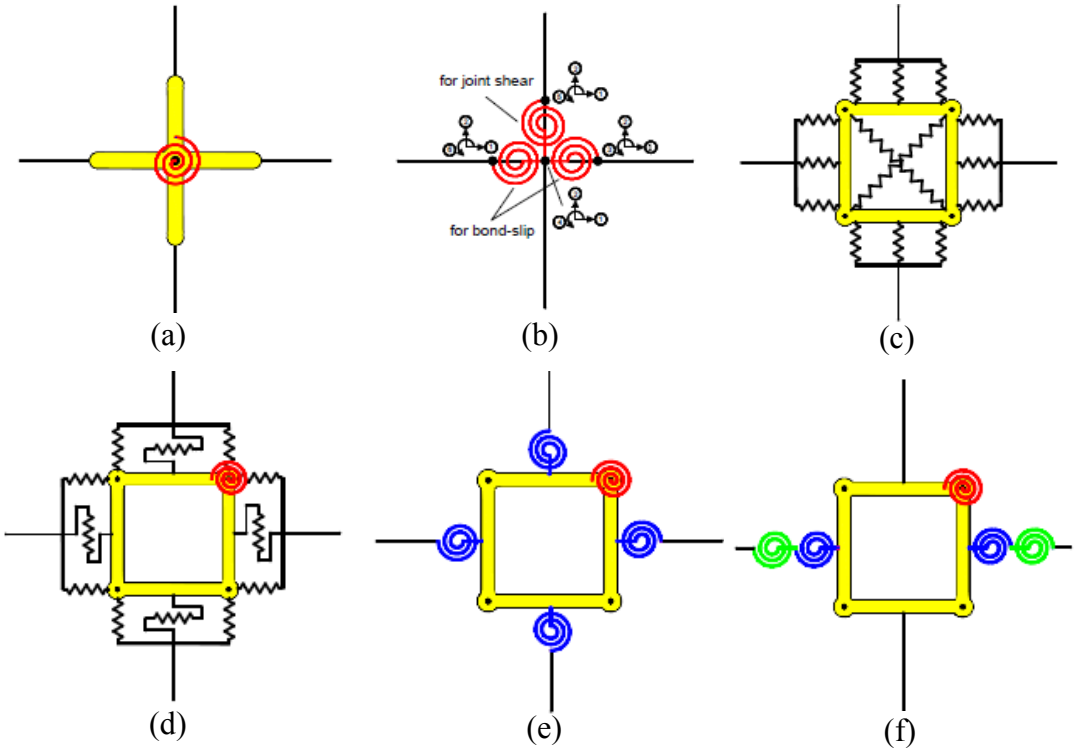

Figure II.13 Existing macro-models for beam-column joints (Celik and Elingwood 2008): (a) Alath and Kunnath (1995), (b) Bidda and Ghobara (1999), (c) Youssef and Ghobarah (2001), (d) Lowes and Altoontash (2003), (e) Altootash and Deierlein (2003), and (f) Shin and LaFave (2004).

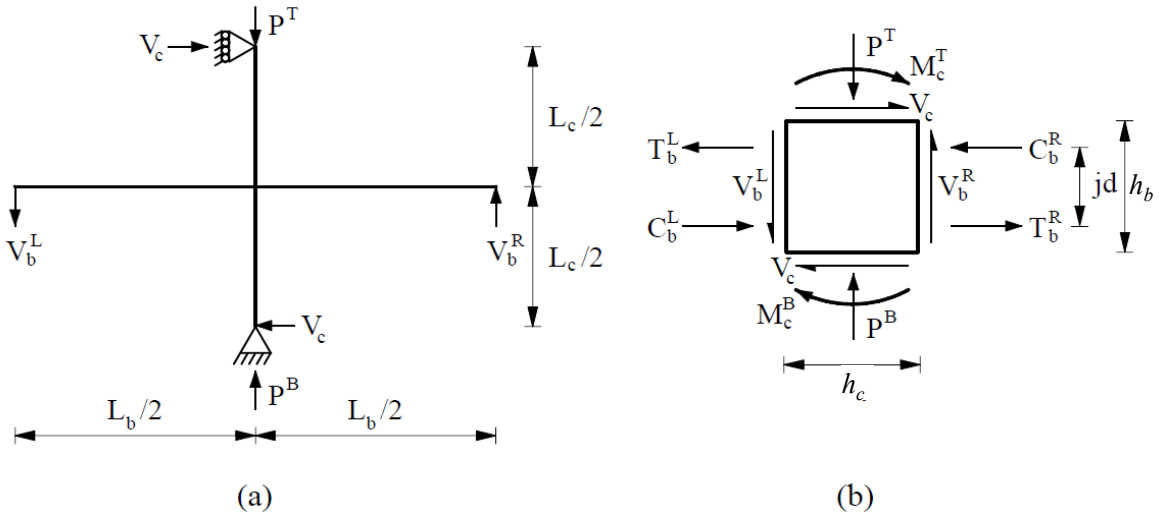

Figure II.14 Interior joint: (a) Global equilibrium and (b) Joint free body diagram (Celik and Elingwood, 2008).

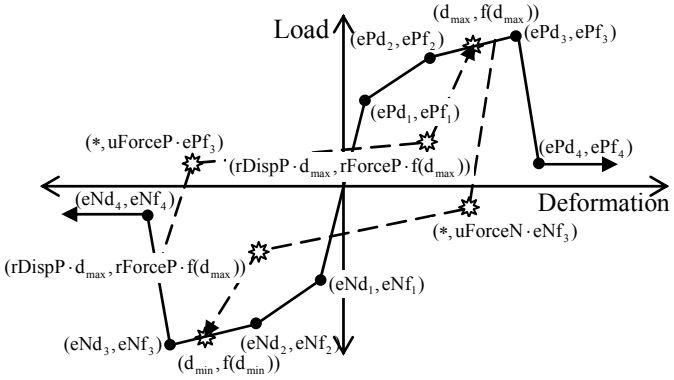

(a) *Pinching4* in Opensees

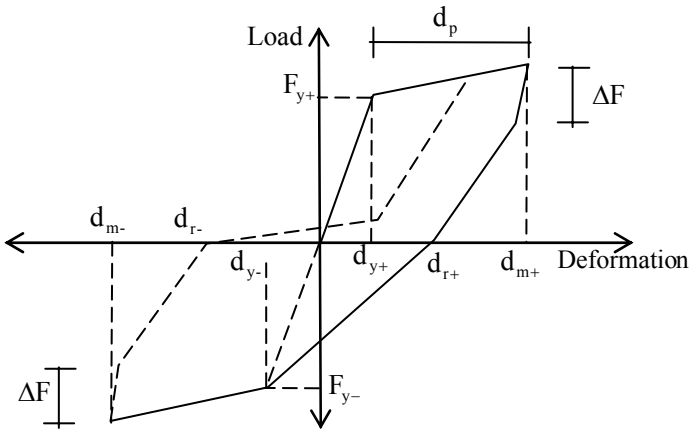

(b) Proposed curve by Pampanin et al. (2003)

Figure II.15 Backbone curves of joint rotational spring.

III Development of Joint Shear Strength Models

This chapter presents the development of shear strength models for unreinforced exterior and corner joints by two different approaches. One model is developed by mechanistic and empirical approach, which is named semi-empirical model. The other model is developed by solely an analytical approach utilizing available mechanistic concepts and formulae and is named analytical model.

III-1 Semi-Empirical Model

In this section, parametric equations are derived based on mechanistic concepts and some coefficients of these equations are determined relying on the database presented in Chapter II. Two parameters, namely the joint aspect ratio and the beam reinforcement index, are selected to derive the shear strength equation, while the effect of column axial load is not included due to the aforementioned reasons in Chapter II. Moreover, in the typical range of column axial load, it is found that joint shear strengths are affected little by the column axial load as shown in Figure II.5. For consistency with current practice, the joint shear strength is assumed to be proportional to the square root of the concrete standard compressive strength (ACI 318-08, 2008).

III-1.1 Joint Aspect Ratio Parameter

Assuming that a single diagonal strut resists all the horizontal shear force in the joint panel, as illustrated in Figure III.1, the equilibrium equation is derived as follows,

$$V_{jh} = c_0 D\cos\theta,\ \theta = \tan^{-1}\left(h_b / h_c\right), \text{ and } \ D = \sigma_d b_j h_s \tag{III.1}$$

where c_0 is a constant to represent strength reduction of the strut due to crack localization in the joint region, it is equal to 1.0 if cracks are distributed in the joint region as a softened concrete strength model assumes, while it is less than 1.0 to consider the reduction of strength estimated from a softened concrete strength model if cracks are localized at the C-C-T nodal zone. D is the compressive force in the diagonal strut with σ_d as its softened concrete strength and h_s is its width at the C-C-T nodal zone, Figure III.1. To express the joint shear strength in terms of $\sqrt{f_c'}$, a practical softening concrete model suggested by Vollum (1998) is adopted to develop a relevant model for the concrete panel of unreinforced joints, i.e.

$$\sigma_d = \frac{a_1\sqrt{f_c'}}{0.8 + 170\,\varepsilon_1} \tag{III.2}$$

where a_1 is a constant with values of 71 psi$^{0.5}$ and 5.9 MPa$^{0.5}$, and ε_1 is the principal tensile strain. For adequacy of Vollum model (1998), Table III.1 presents that Equation (III.2) is almost identical with another softened concrete strength model proposed by Zhang and Hsu (1998) within $0.003 \le \varepsilon_1 \le 0.004$ where the joint failure expects as subsequently discussed,

$$\sigma = \frac{\widetilde{a}_1 \sqrt{f'_c}}{\sqrt{1 + 250\,\varepsilon_1}} \tag{III.3}$$

where $\widetilde{a}_1$ is a constant with values of 70 psi$^{0.5}$ and 5.8 MPa$^{0.5}$. Zhang and Hsu model (1998) was developed using their test data and it has been adopted by other researchers.

In the existing analytical models (Vollum, 1998; Hwang and Lee, 1999), the strain compatibility equations in an average sense (Equations II.18a and b) are adopted to determine ε_1, assuming that the principal tensile direction is simply orthogonal to the assumed diagonal strut. Since the compatibility equations in an average sense are generally valid for the membrane element having longitudinal and transverse reinforcement, these equations may not be applicable to unreinforced exterior joints for two reasons: (1) there is no longitudinal and transverse reinforcement in the joint panel, and (2) the angle, θ, is defined by the given joint geometry. The softening SAT model by Hwang and Lee (1999) takes the vertical strain as the tensile yield strain of column reinforcement to calculate the principal tensile strain. Contrarily, the column bars located in the nodal zone of diagonal strut is subjected to compression, as presented in Figure III.1. Moreover, the assumed yield strain is not representative if the reinforcement does not yield.

In this study, the principal tensile strain at the joint failure is determined by comparing the concrete strength calculated by Equation (III.2) with that of the C-C-T node suggested by previous researchers and current codes. The selection of the C-C-T node is supported by the observation of literature experimental tests that the joint failures are generally initiated adjacent to the anchorage hook of beam longitudinal bars being in tension where the node is considered as a node anchoring one tie, i.e. C-C-T node, refer to Figure III.1. Similarly, the joint shear strength model by Vollum (1998) defines the joint shear failure when the maximum diagonal stress at the C-C-T node reaches the cracked concrete strength, as presented in Chapter II. The strength reduction factors for a C-C-T node in the literature and codes are compared in Table III.2, where code safety factors are excluded for proper comparison. Figure III.2 shows that the principal tensile strain at the joint failure can be considered to have an average value of 0.0035 to be used in Equation (III.2) by the comparison with different strength reduction factors presented in Table III.2 for concrete strength ranging from 3000 psi (20.7 MPa) to 7000 psi (48.3 MPa). The selected principal tensile strain at joint failure is justified by a conservative choice within mean value plus about one-half standard deviation from the published experimental data presented in Table III.3. In addition, the principal tensile strain is assumed to be slightly greater for a higher joint aspect ratio based on the joint shear strain measured from the subsequent experimental tests of this study. For simplicity, the principal tensile strain is proposed to be 0.0035 for $h_b/h_c = 1.0$ and 0.0040 for $h_b/h_c = 2.0$ as follows,

$$\varepsilon_1 \approx 0.0035 + 0.0005\left(\frac{h_b}{h_c} - 1\right) \tag{III.4}$$

The horizontal length of the C-C-T node, Figure III.1, is expressed using a constant *k* as follows,

$$h_s \sin\widetilde{\theta} = kh_c \tag{III.5}$$

where $\widetilde{\theta}$ is the angle of C-C-T node. Substituting Equations (III.2), (III.4) and (III.5) into Equation (III.1), the equilibrium equation becomes

$$V_{jh} = c_0 \left[\frac{a_1 \sqrt{f_c'}\, b_j k h_c}{\left(0.8 + 170\varepsilon_1\right) \sin\widetilde{\theta}} \right] \cos\theta \tag{III.6}$$

Dividing both sides by $\sqrt{f_c'} b_j h_c$, Equation (III.6) becomes

$$\frac{V_{jh}}{b_j h_c \sqrt{f_c'}} = a_2 \frac{\cos\theta}{1.31 + 0.085 \dfrac{h_b}{h_c}} \tag{III.7}$$

where $a_2 = c_0\, a_1\, k / \sin\widetilde{\theta}$ is a constant determined from the experimental database of unreinforced exterior joints. From the experimental database, it is found that the scatter in the joint shear strengths for a given joint aspect ratio is bounded between upper and lower limits. This finding is explained later by the analytical model developed in the subsequent section. For the upper limit on V_{jh}, a_2 is defined as 23 for psi units (1.9 for MPa units) by choosing $\gamma = 11.7$ for $h_b / h_c = 1.0$ from (Pantelides et al., 2002) and for the lower limit on V_{jh}, a_2 is defined as 10 for psi units (0.8 for MPa units) based on the comparison with the experimental database. An interesting finding is that the same value of a_2 for the upper limit is obtained by selecting relevant values of the coefficients as follows: (1) original value of a_1, i.e. 71 $\text{psi}^{0.5}$ and 5.9 $\text{MPa}^{0.5}$ according to Vollum (1998), (2) $c_0 = 1$ for the case of distributed cracks in the joint region, (3) k = 0.325 as a mean value of minimum, 0.25, and maximum, 0.4, from Hwang and Lee (1999) and Vollum (1998), respectively, and (4) $\sin\widetilde{\theta} = 1$ as commonly used in SAT models, e.g. (Hwang and Lee, 1999). It is worth mentioning that $\gamma = 11.7$ for $h_b / h_c = 1.0$ is similar to the shear strength for exterior joints, $\gamma = 12.0$, from ACI 352-02. The curves of Equation (III.7) for the proposed two values of a_2 are plotted on the experimental tests from the database for $0.8 \le h_b / h_c \le 2.2$ in Figure III.3. It is shown that Equation (III.7) and the two values of a_2 accurately represent the upper and lower limits of the joint shear strength from the database for different values of the joint aspect ratio.

Table III.1 Comparison of the softened concrete strength models.

f_c' (psi)	$\varepsilon_1 = 0.0030$		$\varepsilon_1 = 0.0035$		$\varepsilon_1 = 0.0040$	
	σ_{Vollum} [*1]	σ_{Zhang} [*2]	σ_{Vollum} [*1]	σ_{Zhang} [*2]	σ_{Vollum} [*1]	σ_{Zhang} [*2]
3000	2981	2894	2799	2796	2639	2707
4000	3442	3342	3233	3229	3047	3126
5000	3849	3736	3641	3610	3407	3495
6000	4216	4093	3959	3954	3732	3829
7000	4554	4421	4276	4271	4031	4135
8000	4868	4726	4572	4566	4309	4421
9000	5163	5013	4849	4843	4570	4689
10000	5443	5284	5111	5105	4818	4943
$\sigma_{\text{Vollum}}/\sigma_{\text{Zhang}}$	1.03		1.00		0.97	

[*1] strain-softened concrete compressive strength using Vollum model (Equation III.2);
[*2] strain-softened concrete compressive strength using Zhang and Hsu model (Equation III.3).

Table III.2 Strength reduction factor for a C-C-T node.

	Reference	η where $f_{c,node} = \eta f_c'$
(a)	Collins and Mitchell (1986)	0.75
(b)	Schlaich and Schäfer (1991)	0.68
(c)	MacGregor (1997)	$0.85\eta_1$, $\eta_1 = 0.55 + \eta_2/\sqrt{f_c'}$ [*1]
(d)	Jirsa et al. (1991)	0.80
(e)	ACI-318-08 Appendix A (2008)	0.68
(f)	AASHTO (1996)	0.75
(g)	CEB-FIP 1990 (1993)	$0.60\left(1 - f_c'/\eta_3\right)$ [*2]
(h)	DD ENV 1992-1-1 (1992)	0.70
(i)	CAN A23.3M94 (1994)	0.75
(j)	NZS 3101:Part 2 (1995)	0.55

[*1] $\eta_2 = 15$ for $\sqrt{f_c'}$ psi$^{0.5}$, $=1.25$ for $\sqrt{f_c'}$ MPa$^{0.5}$;
[*2] $\eta_3 = 36250$ for f_c' psi, $=250$ for f_c' MPa.

Table III.3 Measured joint shear strain and approximation of principal tensile strain.

Specimen	h_b/h_c	$P/A_g f_c'$	Shear strain γ_{xy}	$\varepsilon_1 \approx \gamma_{xy}/2$
Clyde[*1]-#2	0.89	0.10	7.18×10^{-3}	3.59×10^{-3}
Clyde[*1]-#6	0.89	0.10	4.81×10^{-3}	2.41×10^{-3}
Clyde[*1]-#4	0.89	0.20	8.45×10^{-3}	4.23×10^{-3}
Clyde[*1]-#5	0.89	0.25	4.84×10^{-3}	2.42×10^{-3}
Pantelides[*2]-#3	1.00	0.10	8.08×10^{-3}	4.04×10^{-3}
Pantelides[*2]-#4	1.00	0.25	4.73×10^{-3}	2.37×10^{-3}
Pantelides[*2]-#5	1.00	0.10	6.10×10^{-3}	3.05×10^{-3}
Pantelides[*2]-#6	1.00	0.25	6.54×10^{-3}	3.27×10^{-3}
Mean				3.17×10^{-3}
Standard Deviation				0.69×10^{-3}
COV				0.22

[*1] from Clyde et al. (2000); [*2] from Pantelides et al. (2002).

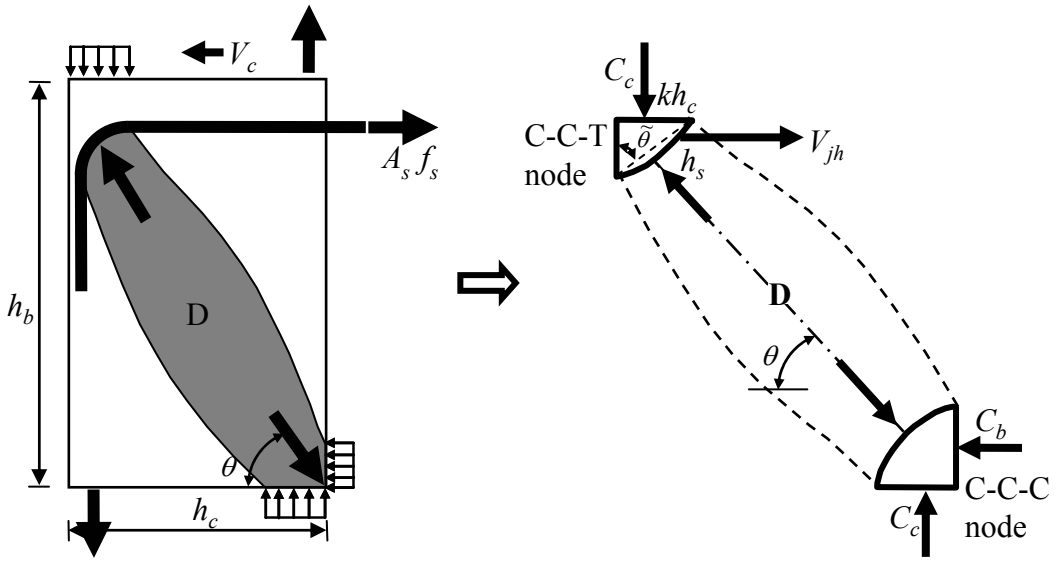

Figure III.1 Single diagonal strut mechanism.

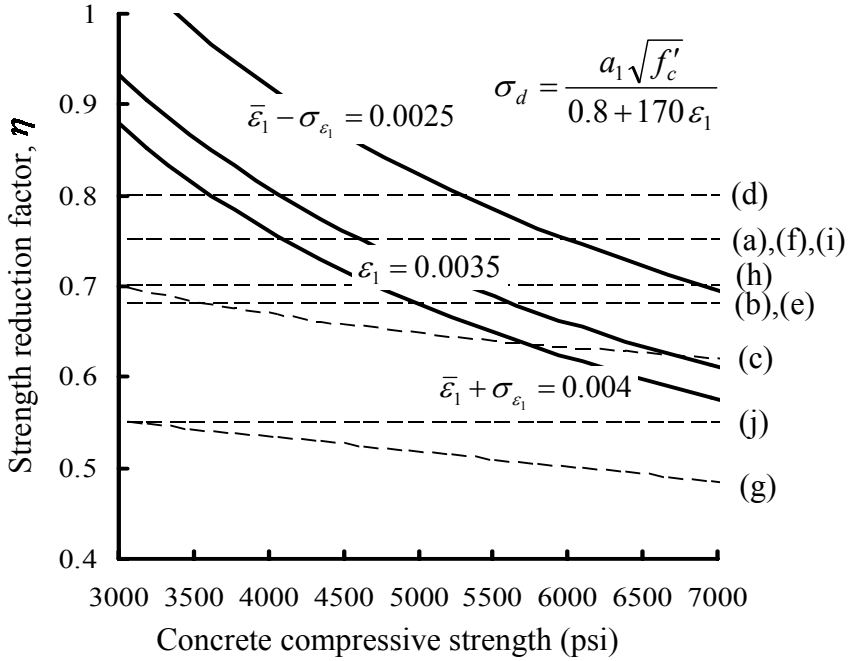

Figure III.2 Comparison of strength reduction factors at C-C-T node (see Table III.2 for (a)–(j) designation).

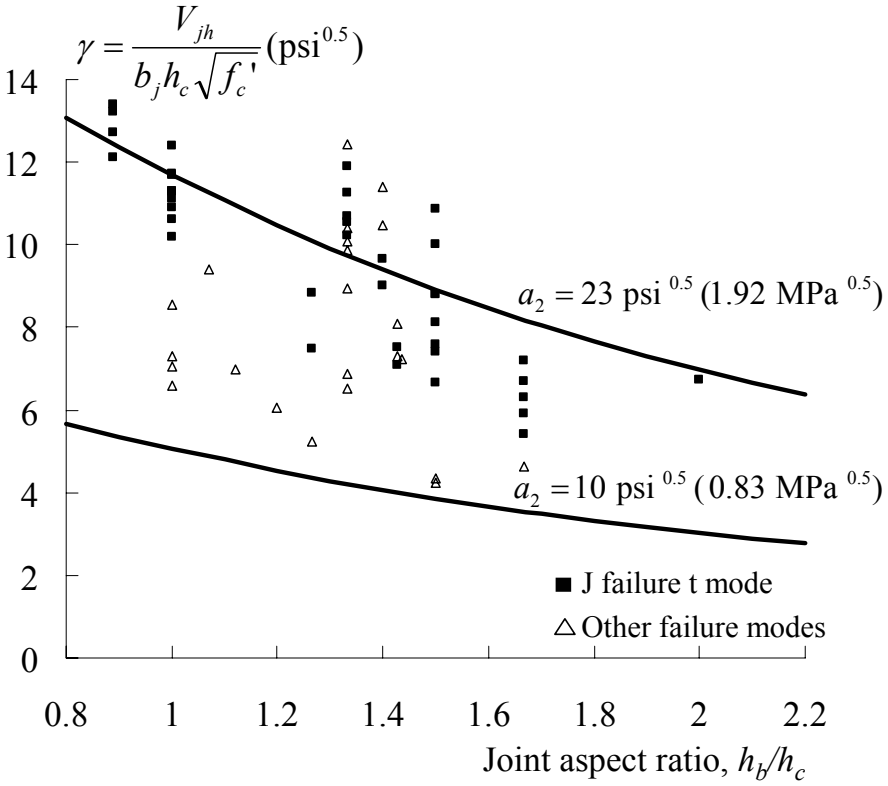

Figure III.3 Comparison of proposed joint aspect ratio equation with database.

III-1.2 Beam Longitudinal Reinforcement Parameter

The global equilibrium equation is derived from Figure III.4 as follows,

$$M_b = V_b \times L = A_s f_s \times jd_b \tag{III.8a}$$

$$V_c = \frac{L + h_c/2}{H} V_b \tag{III.8b}$$

where V_b and V_c are the beam and column shear forces, respectively, L is the length from the beam inflection point to the column face, H is the height between upper and lower column inflection points, A_s and f_s are the area and stress of beam reinforcement in tension, respectively, d_b is the effective depth of the beam, and jd_b indicates the internal moment arm of the beam cross-section at the column face. Accordingly, the horizontal shear force of the joint panel is calculated as follows,

$$V_{jh} = A_s f_s - V_c = A_s f_s \left(1 - \frac{L + h_c/2}{H} \frac{jd_b}{L}\right) \tag{III.9}$$

It is assumed that the beam reinforcement ratio affects the shear strength of unreinforced exterior joints showing the BJ failure mode only. This assumption is based on the fact that the joint shear strength for J failure does not increase beyond a certain amount of beam reinforcement as presented in Figure II.4. Therefore, $f_s = f_y$ can be used in Equation (III.9) assuming that the material of the beam reinforcement is elastic-perfectly-plastic (EPP). Dividing Equation (III.9) by $\sqrt{f_c'} b_j h_c$, the following equation is obtained,

$$\frac{V_{jh}}{b_j h_c \sqrt{f_c'}} = \left(\frac{A_s f_y}{b_j h_c \sqrt{f_c'}}\right)\left(1 - \frac{L + h_c/2}{H} \frac{jd_b}{L}\right) \tag{III.10}$$

Approximation can be made as follows,

$$jd_b = 0.8 h_b \Rightarrow \frac{L + h_c/2}{H} \frac{jd_b}{L} = \frac{L + h_c/2}{L} \frac{0.8 h_b}{H} \approx 0.85 \frac{h_b}{H} \tag{III.11}$$

Finally, Equation (III.10) can be simplified as follows,

$$\frac{V_{jh}}{b_j h_c \sqrt{f_c'}} \approx \left(\frac{A_s f_y}{b_j h_c \sqrt{f_c'}}\right)\left(1 - 0.85 \frac{h_b}{H}\right) = \mathrm{RI_b} \tag{III.12}$$

Based on the above equation, a non-dimensional parameter, referred to as the beam reinforcement index ($\mathrm{RI_b}$), is defined as $\left(A_s f_y / b_j h_c \sqrt{f_c'}\right)\left(1 - 0.85\, h_b / H\right)$ in this study. This parameter directly represents the joint shear demand at the onset of beam reinforcement yielding.

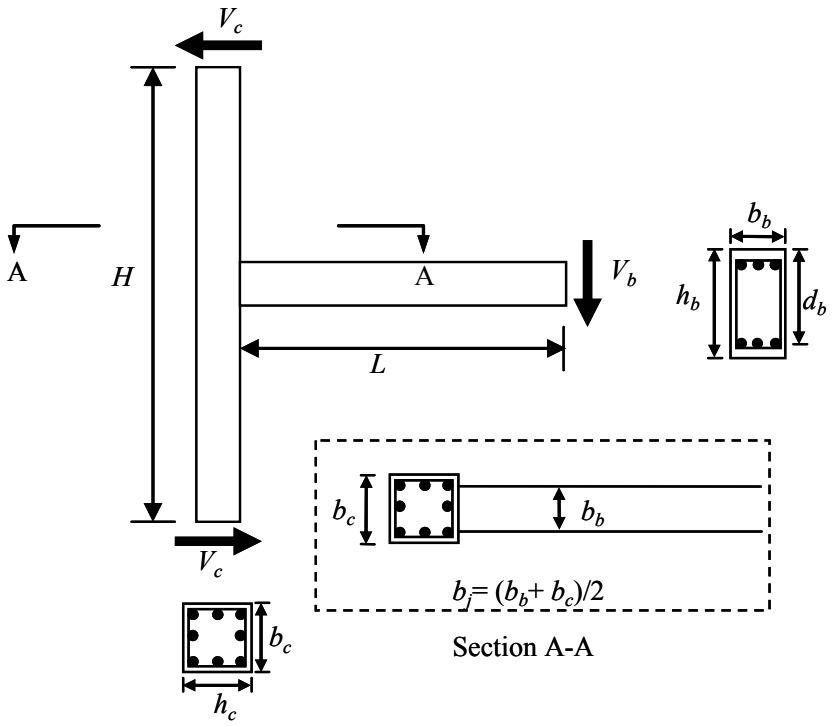

Figure III.4 Global equilibrium of an exterior beam-column joint.

III-1.3 Development of Semi-Empirical Model

To develop a semi-empirical model, two basic concepts are assumed as follows: (1) maximum and minimum joint shear strengths are affected by the joint aspect ratio and they are independent of the beam reinforcement index, and (2) joint shear strength is linearly proportional to beam reinforcement index between maximum and minimum joint shear strengths. In the first assumption, the maximum and minimum joint shear strengths dependency on joint aspect ratio is justified by the plots of Equation (III.7) on Figure III.3. The second assumption is based on the observation of low joint aspect ratio data from the database as shown in Figure II.4 in Chapter II. For the case of high joint aspect ratio, the same assumption is also made in this study with few data on Figure II.4 and utilizing the observation that the joint aspect ratio affects the equilibrium.

When the beam reinforcement index is located between the maximum and minimum strengths determined by Equation (III.7), the joint shear strength is equal to the beam reinforcement index multiplied by an over-strength factor, $\Phi \geq 1.0$. This factor considers the increase of beam reinforcement tensile stress due to strain hardening after beam reinforcement yielding. The over-strength factor is larger for smaller beam reinforcement index because a larger plastic strain is expected. For simplicity, Φ is assumed to be 1.25, i.e. $f_s = 1.25 f_y$, at the minimum joint shear strength and decreases linearly to $\Phi = 1.0$, i.e. $f_s = f_y$ at the maximum joint shear strength, refer to Figure III.5. It is to be noted that the over-strength factor 1.25 is commonly adopted to account for the effect of strain hardening for large curvature ductility (French and Moehle, 1991). Finally, the shear strength equation is proposed as follows,

$$\frac{V_{jh}}{b_j h_c \sqrt{f_c'}} = \Phi \left[\left(\frac{A_s f_y}{b_j h_c \sqrt{f_c'}} \right) \left(1 - 0.85 \frac{h_b}{H} \right) \right] \tag{III.13a}$$

$$a_{\min} \frac{\cos\theta}{1.31 + 0.085 \left(h_b / h_c \right)} \leq \frac{V_{jh}}{b_j h_c \sqrt{f_c'}} \leq a_{\max} \frac{\cos\theta}{1.31 + 0.085 \left(h_b / h_c \right)} \tag{III.13b}$$

where $a_{\min}$ is 10 for psi units (0.8 for MPa units) and $a_{\max}$ is defined as 23 for psi units (1.9 for MPa units). The procedures to predict the joint shear strength by the proposed model are summarized as follows:

1. Input the joint geometry, concrete strength, and joint aspect ratio;
2. Determine the minimum, $Y_{\min}$, and maximum, $Y_{\max}$, joint shear strengths as shown in Figure III.5;
3. Calculate the beam reinforcement index by Equation (III.12);
4. Check if the calculated beam reinforcement index is located between X_1 and X_2. If so, interpolate for the corresponding over-strength factor, Φ, as shown in Figure III.5; and
5. Calculate the joint shear strength by Equation (III.13).

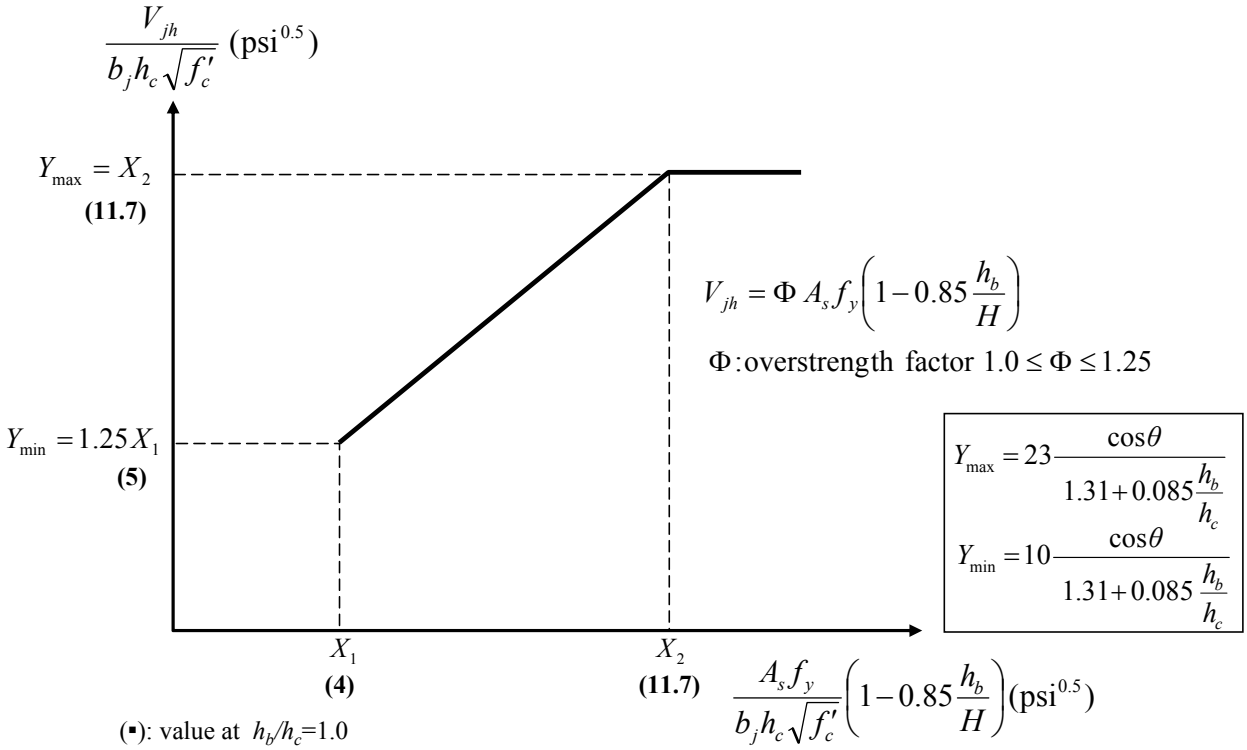

Figure III.5 Illustration of the proposed semi-empirical model.

III-1.4 Evaluation of Semi-Empirical Model

For verification of the semi-empirical model, the shear strengths of the database specimens presented in Chapter II are predicted and compared with their experimental results. The accuracy of the semi-empirical model is also compared with five existing strength models proposed by Vollum (1998), Hwang and Lee (1999), Bakir and Boduroğlu (2002), Hegger et al. (2003), and Tsonos (2007), refer to Figure III.6. It is worth mentioning that these five models are selected because they include either the development of a new strength equation or a modification of an existing one for unreinforced exterior joints. The proposed semi-empirical model predicts the joint shear strengths of the database with a mean value of 0.95 for the ratio between the test results and model predictions and a corresponding coefficient of variation (COV) of 16% as shown in Figure III.6(a). When the six tests by Parker and Bullman (1997) are excluded, the accuracy of the proposed model is improved to a mean value of 0.97.

Vollum (1998) model includes the effect of the joint aspect ratio but this model does not consider the change of the joint shear strength with the variation of beam longitudinal reinforcement. Due to the absence of beam longitudinal reinforcement parameter, this model overestimates the joint shear strength for the specimen showing BJ failure mode, while it shows accurate predictions for the specimens failing in J mode in which the joint shear strength is rarely influenced by the beam reinforcement. The evaluation results using this model are shown in Figure III.6(b).

Hwang and Lee (1999) model has been originally developed for reinforced joints and applied to unreinforced joints. As shown in Figure III.6(c), this model might be inappropriate for unreinforced joints because of the following reasons: (1) the average strain compatibility equations are not applicable to unreinforced joints as previously discussed, (2) column intermediate bars may not function as tension ties because they require steep angle of inclination of the struts, (3) it is assumed that the beam and the column reinforcements are yielding regardless of the joint shear failure mode, (4) only beneficial effect of column axial load on the joint shear strength is included, and (5) this model highly depends on the estimate of the diagonal strut width (Hwang and Lee, 2002).

Bakir and Boduroğlu (2002) mode shows good agreement with test data due to the inclusion of beam longitudinal reinforcement ratio, $100 A_s / b_b d_b$, and joint aspect ratio, h_b / h_c, refer to Figure III.6(d). However, this model has the defect that the parameter for beam longitudinal reinforcement ratio is expresses as an exponential function having an exponent value of 0.4289, which is determined by a statistical regression approach with relatively small data set.

Hegger et al. (2003) model includes the parameters of joint aspect ratio and column longitudinal reinforcement ratio. The evaluation results (Figure III.6(e)) show consistent overestimation of the joint shear strength. Based on the overestimation by this model, it can be concluded that the column reinforcement ratio is not an influencing parameter to predict the shear strength of unreinforced joints. This is attributed to the fact that the column reinforcement

ratio parameter was derived from best fitting of test data with large scatter for reinforced exterior joints.

Tsonos (2007) model overestimates the joint shear strengths of the database specimens, as shown in Figure III.6(f). This overestimation results from the use of the overly simplified average stress equilibrium equation and the increase of joint shear strength with increase of the joint aspect ratio, which is opposite of the observation from the database. This model was originally developed for reinforced joints and extended to unreinforced joints. Therefore, this model is inappropriate for predicting the shear strength of unreinforced joints.

From the above validation using a large experimental data set, the proposed semi-empirical model is shown to be more accurate and consistent for predicting the shear strength of unreinforced exterior joints than other existing models. This model can be easily implemented in many existing nonlinear structural analysis programs and also extended to other types of unreinforced joints for simulating older-type RC buildings, which is shown in Chapter VII.

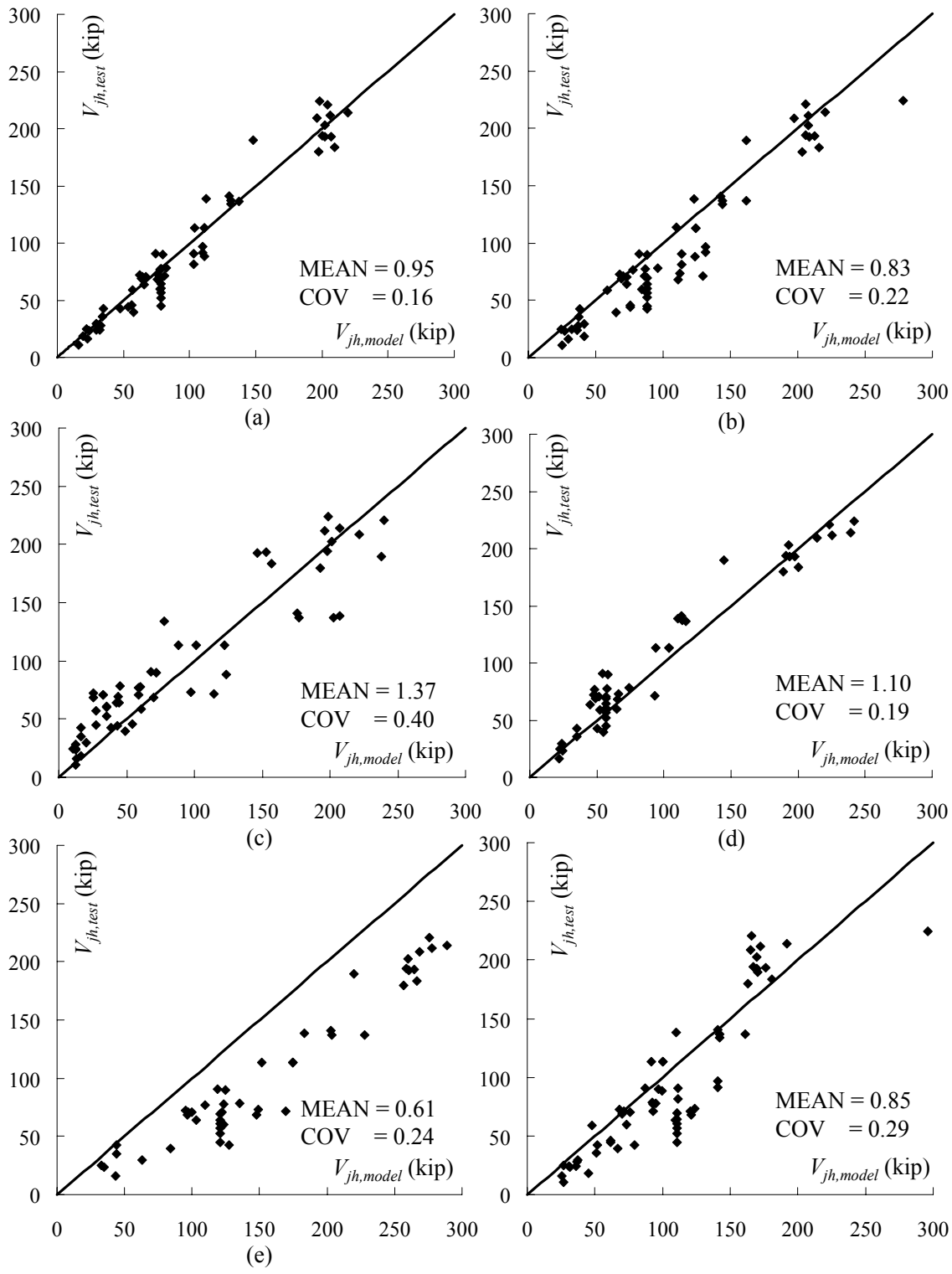

Note: Mean and COV = Coefficient of Variation for $V_{jh,test}/V_{jh,model}$, 1 kip = 4.45 kN

Figure III.6 Comparison of evaluation results: (a) Proposed model, (b) Vollum (1998), (c) Hwang and Lee (1999), (d) Bakir and Boduroğlu (2002), (e) Hegger et al. (2003), and (f) Tsonos (2007).

III-2 Analytical Model

III-2.1 Background

There have been many analytical studies to better assess the shear strength of unreinforced joints. As a result, several analytical models have been developed based on the average stress assumption or the strut-and-tie (SAT) approach with the average strain compatibility. However, the average principal stresses and strain compatibility equation using beam and column longitudinal reinforcement strains are inappropriate to represent the realistic behavior of unreinforced exterior joints where the joint shear failure is localized. Besides, the SAT approach faces the critical issue of estimating the diagonal strut area because the joint shear strength is sensitive to this estimated area (Hwang and Lee 2002).

From the literature study in Chapter II, the analytical joint strength model developed in this study is motivated by the following observations. First, it is reported that unreinforced exterior joints having the same concrete strength and geometry fail at different levels of joint shear stress demand with changing beam reinforcement ratio. This is an interesting observation considering that the unreinforced exterior joint resembles an unconfined concrete rectangular cuboid with seemingly unique strength. Second, to obtain the reduced shear strength of unreinforced exterior joints for joint shear failure following beam reinforcement yielding, two modification methods are adopted in the existing models as discussed in Section II-2.5: (1) directly reducing the joint shear strength by a ductility factor (Park, 1997; Hakuto et al., 2000), and (2) reducing the area of diagonal strut by a ductility factor (Hwang et al., 2001). The relationship between the reduction of joint shear strength and the ductility factor is proposed empirically in each model. The ductility factor can be defined in different ways and it includes the deformation of other members in addition to the joint distortion. Therefore, the empirically proposed relationships can not be generalized to other cases. Moreover, these two modification methods require monitoring the ductility factor during the analysis of the specimen or the frame, which means that it is impossible to predict the joint shear strength before analyzing the whole frame.

The newly proposed analytical approach is intended to fulfill the following objectives:

1. For two joint failure modes, i.e. joint shear failure with and without beam reinforcement yielding, the proposed analytical model accurately predicts the shear strength of unreinforced exterior joints by a consistent procedure, i.e. without including a ductility factor;
2. The solution algorithm is suitable for practical applications;
3. The new approach does not require the estimation of the diagonal strut area, A_{str}.
4. The new approach can be used to establish an envelope of the shear stress–strain relationship which can be transformed to the moment–rotation relationship of a joint rotational spring representing the joint region.

III-2.2 Development of Analytical Model

III-2.2.1 Assumption

Tests by Wong (2005) show that the joint shear strength for the detail of beam reinforcement hook bent out of the joint region is less than that for beam reinforcement hook bent into the joint region, as shown in Figure III.7. The reduction of the joint shear strength for the former detail can be related to less contribution of the diagonal strut crossing each corner of the joint panel if the development lengths are the same for both details. The comparison between the two different details motivates the assumption that the joint shear is resisted by two inclined struts in the joint region and their contributions are affected by the anchorage details of the beam longitudinal tension reinforcement.

In the proposed model, two inclined struts are first assumed to resist the horizontal joint shear (Figure III.8) in parallel, where the horizontal joint shear force is resisted by the sum of the two horizontal components of the two struts but the shear distortion is uniformly distributed. The strut named as ST1 is developed by the 90^{o} hook of beam reinforcement, while the other inclined strut (ST2) is developed by the bond resistance of the concrete surrounding the beam reinforcement. The contribution of ST2 has been generally ignored in single strut models for unreinforced joints. In this study, the anchorage detail of beam longitudinal bars is limited to both hooks of the top and bottom bars bent into the joint region. Presumably, the fraction of each strut in this detail can be determined by the level of beam reinforcement tensile stress which is related to the bond resistance, as discussed later in this section.

The second assumption is that the joint shear failures are initiated adjacent to the top node of ST1 under the loading condition of top beam longitudinal reinforcement in tension. This assumption is made for two reasons: (1) the top node is considered as a node anchoring one tie, i.e. C-C-T node, and (2) the crack width is greatest at the top node. Hence, such crack morphology reduces the strength of the nodal zone, which can be estimated using a softened concrete constitutive model. In particular, this crack pattern is observed in unreinforced exterior and corner joints from published tests. Therefore, the proposed model is applicable to these two unreinforced joints because the shear strength of exterior joints with lateral beams on two sides of the joint increases significantly compared with the other two cases (Zhang and Jirsa, 1982; Ohwada, 1977).

The third assumption is that the proposed model uses the softening concrete model suggested by Vollum (1998), i.e. Equation (III.2), and the principal tensile strain equation proposed in the semi-empirical model, i.e. Equation (III.4), for developing this analytical model.

III-2.2.2 Equilibrium

The joint shear force is estimated from the global equilibrium of a joint panel as derived in Equation (III.9). By approximation, the equation is simplified as follows,

$$V_{jh} = A_s f_s - V_c \approx A_s f_s \left(1 - 0.85 \frac{h_b}{H}\right) \quad \text{(III.14)}$$

Total horizontal joint shear force is assumed to be the sum of shear resistances by two struts ST1 and ST2 shown in Figure III.8. The equilibrium of each strut in horizontal direction is derived using bond stress between beam longitudinal reinforcement and surrounding concrete in the joint region.

$$V_{jh} = V_{jh,ST1} + V_{jh,ST2} \quad \text{(III.15a)}$$

$$V_{jh,ST1} = A_s f_s - n\pi\phi_b \int_0^{l_h} \mu(f_s)\, dx \quad \text{(III.15b)}$$

$$V_{jh,ST2} = n\pi\phi_b \int_0^{l_h} \mu(f_s)\, dx - V_c \quad \text{(III.15c)}$$

where n is the number of beam longitudinal bars in tension with diameter ϕ_b, and V_c is the shear force in the column. Note that $\mu(f_s)$ is the bond stress distribution along the beam longitudinal bar (Figure III.8) as a function of the tensile stress of the bar, f_s, which varies with the distance x, i.e. $f_s = f_s(x)$. The x-axis and l_h are depicted in Figure III.8. The horizontal projection of the width of the diagonal strut ST1 at the nodal zone is estimated using two available models: (1) $a_c = 0.4\, h_c$ by Vollum (1998), and (2) $a_c = \left(0.25 + 0.85P / f_c' A_g\right) h_c$ by Hwang and Lee (1999). Note that P is the column axial load and A_g is the gross area of the column cross-section. Therefore, the horizontal projection of the inclined strut ST2 can be obtained as follows,

$$l_h = h_c - a_c \quad \text{(III.16)}$$

In this study, the horizontal projection l_h is investigated from $0.6h_c$ corresponding to Vollum (1998) to $0.75h_c$ corresponding to Hwang and Lee (1999) with assuming column axial, P=0.

The column shear force is excluded in the equilibrium of the diagonal strut ST1, Equation (III.15b), and included in the equilibrium of the inclined strut ST2, Equation (III.15c), because most of the column shear force is concentrated in the middle of the column cross-section due to flexural cracks forming at both sides of the rectangular column cross-section under reversed cyclic loading. In addition, the vertical component of ST2 is equilibrated by an inclined strut in the column, as shown in Figure III.8, where the horizontal components of ST2 and this inclined strut in the column are represented by $V_{jh,ST2}$ in Equation (III.15c).

III-2.2.3 Fraction Factor

The contribution of struts ST1 and ST2 shown in Figure III.8 to the total horizontal joint shear force can be expressed using a fraction factor α as follows,

$$V_{jh,ST1} = \alpha V_{jh} \quad \text{(III.17a)}$$

$$V_{jh,ST2} = (1 - \alpha) V_{jh} \quad \text{(III.17b)}$$

This fraction factor is expressed as a function of the tensile stress of the beam reinforcement because it is related to the bond deterioration of this reinforcement. Obviously, the fraction factor increases as the bond strength deteriorates because ST1 strut contribution dominates after bond failure occurs (Fenwick, 1994). In this model, the bi-uniform bond strength model proposed by Lehman and Moehle (2000) is extended to be tri-uniform and adopted to represent the tri-linear behavior of the reinforcing steel. The bond strength in elastic beam tensile reinforcement, μ_E, is $12\sqrt{f_c'}$ psi$^{0.5}$ ($1.0\sqrt{f_c'}$ MPa$^{0.5}$) and that in inelastic beam tensile reinforcement, μ_Y, is $0.5\,\mu_E$. The residual bond strength, μ_R, is selected from the CEB-FIP (1990) as $0.15\,\mu_E$.

The elastic bond strength is investigated by the following approach. The basic development length of standard hooks in tension, l_{dh}, is proposed by ACI 318-08 (2008) as follows,

$$l_{dh} = \frac{0.02\phi_b f_y}{\sqrt{f_c'}} \text{ (in. and psi units)} \qquad \text{(III.18)}$$

On the other hand, the development length of hooks is also derived by the equilibrium equation in terms of elastic bond strength, μ_E, when f_s=f_y,

$$\pi\,\phi_b\, l_{dh}\, \mu_E = \frac{\pi\,\phi_b^2}{4} f_y \Rightarrow l_{dh} = \frac{\phi_b f_y}{4\mu_E} \qquad \text{(III.19)}$$

Equation (III.18) is almost identical to Equation (III.19) if the elastic bond strength is equal to $12\sqrt{f_c'}$ psi$^{0.5}$. Sezen (2000) reached a similar conclusion in an analogous manner. The considered bond-slip model is illustrated in Figure III.9 with reference to the CEB-FIP model (1990). It is noted that in this study, the effects of cover depth and bar spacing on bond strength are not explicitly accounted for within the joint region. However, these effects are implicitly accounted for by expressing the bond stress distribution along the beam bar $\mu(f_s)$, Figure III.8, as a function of the tensile stress of the bar, f_s.

The proposed model derives the fraction factor α from the tri-linear stress-strain model of the reinforcing steel as shown in Figure III.10. Juxtaposing Equations (III.14), (III.15b) and (III.17a), the fraction factor α is defined as follows,

$$A_s f_s - n\,\pi\,\phi_b \int_0^{l_h} \mu(f_s)dx = \alpha\, A_s f_s \left(1 - 0.85\frac{h_b}{H}\right) \Rightarrow \alpha = \frac{H}{H - 0.85h_b}\left(1 - \frac{4}{\phi_b}\frac{\int_0^{l_h}\mu(f_s)dx}{f_s}\right) \qquad \text{(III.20)}$$

where $A_s = n\,\pi\,\phi_b^2/4$ is used in Equation (III.20). The assumed breaking points of beam longitudinal bar stress (f_o, f_p, and f_r) and intermediate values of the fraction factor (α_1 and α_2) are defined below.

Derivation of f_o

The contribution of ST1 is negligible as long as the bond strength of ST2 is able to resist all of the horizontal shear force. The tensile stress of beam reinforcement at this point, f_o in Figure III.10, is given by

$$f_o = \frac{4}{\phi_b}\mu_E l_h \tag{III.21}$$

Derivation of α_1

The fraction factor α_1 corresponds to the onset of yielding of beam reinforcement at the column face. Therefore,

$$\alpha_1 = \frac{H}{H - 0.85h_b}\left(1 - \frac{4}{\phi_b}\frac{\mu_E}{f_y}l_h\right) \tag{III.22}$$

where f_y is the yield strength of the beam longitudinal reinforcement.

Derivation of f_p and f_r

The tensile stress f_p is defined when the beam reinforcement yielding propagates over the width of ST2. Therefore, the bond strength of concrete surrounding the beam reinforcement is equal to μ_Y over the entire length l_h. Accordingly and referring to Figure III.10, one obtains the following,

$$f_p = f_y + \frac{4}{\phi_b}\mu_Y l_h \tag{III.23}$$

The tensile stress f_r corresponding to $\alpha = 1.0$ is expressed implicitly using Eq. (18) since the bond distribution cannot be explicitly defined at $\alpha = 1.0$. It is to be noted that the tensile stress f_p can be equated to f_r if α_2 corresponding to f_p is equal to 1.0, Figure III.10. Therefore, the tensile stress value of the beam reinforcement f_r corresponding to $\alpha = 1.0$ is expressed as follows,

$$f_r = \frac{4}{\phi_b}\frac{H}{0.85h_b}\int_0^{l_h}\mu(f_r)dx \geq f_p \tag{III.24}$$

Derivation of α_2

The fraction factor α_2 is defined when the tensile stress of the beam longitudinal reinforcement at the column face reaches f_p. Therefore,

$$\alpha_2 = \frac{H}{H - 0.85h_b}\left(1 - \frac{4}{\phi_b}\frac{\mu_Y}{f_y + \frac{4}{\phi_b}\mu_Y l_h}l_h\right) \leq 1.0 \tag{III.25}$$

III-2.2.4 Definition of Joint Shear Failure

The joint shear strength is defined as the horizontal joint shear force when the horizontal shear force resisted by ST1 reaches its capacity as mentioned earlier. The capacity of ST1 can be estimated as the minimum joint shear strength at which ST1 takes all horizontal joint shear force, i.e. the fraction factor can be set to 1.0. Using the parametric equation of joint aspect ratio, Equation (III.7), the horizontal shear capacity of ST1 ($V_{jh,ST1,\max}$) is obtained as

$$V_{jh,ST1,\max} = c\frac{b_j\, h_c \sqrt{f_c'}\cos\theta}{1.31 + 0.085\left(\frac{h_b}{h_c}\right)},\ \theta = \tan^{-1}\left(\frac{h_b}{h_c}\right) \tag{III.26}$$

where c is a constant to be determined by literature test data. The expression in Equation (III.26) makes use of the findings from the semi-empirical model without consideration of the effect of the beam reinforcement. To predict the joint shear strength, the constant c is obtained for the case of the minimum joint shear strength at which the fraction factor can be set to 1.0. From Hakuto et al. (2000), the normalized horizontal joint shear stress $\gamma = 4$ psi$^{0.5}$ (0.33 MPa$^{0.5}$) is taken as the minimum joint shear strength to trigger the joint shear failure for a joint aspect ratio, $h_b / h_c = 500/460 \approx 1.1$, i.e., $\theta = 47.4^{\circ}$. Applying this suggestion to define the constant c, one obtains

$$c\frac{\cos(0.83)}{1.31 + 0.085 \times 1.1} = \gamma \ \Rightarrow c = 2.07\gamma \tag{III.27}$$

Following the fraction factor function in Figure III.10 and the determined value of c from Equation (III.27), the joint shear strength is calculated by an iterative procedure using the algorithm illustrated in Figure III.11.

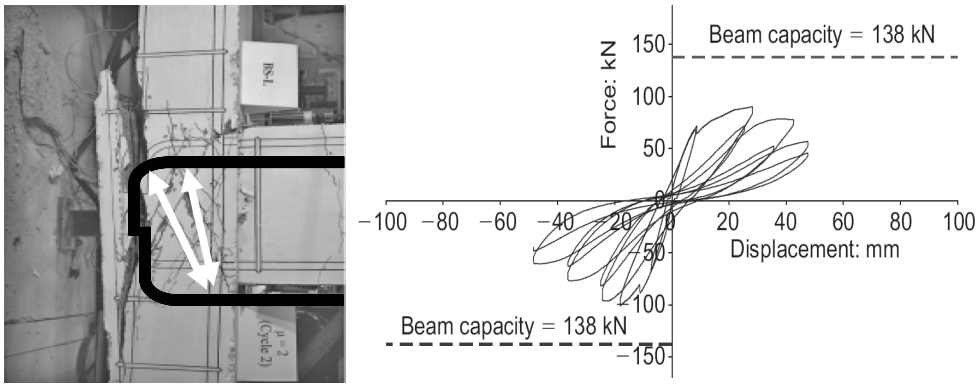

(a) Beam reinforcement bent inside the joint

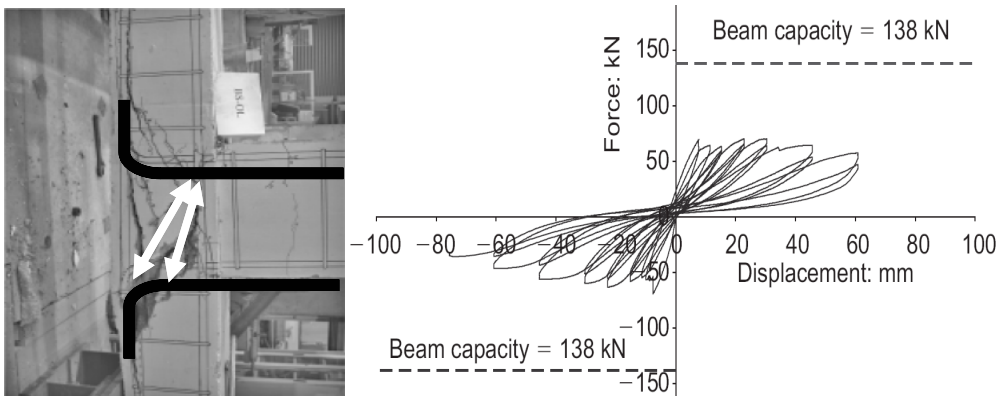

(b) Beam reinforcement bent outside the joint

Figure III.7 Tests with different beam reinforcement anchorage details (Wong 2005).

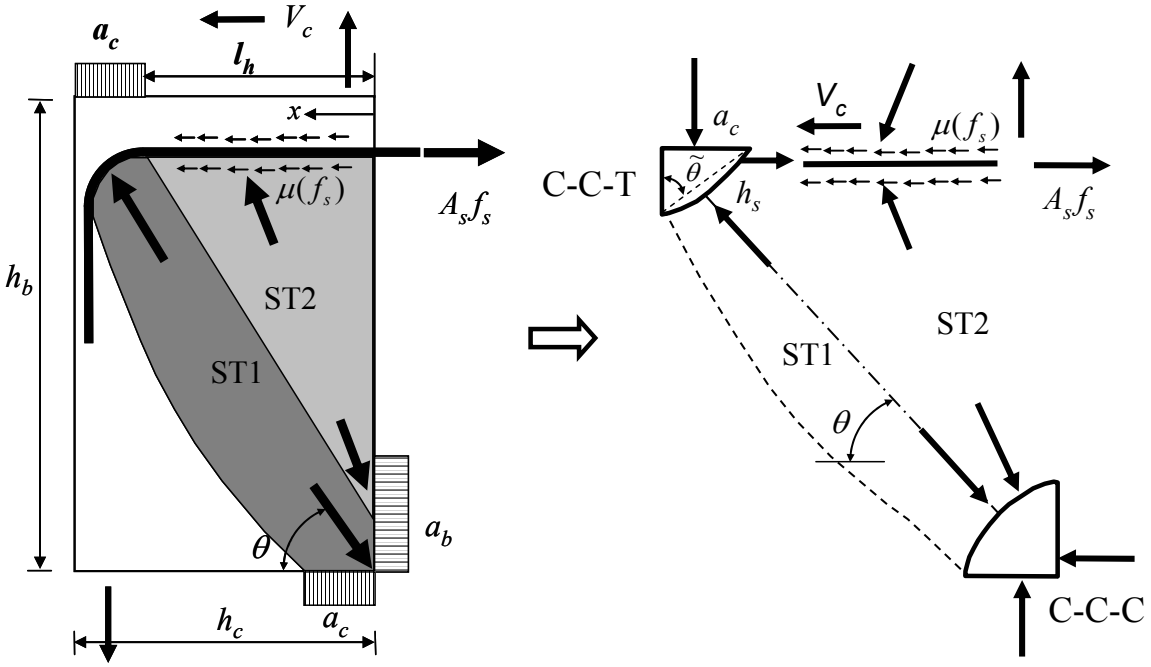

Figure III.8 Two inclined struts in unreinforced exterior joints.

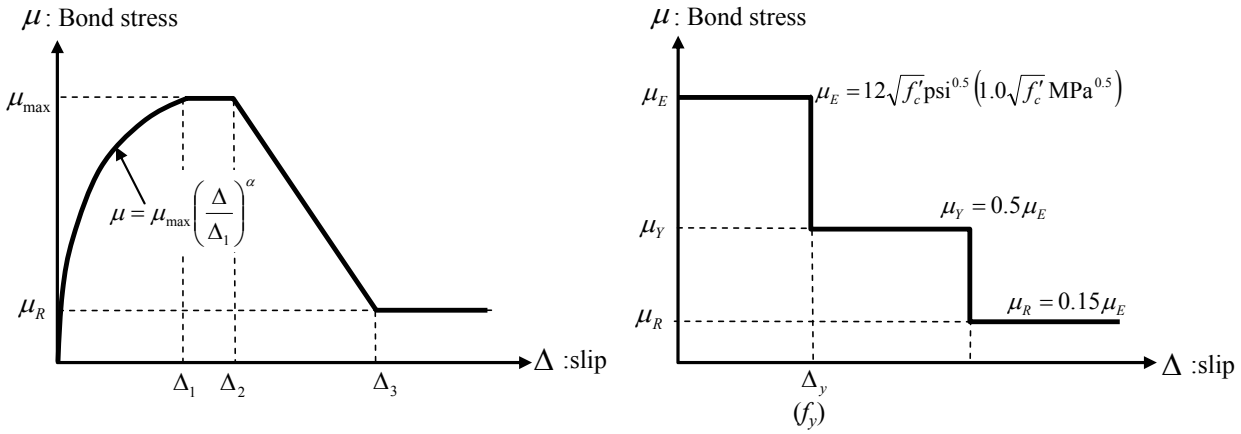

(a) Bond-slip relationship in CEB-FIP (1990) (b) Adopted bond-slip relationship

Figure III.9 Adopted bond strength model.

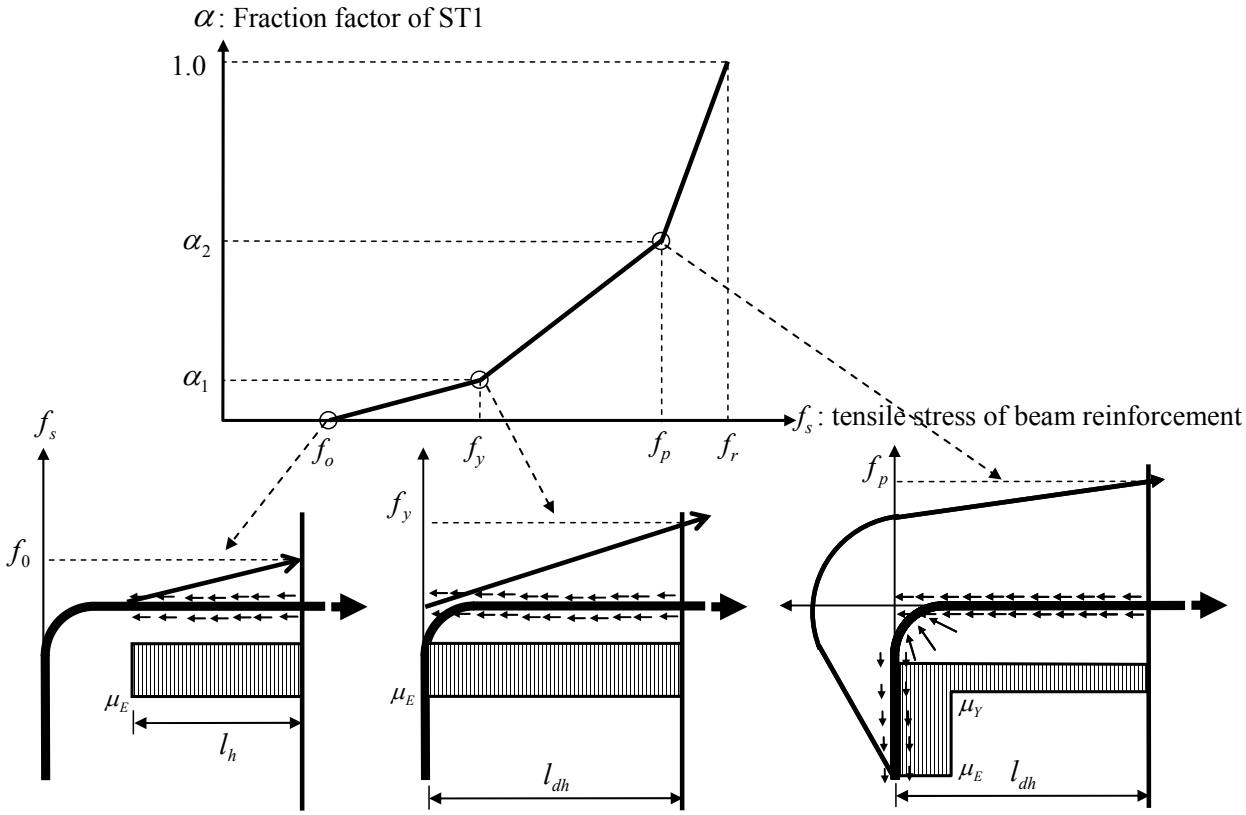

Figure III.10 Trilinear curve of fraction factor.

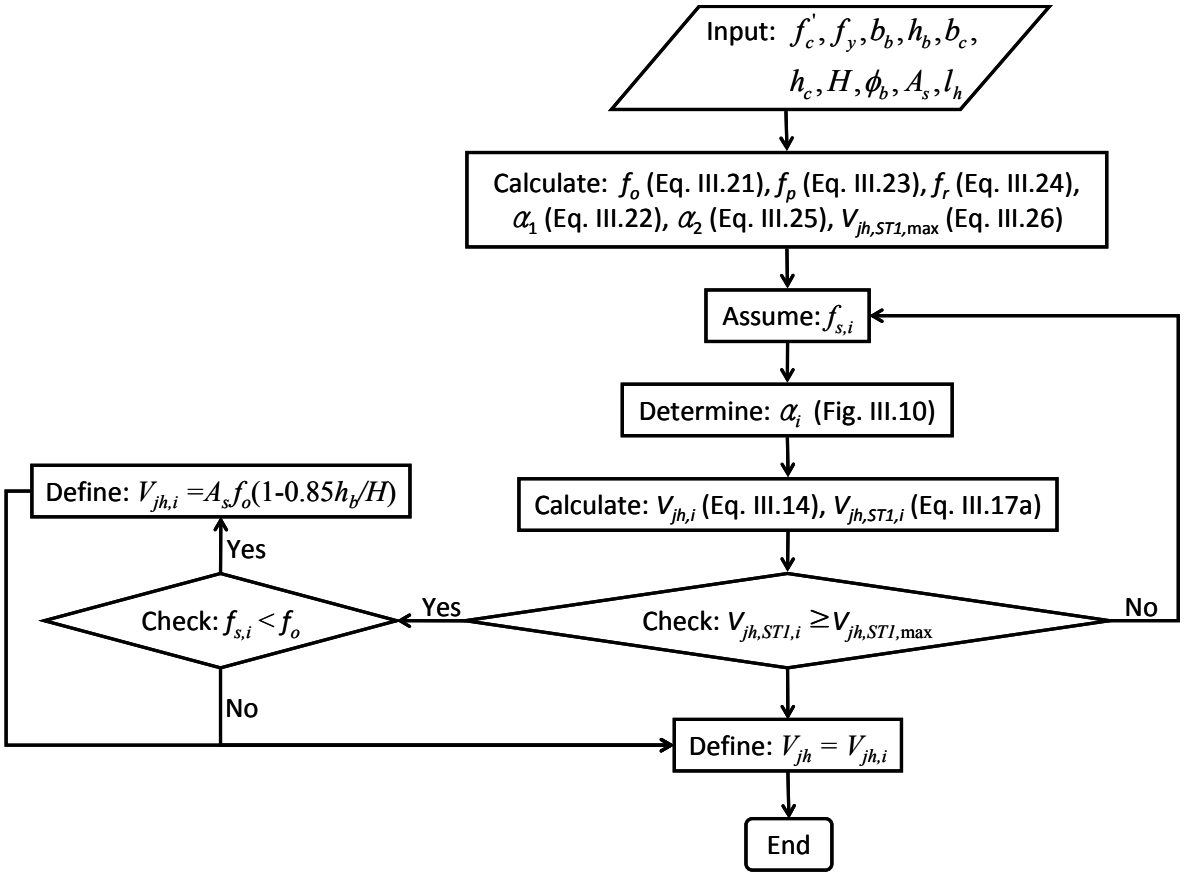

Figure III.11 Solution algorithm of proposed analytical joint shear strength model.

III-2.3 Evaluation of Analytical Model

III-2.3.1 Evaluation of Literature Database

The experimentally determined shear strengths of unreinforced exterior joints from the database are compared with the predictions by the proposed analytical model in Table III.4. The proposed analytical model predicts the joint shear strengths of the database with a mean value of 0.99 for the ratio between the test results and model predictions and a corresponding coefficient of variation (COV) of 14% as shown in Table III.4. These predictions are based on $l_h = 0.65h_c$ which is obtained from Table III.5 indicating that the analytical predictions are acceptable for the listed values of l_h and better correlated with the experimental results for $l_h = 0.65h_c$. In Table III.4, the designated failure types are defined in Chapter II and Y in parenthesis indicates beam reinforcement yielding. In Figure III.12, the evaluation results using the proposed model are compared with those from two existing analytical strength models proposed by Hwang and Lee (1999) and by Tsonos (2007).

III-2.3.2 Prediction of Joint Failure Mode

The proposed analytical model can predict the joint shear strength for two joint failure modes, i.e. with and without yielding of beam reinforcement, which are designated as BJ and J, respectively. The concept is illustrated in Figure III.13 to explain how to obtain different joint shear strengths in two identical unreinforced exterior joints except for beam longitudinal reinforcement ratio.

Suppose two types of beam longitudinal bars: one has high beam reinforcement ratio, e.g. 4-#8, and the other has low beam reinforcement ratio, e.g. 3-#8. The capacity of ST1, $V_{jh,ST1,\max}$, is not changed as long as the joint aspect ratio, global and sectional dimensions, and concrete strength are the same. First, assume a certain stress level for beam bars, f_s, for both cases. From the assumed f_s, total joint shear forces, V_{jh}, can be calculated using Equation (III.14) which gives a greater value for the case of beam with high reinforcement ratio ($V_{jh,high}$) than that for the case of beam with low reinforcement ratio ($V_{jh,low}$), while the fraction factor, α, is the same because the same stress f_s is assumed. For the same fraction factor, if the demand of ST1 reaches its capacity for beam with high reinforcement ratio, i.e. $\alpha = \alpha_{high} \Rightarrow V_{jh,high}\,\alpha_{high} = V_{jh,ST1,\max}$, the demand of ST1 for beam with low reinforcement ratio must be less than its capacity, i.e. $V_{jh,low}\,\alpha < V_{jh,ST1,\max}$. In other words, the stress level in the beam longitudinal reinforcement for beam with low reinforcement ratio has to increase and consequently the fraction factor also increases until the demand of ST1 reaches its capacity, i.e. $\alpha = \alpha_{low} \Rightarrow V_{jh,low}\,\alpha_{low} = V_{jh,ST1,\max}$. Therefore, the fraction factor $\alpha_{low} > \alpha_{high}$ since the total joint shear force $V_{jh,low} < V_{jh,high}$.

From the evaluation results of the test data and failure modes for unreinforced exterior joints, the proposed analytical model is verified to possess high accuracy. It is indispensible to assure the prediction of beam reinforcement yielding in this model to justify the fraction factor. The accuracy of this model for predicting the beam reinforcement yielding is clearly shown in

Table III.4, where the yielding is indicated as Y. Therefore, the proposed model is capable of predicting the joint failure mode without using modification of the diagonal strut width and without the need for the estimation of a ductility factor.

III-2.3.3 Principle of Analytical Model

The basic approach of the proposed model is to model a joint region with two inclined struts and the contribution of each strut to the total joint shear is formulated using the bond resistance of the concrete surrounding the beam longitudinal tension reinforcement. The capacity of the diagonal strut STI is defined to be less than that defined in single strut models. For a certain joint aspect ratio, the prediction of the proposed model begins with the joint shear strength when the fraction factor $\alpha = 1$ and the joint shear strength increases as the fraction factor decreases because the multiplication of the joint shear strength and the fraction factor, i.e. the strength of the diagonal strut ST1, is fixed as long as the joint aspect ratio is unchanged.

For example, the contribution of ST1 is found to be around 0.35 for J type failure from Table III.4 and therefore for a joint aspect ratio of $h_b/h_c = 1.0$, joint shear strength for J type failure is calculated to be $4.2/0.35 = 12.0 b_j h_c \sqrt{f_c'}$ $\text{psi}^{0.5}$ which shows good agreement with experimental results from literature in Figure III.3. Note that $4.2 b_j h_c \sqrt{f_c'}$ corresponds to the capacity of ST1 (i.e. $\alpha = 1$) at $h_b/h_c = 1.0$. The approach in applying the proposed model is therefore opposite to that of existing models which first predicts an upper limit value of the joint shear strength for J type failure and then reduces this shear strength by a ductility factor for BJ type of failure.

III-2.3.4 Preliminary Simulation of Literature Tests using Analytical Model

There have been several attempts to simulate RC frames including the joint flexibility. Due to the inherent complex behavior of RC joints, simplified rotational spring elements have been usually used to represent the combination of shear deformation of joint panel and the rotation due to bar slippage. The proposed analytical model predicts the joint shear strength from the tensile stress of the beam longitudinal reinforcement under the assumption that the principal tensile strain at the onset of joint failure is pre-defined by the joint aspect ratio. Therefore, the proposed model can provide the envelope of joint shear stress–strain relationship which can be transformed into the moment–rotation relationship of the rotational spring. From strain compatibility and Equation (III.12), the joint shear stress and strain are given by

$$v_{jh} \approx \frac{A_s f_s}{b_j h_c}\left(1 - 0.85\frac{h_b}{H}\right) \tag{III.28a}$$

$$\gamma_{xy} = \sqrt{4\left(\varepsilon_1 - \frac{\varepsilon_y}{2}\right)^2 - \varepsilon_y^2} \tag{III.28b}$$

where ε_y is the compressive (negative) strain from the column in the vertical direction. In most tests, the compressive strain ε_y is negligible because the applied column axial load ratio is low, i.e. $P/f'_c h_c b_c \le 0.2$ where P is the column axial load. Therefore, the shear strain γ_{xy} at the joint failure can be approximated as two times the pre-defined principal tensile strain (ε_1) which is defined in Equation (III.4).

In the J failure mode, joint shear stress–strain relationship is assumed to be linear before joint shear failure, while in the BJ failure mode, joint shear stress–strain relationship is assumed to be bilinear, as shown in Figure III.14. Knowing the frame and joint dimensions, the moment–rotation relationship of the rotational spring is obtained from the shear stress–strain relationship of the joint and bond-slip relationship for implicit joint modeling. Moment at the joint center is calculated using Equation (II.30a) and rotation at the beam-joint interface is added to Equation (II.30b). The joint rotation is rewritten here as

$$\theta_j = \gamma_{xy} + \Delta_{slip} / jd_b \tag{III.29}$$

where θ_j is the joint rotation, and Δ_{slip} is the relative movement of beam reinforcement with respect to the perimeter of the joint panel. In an implicit joint modeling, joint rotation is defined as the sum of the joint shear strain and slip rotation (Figure III.14). The slip is defined to be equal to the integral of the beam longitudinal bar strain within the joint region. Consequently, the bar stress–slip relationship is defined as follows,

$$\text{for } f_s < f_y: \ \Delta_{slip} = \int_0^{l_s} \frac{\mu_E}{E}\frac{4}{\varphi_b} x\,dx = \frac{\mu_E}{E}\frac{2}{\varphi_b} l_s^2 \tag{III.30a}$$

$$\begin{aligned} \text{for } f_s \ge f_y: \ \Delta_{slip} &= \int_0^{l_E} \frac{\mu_E}{E}\frac{4}{\phi_b} x\,dx + \int_{l_E}^{l_Y + l_E} \left\{ \frac{f_y}{E} + \frac{\mu_Y}{E_h}\frac{4}{\phi_b}\left(x - l_E\right) \right\} dx \\ &= \frac{\mu_E}{E}\frac{2}{\phi_b} l_E^2 + \frac{f_y}{E} l_Y + \frac{\mu_Y}{E_h}\frac{2}{\phi_b} {l_Y}^2 \end{aligned} \tag{III.30b}$$

where E and E_h are the elastic and hardening moduli of the beam reinforcement, respectively, $l_s = \frac{f_s}{\mu_E}\frac{\phi_b}{4}$, $l_E = \frac{f_y}{\mu_E}\frac{\phi_b}{4}$, and $l_Y = \frac{f_s - f_y}{\mu_Y}\frac{\phi_b}{4}$, refer to Figure III.15 (Lowes and Altoontash, 2003). It is assumed that the elastic anchorage length l_E can be extended to the tail of the hook, based on the tensile strain distribution of hooked bars in the exterior beam-column joints (Scott, 1992) and the slip is also expected along the tail (Ueda et al., 1986).

The simulations of two tests from (Wong, 2005) are performed in OpenSees (2010), an open source program for conducting earthquake engineering simulations. The specimens are modeled as two different types: the first model is constructed such that one dimensional beam and column elements intersect at the joint where the orthogonality between the beam and the column is maintained (Figure III.16(a)), while the other model is identical with the first model other than the joint region which is modeled with a rotational spring and rigid panel (Figure III.16(b)). Zero length rotational spring is used to simulate the joint rotation and joint offset

option is used to rigidly link the center of the joint with column and beam faces. The "*Hysteretic Material*" in OpenSees (2010) is used for defining a multi-linear response of the rotational spring.

The comparisons of test results with predictive simulations are presented in Figures III.17(a) and (b) for J failure and BJ failure specimen, respectively. These comparisons illustrate that the proposed model accurately predicts the strength and deformation at joint shear failure for both J and BJ failure types. It is noted that both specimens are symmetrical with respect to positive and negative loading directions. The lower initial stiffness in the simulation results from the simplified linear and bilinear joint shear stress–strain relationships for J and BJ failure, respectively. In recent studies by Kim and LaFave (2007), and Anderson et al. (2008), high stiffness is assigned in the joint shear stress–strain relationship up to the initiation of diagonal cracking and reduced linear stiffness follows up to the next critical point. In this regard, the initial stiffness of the joint shear stress–strain relationships assumed in this study underestimates the real initial stiffness, which is more significant in the J failure type. Finally, it is noted that the post-failure behavior of the joint is qualitatively represented by dotted lines in Figure III.17. From the results of experimental tests conducted in this study, the accurate initial stiffness and post-failure behavior are evaluated in Chapter VII.

Table III.4 Prediction of joint shear strength using the proposed analytical model.

Reference	Specimen	f'_c (ksi)	$f_{y,beam}$ (ksi)	$V_{jh,test}$ (kip)	$V_{jh,model}$ (kip)	$\frac{V_{jh,test}}{V_{jh,model}}$	Fraction Factor (α)	$f_{s,model}$ (ksi)	Failure Mode
Antonopoulos & Triantafillou	C-1	84.8	84.8	24.4	28.3	0.86	0.37	49.2	J
	C-2	84.8	84.8	24.2	30.2	0.80	0.39	52.4	J
	T-C	84.8	84.8	28.1	30.6	0.92	0.39	53.1	J
Clyde et al.	02	65.9	65.9	213.9	217.3	0.98	0.36	61.8	J
	06	65.9	65.9	211.4	207.8	1.02	0.36	59.1	J
	04	65.9	65.9	208.9	200.2	1.04	0.35	57.0	J
	05	65.9	65.9	220.8	206.3	1.07	0.36	58.7	J
El-Amoury & Ghobara	T0	61.6	61.6	91.3	108.1	0.82	0.40	63.0(Y)	BJ
Engindeniz	SP1-NS	45.7	45.7	81.4	109.5	0.74	0.34	48.3(Y)	CF
	SP1-EW	45.7	45.7	90.4	109.5	0.83	0.34	48.3(Y)	CF
	SP2-NS	45.7	45.7	91.7	120.3	0.76	0.36	53.0(Y)	J
	SP2-EW	45.7	45.7	96.9	120.3	0.81	0.36	53.0(Y)	J
Gencoğlu & Eren	RCNH1	76.1	76.1	10.9	14.2	0.77	0.58	78.7(Y)	BF
Ghobara & Said	T-1	61.6	61.6	124.5	107.8	1.08	0.40	63.2	BJ
	T-2	61.6	61.6	117.0	107.8	1.08	0.40	63.2	BJ
Hanson & Connor	V	51.0	51.0	138.4	130.8	1.06	0.31	37.6	J
	7	51.0	51.0	189.7	160.2	1.18	0.33	46.1	BJ
Hwang et al.	0T0	63.1	63.1	224.1	199.4	1.12	0.48	73.5(Y)	BJ
Karayannis et al.	A0	84.1	84.1	18.2	17.5	1.04	0.77	95.7(Y)	BJ
	B0	84.1	84.1	44.4	53.4	0.83	0.50	97.4(Y)	BJ
	C0	84.1	84.1	45.9	51.2	0.90	0.52	88.0(Y)	BJ
Liu	RC-1	46.9	46.9	29.3	30.8	0.95	0.44	55.0(Y)	BJ
Ortiz	BCJ1	104.4	104.4	68.8	71.0	0.97	0.32	69.0	J
	BCJ3	104.4	104.4	72.4	70.2	1.03	0.32	68.2	J
	BCJ5	104.4	104.4	70.6	73.9	0.96	0.33	71.8	J
	BCJ6	104.4	104.4	70.8	71.7	0.99	0.32	69.7	J
Parker & Bullman	4a	82.7	82.7	43.0	66.7	0.67	0.42	55.8	CF
	4b	82.7	82.7	50.3	66.7	0.78	0.42	55.1	J
	4c	82.7	82.7	62.0	66.7	0.96	0.42	55.1	J
	4d	82.7	82.7	54.7	66.7	0.85	0.42	55.1	J
	4e	82.7	82.7	58.4	66.7	0.91	0.42	55.1	J
	4f	82.7	82.7	66.7	66.7	1.04	0.42	55.1	J
Pantelides et al.	01	66.5	66.5	193.2	191.7	1.01	0.39	53.7	J
	02	66.5	66.5	179.6	185.7	0.97	0.38	52.1	J
	03	66.5	66.5	183.4	193.6	0.95	0.39	54.3	J
	04	66.5	66.5	202.7	188.7	1.07	0.39	52.9	J
	05	66.5	66.5	192.6	188.9	1.02	0.39	52.9	J
	06	66.5	66.5	193.9	187.4	1.03	0.39	52.5	J
Sagbas	ED1	50.6	50.6	134.1	117.2	1.14	0.41	45.5	BJ
Sarsam & Phipps	EX-2	75.4	75.4	39.6	49.2	0.80	0.45	67.3	BJ
Scott & Hamil	C4ALN0	75.7	75.7	24.8	24.8	1.00	0.32	44.8	P
	C4ALH0	75.7	75.7	42.3	33.9	1.25	0.37	61.0	P
	C6LN0	75.7	75.7	23.4	26.4	0.89	0.33	47.6	J
	C6LH0	75.7	75.7	35.4	33.5	1.06	0.37	60.4	J
Uzumeri	SP1	50.3	50.3	140.9	116.5	1.21	0.41	45.2	BJ
	SP2	50.6	50.6	136.9	117.2	1.17	0.41	45.5	BJ
	SP5	50.4	50.4	136.7	121.7	1.12	0.44	47.3	BJ

Table III.4 Prediction of joint shear strength using the proposed analytical model-*continued*.

Reference	Specimen	f_c' (ksi)	$f_{y,beam}$ (ksi)	$V_{jh,test}$ (kip)	$V_{jh,model}$ (kip)	$\frac{V_{jh,test}}{V_{jh,model}}$	Fraction Factor (α)	$f_{s,model}$ (ksi)	Failure Mode
Wong	BS-L	75.4	75.4	70.9	71.1	1.00	0.39	56.7	J
	BS-U	75.4	75.4	76.7	71.2	1.08	0.39	56.8	J
	BS-L-LS	75.4	75.4	77.5	71.7	1.08	0.39	57.2	J
	BS-L-300	75.4	75.4	113.5	84.7	1.34	0.46	64.0	BJ
	BS-L-600	75.4	75.4	63.8	66.3	0.96	0.36	55.9	J
	BS-L-V2T10	75.4	75.4	89.7	72.5	1.24	0.40	57.8	J
	BS-L-V4T10	75.4	75.4	90.6	69.0	1.31	0.39	55.0	J
	JA-NN03	75.4	75.4	68.9	68.9	0.99	0.53	80.9(Y)	BJ
	JA-NN15	75.4	75.4	69.9	69.5	1.05	0.54	81.6(Y)	BJ
	JB-NN03	75.4	75.4	70.4	76.3	0.93	0.60	86.5(Y)	BJ
Woo	Model 5	55.8	55.8	16.8	19.9	0.81	0.46	54.9	BJ
						$\frac{V_{jh,test}}{V_{jh,model}}$: Mean = 0.99, Coefficient of variation=0.14			

Notes: 1ksi = 6.90 MPa; 1 in. = 25.4 mm; 1kip = 4.45 kN; $1.0\sqrt{f_c'}$ psi$^{0.5}$ = $0.083\sqrt{f_c'}$ MPa$^{0.5}$

Table III.5 Statistics of evaluation results for investigated values of l_h.

	$l_h = 0.6h_c$	$l_h = 0.65h_c$	$l_h = 0.7h_c$	$l_h = 0.75h_c$
Mean	1.020	0.989	0.959	0.931
COV	0.144	0.143	0.143	0.142

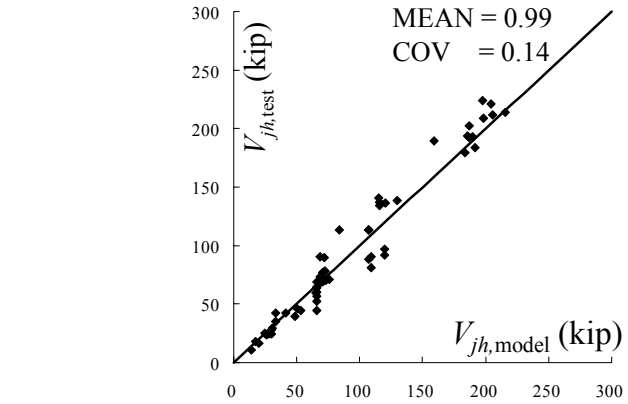

(a) Proposed model

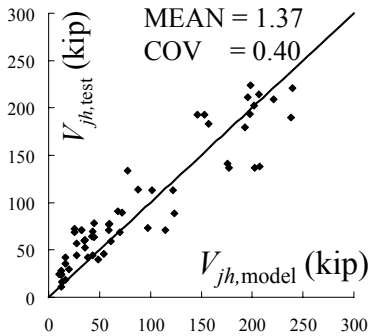

(b) Hwang and Lee (1999)

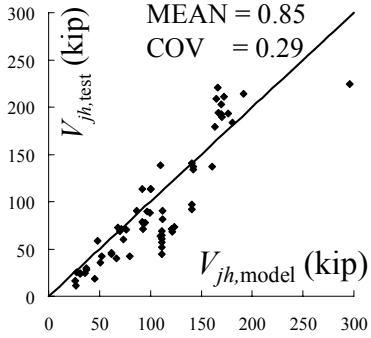

(c) Tsonos (2007)

Figure III.12 Comparison of evaluation results with existing analytical models.

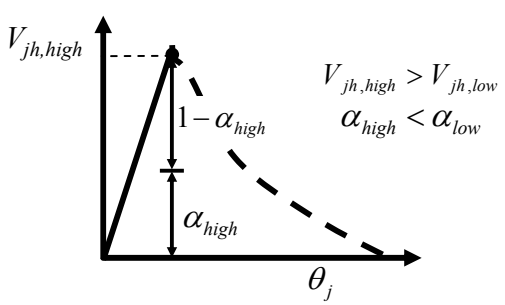

(a) Joint with high beam reinforcement ratio

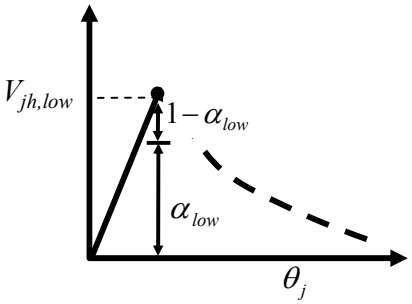

(b) Joint with low beam reinforcement ratio

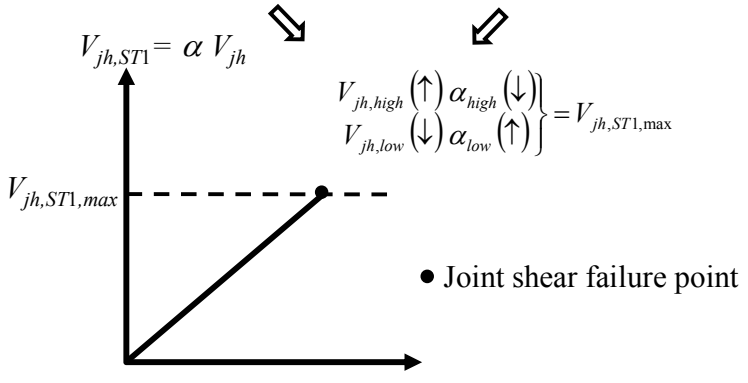

(c) Joint shear demand of ST1

Figure III.13 Illustration of two different shear strengths in the same joint.

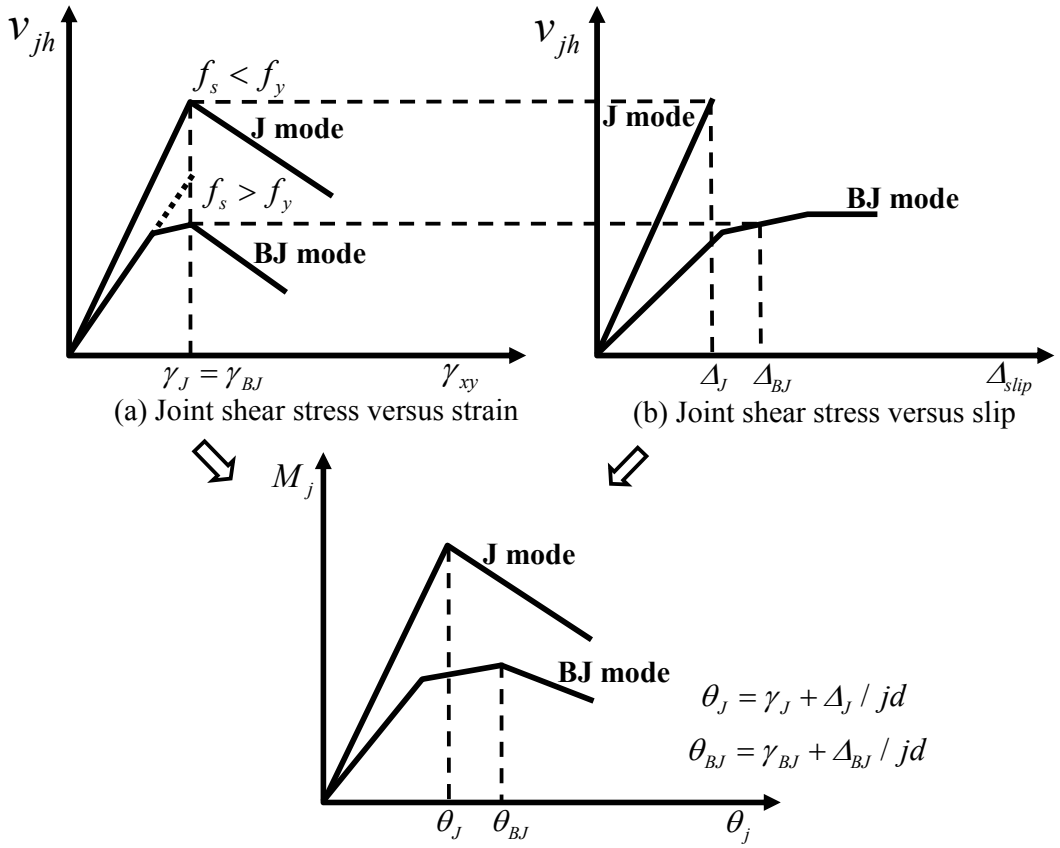

(a) Joint shear stress versus strain (b) Joint shear stress versus slip

(c) Moment versus rotation in the joint

Figure III.14 Relationship of moment versus joint rotation.

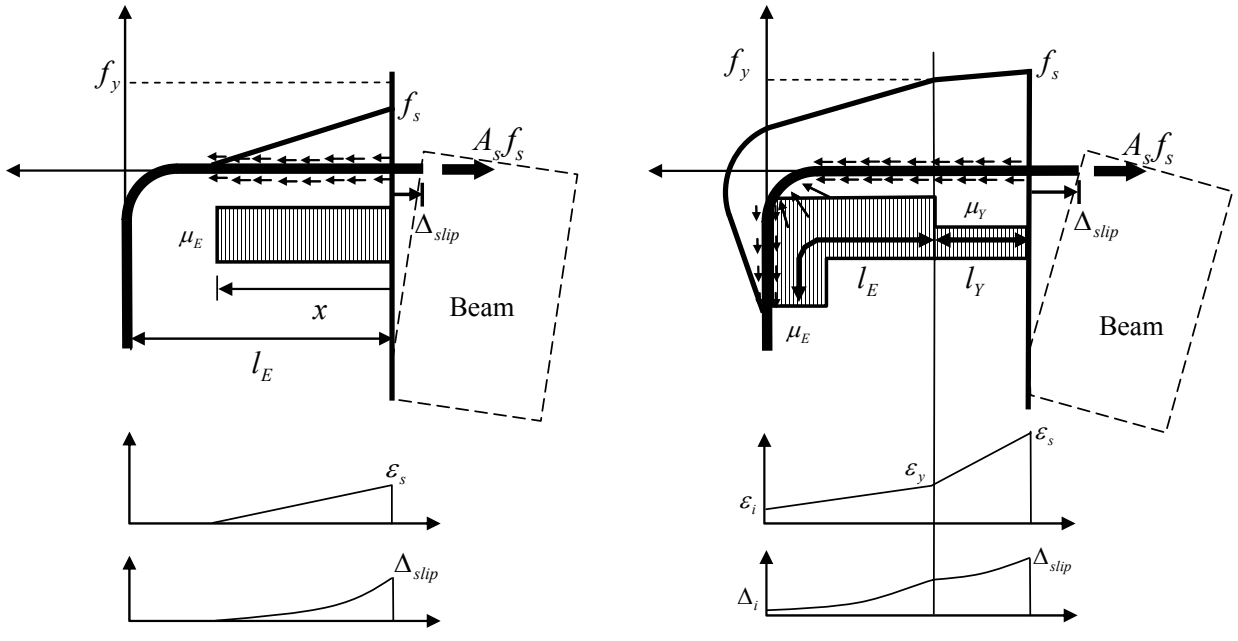

(a) Elastic bond distribution (b) Inelastic bond distribution

Figure III.15 Bond distribution along the hooked bar.

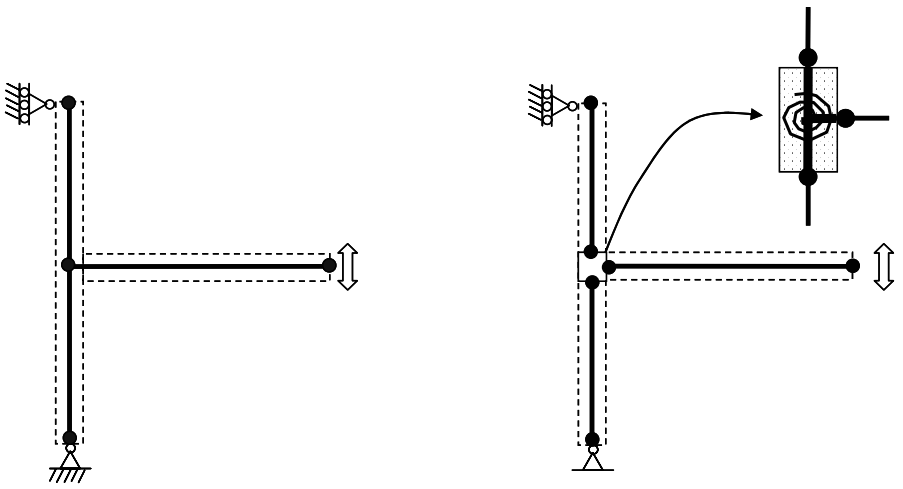

(a) Conventional center-to-center node (b) Rotational spring with rigid links

Figure III.16 Modeling of joint region.

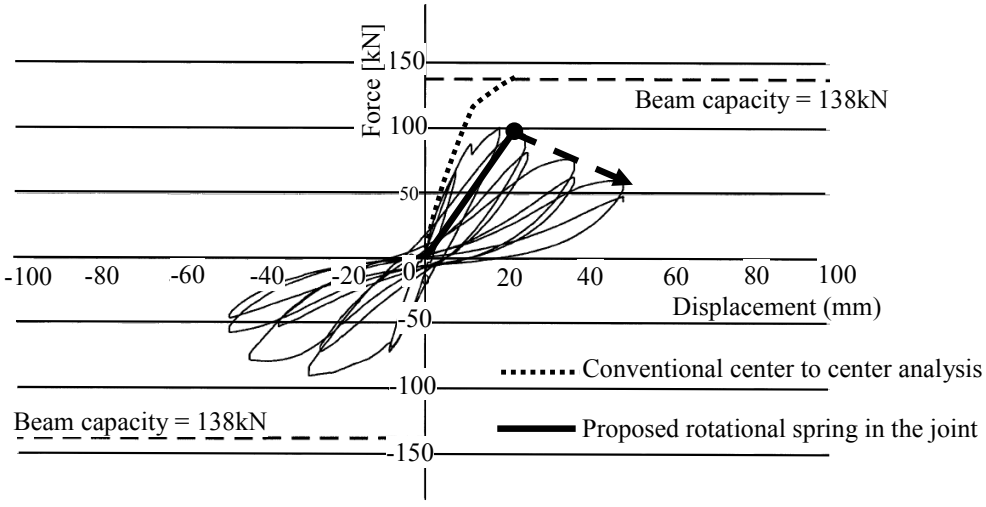

(a) J failure (BS-L)

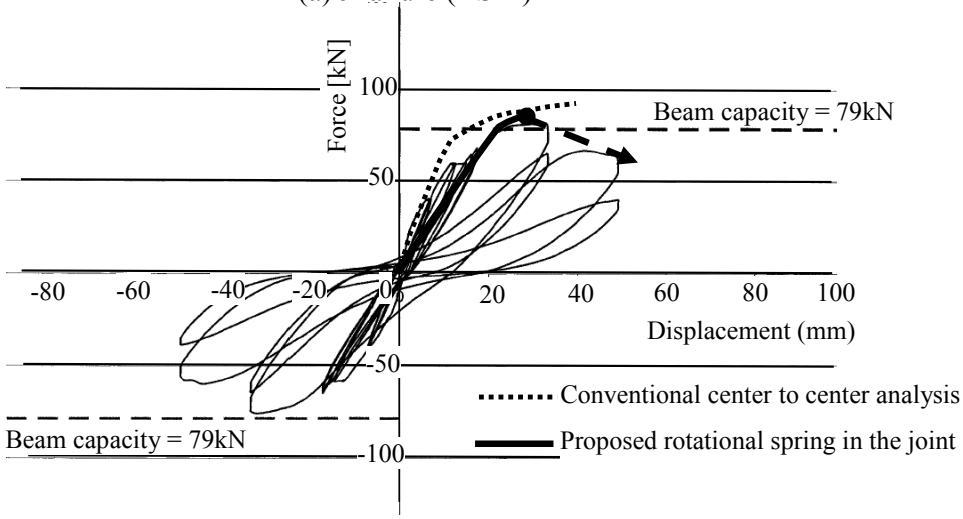

(b) BJ failure (JA-NN03)

Figure III.17 Simulation of tests by (Wong, 2005) using the proposed analytical model.

IV Experimental Program

This chapter describes the details of the experimental program on unreinforced corner joint tests. The experimental program includes specimen design, construction, material properties, loading protocol, test setup and instrumentation. The experimental program was performed in *nees@berkeley* laboratory located at Richmond Field Station, University of California, Berkeley.

IV-1 Specimen Design and Details

Four full-scale unreinforced corner joint specimens were built to assess the vulnerability of old RC buildings. Based on the parametric study in Chapter II, the specimens were designed considering two parameters: (1) joint aspect ratio and (2) the amount of longitudinal beam reinforcement. For different joint aspect ratio, two beam depths were considered for the same column depth leading to joint aspect ratios (h_b/h_c) of 1.00 and 1.67, as shown in Figure IV.1. In addition, two values of beam longitudinal reinforcement ratios were adopted for each of the two beam depths: 4-#6 at top and bottom as low beam longitudinal reinforcement ratio, and 4-#8 at top and 4-#7 at bottom as high beam longitudinal reinforcement ratio as shown in Figure IV.1, where the beam reinforcement index (RI_b) for each of the four specimens is presented. It is noted that the beam reinforcement indices presented in Figure IV.1 were calculated with the design strengths that f_c' and f_y were assumed to be 3.5 ksi (24.1 MPa) and 68 ksi (469 MPa), respectively. The actual value of beam reinforcement index for each of the four specimens is presented in Table IV.1. The beam longitudinal reinforcement was selected with the aim that the specimens having low beam reinforcement ratio were subjected to joint failure with beam longitudinal reinforcement yielding, while joint failure was expected without beam reinforcement yielding in the specimens having high beam reinforcement ratio. In this matrix, specimen SP1 is corresponding to low aspect ratio and low beam reinforcement, specimen SP2 low aspect ratio and high beam reinforcement, specimen SP3 high aspect ratio and low beam reinforcement, and specimen SP4 high aspect ratio and high beam reinforcement.

To focus on the failure of corner joints, the beams and the columns were designed according to the strong column/weak beam scheme as shown in Table IV.1, where the columns to beams flexural strength ratio (M_R) was greater than 1.4 for all the specimens. Flexural strength ratio, M_R, is defined as the sum of the flexural capacities of the column above and below the joint divided by that of the beam. It is noted that for conservative estimation, top four reinforcing bars the slab were considered to calculate the flexural strength of the beams according to the effective slab width specified in the ASCE 41, while the column axial load was not considered to calculate the flexural strength of the column. Columns were designed to remain elastic until beams yielded. In addition, the same number of column longitudinal bars was placed in each side of column considering the role of column intermediate bars (Hwang et al. 2005). As a result, 8-#8 bars were

placed in specimens SP1 and SP2, and 8-#10 bars were placed in specimens SP3 and SP4. Sufficient shear reinforcement was provided in the beams and the column to avoid shear and torsional failures.

All four specimens had the same slab section and reinforcement, i.e. 6 in. (152.4 mm) thickness and #3@12 in. (304.8 mm) double layers in both directions. Slab top reinforcement extended to the back of the orthogonal beam with 90° hook, while slab bottom reinforcement stopped at 6 in. (152.4 mm) from the beam-slab interface without 90° hook. The configuration of the specimens and their design details are summarized in Figure IV.1, and complete drawings are presented in Appendix A.

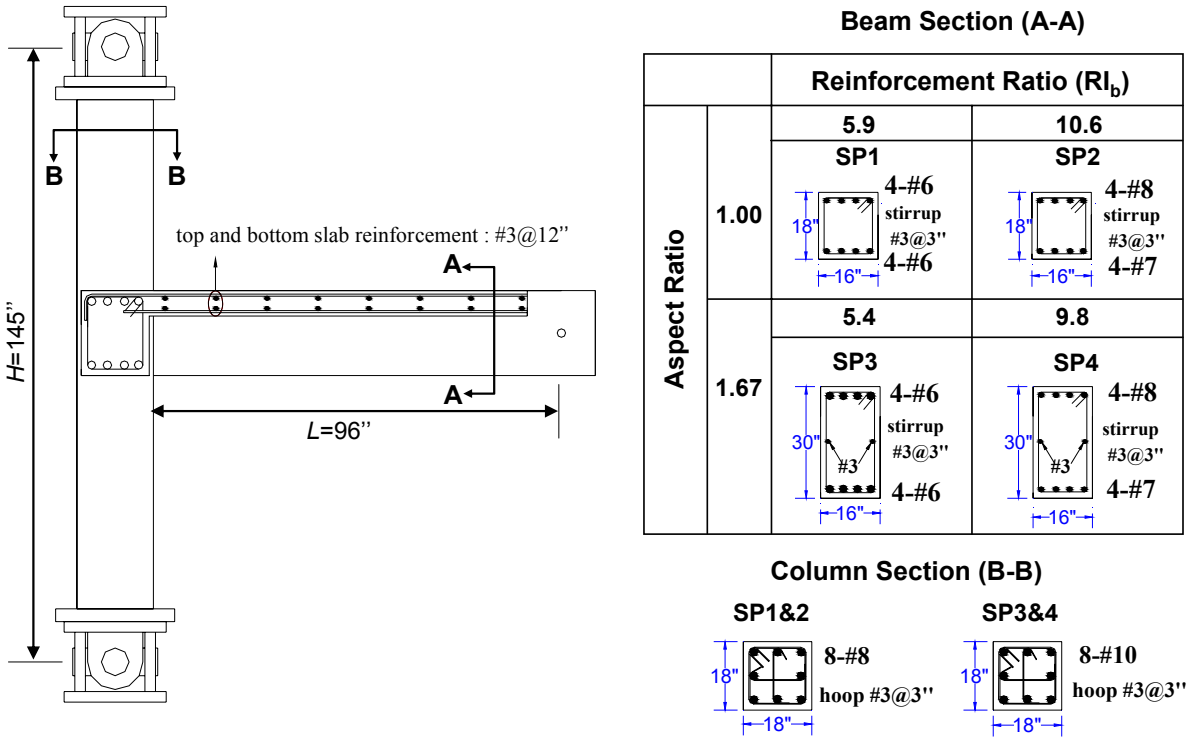

Notes: 1. RI_b is beam reinforcement index calculated using Equation (III.12)
2. 1" = 25.4 mm

Figure IV.1 Specimen details and test matrix.

Table IV.1 Design values of joint shear and flexural strength ratio.

Specimen	h_b/h_c	RI_b, psi$^{0.5}$ (MPa$^{0.5}$)	$M_R = \frac{\sum M_{col}}{M_{beam}}$
SP1	1.00	5.9 (0.49) [6.8 (0.56)]*	2.8
SP2	1.00	10.6 (0.88) [11.2 (0.93)]	1.9
SP3	1.67	5.4 (0.45) [6.2 (0.51)]	2.0
SP4	1.67	9.8 (0.81) [9.8 (0.81)]	1.4

Notes:
1. The strengths are calculated for negative bending, i.e. top in tension.
2. [ ]* is the RI_b using actual material properties.

IV-2 Specimen Construction

The four specimens were constructed outside the *nees@berkeley* laboratory. The specimen construction sequence is illustrated in Figure IV.2. A local contractor constructed the specimens in two phases: the first phase included SP1 and SP2 (low aspect ratio specimens) and the second phase included SP3 and SP4 (high aspect ratio specimens). In each phase of construction, different concrete mixes were used. The ratio of water to cement (W/C) was 0.75 in the first phase and 0.62 in the second phase. The details of the two concrete mix designs are described in Appendix B.

The design details of the beams and the column longitudinal reinforcement induced a conflict of placing the beam and column of exterior (Ext.) and interior (Int.) bars in the joint region. To resolve this conflict, the beams exterior and interior bars were placed inside the column exterior and interior bars as shown in Figure IV.3(a). Another conflict of reinforcement detail was that the longitudinal bars of the two orthogonal beams were crossing each other in the joint region. Thus, the top and bottom reinforcing bars of the East-West (EW) beam were placed under those of the North-South (NS) beam, Figure IV.3(b). As a result of these reinforcement details, the two orthogonal beams, assumed to be nominally identical, had different cover concrete thickness in the beams cross-section. The cover concrete thickness of the beam cross-sections were measured after testing and the values are listed in Table IV.2. In addition, couplers were embedded with screw-type headed bars in the column, as shown Figure IV.4. The couplers were utilized to install the bi-directional swivels on top and bottom of the column. Concrete was placed and vibrated in the vertical position from the pre-mix truck. Concrete casting was in two stages: (1) lower column, beam and slab, and (2) upper column. Specimens SP1 and SP2 were cured for 60 days prior to stripping their forms, while specimens SP3 and SP4 were cured for 20 days before stripping their forms.

Prior to testing of each of the four specimens, a forklift was used to transport the specimens from outside the laboratory to the test rig inside the laboratory. Figure IV.5 shows two photographs of SP1 during and after transporting it to the test rig.

Table IV.2 Measured cover concrete thickness of beam cross-sections.

Specimen	Cover concrete thickness [in. (mm)]			
	EW		NS	
	Top	Bottom	Top	Bottom
SP1	3.00 (76.2)	1.50 (38.1)	2.50 (63.5)	2.00 (50.8)
SP2	2.50 (63.5)	1.50 (38.1)	1.50 (38.1)	2.00 (50.8)
SP3	3.00 (76.2)	1.50 (38.1)	2.50 (63.5)	2.00 (50.8)
SP4	3.00 (76.2)	1.25 (31.8)	2.00 (50.8)	2.25 (57.2)

(a) Formwork

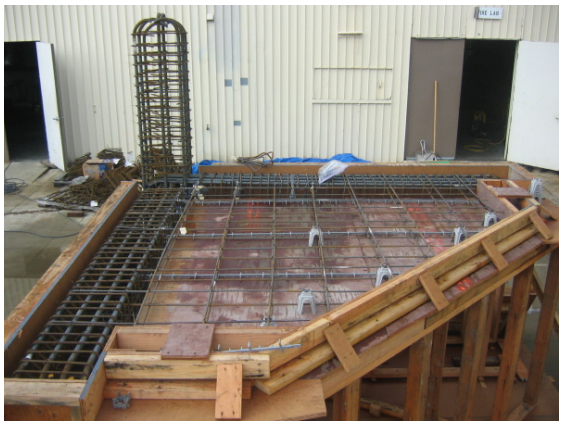

(b) Installation of reinforcing bars

(c) Concrete casting

(d) Stripped specimen

Figure IV.2 Specimen construction sequence.

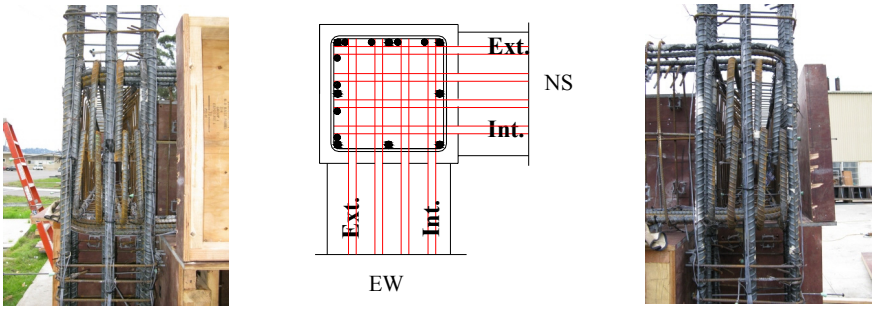

(a) Conflict of the beams and column longitudinal bars

EW direction

NS direction

(b) Conflict of EW and NS beams longitudinal bars

Note: 1" = 25.4 mm

Figure IV.3 Placement of beam and column reinforcement at corner joint.

Figure IV.4 Couplers and headed bars at top and bottom of column.

(a) During transporting SP1

(b) Placing SP1 on the test rig

Figure IV.5 Transportation specimen SP1.

IV-3 Material Properties

A design concrete compressive strength for the tested full-scale specimens was selected based on the values used in the literature column and joint specimens substructuring old existing RC buildings. The mean concrete compressive strength in a database of 56 non-ductile column specimens was 3.7 ksi (25.5 MPa) in Ghannoum (2007) and the design concrete strength of unreinforced joint specimens tested in Cornell University was 3.5 ksi (24.1 MPa) in Beres et al. (1992). Based the above values, concrete strength of all specimens targeted a 28 day compressive strength of 3.5 ksi (24.1 MPa). Maximum aggregate size was 1 in. (25.4 mm) to be relevant for the full-scale specimen. Two mix designs were used because the first mix showed less strength than specified after 28 days. The concrete properties of the four specimens are summarized in Table IV.3. More information including mix design and strength gain with time are provided in Appendix B.

Grade 60 A706 deformed reinforcing steel bars were used for all the specimens. Used bar sizes in metric units were 10 mm (D10), 19 mm (D19), 22 mm (D22), 25mm (D25), and 32mm (D32) compatible with #3, #6, #7, #8, and #10 in US standard bars, respectively. The summary of reinforcing steel bar properties is given in Table IV.4. More information of properties of reinforcing steel bars from coupon tests is presented in Appendix B.

Table IV.3 Concrete material properties.

Property	SP1	SP2	SP3	SP4
Compressive strength f_c' [ksi (MPa)]	3.58 (24.7)	3.53 (24.3)	3.60 (24.8)	3.96 (27.3)
Strain at peak stress ε_o	0.0019	0.0019	0.0024	0.0024
Initial tangent modulus E_c [ksi (GPa)]	3570 (24.6)	3850 (26.5)	3130 (21.5)	3300 (22.7)
Splitting tensile strength f_{ct} [ksi (MPa)]	0.34 (2.34)	0.34 (2.34)	0.32 (2.21)	0.44 (3.03)
Age of testing [days]	295	358	378	421

Table IV.4 Reinforcing steel material properties.

Property	#3 (D10)	#6 (D19)	#7 (D22)	#8 (D25)	#10 (D32)
Yield stress f_y [ksi (MPa)]	73.5* (507)	78.6 (542)	73.3 (505)	72.2 (498)	68.3 (471)
Ultimate stress f_u [ksi (MPa)]	115.0 (794)	104.5 (721)	103.1 (711)	102.6 (708)	100.5 (693)
Yield strain ε_y	0.0035*	0.0028	0.0027	0.0025	0.0023
Ultimate strain ε_u	0.105	0.120	0.120	0.120	0.120
Elastic Modulus E_s [ksi (GPa)]	28200 (195)	27900 (193)	26700 (184)	28900 (213)	29600 (204)

*: Yield stress and strain are estimated using 0.1% offset method.

IV-4 Loading Protocols

In this section, the beams lateral and column axial loading protocols are discussed. The lateral loads were specified at the tested beam ends using displacement controls, while the column axial load was specified using force control.

IV-4.1 Beams Lateral Loading

The lateral load was applied in a quasi-static (0.02 in./sec.) manner through displacement control at the end of each beam. The applied displacement alternated between the two beams, i.e. one beam remained at a reference point during the loading of the other orthogonal beam. Both beams were pulled down to one quarter of the estimated yield displacement (Δ_y) which is defined as the reference point, $\Delta_0 = \Delta_y / 4$. The yield displacement was estimated by conventional analysis for the beam-column subassemblies of the specimens using OpenSees (2010) and it was found to be 1.24 in. (31.5 mm) for SP1 and SP2, and 0.92 in. (23.4 mm) for SP3 and SP4. This initial pull-down loading was intended to simulate gravity load prior to lateral loading and to cause beam yielding first under downward loading so that the contribution of slab reinforcement be investigated. The number of loading groups prior to yielding was limited to three groups to reduce unnecessary effect of low-cycle fatigue on the joint. In each group of loading, two reversed cycles were applied for each beam. In the inelastic loading groups, the peak displacement of the current loading group was determined as 1.5 times that of the previous loading group. It is noted that a single low-level cycle of 1/3 of the previous displacement level, was applied after each group of cycles in the inelastic loading group to quantify the stiffness degradation. The sequence and protocol of the displacement-controlled loading are depicted in Figure IV.5 and Figure IV.6, respectively, and the applied beam displacement history is presented in Table IV.5.

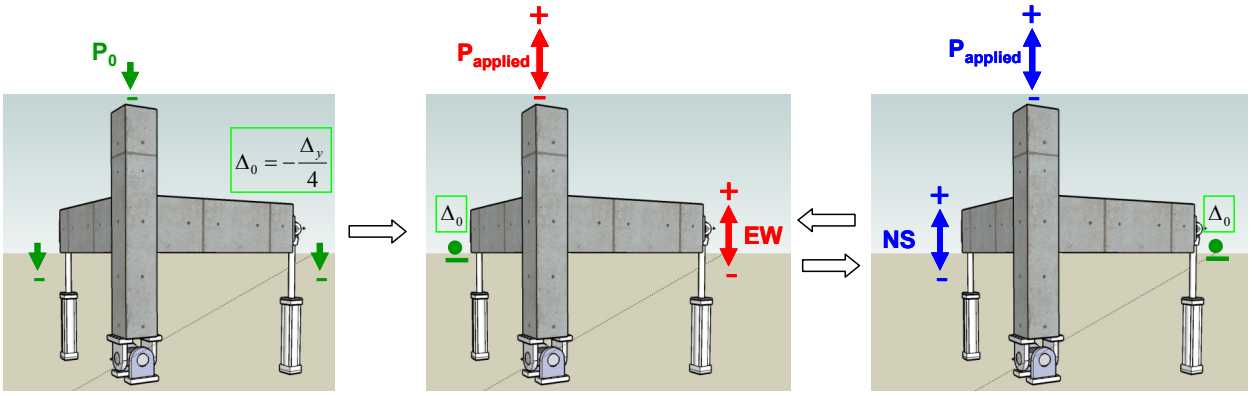

(a) Pull-down before testing (b) Loading EW beam (c) Loading NS beam

Figure IV.5 Loading sequence.

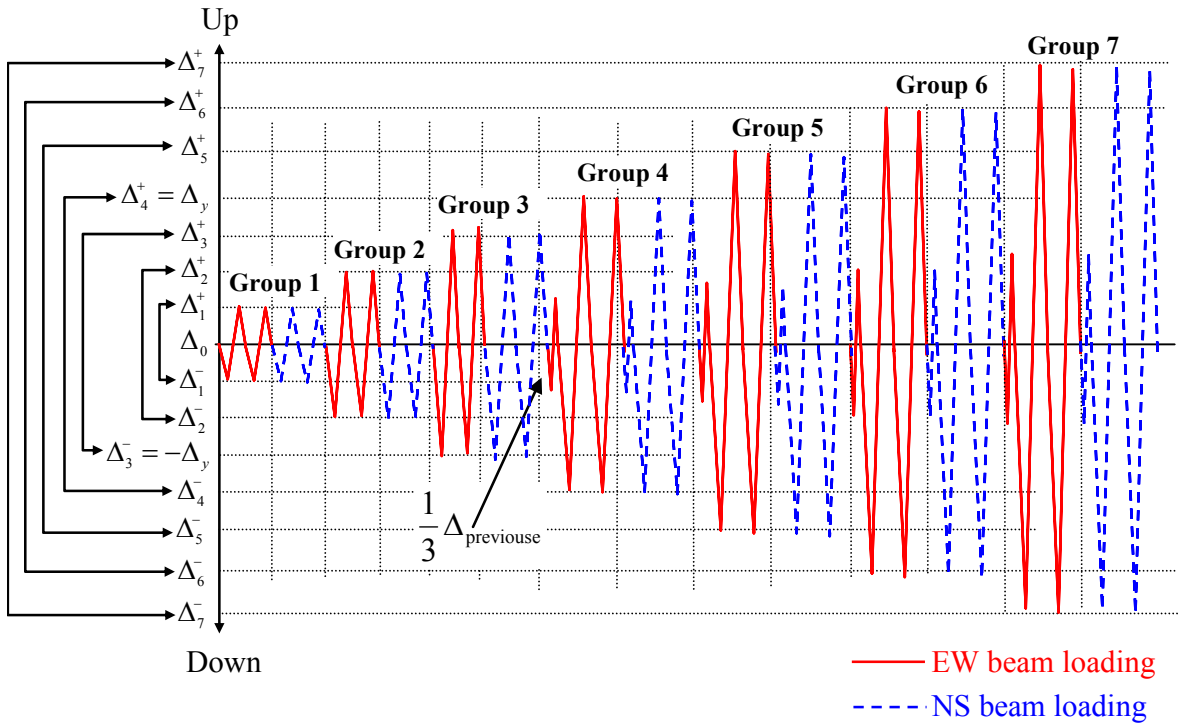

Figure IV.6 Applied beam displacement history.

Table IV.5 Applied beam displacement values for loading groups.

	Pull-down	Group 1	Group 2	Group 3	Group 4	Group 5	Group 6	Group 7
Δ^+	$\Delta_0 = -\frac{\Delta_y}{4}$	0	$0.25\Delta_y$	$0.5\Delta_y$	Δ_y	$1.75\Delta_y$	$2.875\Delta_y$	$4.563\Delta_y$
Δ^-		$-0.5\Delta_y$	$-0.75\Delta_y$	$-\Delta_y$	$-1.5\Delta_y$	$-2.25\Delta_y$	$-3.375\Delta_y$	$-5.063\Delta_y$

Note: $\Delta_y = 1.24$ in. (31.5 mm) for SP1 and SP2; $\Delta_y = 0.92$ in. (23.4 mm) for SP3 and SP4.

IV-4.2 Column Axial Loading

Column axial load varied during the tests to simulate the overturning effect on column during earthquake shaking. Prior to the tests, a reasonable range of axial load variation in corner columns was estimated for a selected prototype building, which was used extensively as a test-bed in the Pacific Earthquake Engineering Research (PEER) center. This building is a 7-story RC framed structure representing the Van Nuys Holiday Inn located in the San Fernando Valley of Los Angeles, California. This building was damaged during 1994 Northridge earthquake. The structural details about Van Nuys Holiday Inn can be found in Krawinkler (2005). It is worth mentioning that this building is used for structural simulation in Chapter VII where the details of beams and columns are presented.

IV-4.2.1 Estimate of Column Axial Load

The transverse (NS direction) perimeter frame of the prototype building was selected and modified to have similar beam and column dimensions to the full-scale specimens as follows,

1. Column layout was changed from rectangular to square plan with three bays in each direction corresponding to the transverse perimeter frame of the prototype building, as shown in Figure IV.7;
2. Column cross-section ($b_c \times h_c$) was changed from $14'' \times 20''$ (356×508 mm) to $18'' \times 18''$ (457×457 mm) considering the change of column layout;
3. Beam width was increased from 14 in. (356 mm) to 16 in. (406 mm) considering the increase of column width;
4. Gravity load on the first story corner column was adjusted to be $0.15 f_c' A_g$ identical with the original prototype building; and
5. Slab contribution to beam flexural strength was not considered.

To estimate the range of axial load variation in corner columns, a nonlinear static (pushover) analysis was performed using OpenSees (2010) for the above modified prototype building. Analytical materials and element models in OpenSees (2010) for the analysis were selected to be similar to those adopted by Paspuleti (2002) in order to confirm the accuracy of the analysis.

1. Concrete material: *Concrete01* for all beam and column cross-section;
2. Reinforcing bars: *Steel02* with hardening ratio of 2%;
3. Beam and column elements: *beamWithHinges* with plastic hinge length being equal to beam depth; and
4. Effective moment of inertia (I_g) for elastic region: $0.5I_g$ for the beams and columns.

The pushover analysis was stopped when the 2nd floor exterior beam reached the negative ultimate moment capacity already calculated from section analysis. From the pushover analysis results, additional compressive axial load on the first story corner column due to overturning moment was approximately 60% of the gravity load ($0.15 f_c' A_g$) for each direction in the 7-story building. Total axial load on the first story corner column was estimated for uni-directional and simultaneous bi-directional loading as follows,

For uni-directional loading

$$0.15 f_c' A_g \left(1-0.6\right) = 0.06 f_c' A_g \le P \le 0.15 f_c' A_g \left(1+0.6\right) = 0.24 f_c' A_g \quad \text{(IV.1a)}$$

For simultaneous bi-directional loading

$$0.15 f_c' A_g \left(1-0.6\times 2\right) = -0.003 f_c' A_g \le P \le 0.15 f_c' A_g \left(1+0.6\times 2\right) = 0.33 f_c' A_g \quad \text{(IV.1b)}$$

Note that column axial load P is positive for compression. The range of column axial load is plotted on the P-M interaction diagram of the first story corner column of the prototype building, refer to Figure IV.8. For uni-directional loading, the axial load on the first story corner column ranged within compression (positive) from $0.06 f_c' A_g$ to $0.24 f_c' A_g$ under which most unreinforced joint tests from literature were conducted (refer to Figure II.5 in Chapter II), and for simultaneous bi-directional loading, it varied from small tension (negative) to $0.33 f_c' A_g$, as shown in Figure IV.8.

IV-4.2.2 Column Axial Loading Equation

The relation between the beam shear and column axial load was obtained from the pushover analysis. The beam shear was calculated by dividing the beam end moment by the distance from the beam inflection point to column face which was assumed to be 8 ft. (2.44 m) considering the specimen dimension. Due to the assumed square plan, the beam shears were assumed to be identical for the two orthogonal directions. The derived equation was applicable to specimens SP3 and SP4 which have the same dimensions of the first story beams and columns, i.e. beam and column dimensions are $16'' \times 30''$ (406×762 mm) and $18'' \times 18''$ (457×457 mm), respectively, as shown in Figure IV.7. The coefficient was adjusted for SP1 and SP2 such that similar column axial loads were applied at the onset of beam yielding for each pair of specimens, i.e. SP1 and SP3, and SP2 and SP4. The beam shear forces for the EW and NS directions, $V_{b,\mathrm{EW}}$ and $V_{b,\mathrm{NS}}$, respectively, at each step were recorded in real time and these forces directly determined the applied column axial load by the following linear equations:

$$P_{\text{applied}} = 95 - 4V_{b,\mathrm{EW}} - 4V_{b,\mathrm{NS}} \quad \text{for specimens SP1 and SP2} \quad \text{(IV.2a)}$$

$$P_{\text{applied}} = 95 - 2V_{b,\mathrm{EW}} - 2V_{b,\mathrm{NS}} \quad \text{for specimens SP3 and SP4} \quad \text{(IV.2b)}$$

Note that the applied column axial load, P_{applied}, is positive for compression, and the beam shear forces, $V_{b,\mathrm{EW}}$ and $V_{b,\mathrm{NS}}$, are positive for upward loading, i.e. additional compressive loads were applied during downward loading of the beams, refer to Figure IV.9. The determined column axial load was applied by two hydraulic actuators located on each side of column and these two actuators were constrained to move equally in the vertical direction.

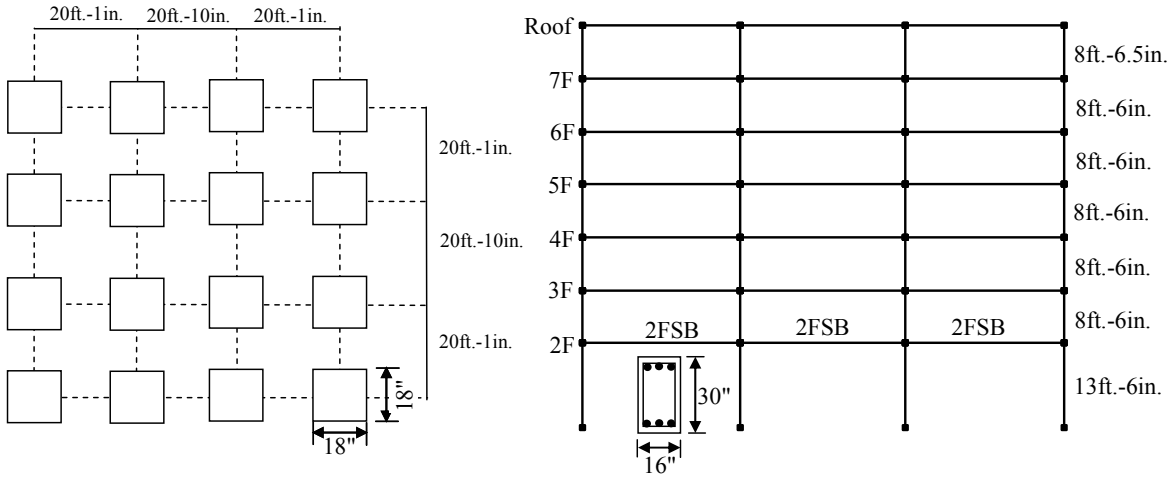

(a) Column layout (b) Elevation

Figure IV.7 Modified prototype building.

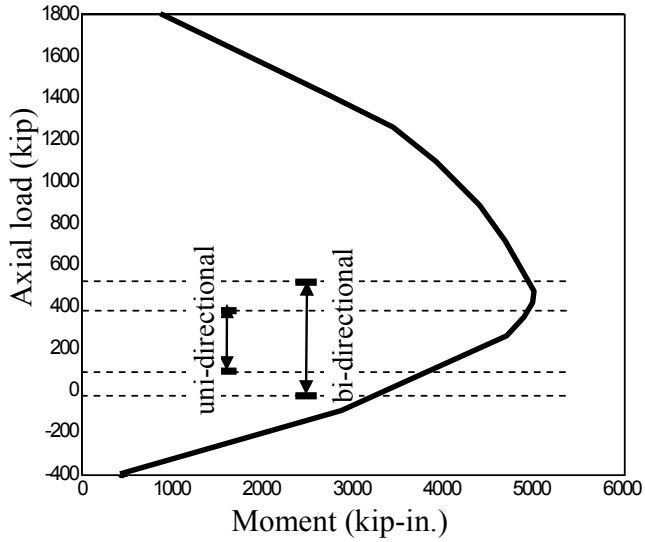

Figure IV.8 Range of column axial load variation in the P-M interaction diagram.

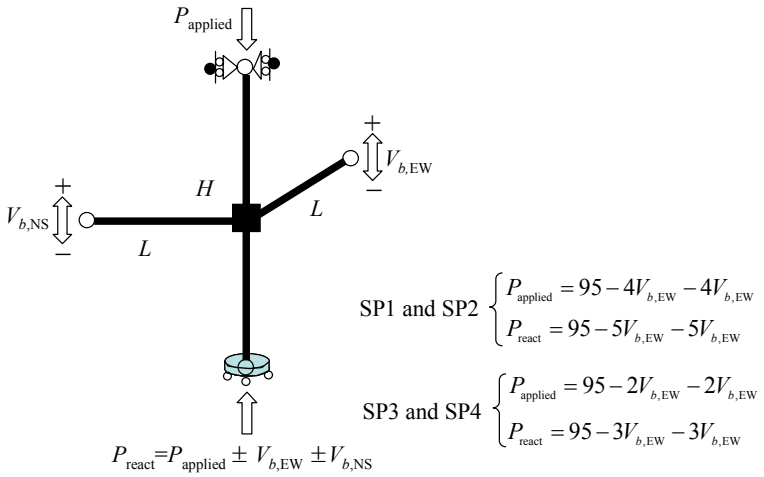

Figure IV.9 Applied column axial load for the four specimens.

IV-5 Test Setup

A special test setup and devices were designed and installed to achieve hinge boundary condition at top and bottom of the column in order to apply variable column axial load and to restrain lateral movement of the specimen, as shown in Figure IV.10. For the hinge boundary conditions, two bi-directional swivels were designed to carry 500 kips of compression and 200 kips of tension. These swivels were connected to the column using embedded couplers and to the vertical loading test frame by bolt connections.

Two W $16\times1/2\times36$ steel beams and built-up boxes were used to apply column axial load using two hydraulic actuators (360-kip-capacity for retraction). The two hydraulic actuators for column loading were supported on the top flange of the bottom W $16\times1/2\times36$ beam and connected to the top W $16\times1/2\times36$ beam using the built-up boxes.

The lateral restraining frame was designed to allow vertical movement of the two column actuators and to prevent lateral movement of the specimen at the top end of the column. Two HSS $12\times12\times1/2$ members were bolted to the reaction wall at one end and they are connected each other by welding tubes of the same size between them. Additional fabrication was performed to provide a space for the built-up box to slide vertically between the two tube members. Another HSS $8\times8\times1/2$ diagonal member was used to provide lateral restraint of the frame. As a result, no P-delta effect was taken into account in this test setup.

In total, four hydraulic actuators were used: two 360-kip-capacity actuators for column loading and two 120-kip-capacity actuators for beams loading. All actuators were connected to adaptor plates. Top and bottom ends of the column were artificially confined by filling hydro-stone between the column and surrounding cylindrical steel ring to prevent local failure during testing, Figure IV.11. The sequence of test setup assemblage is presented in Figure IV.12. The complete test setup drawings are presented in Appendix A.

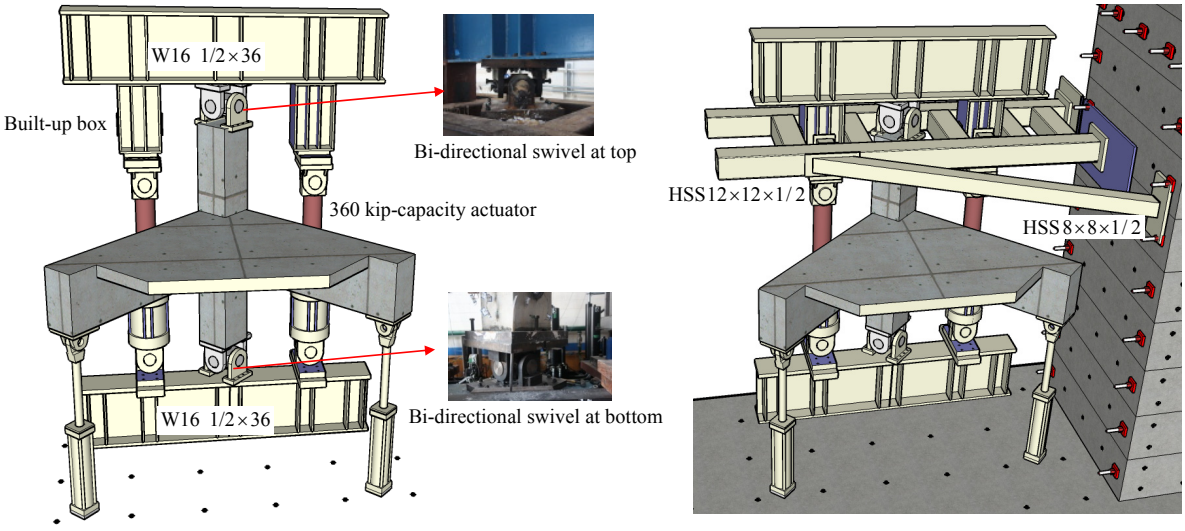

(a) Vertical frame and swivels (b) Lateral restraining frame

Figure IV.10 Design of test frame.

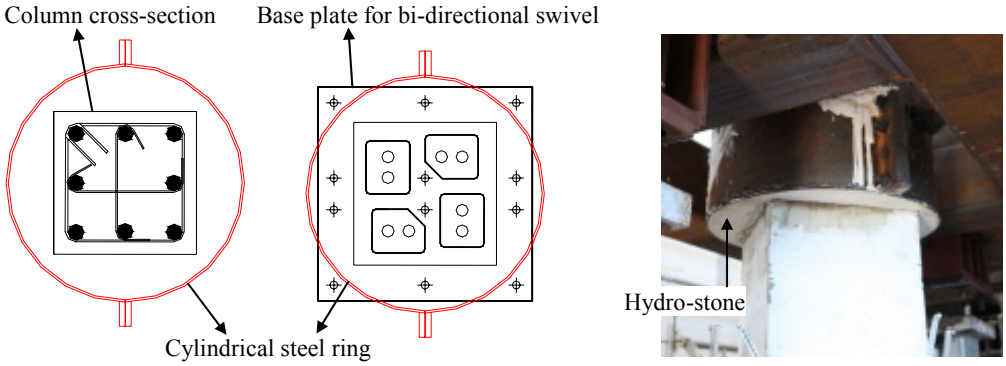

Figure IV.11 Confinement of the column at the boundary.

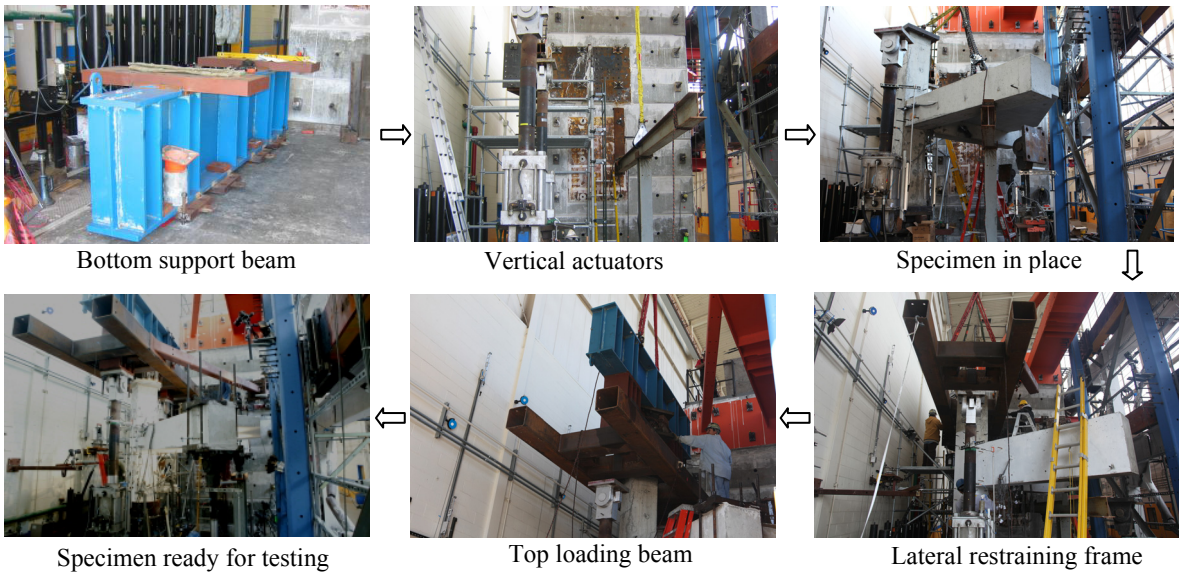

Figure IV.12 Assembling test setup.

IV-6 Instrumentation

During the test, external and internal instrumentations were used to monitor: (1) beam shear and column axial forces, (2) beams and column deformations, (3) joint shear strains, (4) strain of reinforcing bars, and (5) global translations. Four load cells measured forces in actuators, seventy eight displacement transducers, and seventy seven strain gages were used.

IV-6.1 Beam Shear and Column Axial Forces

The two 360-kip-capacity and two 120-kip-capacity hydraulic actuators were used to apply column axial load and beam shear forces, respectively. As described in Section IV.4, two beam actuators were operated under displacement control and two column actuators were driven by force control to apply the total force calculated from beams shear forces. Applied forces were monitored by built-in load cells in the actuators. The load cells were calibrated before testing as shown in Figure IV.13. On each actuator, a displacement transducer was installed for beam actuators to apply beam shear by displacement control and for column actuators to have equal vertical displacement during loading of both actuators.

Figure IV.13 Calibration of load cell of the column axial loading actuator.

IV-6.2 Beams and Column Deformations

Forty six of displacement transducers were installed on the column and beam to measure flexural curvature of the beams and column, column axial deformation, relative deformation at beam-joint interface, and twisting of the beams. Threaded rods of 7/16 in. (11.1 mm) diameter were placed on pre-defined locations with most of the length of each rod, except the middle 3 in. (76.2 mm), wrapped by teflon tubes in advance to avoid bond between the rod and surrounding concrete as shown in Figure IV.14.

The beam and column were divided into several segments as shown in Figure IV.15 to evaluate the variation of curvature. The curvature of each segment in the column and beams is calculated by the relative deformations between tension and compression zones. For example, the curvature of the beam i^{th} segment, $\phi_{B,i}$, is obtained from

$$\phi_{B,i} = \frac{\Delta_{B,b,i} - \Delta_{B,t,i}}{b_{b,i} h_{b,i}} \tag{IV.3}$$

where $\Delta_{B,b,i}$ and $\Delta_{B,t,i}$ are deformation of bottom and top displacement measuring gages in the beam i^{th} segment, respectively, and $b_{b,i}$ and $h_{b,i}$ are gage length and vertical distance between gages of the beam i^{th} segment, respectively. The column curvature is calculated by a similar equation below with averaging relative deformations in each two opposite two sides, refer to Figure IV.15.

$$\phi_{C,i} = \frac{\overline{\Delta}_{C,l,i} - \overline{\Delta}_{C,r,i}}{b_{c,i} h_{c,i}} \tag{IV.4}$$

where $\overline{\Delta}_{C,l,i}$ and $\overline{\Delta}_{C,r,i}$ are respectively average deformation of left and right displacement measuring gages of the column i^{th} segment in one direction of bending, and $b_{c,i}$ and $h_{c,i}$ are gage length and horizontal distance between gages of the column i^{th} segment, respectively, as shown in Figure IV.15.

During testing, the column axial deformation was measured by two wire potentiometers installed between the top and bottom W $16 \times 1/2 \times 36$ steel beams on both sides of the column as shown in Figure IV.16. The column axial deformation is determined as the average of these two measurements.

The relative deformation at the beam-joint interfaces was measured and transformed into the rotation. Two displacement transducers were mounted on angles attached to aluminum tubes, which were rigidly attached to the column face by the spring tension. Frictionless plates were firmly bolted to threaded rods embedded in the beam 1 in. (25.4 mm) from the beam-joint interface, as shown in Figure IV.17. The relative deformations, $\Delta_{BJ,b}$ (bottom) and $\Delta_{BJ,t}$ (top), were assumed to be the relative translation between displacement transducer and frictionless plate. Dividing the relative deformations by the distance between top and bottom transducer, h_{bj} in Figure IV.17, the rotation at the beam-joint interface, θ_S, is obtained as

$$\theta_S = \frac{\Delta_{BJ,b} - \Delta_{BJ,t}}{h_{bj}} \tag{IV.5}$$

Due to the presence of the RC slab, a beam in the longitudinal direction is subjected to torsion during transverse beam loading. Twisting of the longitudinal beam was measured at three locations along its span, as shown in Figure IV.18. The twisting angle at the i^{th} location, $\theta_{T,i}$, is calculated by

$$\theta_{T,i} = \frac{\Delta_{L,i} - \Delta_{R,i}}{b_t} \tag{IV.6}$$

where $\Delta_{L,i}$ and $\Delta_{R,i}$ are the vertical displacement of left and right side at i^{th} location, respectively, and b_t is the distance between the left and right transducers.

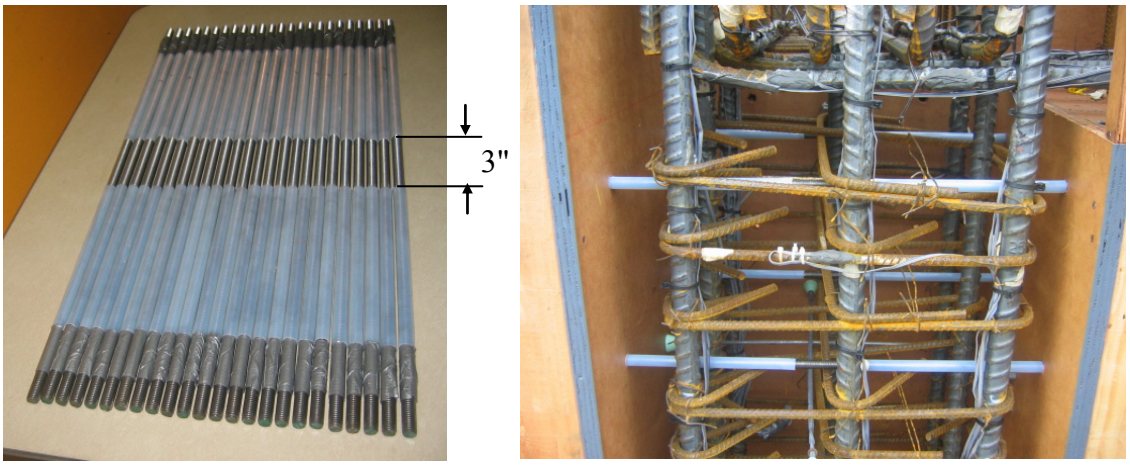

Figure IV.14 Threaded rods for instrumentation.

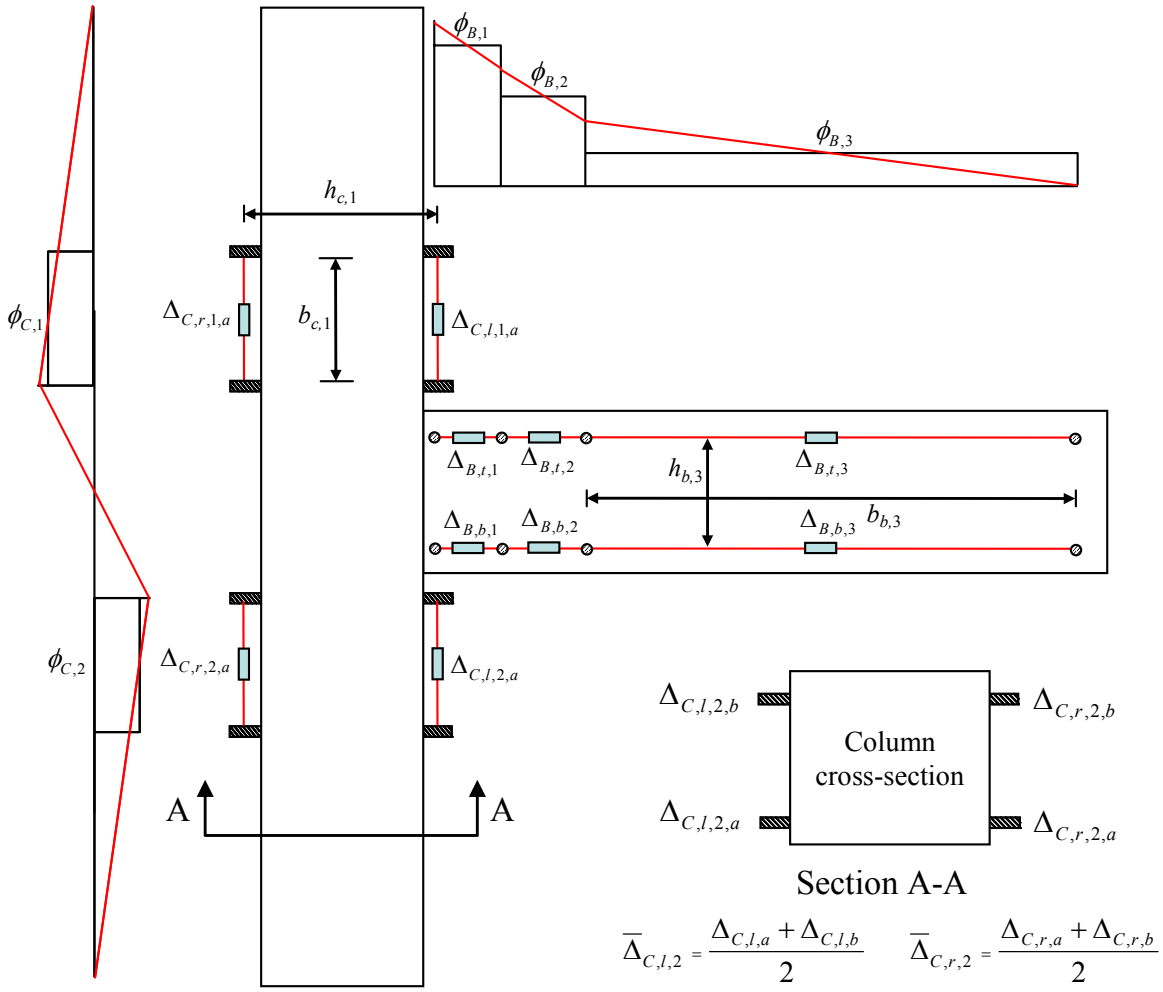

Figure IV.15 Instrumentation for beam and column flexural deformations.

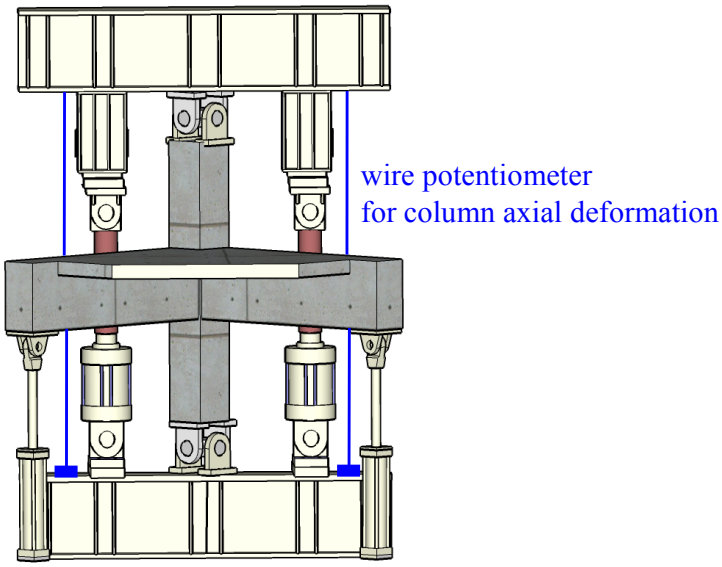

Figure IV.16 Instrumentation for column axial deformation.

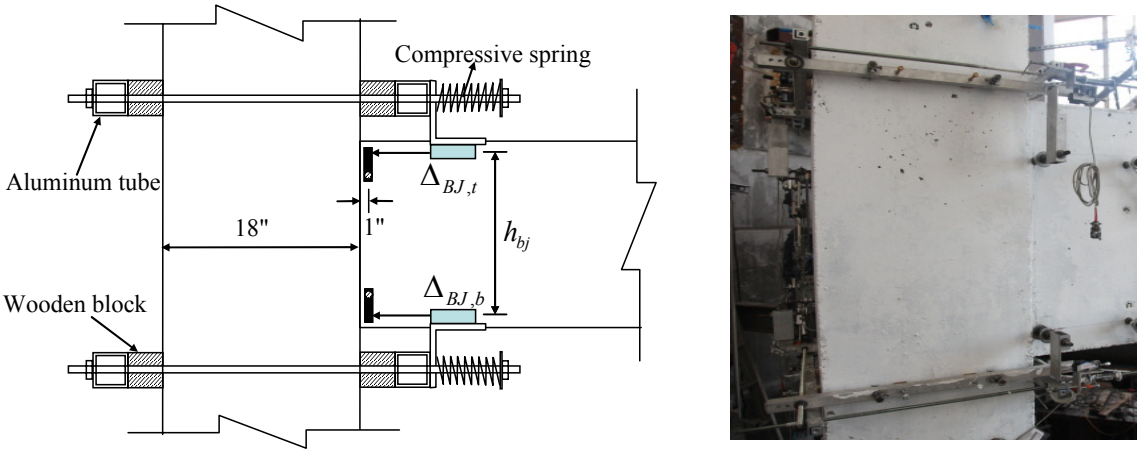

Figure IV.17 Instrumentation for rotation at the beam-joint interface.

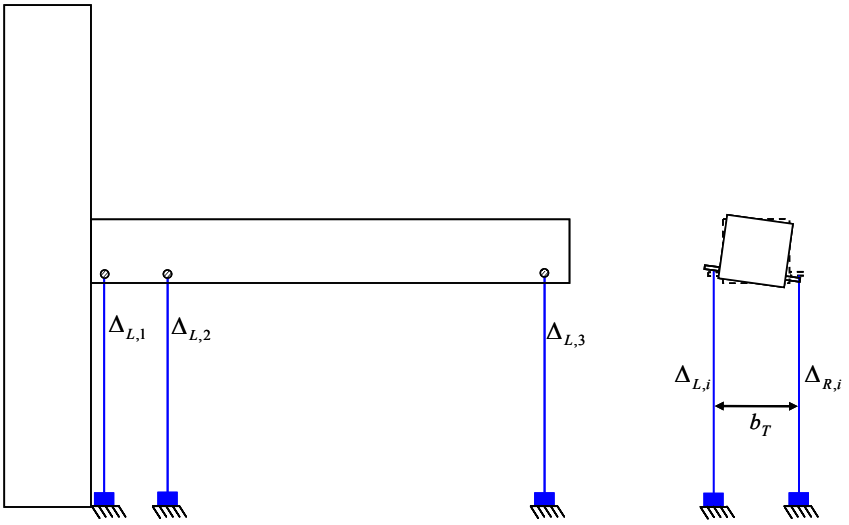

Figure IV.18 Instrumentation for beam twisting.

IV-6.3 Joint Shear Strains

The joint shear strain has been measured in several different methods reported in the literature as depicted in Figure IV.19. After reviewing this literature on joint shear strain measurements, the instrumentation of four sides and two diagonals was adopted and fixtures were installed in the outside of joint panel to allow expansion due to crack opening and sliding as shown in Figure IV.20. This choice of joint shear strain instrumentation was based on two reasons: (1) tests from literature (refer to Figure I.2 in Chapter I) showed that joint shear cracks propagated to the column above and below the joint, which is requiring measurements to be installed outside the joint panel and (2) shear strain measurements within the joint panel is highly affected by the crack location particularly in case of unreinforced joints because concrete in this case is damaged into several pieces that can move freely due to absence of transverse reinforcement to hold these pieces together, which is again requiring measurements outside the joint panel to avoid constraining or missing such moments.

The displacement potentiometers were mounted on specially designed aluminum braces made from aluminum tubes. Two aluminum (1 in. (25.4 mm) square section and 24 in. (610 mm) long) tubes were secured to both sides of the column by pre-tensioned springs. The pre-tensioning force was only high enough to hold the instrumentation frame without constraining the local deformations such as dilatation of the column concrete. Each aluminum tube was positioned through two wooded blocks placed against the column face. One wooded block was attached to concrete using pre-drilled screw to fix the instrumentation position, refer to Figure IV. 20, while the other wooden block was placed against the concrete by friction to allow for unrestrained dilatation of the concrete column between these blocks.

From this instrumentation, joint shear strain, γ_{xy}, can be calculated using trigonometric law as

$$\gamma_{xy} = \frac{1}{4}\left\{ \sum_{i=1,2,5,6} \left(\omega_i' - \omega_i^0\right) - \sum_{j=3,4,7,8} \left(\omega_j' - \omega_j^0\right) \right\} \tag{IV.7}$$

where ω_i^o and ω_i' are the initial angle and deformed angle of the i^{th} corner in the joint panel, respectively. These angles in undeformed and deformed shapes are illustrated in Figure IV.21.

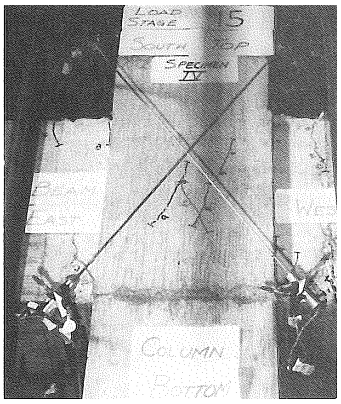

(a) Two diagonals measurement (Meinheit and Jirsa, 1977)

(b) Two relative beam-column deformations (Pampanin et al., 2003)

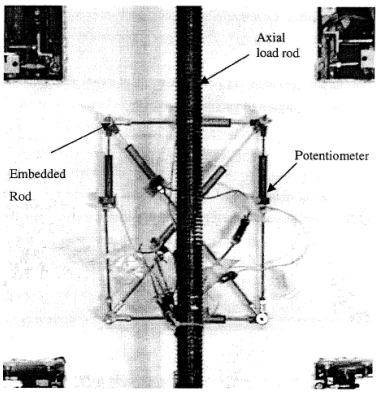

(c) Six measurements using rods within the joint region (Walker, 2001)

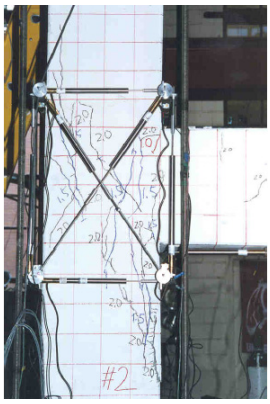

(d) Six measurements using rods outside the joint (Pantelides et al., 2002)

Figure IV.19 Joint shear strain instrumentations in literature.

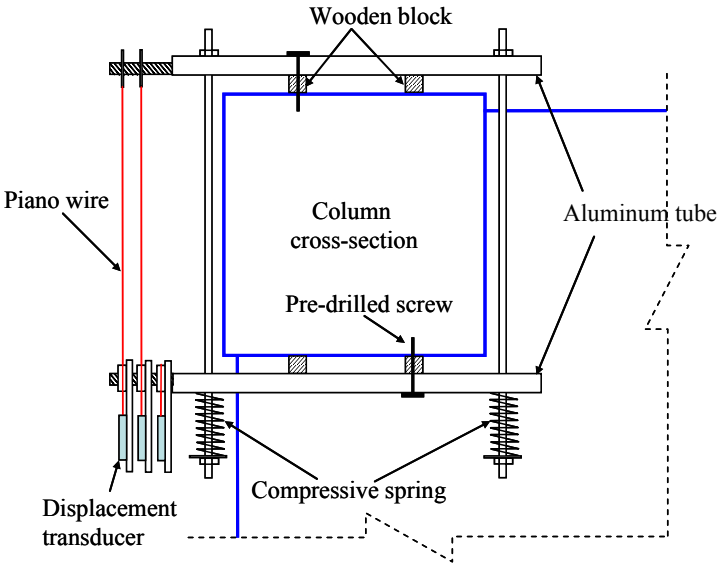

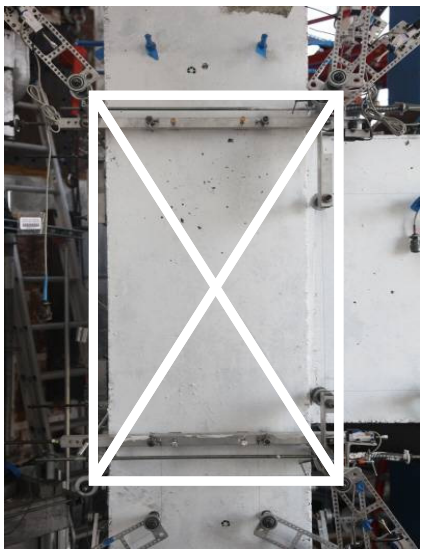

Figure IV.20 Instrumentation for joint shear strain in this study.

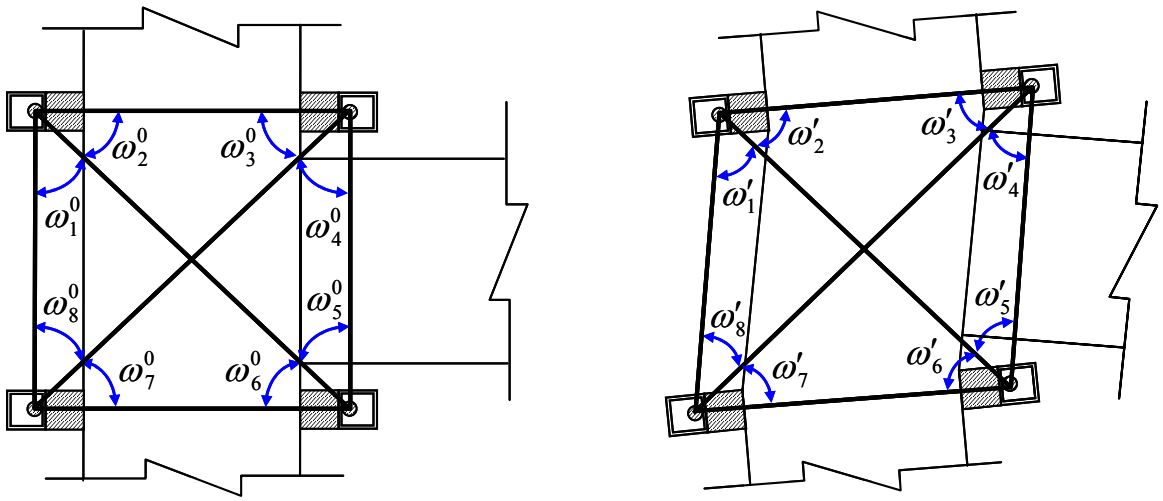

(a) Original joint geometry (b) Deformed joint geometry

Figure IV.21 Joint shear strain calculation.

IV-6.4 Strain Gages

A total of seventy five strain gages were installed on the longitudinal and transverse beam reinforcement, column reinforcement, and slab reinforcement. The used strain gages had post-yield deformation capacity of 10–15% strain with gage size of 0.20 in. by 0.08 in. (5 mm by 2 mm). Each strain gage glued to the surface of a reinforcing bar was coated by wax, butyl rubber, and epoxy.

Among the beam reinforcements, four beam longitudinal bars located on interior and exterior bars at top and bottom were selected for measuring strains. Each bar had 5 strain gages: (1) hook tail, (2) hook bending point, (3) middle of joint, (4) beam-column interface, and (5) $d_b/2$ from the interface, where d_b is the effective beam depth. The layout of strain gages on beam reinforcement is shown in Figure IV.22. The instrumentation of beam reinforcement strains was intended to determine the onset and propagation of the beam longitudinal bars yielding, to evaluate the bond deterioration within the joint region, and to calculate the joint shear stresses. Only one stirrup was instrumented with one strain gage as shown in Figure IV.22 because shear failure was not expected in any of the beams.

In the column, strain gages were mounted on four longitudinal bars at each corner and two intermediate bars only on the open sides where beams were not framing in. The layout of strain gages on column reinforcement is shown in Figure IV.23. The strain gage data at corners were used to confirm that the column longitudinal bars were elastic during testing and the strain gages of the intermediate bars were used to investigate whether these bars acted as tension ties as postulated in Hwang et al. (2005). Only two transverse ties were instrumented with two strain gages each as shown in Figure IV.23 because shear failure was not expected in any of the columns.

In the slab, four top and two bottom reinforcing bars were gaged with strain gages in each direction. The layout of strain gages on slab reinforcement is shown in Figure IV.24.The slab reinforcement strain data were used to estimate the effective slab width and to observe the behavior of possible insufficient anchorage detail of the bottom bars.

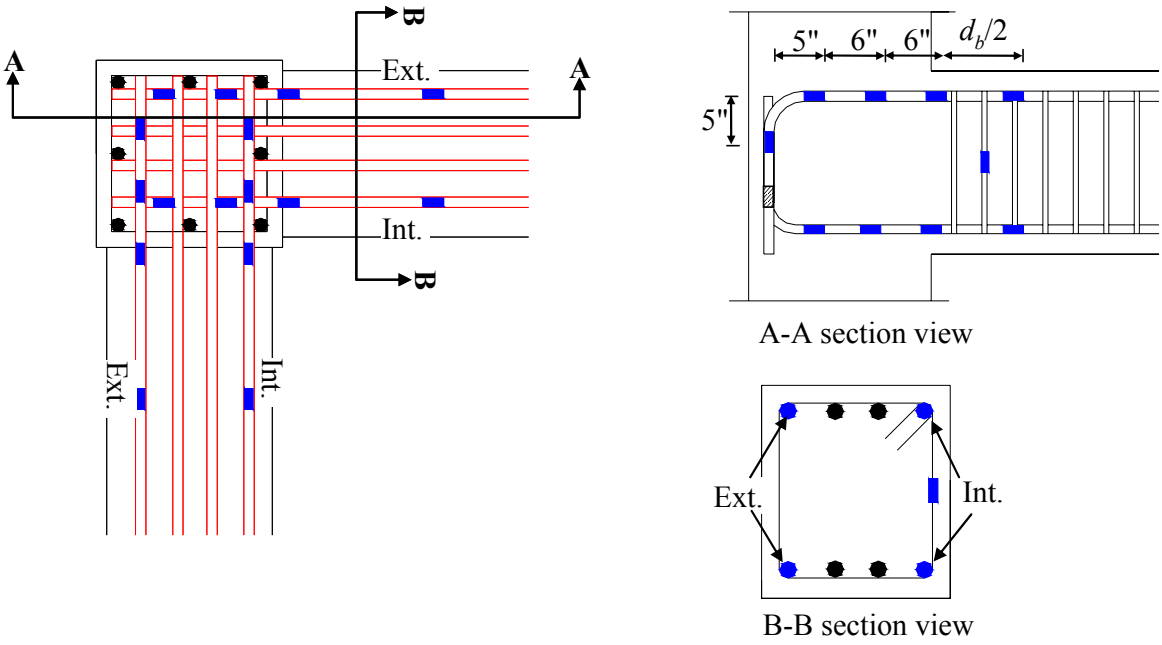

Note: 1" = 25.4 mm

Figure IV.22 Strain gages on beam reinforcement.

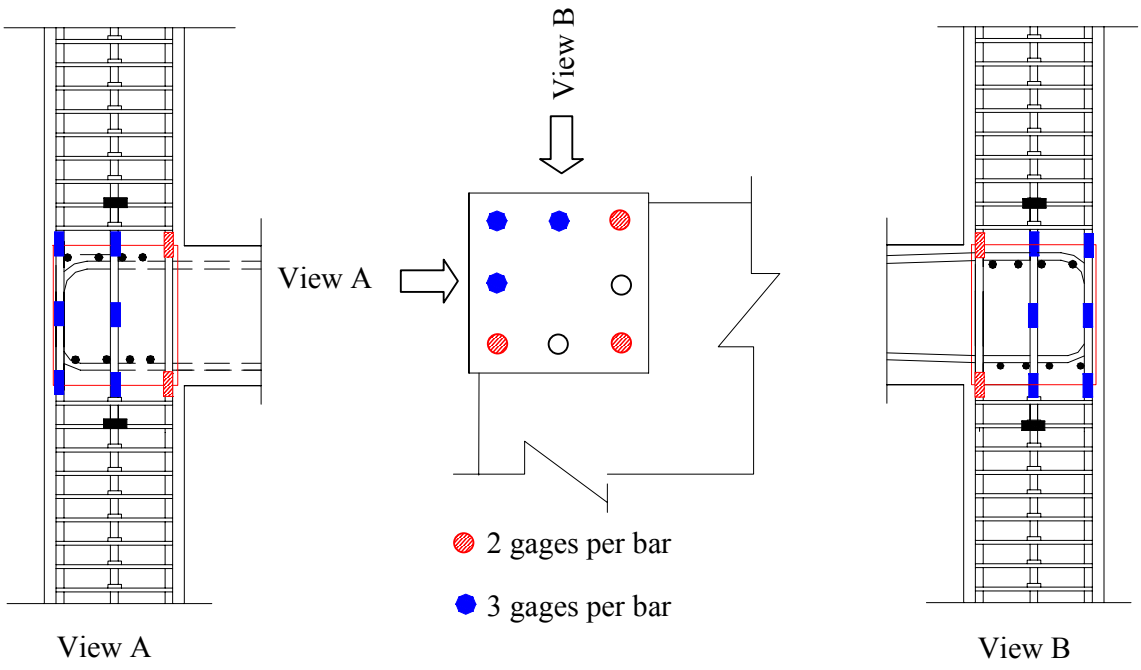

Figure IV.23 Strain gages on column reinforcement.

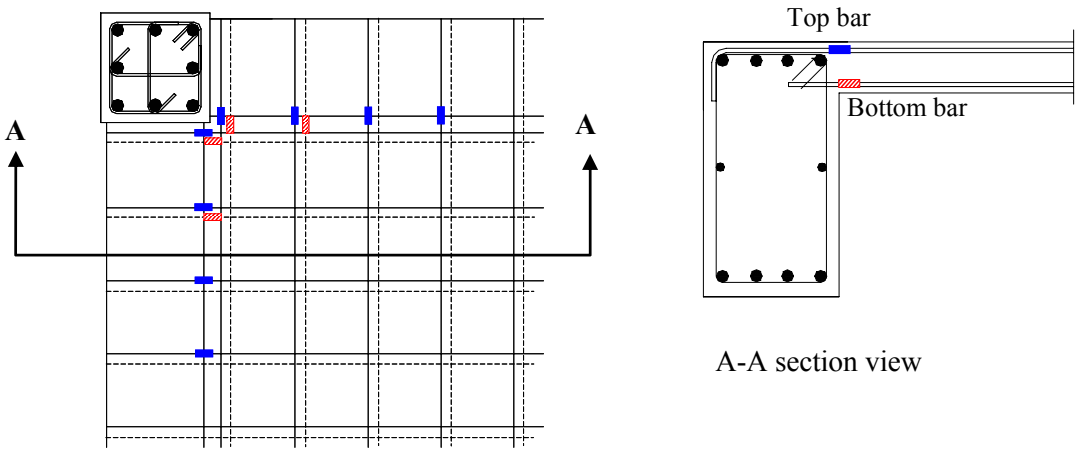

Figure IV.24 Strain gages on slab reinforcement.

IV-6.5 Global Translations

The global translations of the test frame and the specimen were measured by displacement transducers and strain gages as shown in Figure IV.25. Translations of top beam of the vertical test frame and the column were monitored to check if the lateral restraining frame functioned as expected. At bottom of column, rotation of the bi-directional swivel was measured to check if the bi-directional swivel functioned as a true hinge. In addition, relative translations between the top and the bottom of the joint panel were measured during longitudinal beam loading. Two strain gages were installed on the diagonal tube bracing member to monitor the stability of the lateral restraining frame.

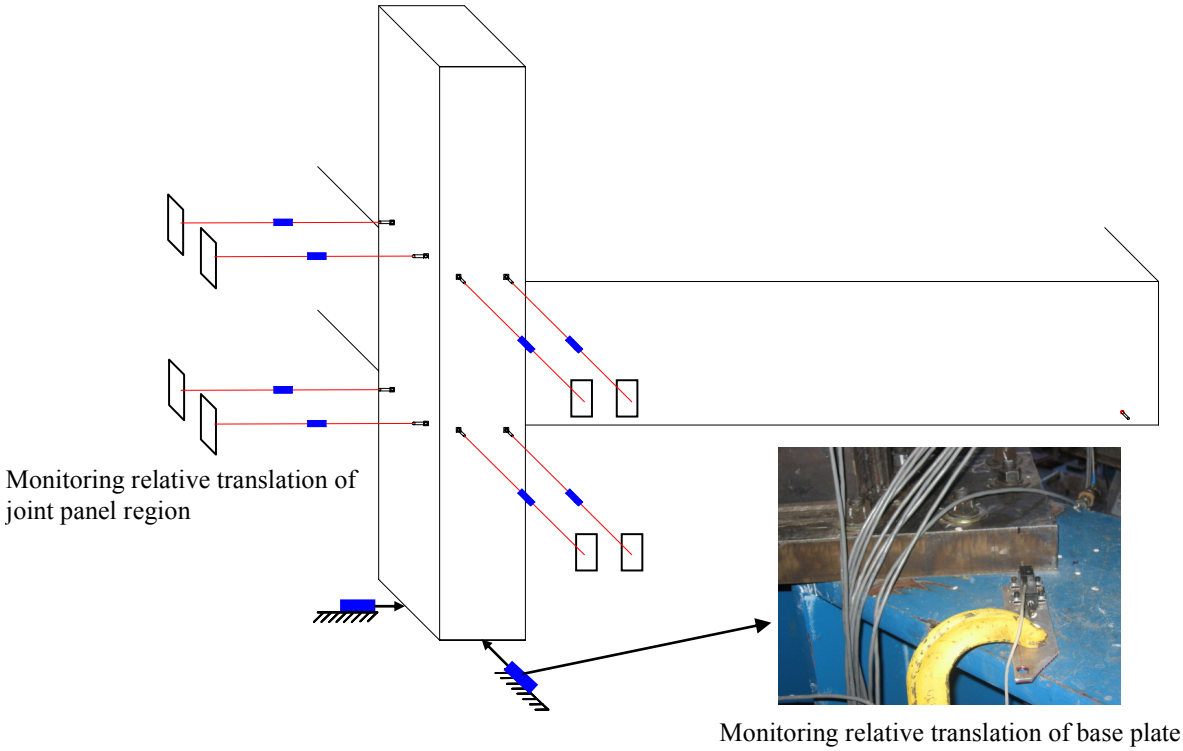

(a) Global translations of specimen

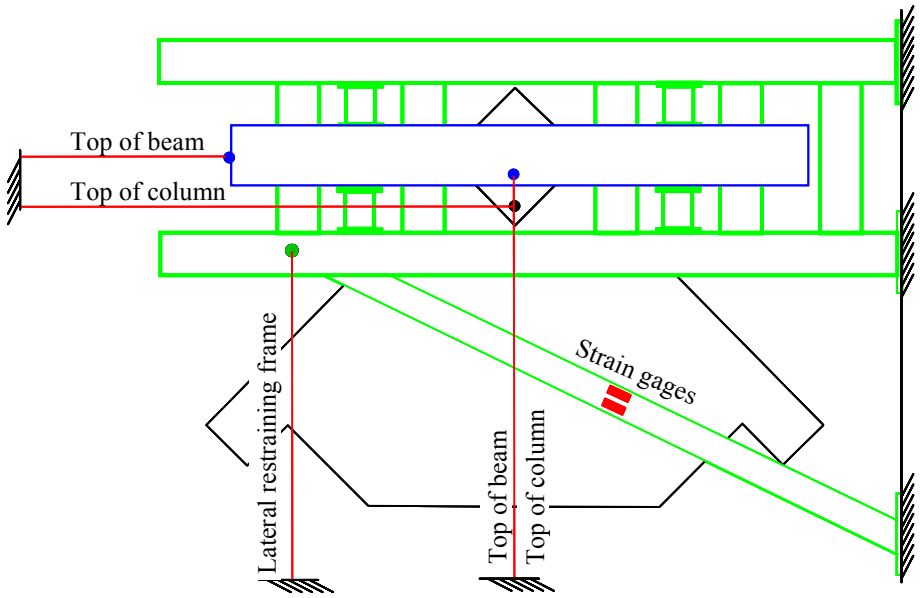

(b) Global translations of test frame

Figure IV.25 Instrumentation for global translation.

V Experimental Results and Observations

This chapter provides the test results including the measured test data and observed damage progression of each specimen. First, the hysteretic responses of the applied load versus drift are presented based on the data measured at the tip of the beam. The applied load was recorded by the load cell embedded in the beams actuators. The drift (Δ) is defined as the beam tip displacement divided by the length of L+0.5b_c, where L=8 ft. (2.44 m) is the tested beam length from the column face to the beam loading point and b_c=18 in. (457 mm) is the column width, as illustrated in Figure IV.1. The beam tip displacement was determined by averaging two displacements measured at both sides of the loading point. In addition, the variation of the axial load and vertical displacement in the column are presented.

Second, the observed damage in each specimen is described in terms of the formation and propagation of cracks and failure of the joint region, beams and slab, aided by high resolution photographs. For clarifying the damage progression, the description of EW direction is followed by NS direction in the sequence of important events, such as first cracking, yielding and peak loading. The damage description is split into two parts: (1) joint region, and (2) beam and slab in each direction. Subsequently, the common observations of the joint region, beams and slab in both directions are summarized.

Third, the joint shear stress versus rotation responses are evaluated. The joint shear stress is calculated by the constant moment arm assumption which is identically used for evaluating the literature database in Chapter II. A constant moment arm is defined as a coefficient times the effective beam depth. As discussed in Chapter II, this coefficient is taken as 0.875 if beam reinforcement does not yield; otherwise, it is taken as 0.9. To estimate the effective depth of the beam cross-section, the measured concrete cover depths at the top and bottom of the beam are utilized and the contribution of slab reinforcement is considered based on the strain gage data. The measure concrete cover depths are given in Chapter IV. For the comparison with the joint shear strength per ASCE41 (2006), joint shear stress, v_{jh}, is normalized by the square root of the concrete compressive strength, $\sqrt{f_c'}$, i.e. $\gamma = v_{jh} \big/ \sqrt{f_c'}$. For joint deformation, joint shear strain, γ_{xy}, and rotation at beam-joint interface, θ_s, due to slip or crack opening were measured. For developing an implicit joint macro-model in this study, the total joint rotation is defined as the sum of joint shear strain and rotation at the beam-joint interface. These are directly evaluated from the recorded data. Detailed information about instrumentation and data reduction are provided in Chapter IV.

Lastly, the strains on beam, slab, and column longitudinal reinforcement are presented. The locations corresponding to the strain gage data are specified in the figures. Some of the strain gages were damaged during specimen construction or during testing. The unrecorded data

of these damaged strain gages are presented as blank bars marked as not applicable (N/A) in the different plots.

V-1 Specimen SP1

V-1.1 Load versus Drift Response

Hysteresis curves of the applied load versus drift are shown in Figure V.1 and values at the first peak of each cyclic loading group are given in Table V.1. Note that the negative (-) and positive (+) signs correspond to beam downward loading and upward loading, respectively.

The first yielding of top reinforcement in both the EW and NS beams was captured from strain gage data between the third loading group ($\Delta = -1.16\%$ in average of Δ_{EW} and Δ_{NS}) and fourth loading group ($\Delta = -1.72\%$ in average) for the downward loading. Meanwhile, the bottom reinforcement yielding in both the EW and NS beams was observed during the fifth loading group, $\Delta_{EW} = 2.03\%$ and $\Delta_{NS} = 2.11\%$, respectively. It is noted that the drift at beam yielding is estimated by conventional analysis for the beam-column subassemblies of the specimens using OpenSees (2010), as mentioned in Chapter IV. The estimated yield drift for SP1 is equal to 1.18% which is the drift at the third group for the downward loading and the fourth group for the upward loading, refer to Table IV.5.

The peak loads of EW beam were achieved at the sixth loading group where the respective drift and applied load were -3.86% and -24.1 kips (-107.2 kN) for the downward loading, and 3.21% and 26.4 kips (117.5kN) for the upward loading. The NS beam reached its peak load at the fifth loading group which is one group prior to the EW beam peak loading. Because the joint was already damaged during the preceding EW beam loading, the NS beam loading could not increase after the peak of the EW beam. It is worth mentioning that the peak loads are greater than the value calculated from beam flexural strength without considering slab contribution, which means that slab reinforcing bars contributed to resisting the applied lateral load. After reaching the peak load, the applied beam load sharply reduced for the downward loading but the strength degradation after peak was less severe for the upward loading, i.e. slab in compression. The hysteretic curve in Figure V.1 clearly shows pinching behavior which was induced by the slip of the beam longitudinal bars, especially the bottom ones, through the joint core due to bond deterioration.

The column axial load was controlled to follow the pre-defined axial loading equation in terms of applied beam shear forces, as presented in Equation (IV.2a). The column axial loading started incorrectly from 83 kips (369 kN) in compression which is less than the intended value of 144 kips (641 kN), as shown in Figure V.2(a). Note that column axial load in the vertical axis of Figure V.2(a) is positive for compression. As a result, due to this error, the true equation of column axial loading used for SP1 is as follows,

$$P_{\text{applied}} = 34 - 4V_{b,\text{EW}} - 4V_{b,\text{NS}} \quad \text{true column axial loading for specimen SP1} \qquad \text{(V.1)}$$

During the test, the column axial load varied from 77 kips (343 kN) in tension to 123 kips (547 kN) in compression instead of 16 kips (71 kN) in tension to 184 kips (819 kN) in compression if the column axial load was correctly applied. Normalizing the maximum column axial tension and compression by the column axial compressive strength, i.e. $f'_c A_g$ where $A_g = h_c \times b_c$, the variation of column axial load ratio ranged from 6.7% (tension) to 10.6% (compression). It is worth mentioning that the change of the applied peak column axial load ($0.1 f'_c A_g$) from the intended peak value of ($0.15 f'_c A_g$) was expected not to make significant difference in results based on the effect of column axial load on the joint shear strength, refer to Figure II.5 in Chapter II. On the other hand, the column and joint of SP1 were subjected to large axial tension which was expected to lower the joint cracking load and shear strength but the results were not affected by this tension based on the measured beam shear forces (Table V.1) and the joint shear stress results subsequently presented in Chapter VI where it was found that the beam shear forces and the joint shear stresses were similar when the column was in compression or in tension.

The vertical displacements were recorded by position transducers installed on both sides of the column between the top and bottom of the test frame. The peak vertical average displacements from the measurements were 0.147 in. (3.73 mm) in elongation and 0.043 in. (1.09 mm) in contraction, refer to Figure V.2(b). Note that vertical displacement in the vertical axis of Figure V.2(b) is positive for contraction.

Table V.1 Load versus drift response of SP1.

Group No.	SP1							
	EW direction				NS direction			
	Downward (-)		Upward (+)		Downward (-)		Upward (+)	
	Δ (%)	V_b (kip)	Δ (%)	V_b (kip)	Δ (%)	V_b (kip)	Δ (%)	V_b (kip)
1	-0.57	-12.4	-0.02	7.1	-0.56	-12.0	-0.01	7.6
2	-0.87	-15.8	0.27	10.3	-0.85	-17.3	0.28	9.9
3	-1.17	-18.5[*1]	0.55	14.2	-1.14	-19.2	0.61	13.8
4	-1.77	-22.4	1.15	20.6	-1.67	-22.7[*1]	1.25	20.6
5	-2.66	-24.0	2.03	25.4[*1]	-2.57	-22.9[#2]	2.11	24.2[*1#2]
6	-3.86	-24.1[#2]	3.21	26.4[#2]	-3.77	-21.1	3.29	23.8
7	-5.36	-19.0	4.99	24.0	-5.31	-12.6	5.05	18.6
8	-7.71	-9.3	7.27	17.4	-	-	-	-

[*1] first yielding of beam reinforcement; [#2] peak loading.
Note: 1 kip = 4.45 kN.

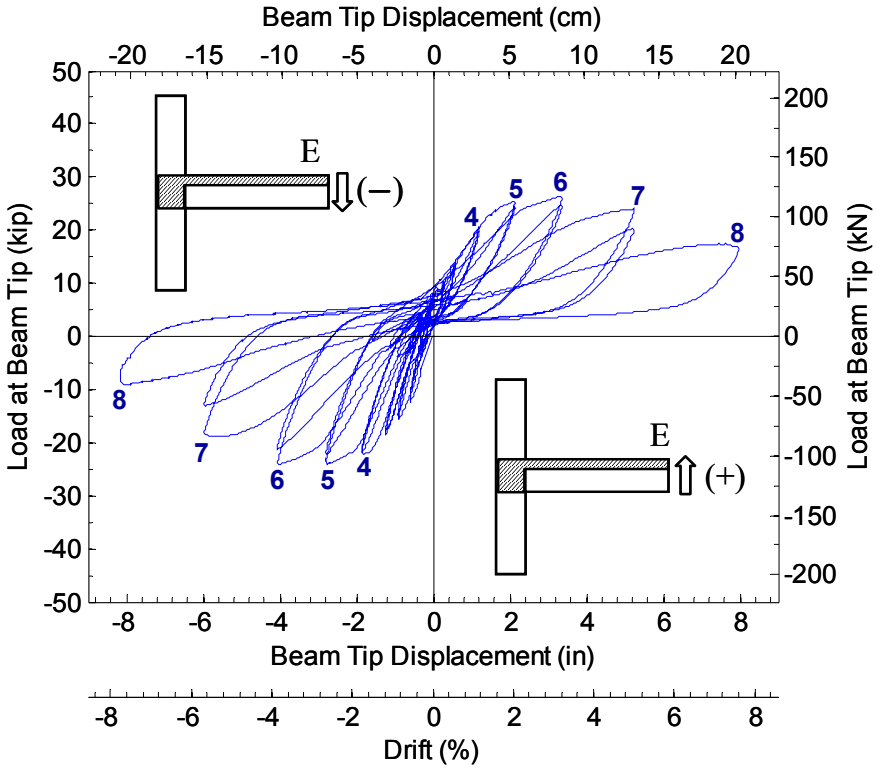

(a) EW direction

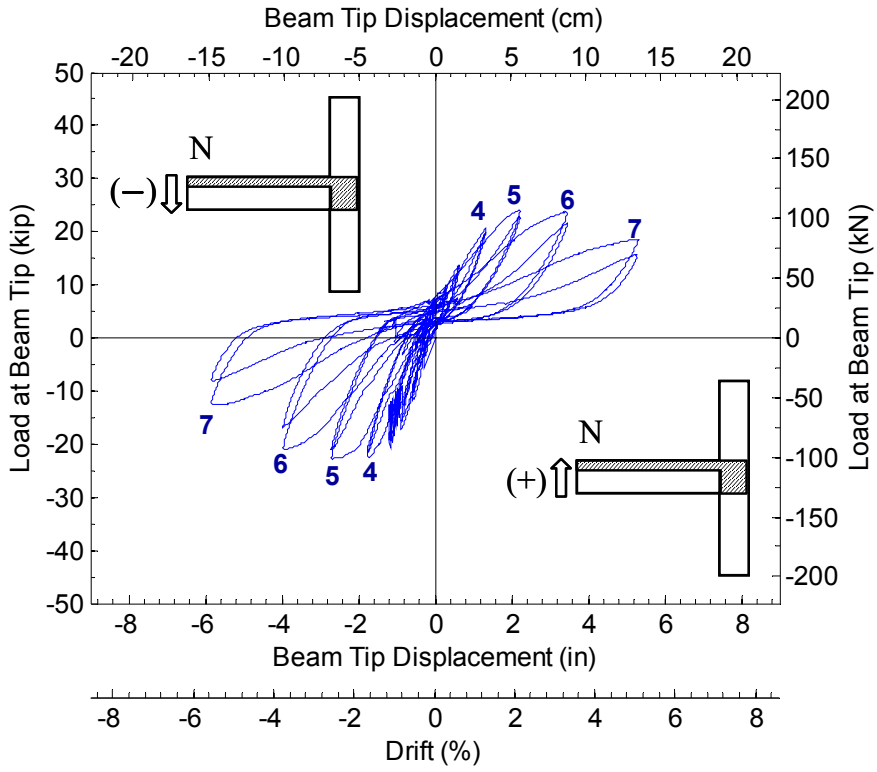

(b) NS direction

Figure V.1 Load versus drift response of SP1.

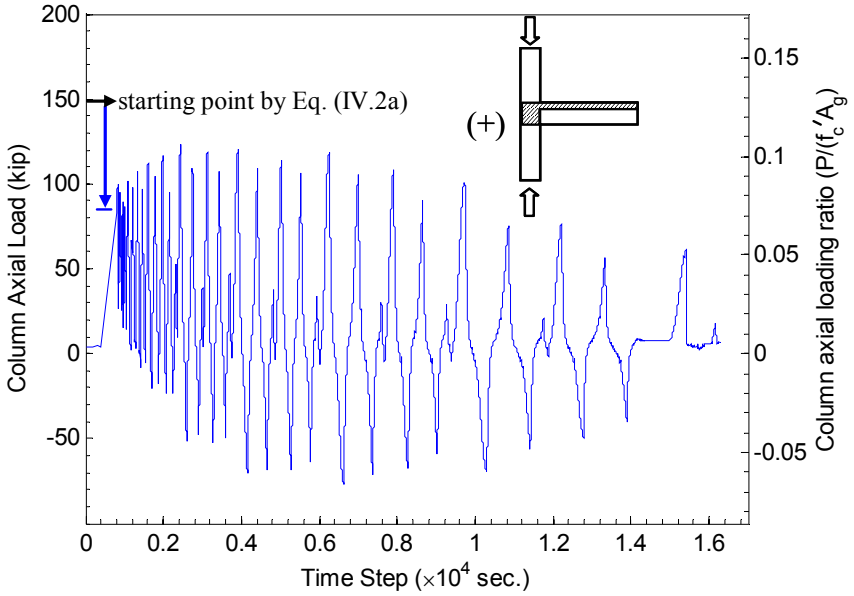

(a) Column Axial Load

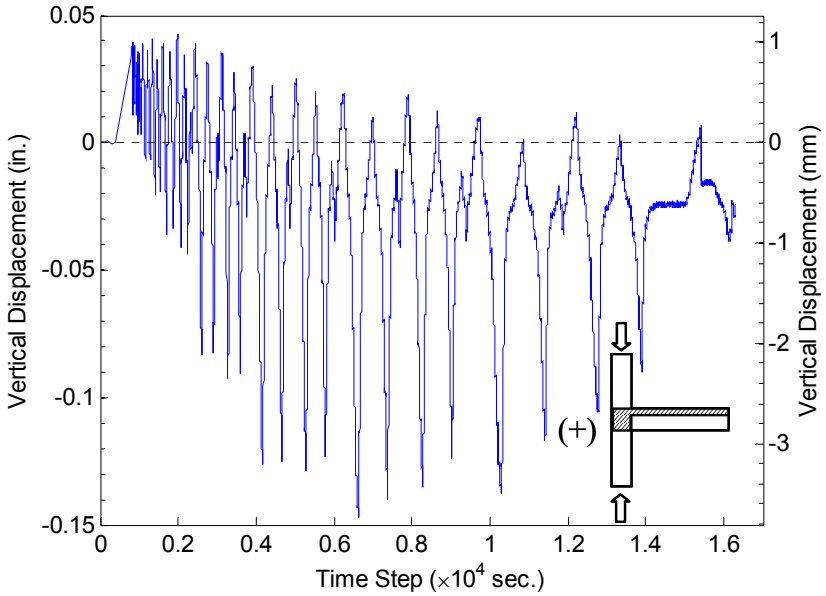

(b) Vertical Displacement

Figure V.2 Column response of SP1.

V-1.2 Observed Damage Progression

The damage progression of the joint in both directions is qualitatively summarized in Table V.2 and using photographs. It is noted that invisible hairline cracks in the shown photographs are marked by added lines to the photographs to emphasize their existence. The existing cracks in the beams and slab were marked after removing the instruments when the specimen was removed from test frame.

V-1.2.1 EW Direction

Joint Region

The joint showed a typical "X" diagonal crack pattern during the EW beam cyclic loading, i.e. longitudinal beam loading. A first hairline diagonal crack (↘) caused by the downward loading, which is referred to as downward diagonal crack hereafter, occurred at the second group ($\Delta_{EW} = -0.87\%$), while a diagonal crack in the opposite direction (↗) caused by the upward loading, which is referred to as upward diagonal crack hereafter, appeared at the fourth group of loading ($\Delta_{EW} = 1.15\%$), refer to Figure V.3(a). For the fifth group, the first downward diagonal crack propagated without new cracks initiating but a new upward diagonal crack initiated at the location of the 90° hook of the beam reinforcement, as shown in Figure V.3(b). At the sixth group where the peak load was achieved, the two major diagonal cracks crossing corners in the joint panel significantly propagated and extended from the joint region to the column, as shown in Figure V.3(c). From the seventh group of loading, the concrete of the joint panel was bulging and dilating away from the column, particularly at the top corner of the joint on the side where there is no beam. At the end of the test, joint cover concrete was completely detached and joint core concrete was split into several parts bounded by the diagonal cracks, as shown in Figure V.3(d).

During the upward loading of NS beam, a horizontal crack was observed at the top of the EW joint panel but no cracks appeared in the downward loading. At the third group of the NS beam upward loading, a hairline horizontal crack initiated from the top of the interface between the column and the EW beam and it propagated across the whole width of the joint panel at the subsequent groups of upward loading, as shown in Figure V.4(a). It is noted that the location of this horizontal crack was close to the top reinforcement in the EW beam.

Beam and Slab

A first flexural hairline crack at the top of the EW beam appeared during pull-down loading prior to testing. At the first group of EW beam downward loading, a splitting crack developed at the top of the beam-joint interface. Simultaneously, splitting cracks developed along the line of beam-slab interface of the L-shape cross-section. Up to the peak load, the splitting crack at the beam-joint interface opened wider and the number and width of flexural cracks in the beam and slab increased. In particular, the splitting crack at the NS beam-slab interface was significant. Cracks on the slab were originated from beam flexural cracks and thus they were connected to

each other. The joint cracks continued to significantly increase until the end of testing, while flexural cracks showed no further propagation and seemed to decrease in width after peak loading because joint deformation was prevailing in the global behavior of the specimen. Therefore, plastic hinge mechanism did not form in the beam. The existing cracks in the EW beam and slab after testing are illustrated in Figure V.5.

During the NS beam loading, inclined cracks occurred at the top of the EW beam due to torsion. The EW beam showed noticeable inclined crack under the NS beam downward loading and it crossed over the whole depth of the EW beam as testing continued. Moreover, the existing splitting cracks at the beam-joint interface widened by the induced torsion during the NS beam loading.

V-1.2.2 NS Direction

Joint Region

The diagonal joint cracking in the NS joint panel showed a different pattern, compared with the EW joint. The first downward diagonal crack (↙) occurred at the fourth group, $\Delta_{NS} = -1.67\%$. During the upward loading at the same group, short hairline horizontal cracks developed in the joint panel at the bottom on the side with beam and the top on the side where there is no beam, and a short hairline diagonal crack (↖) appeared in the joint panel. For subsequent downward loading of the NS beam, the existing diagonal crack was growing longer and wider without formation of new diagonal cracks, while multiple diagonal cracks newly developed under the upward loading. Significant increase of crack width was observed at the sixth group of NS beam loading, which followed the peak of the EW beam loading. The concrete of the NS joint panel split into several pieces and bulged out at the seventh group, which was similar to the observation made in the EW joint panel. The NS joint damage progression is shown in Figure V.6.

During the upward loading of the EW beam, two horizontal cracks were observed at the top of the NS joint panel at the fourth group of loading. The upper horizontal crack closed and the lower horizontal crack widened starting from the fifth group of loading, as shown in Figure V.4(b). The upper horizontal crack was on the line of the slab top surface, and the lower horizontal crack at the top of joint and another horizontal crack at the bottom of the joint were close to the top and bottom reinforcement of the NS beam, respectively. Unlike the EW joint panel, a horizontal crack also formed at the bottom of the NS joint panel during the EW beam downward loading in the fifth group of loading but its width was much smaller than the top horizontal crack width.

Beam and Slab

Multiple flexural cracks took place in the beam and slab and propagated as the loading increased. A splitting crack developed along the EW beam-slab interface line during the NS beam loading similar to the observation made for the EW beam loading. In general, the crack pattern of the beam and slab looked similar for the EW and NS loadings but crack propagation was more severe in the EW side. The splitting crack propagation at the beam-joint interface was observed

from the photographs taken at the sixth group of loading, as indicated by the arrow in Figure V.6(c). During the EW beam loading, torsional inclined cracks also occurred in the NS beam. The existing cracks in the NS beam and slab after testing are shown in Figure V.5.

V-1.2.3 Summary

During the longitudinal beam loading, flexural cracks initiated in the beam and slab at the early stage of loading followed by diagonal cracks in the joint region and splitting crack at the beam-joint interface. With increase of loading, existing diagonal cracks in the joint region as well as flexural cracks in the beam and slab propagated and widened. In particular, slab cracks formed a grid pattern on the top of the slab in both directions of loading (Figure V.5(c)). Finally, joint cracks dominated the failure of the specimen at the peak loading.

Joint diagonal cracks occurred between the drift level of 1.20% and 1.72%, except for first downward joint crack in the EW direction which appeared at the loading to 0.87% drift. The early occurrence of joint crack for the EW beam downward loading is attributed to the larger cover concrete thickness of the EW beam cross-section. Visible propagation of joint diagonal cracks was observed at the fifth group of loading and at subsequent loading up to the peak loads at $\Delta_{down} = -3.72\%$ and $\Delta_{up} = 3.25\%$ where the joint diagonal cracks were significantly open. Thereafter, the cover concrete of the joint panel began to bulge and finally spalled off. The joint core concrete was also crushed based on observations of the specimen after removing the loose cover concrete.

Splitting cracks at beam-joint interface and beam-slab interface were more crucial than other flexural cracks. No plastic hinge mechanisms formed in any of the beams. Figure V.7 confirms that the specimen experienced joint failure without beam hinging.

During the orthogonal beam loading, horizontal cracks appeared in the joint panel in the transverse direction which is perpendicular to the loading beam. The formation of the horizontal cracks is explained using free body diagram of the joint region in Chapter VI. Inclined cracks occurred in the beam due to torsion. These inclined cracks were considerable under the orthogonal beam downward loading, i.e. slab in tension.

Table V.2 Qualitative damage description of SP1.

Drift (%)	EW direction	NS direction
$\Delta_0 = -0.3$	- First flexural crack from top of beam	-
$\Delta_{up} = -0.02$ $\Delta_{down} = -0.57$	- Additional flexural cracks in beam and slab	- First flexural crack at top of beam
$\Delta_{up} = 0.28$ $\Delta_{down} = -0.86$	- First downward diagonal crack in joint - Splitting crack at beam-joint interface	- Additional flexural cracks in beam and slab
$\Delta_{up} = 0.58$ $\Delta_{down} = -1.16$	- First yielding of one of beam top bars	-
$\Delta_{up} = 1.20$ $\Delta_{down} = -1.72$	- First upward diagonal crack in joint	- First downward diagonal crack in joint - First upward diagonal crack in joint - Yielding of beam top bars
$\Delta_{up} = 2.07$ $\Delta_{down} = -2.62$	- Second upward diagonal crack in joint - Propagation of splitting crack at beam-joint interface - First yielding of beam bottom bars	- Additional upward diagonal cracks in joint - First yielding of beam bottom bars
$\Delta_{up} = 3.25$ $\Delta_{down} = -3.72$	- Large opening of joint diagonal cracks - Large opening of splitting crack at beam-joint interface	- Large opening of joint diagonal cracks
$\Delta_{up} = 5.02$ $\Delta_{down} = -5.34$	- Bulging of joint cover concrete - Separation of concrete wedge from corner of joint on the free side where there is no beam - Reduction of width of beam flexural cracks	- Spalling of joint cover concrete - Separation of concrete wedge from corner of joint on the free side where there is no beam - Reduction of width of beam flexural cracks
$\Delta_{up} = 7.27$ $\Delta_{down} = -7.71$	- Spalling of joint cover concrete - Crushing of joint core concrete	-

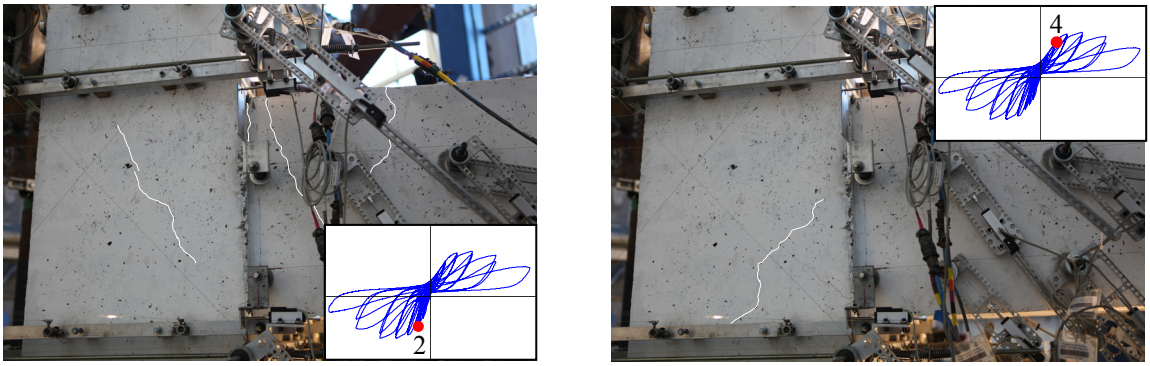

(a) First joint crack

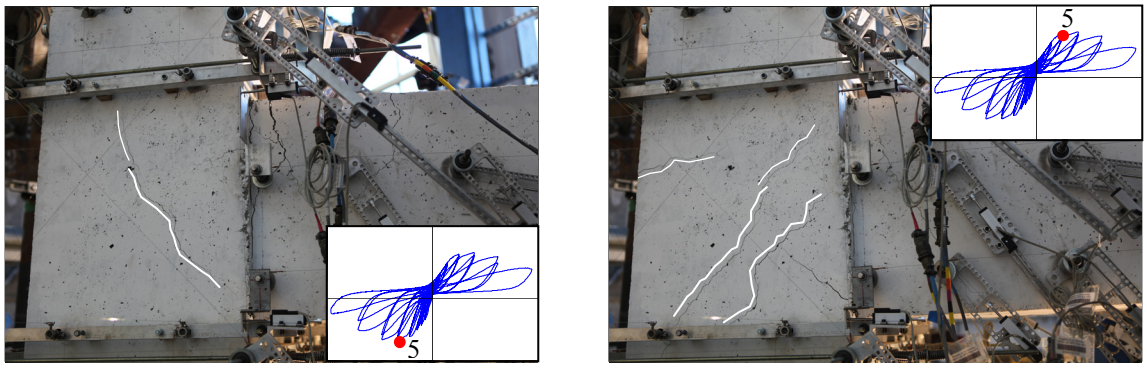

(b) Propagation of joint cracking

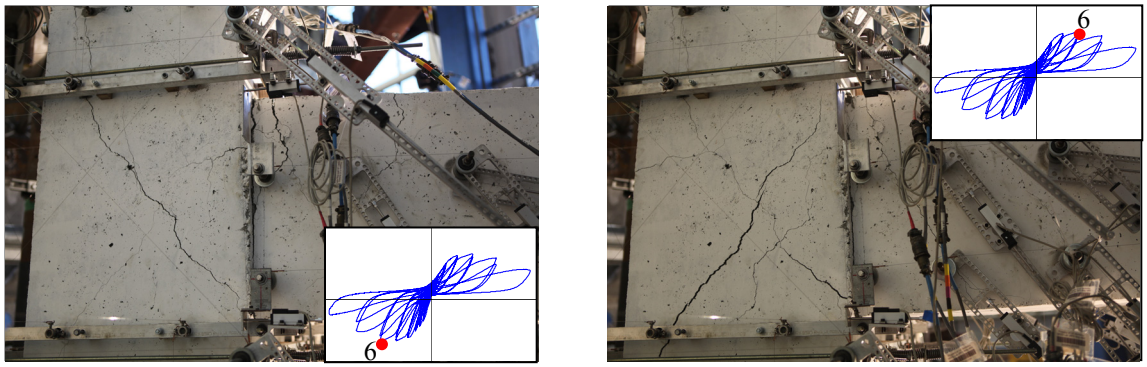

(c) Joint cracking before joint failure

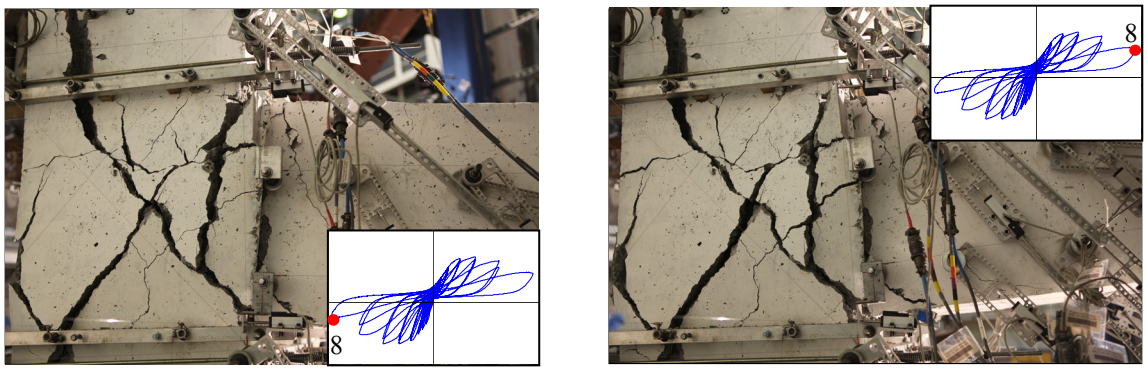

(d) Joint damage at the end of test

Figure V.3 Damage progression of joint in EW direction, SP1.

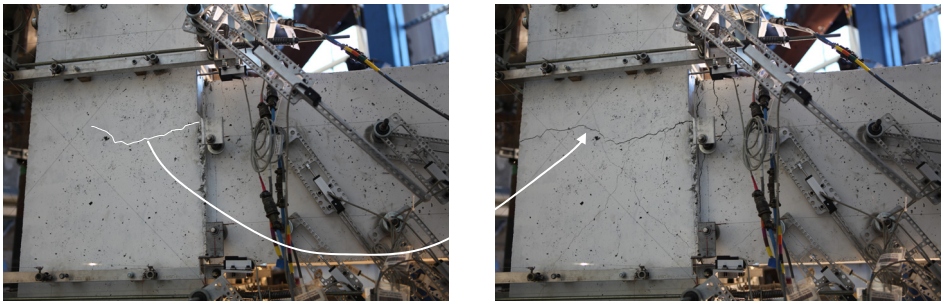

$\Delta_{NS} = 0.61\%$ $\Delta_{NS} = 2.11\%$

(a) Horizontal crack in EW joint by NS beam loading

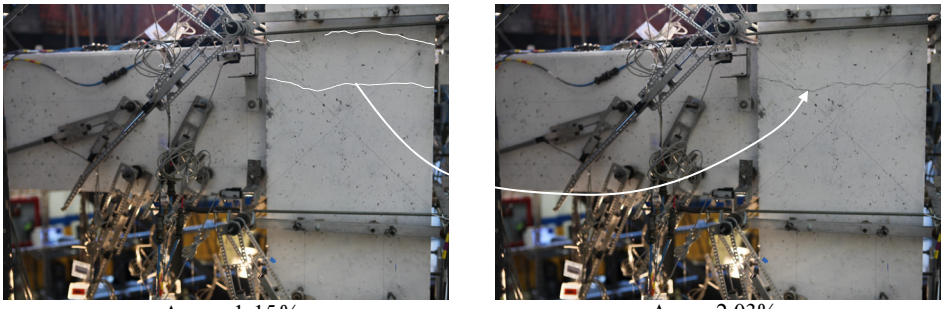

$\Delta_{EW} = 1.15\%$ $\Delta_{EW} = 2.03\%$

(b) Horizontal cracks in NS joint by EW beam loading

Figure V.4 Propagation of horizontal crack in joint panel, SP1.

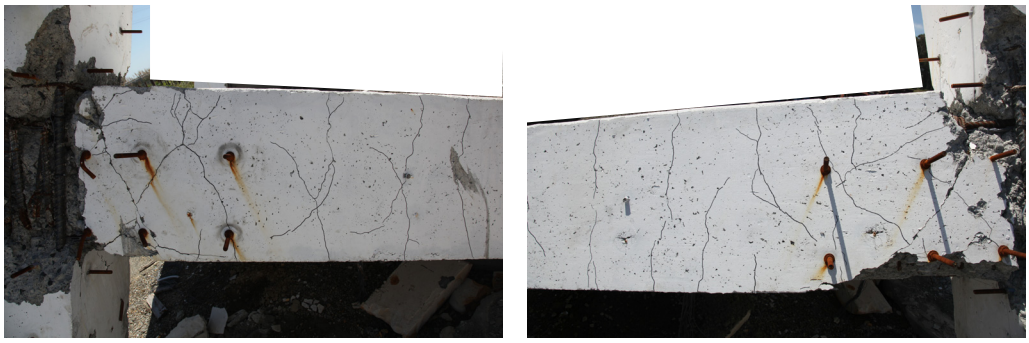

(a) Cracks in EW beam (b) Cracks in NS beam

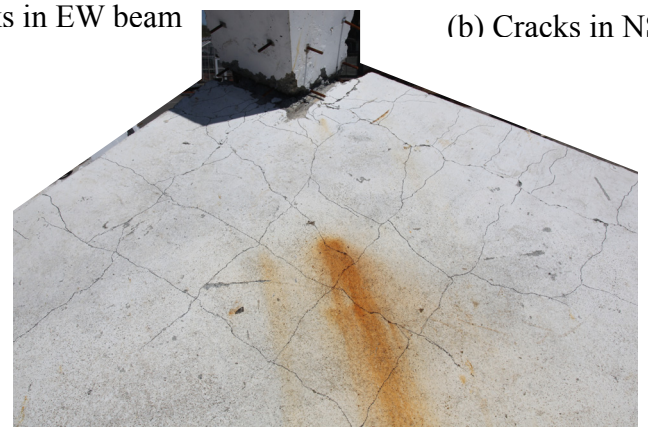

(c) Cracks on slab

Figure V.5 Existing cracks after testing, SP1.

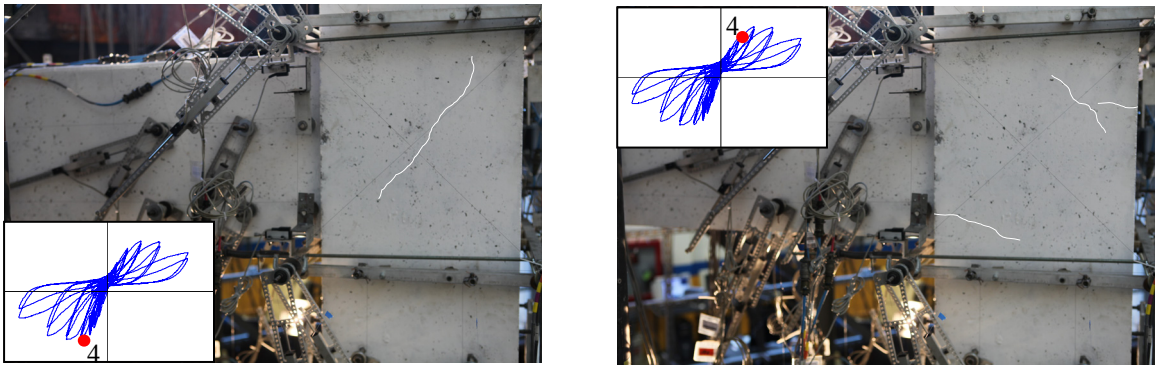

(a) First joint crack

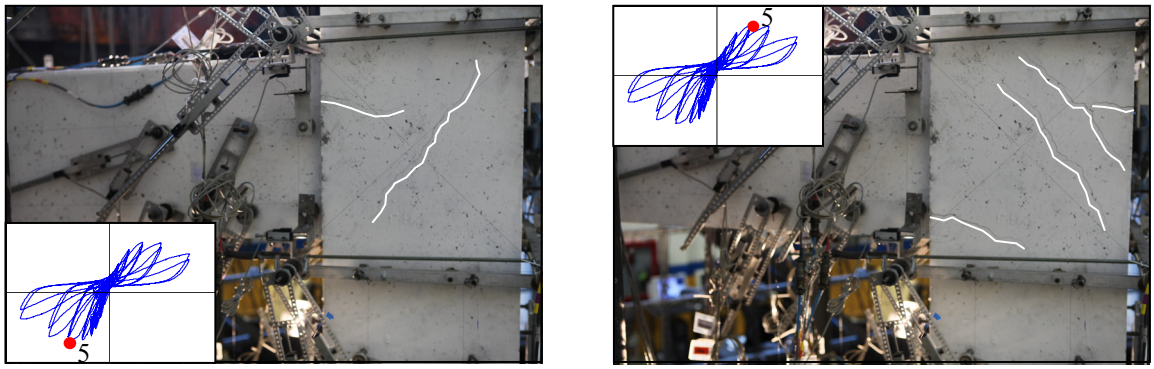

(b) Propagation of joint cracking

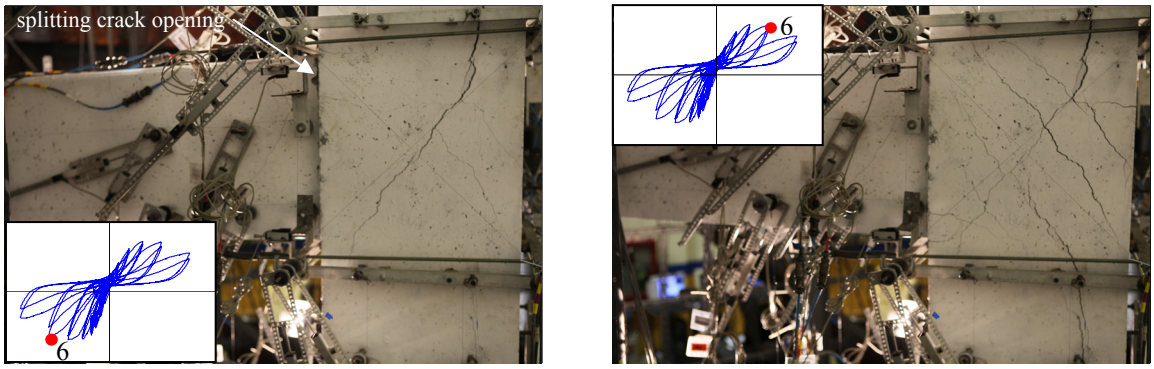

(c) Joint cracking before joint failure

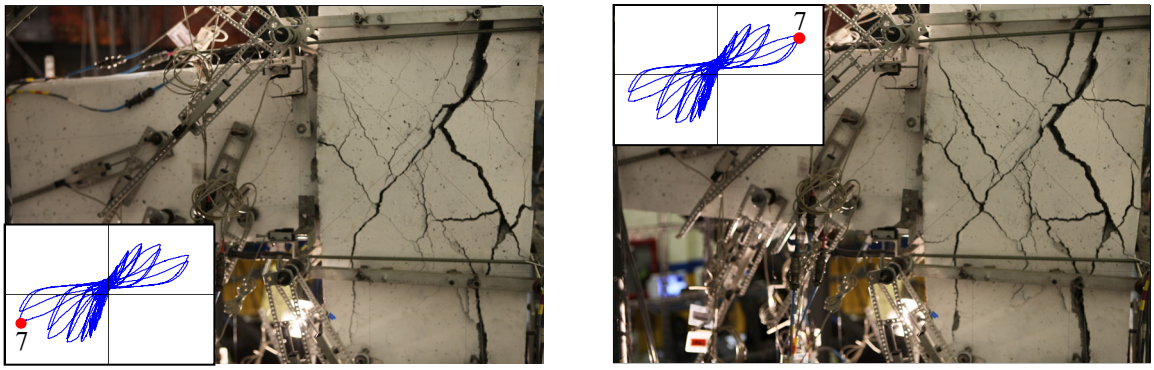

(d) Joint damage at the end of test

Figure V.6 Damage progression of joint in NS direction, SP1.

(a) Global view of specimen

(b) Inside corner joint

(c) NS beam

(d) EW beam

Figure V.7 Failure of SP1 after removing concrete fragments.

V-1.3 Joint Shear Stress versus Rotation Response

The hysteretic responses of joint shear stress versus strain are presented in Table V.3 and Figure V.8. To estimate the joint shear stress, the constant moment arm was assumed to be 0.9 times the effective beam depth because beam longitudinal reinforcement yielded before joint shear failure. Based on the strain measurement of the slab reinforcement, as discussed in the next section, top four slab reinforcing bars in the EW direction and top two slab reinforcing bars in the NS direction were considered in estimating the effective beam depth for negative bending, i.e. beam downward loading. The calculated joint shear stresses in the EW direction at the peak loading were 509 psi (3.51 MPa) for the downward loading and 508 psi (3.51 MPa) for the upward loading; in the NS direction, they were 474 psi (3.27 MPa) for the downward loading and 482 psi (3.33 MPa) for the upward loading. Normalizing these joint shear stresses $\gamma = v_{jh} \Big/ \sqrt{f_c'}$ in the EW direction were 8.5 $psi^{0.5}$ (0.71 $MPa^{0.5}$) for both downward and upward loading; they were 7.9 $psi^{0.5}$ (0.66 $MPa^{0.5}$) for the downward loading and 8.1 $psi^{0.5}$ (0.67 $MPa^{0.5}$) for the upward loading in the NS direction. It is noted that the peak loads in both directions were larger under the upward loading but the joint shear stresses are calculated to be similar for the downward than that for the upward loading. This is because smaller effective beam depth was estimated for the downward than that for the upward loading. In other words, contribution of the slab reinforcement and larger cover concrete thickness reduced the effective beam depth for negative. It is also worth mentioning that the joint shear strengths, which were defined as the maximum normalized joint shear stress, were greater than the shear strength suggested by the ASCE41 as indicated by the dashed lines in Figure V.8.

The joint shear strains measured in the EW and NS joint panels at the peak loading were 0.0024 rad. and 0.0002 rad., respectively, for the downward loading, and 0.0079 rad. and 0.0042 rad., respectively, for the upward loading, as shown in Figure V.8. It is also shown that joint shear strain was, in general, smaller under the downward loading than under the upward loading. On the other hand, the hysteretic responses of the rotation at the beam-joint interface show that this rotation was much greater under the downward loading, refer to Figure V.9. Therefore, the total joint rotation, which was defined in this study as the sum of joint shear strain and the rotation at the beam-joint interface, was almost symmetric for both downward and upward loadings, as shown in Figure V.10. From this figure, the total rotation values corresponding to peak shear strength were 0.017 rad. for the downward loading and 0.019 rad. for the upward loading in the EW direction, and 0.014 rad. for the downward loading and 0.012 for the upward loading in the NS direction. In general, the total rotation in the NS joint panel was greater than that in the EW joint panel at the same level of drift. This was a result from the sequence of beam loading where the EW beam loading preceded the NS beam loading.

Table V.3 shows that the contribution of joint rotation to total drift started to increase after beam reinforcement yielding. Subsequently, total drift after the peak loading was mostly due to this joint rotation.

Table V.3 Joint response of SP1.

Dir.	EW											
Group No.	Downward						Upward					
	v_{jh} (psi)	γ (psi$^{0.5}$)	Δ (rad)	γ_{xy} (rad)	θ_j (rad)	θ_j/Δ	v_{jh} (psi)	γ (psi$^{0.5}$)	Δ (rad)	γ_{xy} (rad)	θ_j (rad)	θ_j/Δ
1	262	4.4	0.0057	-	-	-	137	2.3	0.00	-	-	-
2	334	5.6	0.0087	0.0003	0.0029	0.33	198	3.3	0.0027	0.00	0.0001	0.04
3	391[*1]	6.5	0.0117	0.0006	0.0026	0.22	274	4.6	0.0055	0.0004	0.0023	0.42
4	473	7.9	0.0177	0.0007	0.0039	0.22	397	6.6	0.0115	0.0017	0.0054	0.47
5	507	8.5	0.0266	0.0009	0.0066	0.25	489[*1]	8.2	0.0203	0.0048	0.012	0.59
6	509[#2]	8.5	0.0386	0.0024	0.017	0.44	508[#2]	8.5	0.0321	0.0088	0.019	0.59
7	401	6.7	0.0536	0.014	0.037	0.69	462	7.7	0.0499	0.013	0.028	0.56
8	197	3.3	0.0771	-	-	-	335	5.6	0.0727	-	-	-
Dir.	NS											
Group No.	Downward						Upward					
	v_{jh} (psi)	γ (psi$^{0.5}$)	Δ (rad)	γ_{xy} (rad)	θ_j (rad)	θ_j/Δ	v_{jh} (psi)	γ (psi$^{0.5}$)	Δ (rad)	γ_{xy} (rad)	θ_j (rad)	θ_j/Δ
1	248	4.2	0.0056	-	-	-	151	2.5	0.00	-	-	-
2	358	6.0	0.0085	0.00	0.0029	0.34	197	3.3	0.0028	0.00	0.0004	0.14
3	397	6.6	0.0114	0.00	0.0031	0.27	275	4.6	0.0061	0.0004	0.0013	0.21
4	470[*1]	7.8	0.0167	0.00	0.0063	0.38	410	6.9	0.0125	0.0017	0.0046	0.37
5	474[#2]	7.9	0.0257	0.0002	0.014	0.54	482[*1#2]	8.1	0.0211	0.0047	0.012	0.57
6	437	7.3	0.0377	0.0036	0.024	0.64	474	7.9	0.0329	0.012	0.022	0.67
7	261	4.4	0.0531	0.0091	0.037	0.70	371	6.2	0.0505	0.027	0.046	0.91
8	-	-	-	-	-	-	-	-	-	-	-	-

[*1] first yielding of beam reinforcement; [#2] peak loading.

Note: 1 psi = 0.0069 MPa; $1.0\sqrt{f_c'}$ psi$^{0.5}$ = $0.083\sqrt{f_c'}$ MPa$^{0.5}$.

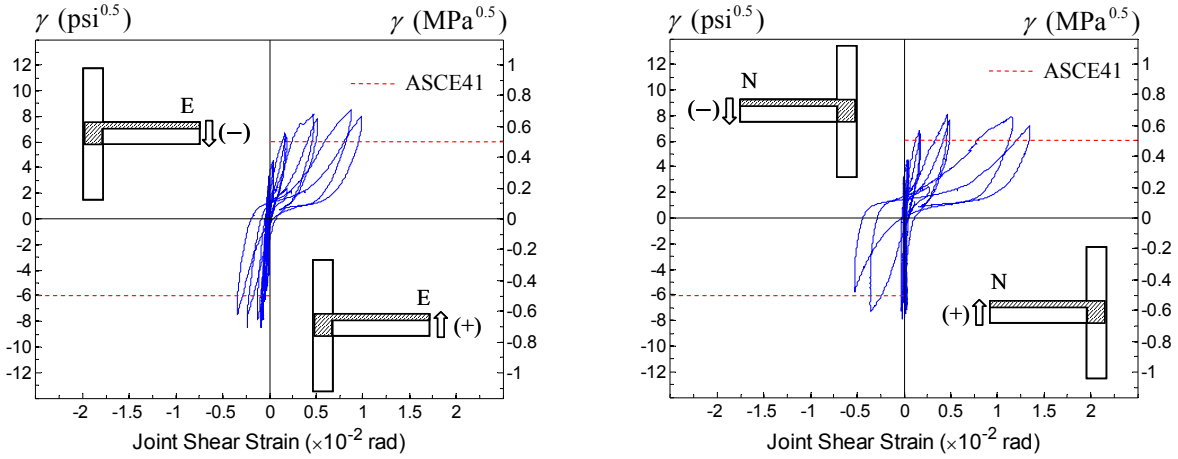

(a) EW direction (b) NS direction

Figure V.8 Joint shear stress versus strain response of SP1.

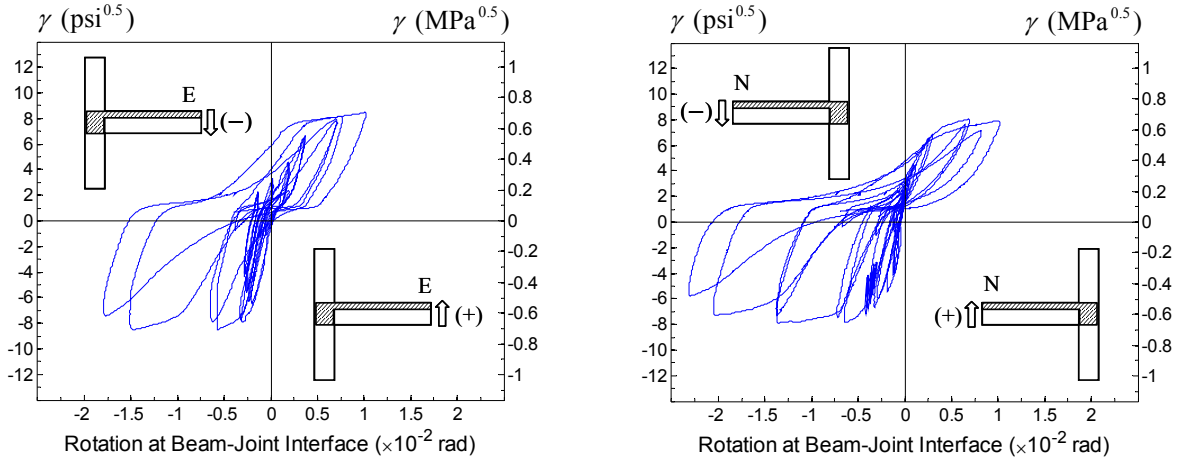

(a) EW direction (b) NS direction

Figure V.9 Joint shear stress versus rotation at beam-joint interface of SP1.

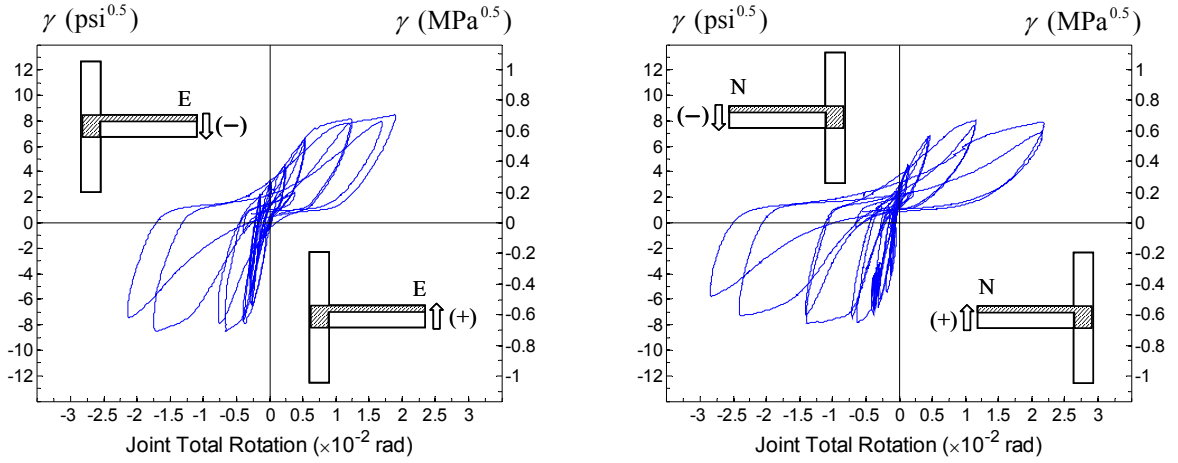

(a) EW direction (b) NS direction

Figure V.10 Joint shear stress versus total rotation of SP1.

V-1.4 Strain Measurements

V-1.4.1 Beam Reinforcement

The strains (vertical axis) of the beam longitudinal bars in the EW and NS directions are plotted against the location of the strain gages (horizontal axis) with increasing drift levels in Figures V.11 and V.12. The labeled drift levels correspond to the loading from the third loading group through the sixth loading group. The strain values in the vertical axis are normalized by the yield strain (ε_y) measured from the coupon tests of reinforcing bars. The notation and numbering of strain gages are illustrated at the top of Figures V.11 and V.12.

Based on the measured strain data, the first yielding of beam top and bottom reinforcing bars in both directions occurred at the beam-joint interface when the loading passed the drift level of about 1.2% which is close to the analytically estimated yield drift. With the increase of drift level after the first yielding, the strains at all gages increased and particularly the strains at the middle of the joint, i.e. gage number 2, showed a big jump at the sixth loading group as symbolized by open circles with solid line in Figures V.11 and V.12. This implies that the beam reinforcement yielding propagated into the joint with the increase of drift. It is also observed that the strains of the EW beam reinforcing bars at the peak were greater that those of the NS beam reinforcing bars due to the previously mentioned reason of loading sequence.

V-1.4.2 Slab Reinforcement

The strain variations of the slab reinforcing bars at the beam-slab interface in the EW and NS directions are presented in Figure V.13. It is noted that the EW and NS slab reinforcing bars were placed in parallel to the EW and NS beams, respectively, and thus they crossed the NS and EW beam-slab interfaces, respectively. The strain values of the EW slab reinforcing bars were greater than those of the NS slab reinforcing bars, which confirmed the observation that the splitting crack at the NS beam-slab interface was wider than the EW beam-slab interface crack. Therefore, different amount of slab reinforcing bars were taken into account for estimating the effective beam depth in each direction.

For the EW slab reinforcement, first yielding of top reinforcing bar located next to the EW beam occurred when the first EW beam reinforcement yielded. At the peak loading, all measured top four reinforcing bars yielded. On the other hand, first yielding of the NS slab top reinforcement took place after passing the drift of 1.7% and top two reinforcing bars yielded at the six group of loading. On the other hand, the first bottom reinforcing bar yielded in the EW direction at the fifth group of loading but this bar slipped from the beam side in the subsequent loading, as shown in Figure V.13. The insufficient anchorage of the bottom reinforcement was likely to induce relatively low strain and slippage from the beam section. Moreover, considering the distance between slab bottom reinforcement and the neutral axis in the L-shape section, slab bottom bars were ignored for calculation of joint shear stress and effective beam depth. As

indicated in Section V-1.3, the calculation of the effective beam depth included four top reinforcing bars for the EW direction and two top reinforcing bars for the NS direction.

V-1.4.3 Column Reinforcement

The strain measurements of column longitudinal bars within the joint region are presented in Figures V.14 and V.15. The measured strain data were assorted according to each of the EW and NS beam loading. The strains of all the column longitudinal bars were less than the yield strain, i.e. 0.0025, until the peak loading, except for the top gage of the bar number 3 in the EW direction which yielded when the column was in tension. Based on the strain measurements, the column longitudinal bars elongated due to the tension in the column during the EW and NS beams upward loadings. The tension in the column and consequent yielding of the one column bar were expected to have little effect on the joint shear strengths considering the joint shear strengths were similar for both column compressive and tensile loading.

To investigate the role of the column intermediate reinforcement, the strains were recorded over the height of the joint during the longitudinal loading in each direction. The tensile strain of the column intermediate bar at the joint mid-height was not greater than the strains measured at both top and bottom of the joint, which is discussed in Section VI.7.

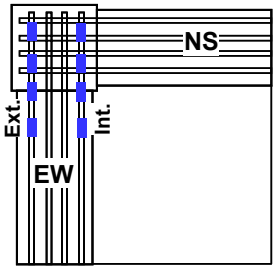

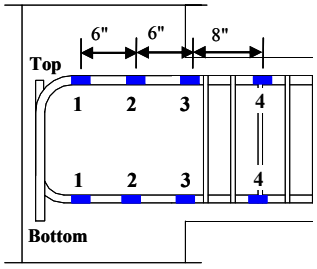

Note: 1" = 25.4 mm

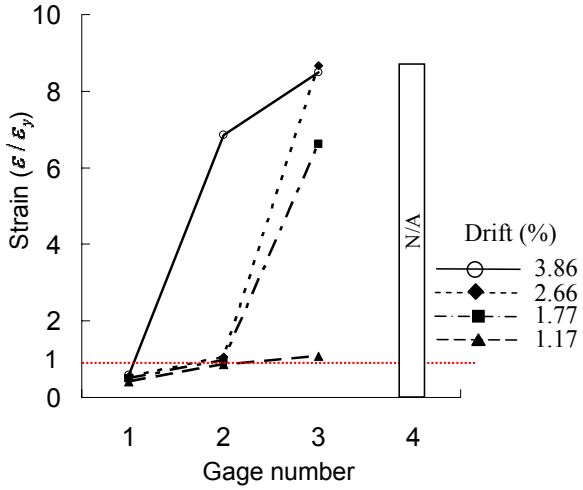

(a) EW-Top-Ext.

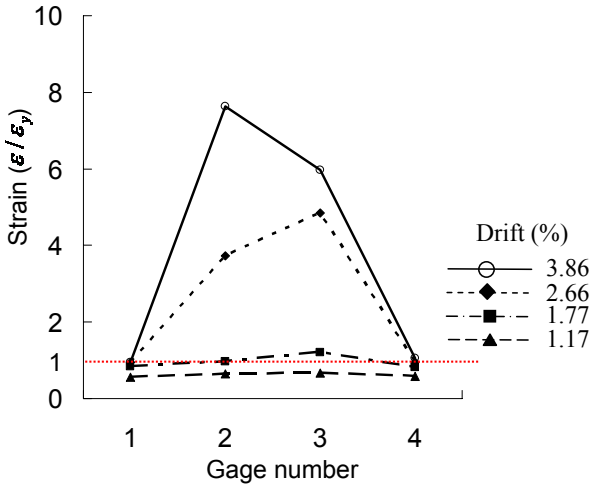

(b) EW-Top-Int.

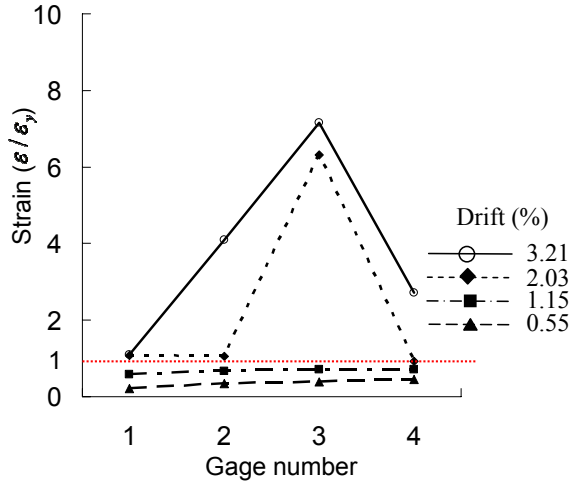

(c) EW-Bottom-Ext.

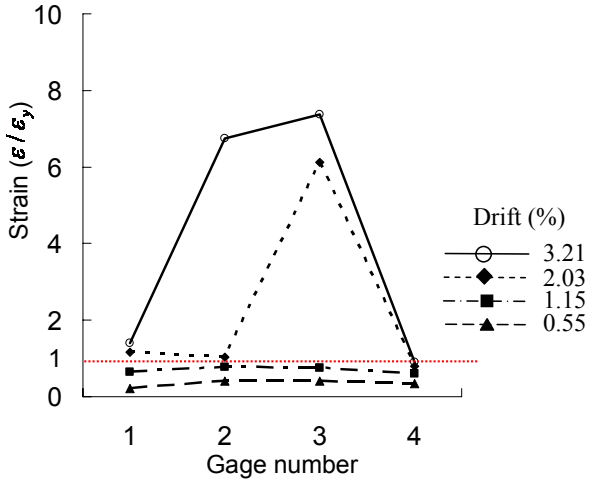

(d) EW-Bottom-Int.

Figure V.11 Strains of the EW beam reinforcing bars of SP1.

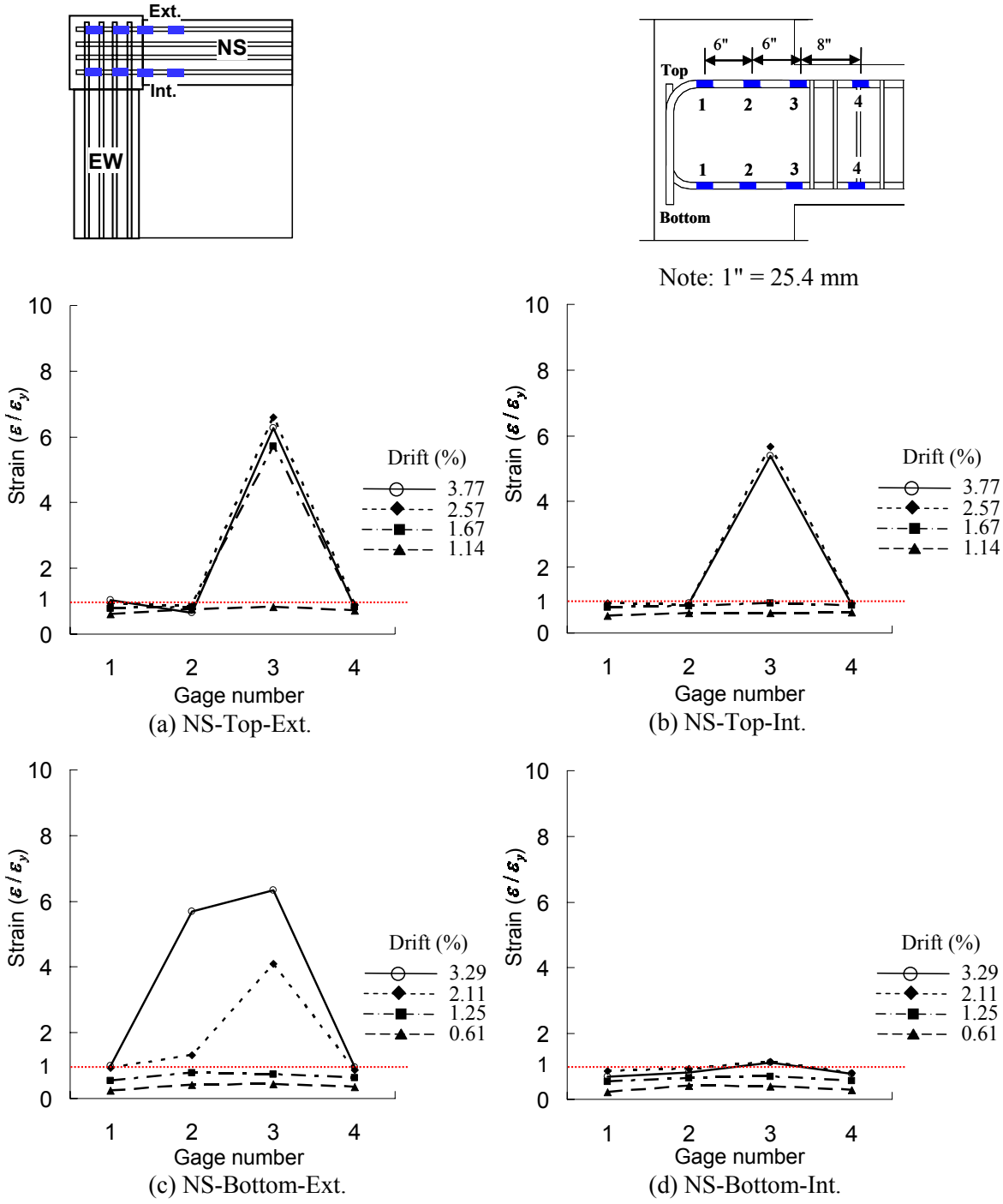

Figure V.12 Strain of the NS beam reinforcing bars of SP1.

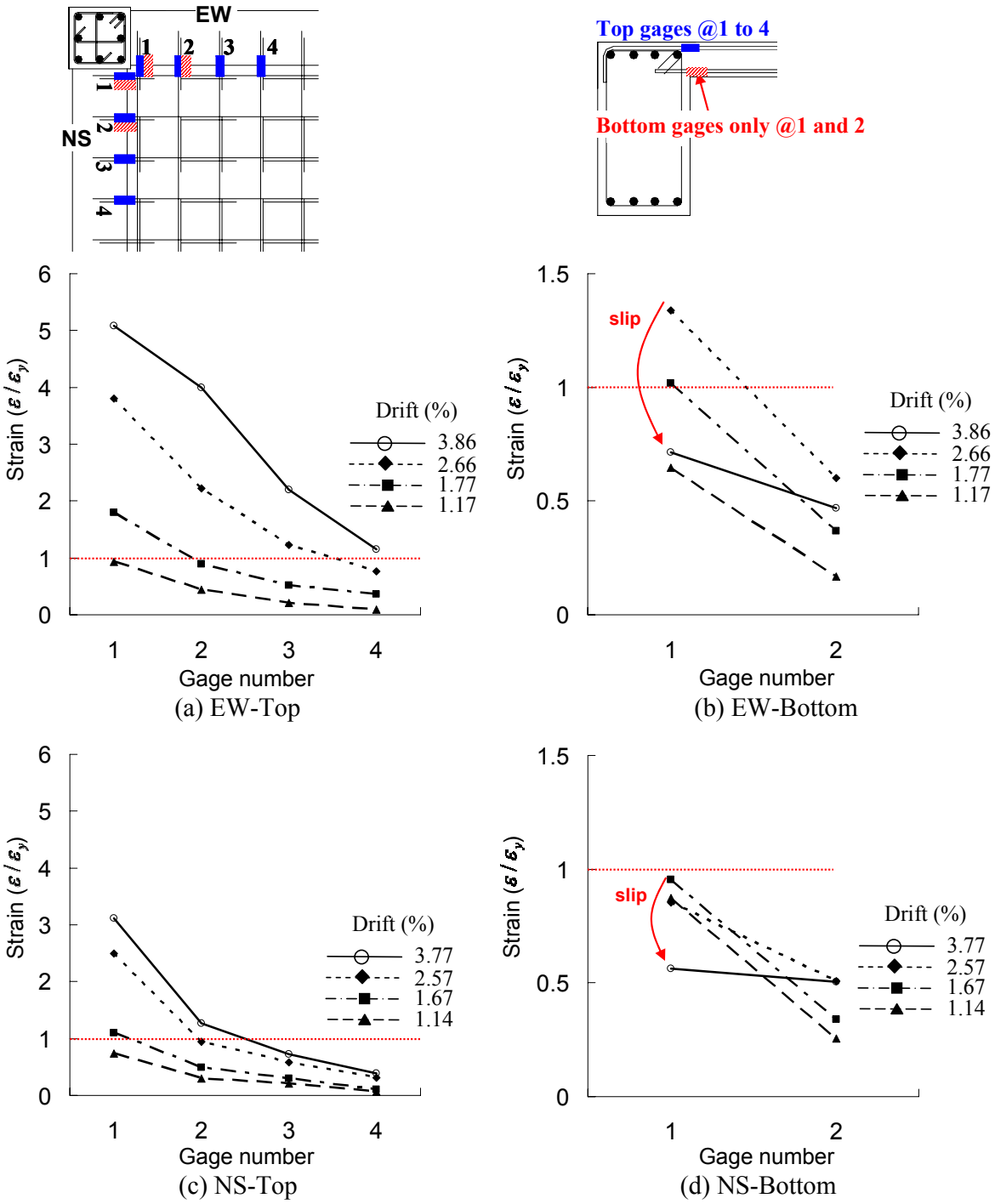

Figure V.13 Strains of the slab reinforcing bars of SP1.

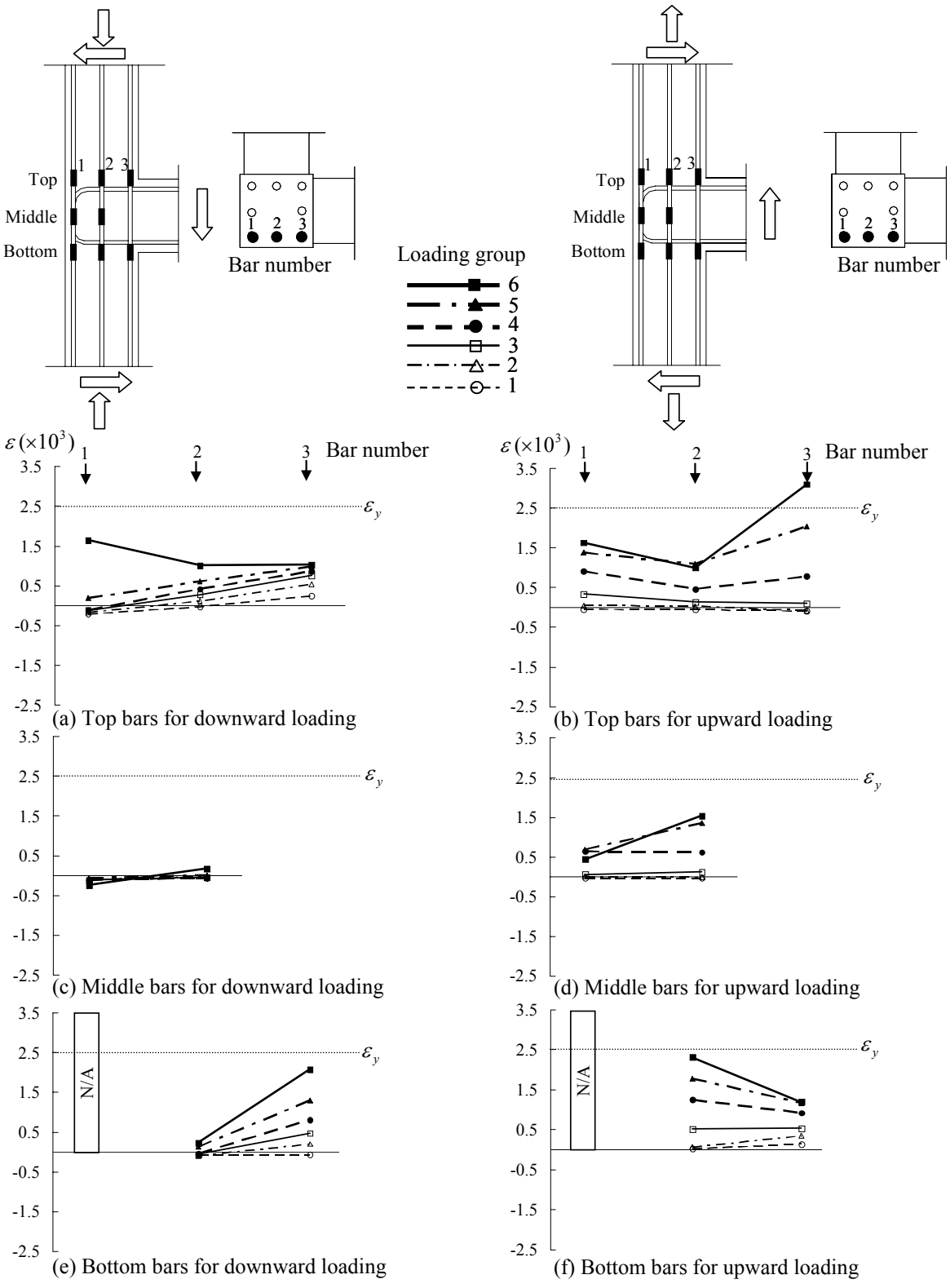

Figure V.14 Strains of the column reinforcing bars for the EW beam loading, SP1.

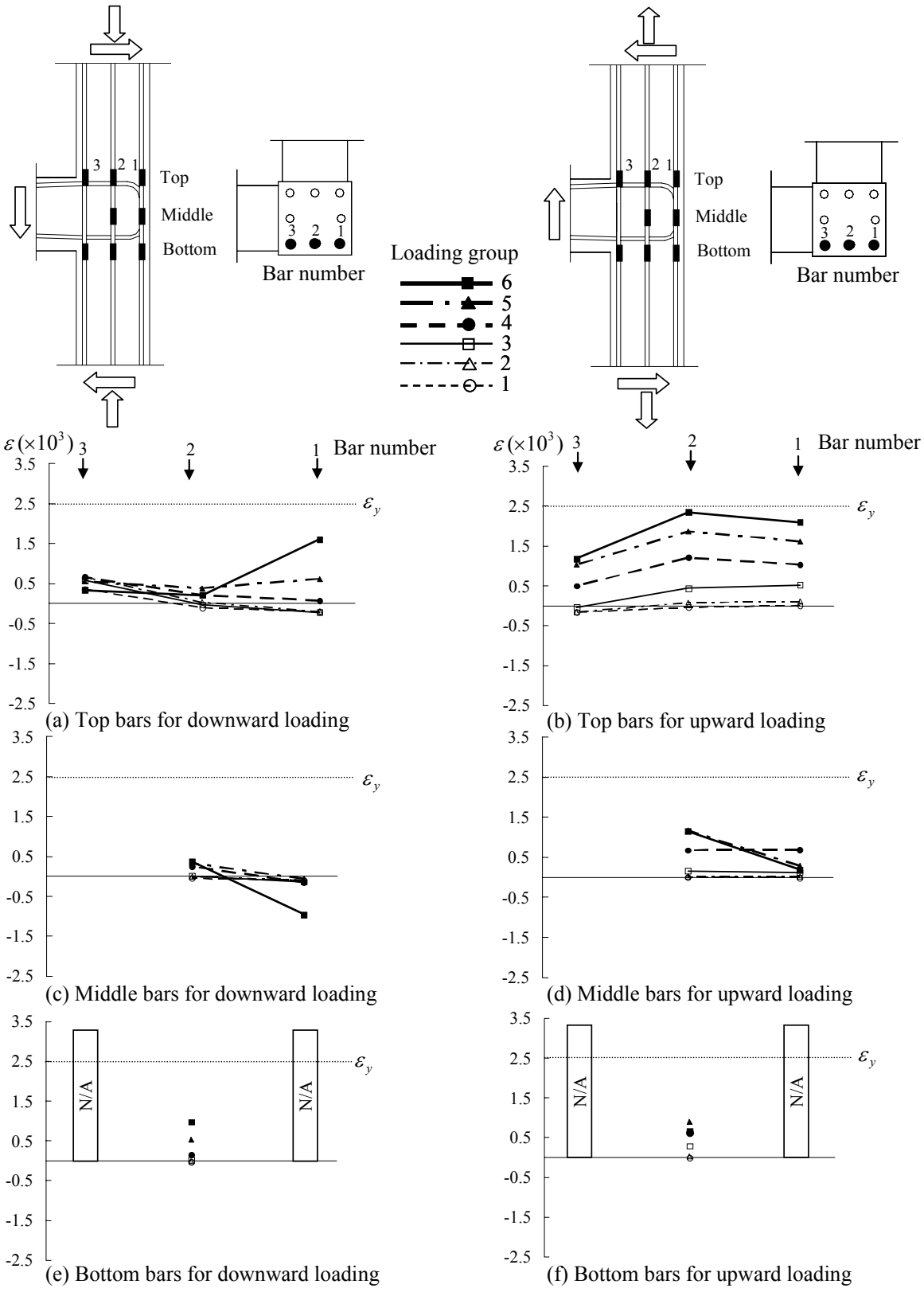

Figure V.15 Strains of the column reinforcing bars for the NS beam loading, SP1.

V-2 Specimen SP2

V-2.1 Load versus Drift Response

The hysteretic applied load versus drift responses of SP2 in the EW and NS directions are shown in Figure V.16 and their values at the peak of each cyclic loading group are given in Table V.4. The first yielding of top reinforcement in both the EW and NS beam occurred at the fourth group of loading ($\Delta_{EW} = -1.75\%$; $\Delta_{NS} = -1.76\%$) where the applied loads were -36.0 kips (-160.1 kN) and -38.3 kips (-170.4 kN), respectively. The bottom reinforcement in both the EW and NS beams yielded during the fifth loading group ($\Delta_{EW} = 2.04\%$; $\Delta_{NS} = 2.06\%$) where the applied loads were 29.6 kips (131.7 kN) and 29.0 kips (129.0 kN), respectively. It is to be mentioned that the top and bottom reinforcement in the beam yielded before reaching the peak of fourth and fifth loading group based on the strain measurement of these bars. By the comparison with the drift when the beam reinforcement yielded in SP1, it was found that the beam reinforcement yielding took place at a similar drift level, i.e. 1.7%. This coincidence can be explained by the fact that the yield curvature is little dependent on the flexural strength if the same dimensions of the cross-section and properties of materials are provided.

The EW beam load reached its peak at the fifth loading group which was right after the loading group when the beam reinforcement yielded. The EW beam downward loading reached its peak at the fifth loading group ($\Delta_{EW} = -2.66\%$), while the peak load for the EW beam upward loading was achieved at the sixth loading group ($\Delta_{EW} = 3.22\%$). The peak loads of EW beam were -36.8 kips (-163.7 kN) for the downward loading and 31.0 kips (137.9 kN) for the upward loading. The peak loading in the NS beam was followed by the EW beam peak loading, which was the same pattern observed in SP1 due to the loading sequence as mentioned in Section V-1.1. After the peak loading in both the EW and NS beams, the applied beam loads slightly reduced during the subsequent group of loading, e.g. from -36.8 to -36.6 for the EW downward loading, and thereafter the applied loads sharply reduced. The strength degradation after peak was more severe for the downward loading, i.e. slab in tension, than for the upward loading, i.e. slab in compression. The pinching behavior caused by the slip of the beam longitudinal bars was observed after the sixth group of loading, refer to Figure V.16. Based on the load-drift responses, the important events in both SP1 and SP2 were observed at similar drift levels although the applied loads of SP2 at the same drift levels were greater than that of SP1 due to the higher beam longitudinal reinforcement ratio in SP2.

The column response of SP2 is shown in Figure V.17. During testing, the column axial loads determined from Equation (IV.2a) were applied. In SP2, the column axial load varied from 22 kips (98 kN) in tension to 260 kips (1157 kN) in compression. The column axial load ratio, $P/\left(f_c' A_g\right)$, ranged from 2.0% (tension) to 22.7% (compression). The peak vertical displacements were 0.118 in. (3.00 mm) in elongation and 0.107 in. (2.72 mm) in contraction.

Table V.4 Load versus drift response of SP2.

Group No.	SP2							
	EW direction				NS direction			
	Downward (-)		Upward (+)		Downward (-)		Upward (+)	
	Δ (%)	V_b (kip)	Δ (%)	V_b (kip)	Δ (%)	V_b (kip)	Δ (%)	V_b (kip)
1	-0.57	-16.5	-0.02	4.2	-0.57	-17.2	-0.01	6.5
2	-0.87	-22.9	0.27	12.4	-0.88	-24.1	0.28	13.9
3	-1.17	-28.4	0.56	15.4	-1.16	-31.0	0.57	17.9
4	-1.75	-36.0[*1]	1.15	24.3	-1.76	-38.3[*1#2]	1.18	23.1
5	-2.66	-36.8[#2]	2.04	29.6[*1]	-2.66	-38.1	2.06	29.0[*1#2]
6	-3.86	-36.6	3.22	31.0[#2]	-3.88	-33.8	3.24	28.4
7	-5.68	-29.1	4.99	28.5	-5.70	-23.6	5.01	22.9
8	-8.06	-19.5	7.30	24.0	-8.05	-17.3	7.31	18.8

[*1] first yielding of beam reinforcement; [#2] peak loading.
Note: 1 kip = 4.45 kN.

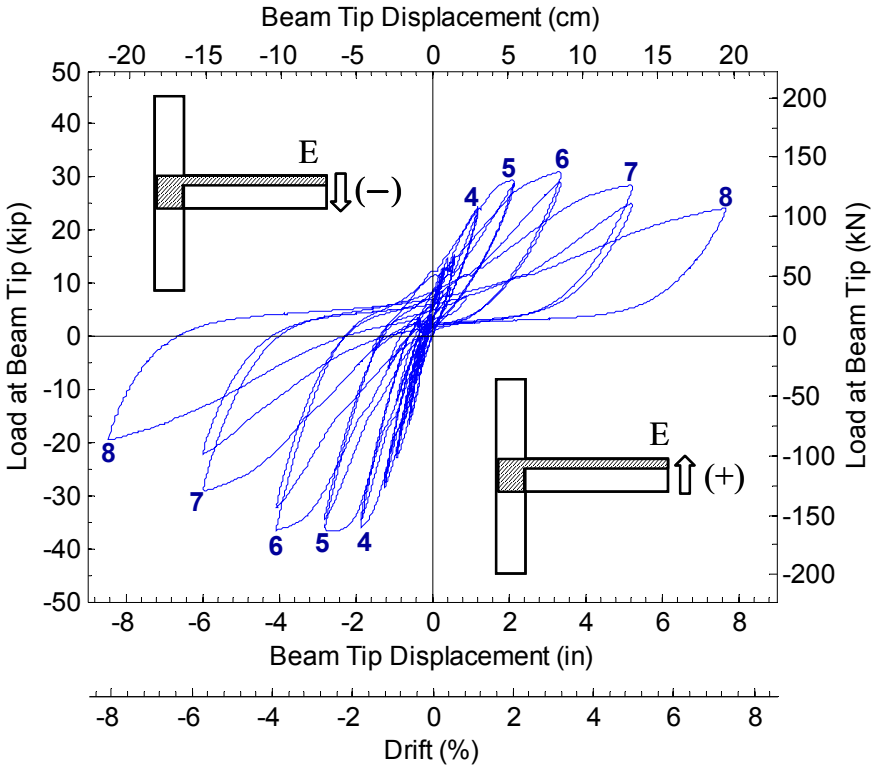

(a) EW direction

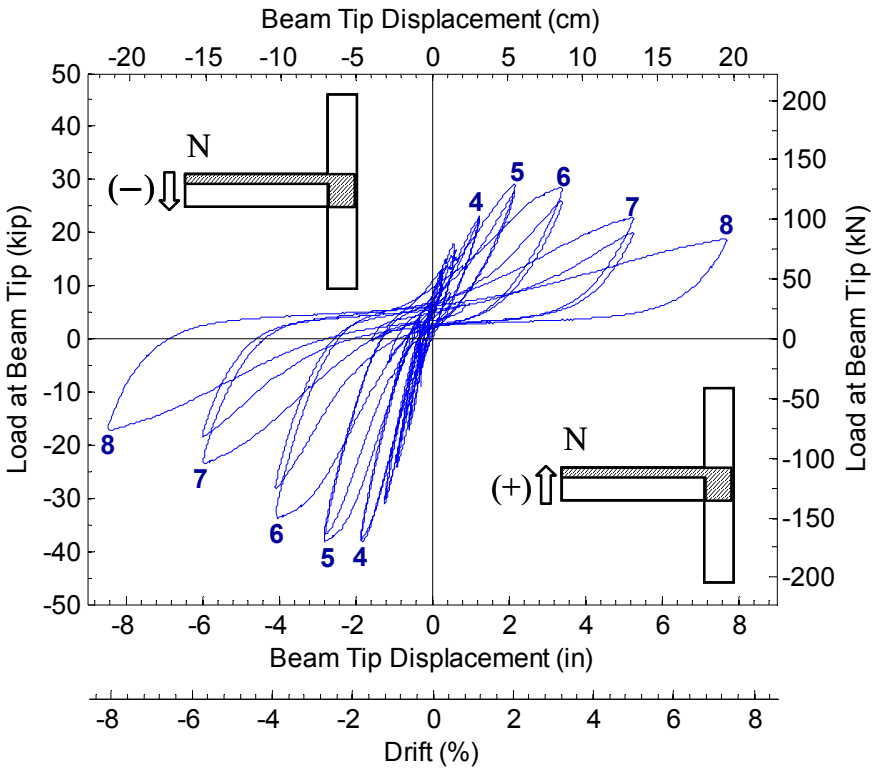

(b) NS direction

Figure V.16 Load versus drift response of SP2.

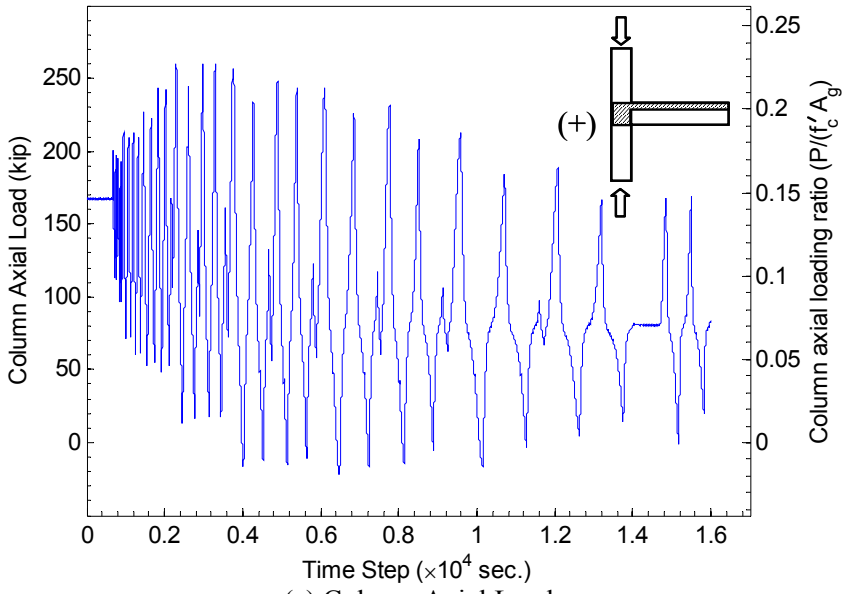

(a) Column Axial Load

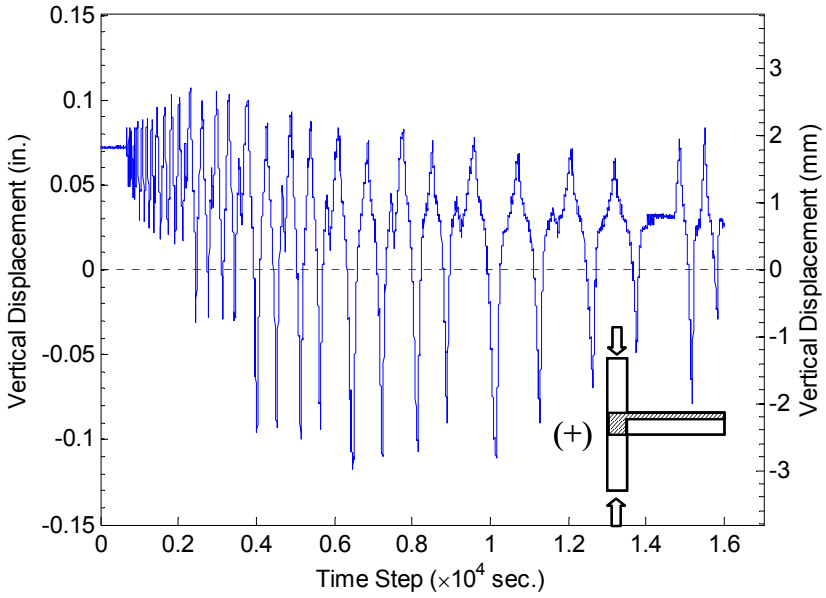

(b) Vertical Displacement

Figure V.17 Column response of SP2.

V-2.2 Observed Damage Progression

The qualitative description of damage progression of SP2 is summarized in Table V.5. The photographs of the specimen taken during testing and at the end of the test are presented in Figures V.18 through V.22.

V-2.2.1 EW Direction

Joint Region

Diagonal cracks formed and deteriorated the joint panel during testing but the crack pattern was slightly different from that observed in SP1. Multiple cracks formed in the joint panel and "X" diagonal crack pattern became dominant with increase of the applied beam loads. A first downward diagonal crack (↘) occurred at the second loading group ($\Delta_{EW} = -0.87\%$), while a first upward diagonal crack (↗) appeared at the fourth loading group ($\Delta_{EW} = 1.15\%$), refer to Figure V.18(a). For the EW beam downward loading, additional diagonal cracks appeared at the fourth group ($\Delta_{EW} = -1.75\%$) where the EW beam top reinforcement yielded, and the two diagonal cracks in the joint panel exclusively widened at the sixth loading group. For the EW beam upward loading, the first upward diagonal crack in the joint panel significantly widened accompanied by additional small cracks. This crack propagation is shown in Figures V.18(b) and (c). By comparison of crack propagation with SP1 at the same drift level, the cracks observed in SP2 showed similar propagation and width. After the peak load, cover concrete in the joint panel began to bulge and finally spalled off. The beam and column reinforcing bars were exposed at the seventh group of loading. At the last loading group, core concrete in the joint region was crushed and the exposed column reinforcing bars did not buckle, refer to Figure V.18(d).

Two horizontal cracks were observed at the top of the EW joint panel during the NS beam upward loading but no horizontal cracks formed during the downward loading. At the third group of the NS beam upward loading, the first horizontal crack developed from the top corner of the joint on the side where there is no beam and the second horizontal crack appeared above the existing horizontal crack at the second cycle in the same loading group. In the subsequent fourth group of the NS beam upward loading, the upper horizontal crack was widening but the lower horizontal crack closed (Figure V.19(a)). It is noted that the location of the upper horizontal crack was close to slab top surface and the lower horizontal crack was close to the top reinforcement in the EW beam.

Beam and Slab

During the first group of the EW beam downward loading ($\Delta_{EW} = -0.57\%$), two flexural cracks were observed at the top of the EW beam. These flexural cracks extended to the slab parallel to the NS beam. During the same group of downward loading, a splitting crack developed at the top of the beam-joint interface. Flexural cracks also developed at the bottom of the EW beam during the upward loading but the width of these cracks was relatively small. With increasing the applied drift level, the splitting crack at the NS beam-slab interface extended towards the end of

the NS beam, and the existing flexural cracks and splitting crack at the beam-joint interface widened until the peak loading. Thereafter, the width of flexural cracks reduced because the damage was localized in the joint region. Consequently, the plastic hinge mechanisms did not form in the beams similar to the observation of SP1.

During the NS beam loading, especially downward loading, inclined cracks occurred in the EW beam due to torsion. These inclined cracks were not significant until the peak loading and moreover these cracks generally closed during the EW beam loading. The beam flexural strength was little affected by the inclined cracks induced by the orthogonal beam loading. The existing cracks in the EW beam and slab after testing are illustrated in Figure V.20.

V-2.2.2 NS Direction

Joint Region

A first downward diagonal crack (↙) occurred at the third loading group ($\Delta_{NS} = -1.16\%$), while a first upward diagonal crack (↖) shortly developed during the fourth loading group ($\Delta_{NS} = 1.18\%$) at the top corner of the joint on the side where there is no beam, refer to Figure V.21(a). On the continued NS beam loading, multiple inclined cracks newly formed in the joint panel and the existing cracks further propagated, refer to Figure V.21(b). A significant propagation of two existing diagonal cracks in the joint panel was observed at the sixth group of the NS beam loading which was the loading group right after the EW beam reached its peak, refer to Figure V.21(c). At the last loading group, cover concrete in the joint panel spalled off and core concrete in the joint region was crushed, refer to Figure V.21(d).

As observed in the EW joint panel, a horizontal crack was observed only at the top of the NS joint panel during the EW beam upward loading. The horizontal crack appeared at the fourth group of the EW beam upward loading, as shown in Figure V.19(b), and cover concrete in the joint panel spalled along this crack after the peak load. This horizontal crack was located at the same level as the top reinforcement of the NS beam.

Beam and Slab

Several hairline flexural cracks and splitting crack at the beam-joint interface developed at the top of the NS beam for the second group of the NS beam loading. Simultaneously, a splitting crack along the EW beam-slab interface began to propagate. Generally, the propagation of flexural cracks was not easily observed but the width of these cracks was expected to reduce after the peak loading. Plastic hinge mechanisms did not form in the NS beam. The marked beam and slab cracks are shown in Figure V.20(b). During the EW beam loading, inclined cracks occurred in the NS beam. In particular, the inclined crack at the bottom of the beam widened and cover concrete in this beam was detached as indicated by the arrow in Figure V.21(d).

V-2.2.3 Summary

For joint cracking, a first joint crack appeared around the drift level of 1.2%, except for the downward diagonal crack in the EW joint where the first crack took place at the loading to 0.87% drift. As the applied drift increased up to the fifth loading group, multiple inclined cracks newly appeared and during this loading group, the existing diagonal cracks further propagated. At the sixth group of loading ($\Delta_{down} = -3.87\%$; $\Delta_{down} = 3.23\%$), one or two of the existing diagonal cracks propagated exclusively. Beyond the sixth group of loading, the joint region was severely damaged showing the spalling of cover concrete and crushing of core concrete in the joint region.

For damage of the beam and slab, first flexural and splitting cracks developed during the first and second groups of loading and these cracks widened up to the sixth group of loading. The propagation of these cracks in the beams and slab was not significant compared with the cracks in the joint panel. After the peak loading, the width of flexural cracks in the beams and slab reduced but splitting cracks at the beam-joint and beam-slab interfaces continuously widened. In SP2, no plastic hinge mechanism formed in both beams.

During the orthogonal beam upward loading, horizontal cracks appeared at the top of joint panel in the transverse direction, while inclined cracks developed in the beam in the transverse direction during the longitudinal beam downward loading. During the subsequent same directional beam loading, these cracks were not observed in general and thus the joint responses were not influenced by the previous orthogonal beam loading. Figure V.22 illustrates that the failure of the specimen was attributed to the severe damage in the joint region.

Table V.5 Qualitative damage description of SP2.

Drift (%)	EW direction	NS direction
$\Delta_0 = -0.3$	-	-
$\Delta_{up} = -0.02$ $\Delta_{down} = -0.57$	- Multiple flexural cracks in beam and slab - Splitting crack at beam-joint interface	- First flexural crack in beam
$\Delta_{up} = 0.28$ $\Delta_{down} = -0.88$	- First downward diagonal crack in joint	- Additional flexural cracks
$\Delta_{up} = 0.57$ $\Delta_{down} = -1.17$	-	- First downward diagonal crack in joint
$\Delta_{up} = 1.17$ $\Delta_{down} = -1.76$	- Second downward diagonal crack in joint - First upward diagonal crack in joint - First yielding of beam top bars	- First upward diagonal cracks in joint - First yielding of beam top bars
$\Delta_{up} = 2.05$ $\Delta_{down} = -2.66$	- Second upward diagonal crack in joint - Widening of existing joint cracks - First yielding of beam bottom bars	- Additional downward and upward diagonal cracks in joint - First yielding of beam bottom bars
$\Delta_{up} = 3.23$ $\Delta_{down} = -3.87$	- Large opening of joint diagonal cracks - Propagation of flexural and splitting crack at beam-joint interface	- Large opening of joint diagonal cracks
$\Delta_{up} = 5.00$ $\Delta_{down} = -5.69$	- Spalling of joint cover concrete - Reduction of width of beam flexural cracks	- Spalling of joint cover concrete - Reduction of width of beam flexural cracks
$\Delta_{up} = 7.31$ $\Delta_{down} = -8.06$	- Crushing of joint core concrete	- Crushing of joint core concrete

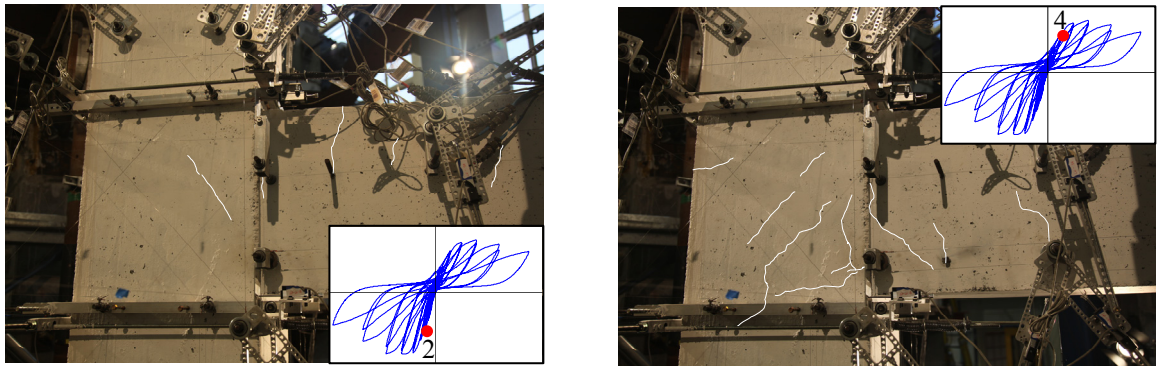

(a) First joint crack

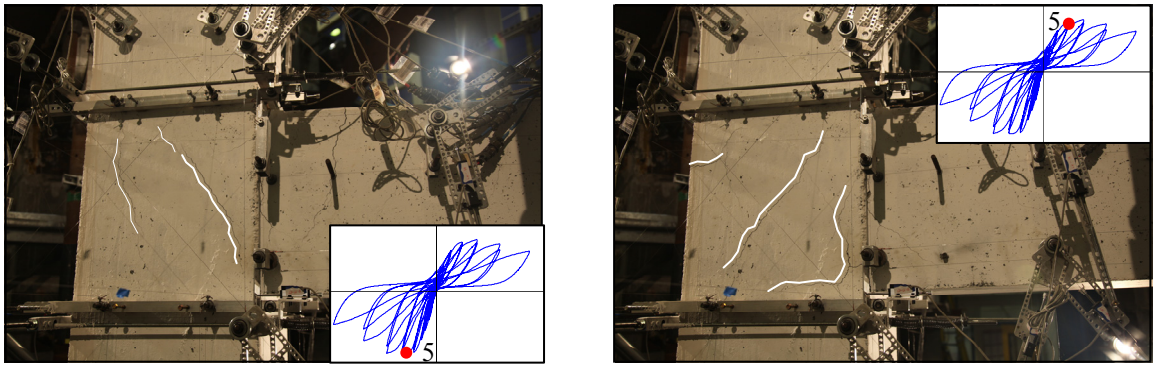

(b) Propagation of joint cracking

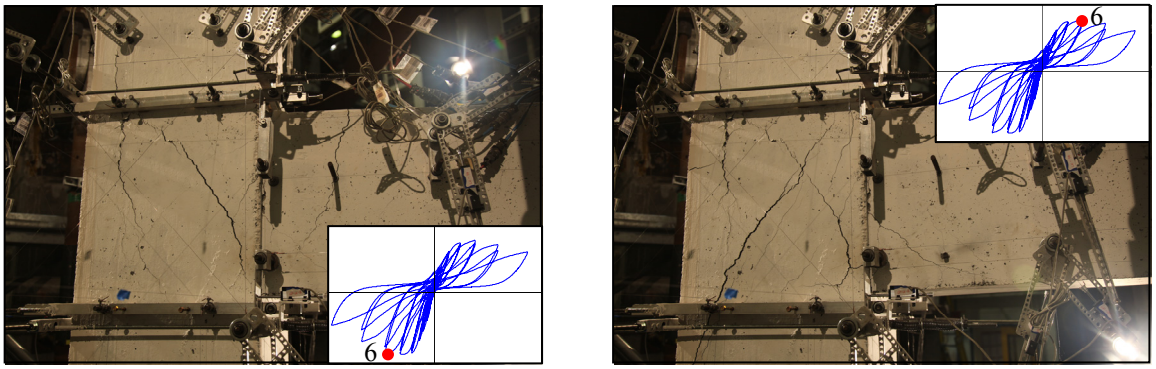

(c) Joint cracking before joint failure

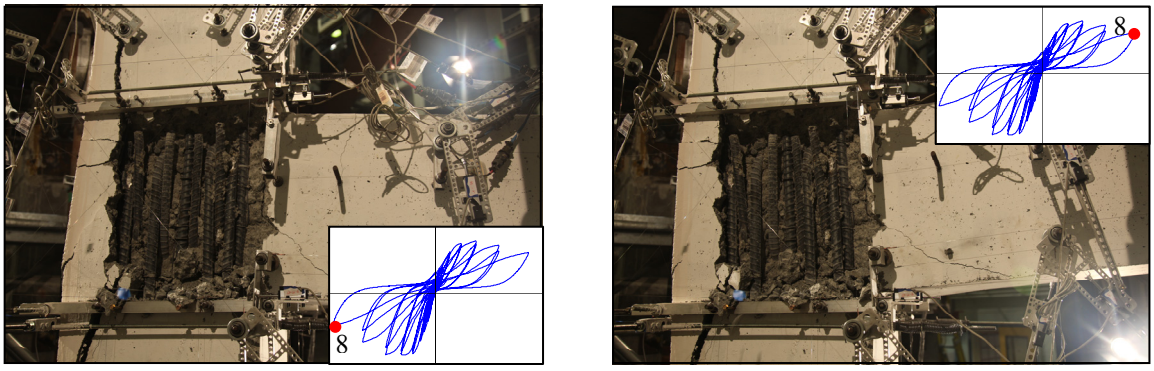

(d) Joint damage at the end of test

Figure V.18 Damage progression of joint in EW direction, SP2.

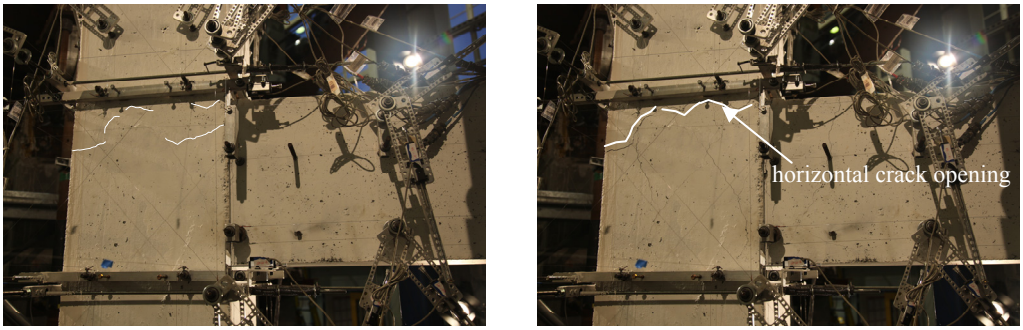

$\Delta_{NS} = 1.18\%$ $\Delta_{NS} = 2.06\%$

(a) Horizontal crack in EW joint by NS beam loading

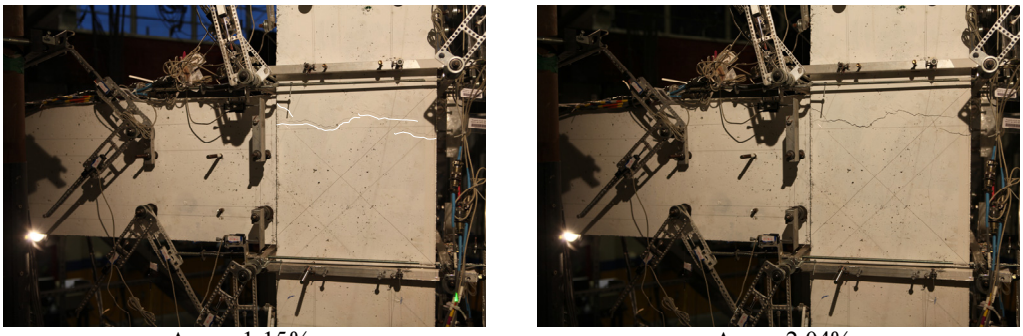

$\Delta_{EW} = 1.15\%$ $\Delta_{EW} = 2.04\%$

(b) Horizontal cracks in NS joint by EW beam loading

Figure V.19 Propagation of horizontal crack in joint panel, SP2.

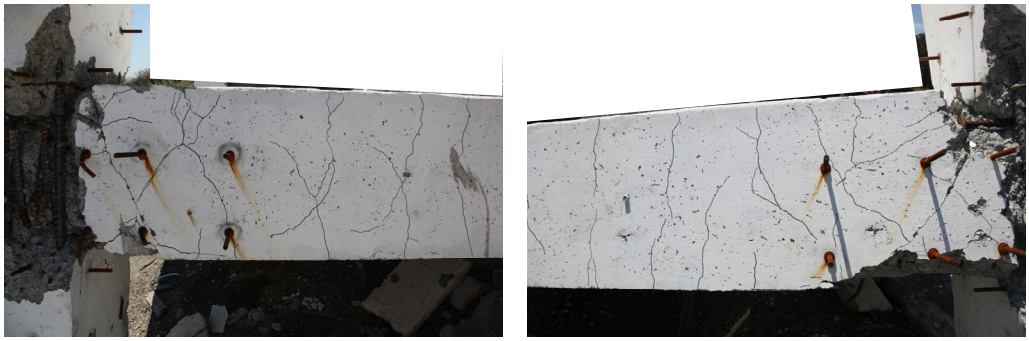

(a) Cracks in EW beam (b) Cracks in NS beam

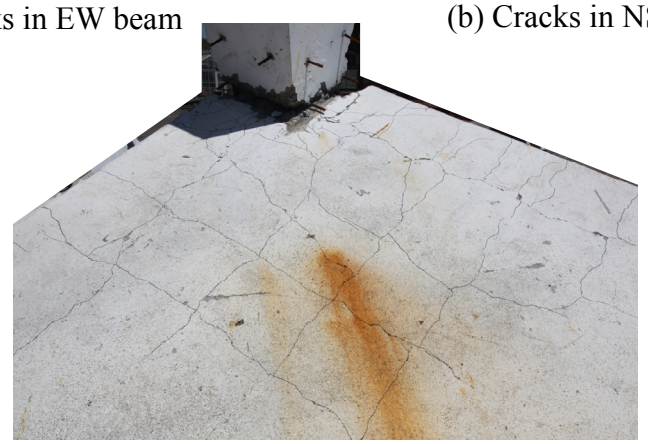

(c) Cracks on slab

Figure V.20 Existing cracks after testing, SP2.

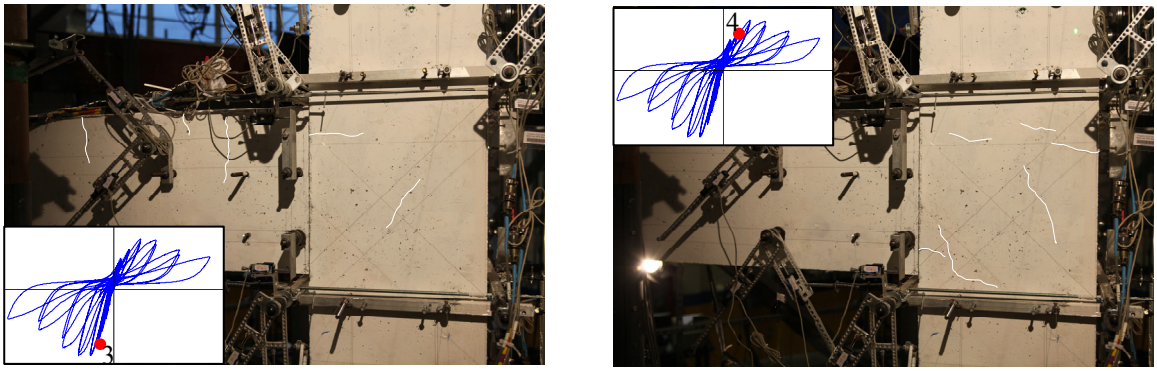

(a) First joint crack

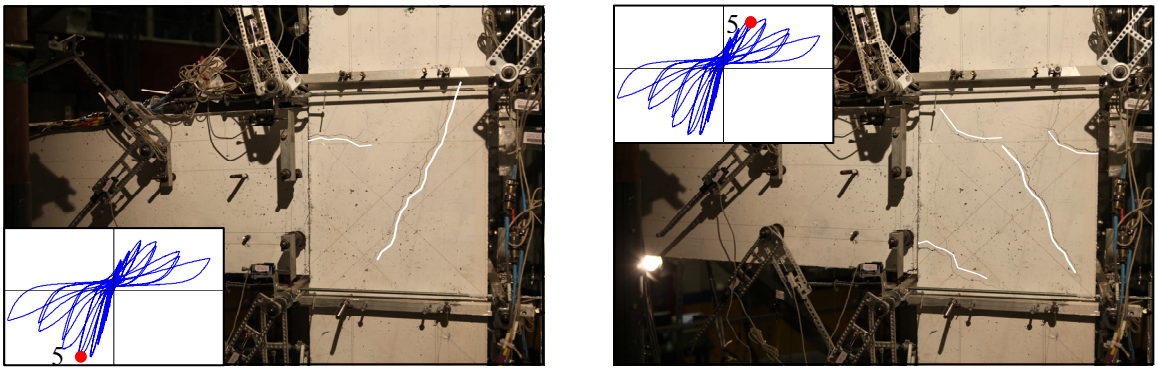

(b) Propagation of joint cracking

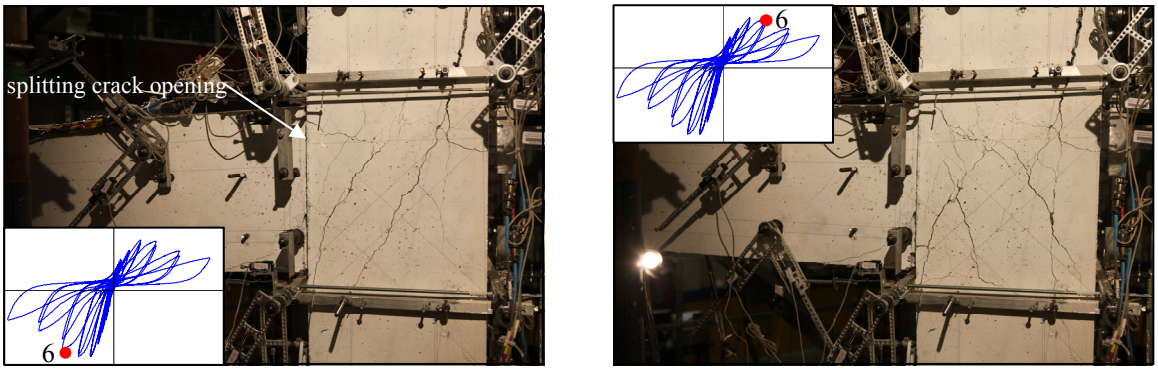

(c) Joint cracking before joint failure

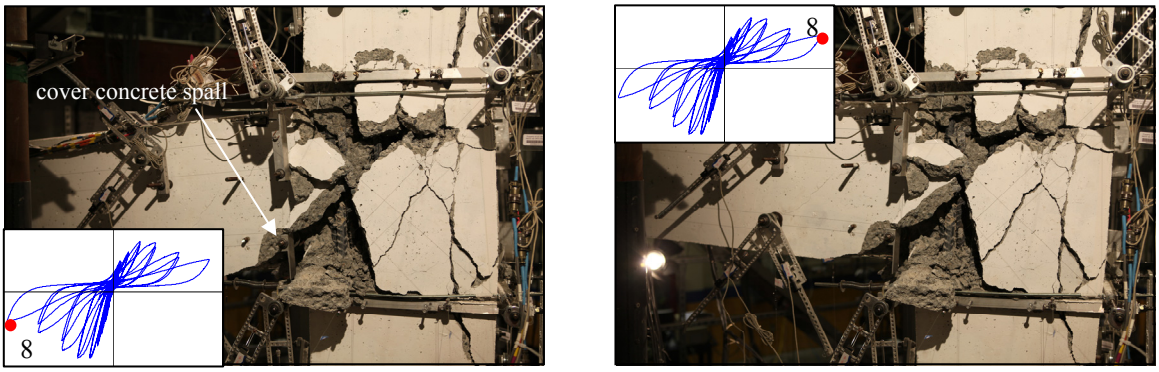

(d) Joint damage at the end of test

Figure V.21 Damage progression of joint in NS direction, SP2.

(a) Global view of specimen

(b) Inside corner joint

(c) NS beam

(d) EW beam

Figure V.22 Failure of SP2 after removing concrete fragments.

V-2.3 Joint Shear Stress versus Rotation Response

The hysteretic responses of joint shear stress versus strain are presented in Table V.6 and Figure V.23. The assumed constant moment arm was taken 0.9 times the beam effective depths because beam reinforcing bars yielded as shown in the subsequent section. Based on the estimation of slab reinforcement contribution discussed in Section VI.5, top two slab bars in both EW and NS direction were considered for estimating the effective depth for negative bending. The maximum joint shear stresses in the EW direction were 753 psi (5.20 MPa) for the downward loading and 597 psi (4.12 MPa) for the upward loading. The corresponding normalized joint shear stresses were 12.7 $psi^{0.5}$ (1.05 $MPa^{0.5}$) and 10.0 $psi^{0.5}$ (0.83 $MPa^{0.5}$), respectively. In the NS direction, the maximum joint shear stresses were 736 psi (5.08 MPa) for the downward loading and 578 psi (3.99 MPa) for the upward loading. The corresponding normalized joint shear stresses were 12.4 $psi^{0.5}$ (1.03 $MPa^{0.5}$) and 9.7 $psi^{0.5}$ (0.81 $MPa^{0.5}$), respectively. It is noted that the NS beam peak loads were larger than those of the EW beam. The joint shear stresses were, however, similar for both directions because of the aforementioned different cover concrete thicknesses in the EW and NS beam cross-sections. The test results showed that the maximum joint shear stresses were greater than the shear strength by the ASCE41 in both directions, as shown in Figure V.23, and also these values were greater than the maximum joint shear stresses of SP1.

Regarding the measured joint deformation, joint shear strains at the first cycle of peak loading were 0.0026 rad. for the downward loading and 0.0117 rad. for the upward loading in the EW direction. In the NS direction, the measured joint shear strains were 0.0012 rad. for the downward loading and 0.0059 rad. for the upward loading, as shown in Figure V.23. The joint shear strains were similar for both SP1 and SP2 at the peak loading, but comparing them at the same level of drift, the joint shear strains were larger in SP2 than those of SP1. Figure V.24 presents the hysteretic response of the rotation at the beam-joint interface. The rotations measured in the EW and NS directions were very close at the same level of drift. The results of total joint rotations are presented in Figure V.25. Total joint rotations at the peak load were 0.013 rad. for the downward loading and 0.021 for the upward loading in the EW direction; 0.008 rad. for the downward loading and 0.011 for the upward loading in the NS direction. Compared with the joint deformation response in SP1 at the same drift levels, SP2 showed larger joint shear strains but smaller rotations at the beam-joint interface and consequently total rotations became similar for both specimens SP1 and SP2.

According to Table V.6, the contribution of joint rotation to total drift was about 40% near the first yielding of beam reinforcement. Subsequently, this contribution increased to about 70%, which confirmed that the failure of specimen SP2 was caused by the joint shear failure.

Table V.6 Joint response of SP2.

Dir.	EW											
Group No.	Downward						Upward					
	v_{jh} (psi)	γ (psi$^{0.5}$)	Δ (rad)	γ_{xy} (rad)	θ_j (rad)	θ_j/Δ	v_{jh} (psi)	γ (psi$^{0.5}$)	Δ (rad)	γ_{xy} (rad)	θ_j (rad)	θ_j/Δ
1	338	5.7	0.0057	-	-	-	80	1.3	0.00	-	-	-
2	469	7.9	0.0087	0.0005	0.0027	0.31	239	4.0	0.0027	0.00	0.0004	0.15
3	581	9.8	0.0117	0.0008	0.0038	0.32	296	5.0	0.0056	0.00	0.0009	0.16
4	737[*1]	12.4	0.0175	0.0015	0.0074	0.42	468	7.9	0.0115	0.0015	0.0032	0.28
5	753[#2]	12.7	0.0266	0.0027	0.013	0.49	570[*1]	9.6	0.0204	0.0047	0.0089	0.44
6	749	12.6	0.0386	0.0073	0.022	0.57	597[#2]	10.0	0.0322	0.012	0.021	0.65
7	596	10.0	0.0568	0.033	0.049	0.86	549	9.2	0.0499	0.019	0.036	0.72
8	399	6.7	0.0806	-	-	-	462	7.8	0.0730	-	-	-
Dir.	NS											
Group No.	Downward						Upward					
	v_{jh} (psi)	γ (psi$^{0.5}$)	Δ (rad)	γ_{xy} (rad)	θ_j (rad)	θ_j/Δ	v_{jh} (psi)	γ (psi$^{0.5}$)	Δ (rad)	γ_{xy} (rad)	θ_j (rad)	θ_j/Δ
1	330	5.6	0.0057	-	-	-	130	2.2	0.00	-	-	-
2	463	7.8	0.0088	0.0001	0.0020	0.23	277	4.7	0.0028	0.0001	0.0012	0.43
3	596	10.0	0.0116	0.0006	0.0031	0.27	360	6.0	0.0057	0.0004	0.0022	0.39
4	736[*1#2]	12.4	0.0176	0.0012	0.0076	0.43	461	7.8	0.0118	0.0019	0.0048	0.41
5	732	12.3	0.0266	0.0033	0.013	0.49	578[*1#2]	9.7	0.0206	0.0059	0.011	0.53
6	649	10.9	0.0388	0.016	0.030	0.77	566	9.5	0.0324	0.012	0.021	0.65
7	453	7.6	0.0570	-	-	-	457	7.7	0.0501	0.028	0.035	0.70
8	332	5.6	0.0805	-	-	-	375	6.3	0.0731	-	-	-

[*1] first yielding of beam reinforcement; [#2] peak loading.

Note: 1 psi = 0.0069 MPa; $1.0\sqrt{f_c'}$ psi$^{0.5}$ = $0.083\sqrt{f_c'}$ MPa$^{0.5}$.

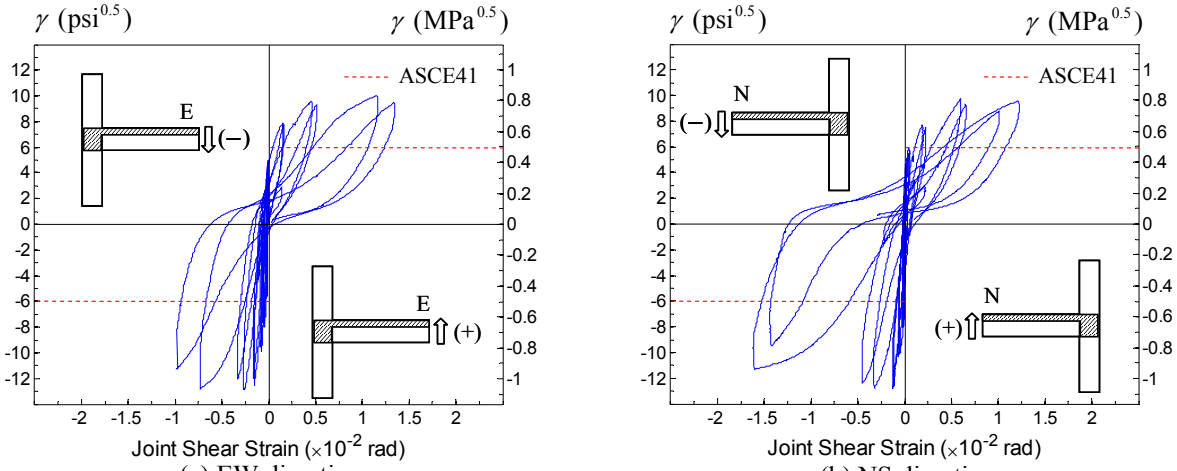

(a) EW direction (b) NS direction

Figure V.23 Joint shear stress versus strain response of SP2.

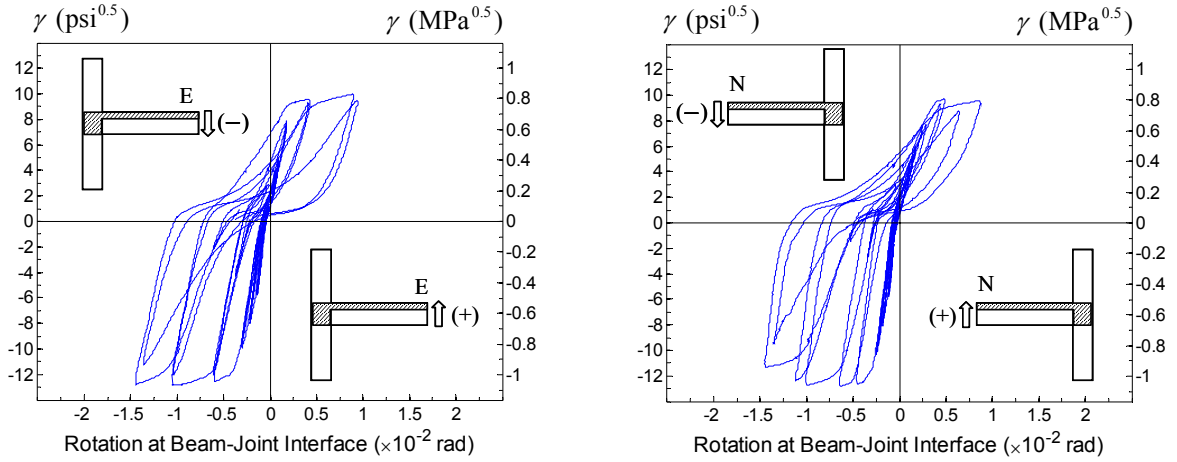

(a) EW direction (b) NS direction

Figure V.24 Joint shear stress versus rotation at beam-joint interface of SP2.

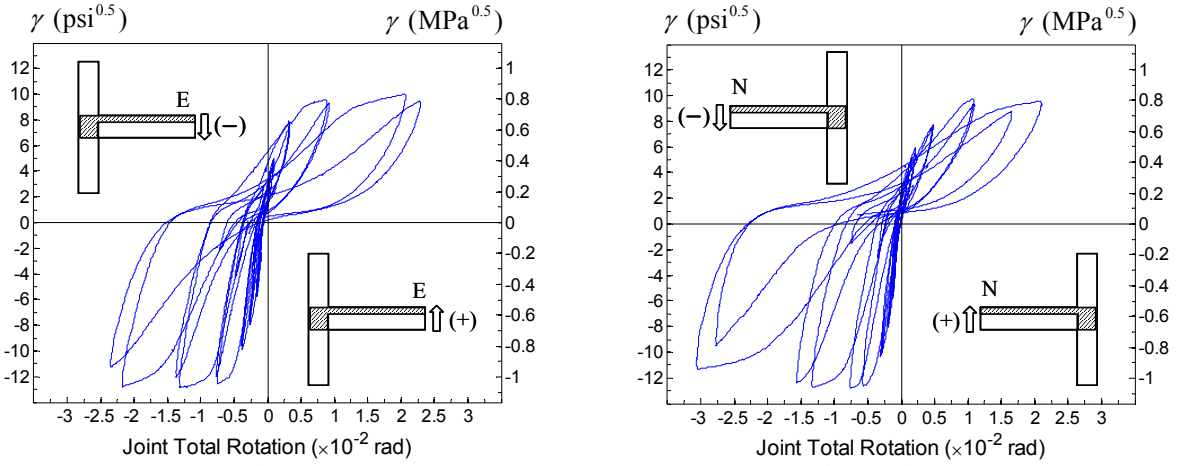

(a) EW direction (b) NS direction

Figure V.25 Joint shear stress versus total rotation of SP2.

V-2.4 Strain Measurements

V-2.4.1 Beam Reinforcement

The strain measurements of the beam longitudinal bars in the EW and NS directions are shown in Figures V.26 and V.27. The labeled drift levels correspond to the loading from the third group through the sixth group. It is noted that the data of the damaged strain gages are presented as blank bars marked as not applicable (N/A) in the plots. For better understanding of the strain distribution, a straight line passing the damaged gage was drawn between the values for the functioning gages. For example, a straight line connected gage numbers 1 and 3 passing through the damaged gage number 2 in Figure V.26(b).

The first yielding of the beam top and bottom reinforcing bars occurred at the beam-joint interface in both directions beyond a drift of about 1.2%, which was similar to the yield drift observed in SP1. The strains of all the gages increased as the applied drift level increased. Based on the strain variation at the gage number 2, which was placed on the mid-width of the joint, the yielding of beam reinforcing bars propagated toward the inside of the joint (Figure V.26), as observed in SP1. The propagation of the beam longitudinal bars yielding, however, was less severe in SP2 than in SP1 because beam flexural strength was higher in SP2.

V-2.4.2 Slab Reinforcement

The strain distributions of the slab reinforcing bars in the EW and NS direction are presented in Figure V.28. The strains of the slab reinforcement were measured at the beam-slab interface. The first yielding of the EW and NS slab top reinforcement occurred at the same loading group where the beam reinforcement yielded, i.e. fourth group of loading, and top two bars yielded at the peak loading. Until the peak loading, only top two bars were shown to yield. Therefore, top two slab bars were taken into account for estimating the effective depth in both directions. Note that in SP1, top four slab bars were included in the EW L-shape beam cross-section and top two slab bars were considered in the NS beam cross-section. On the other hand, the first slab bottom reinforcing bar yielded in the EW direction only and the slippage of this bar was observed as shown in Figure V.28. This was a consistent observation for both SP1 and SP2 because slab bottom bars were placed relatively close to the neutral axis of the L-shape section with insufficient anchorage.

V-2.4.3 Column Reinforcement

The strain results of the column longitudinal reinforcement are presented in Figures V.29 and V.30. The strains of all the column longitudinal bars were less than the yield strain, i.e. 0.0025, until the peak loading, except for the top gage of the bar number 3 in the EW direction which yielded at the sixth group of loading. The column longitudinal bars began to elongate from the fourth group of the EW and NS beams upward loading, as shown in Figures V.29 and V.30,

because the column was subjected to small tension. This response was consistent with the measured column vertical displacement as shown in Figure V.17(b).

The strain distribution of the column intermediate reinforcing bars was measured over the height in the joint region. The tensile strain in these bars at the joint mid-height was less than those at either or both top and bottom of the joint, which led to the conclusion that the column intermediate reinforcing bars did not act as a tension tie in the joint panel.

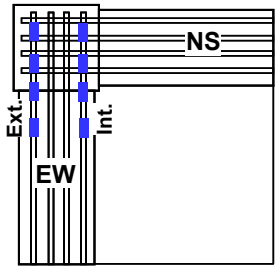

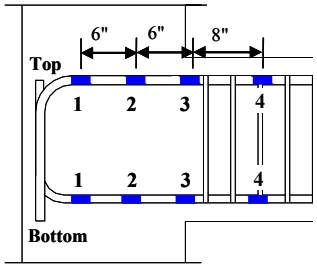

Note: 1" = 25.4 mm

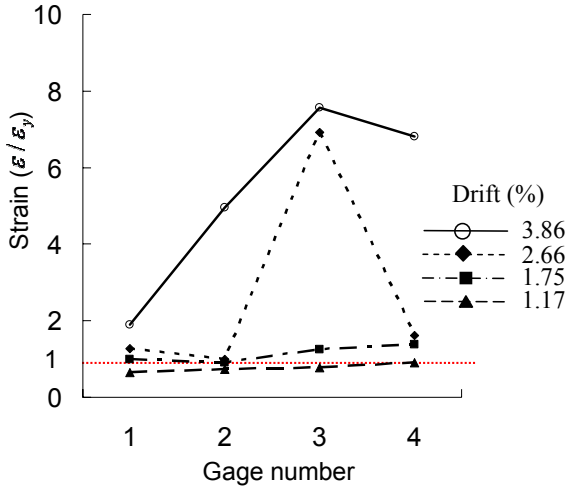

(a) EW-Top-Ext.

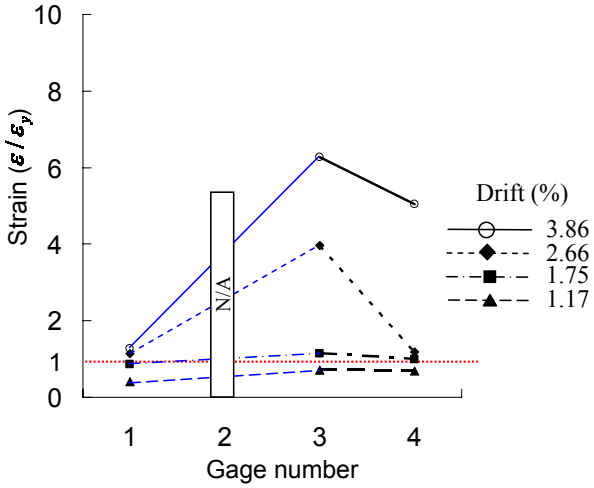

(b) EW-Top-Int.

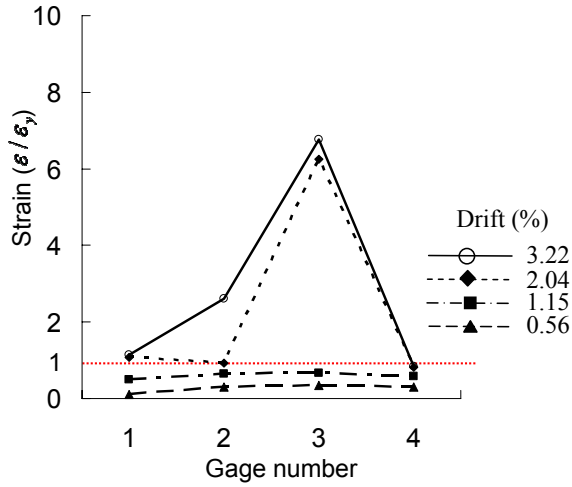

(c) EW-Bottom-Ext.

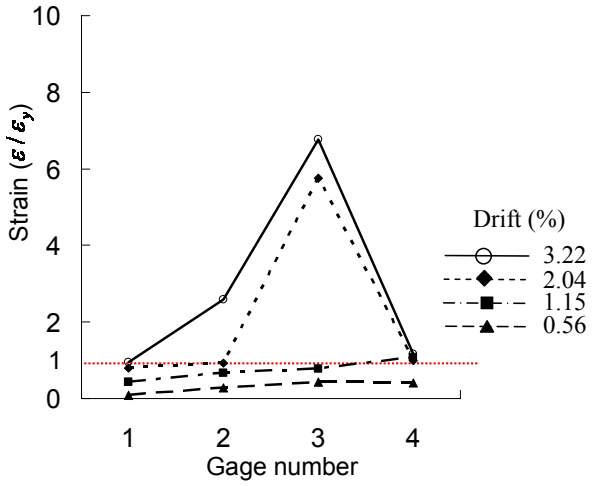

(d) EW-Bottom-Int.

Figure V.26 Strains of the EW beam reinforcing bars of SP2.

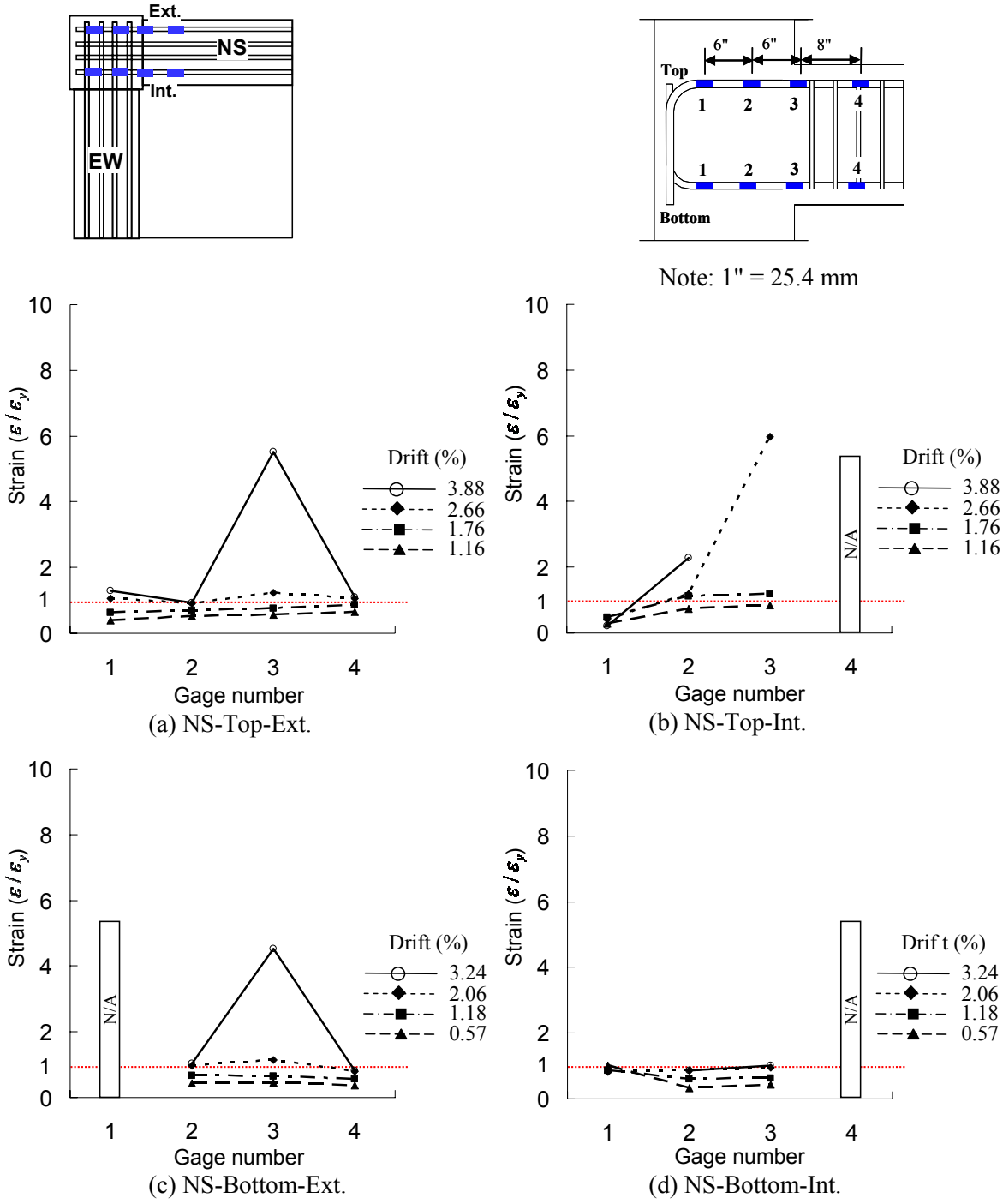

Figure V.27 Strains of the NS beam reinforcing bars of SP2.

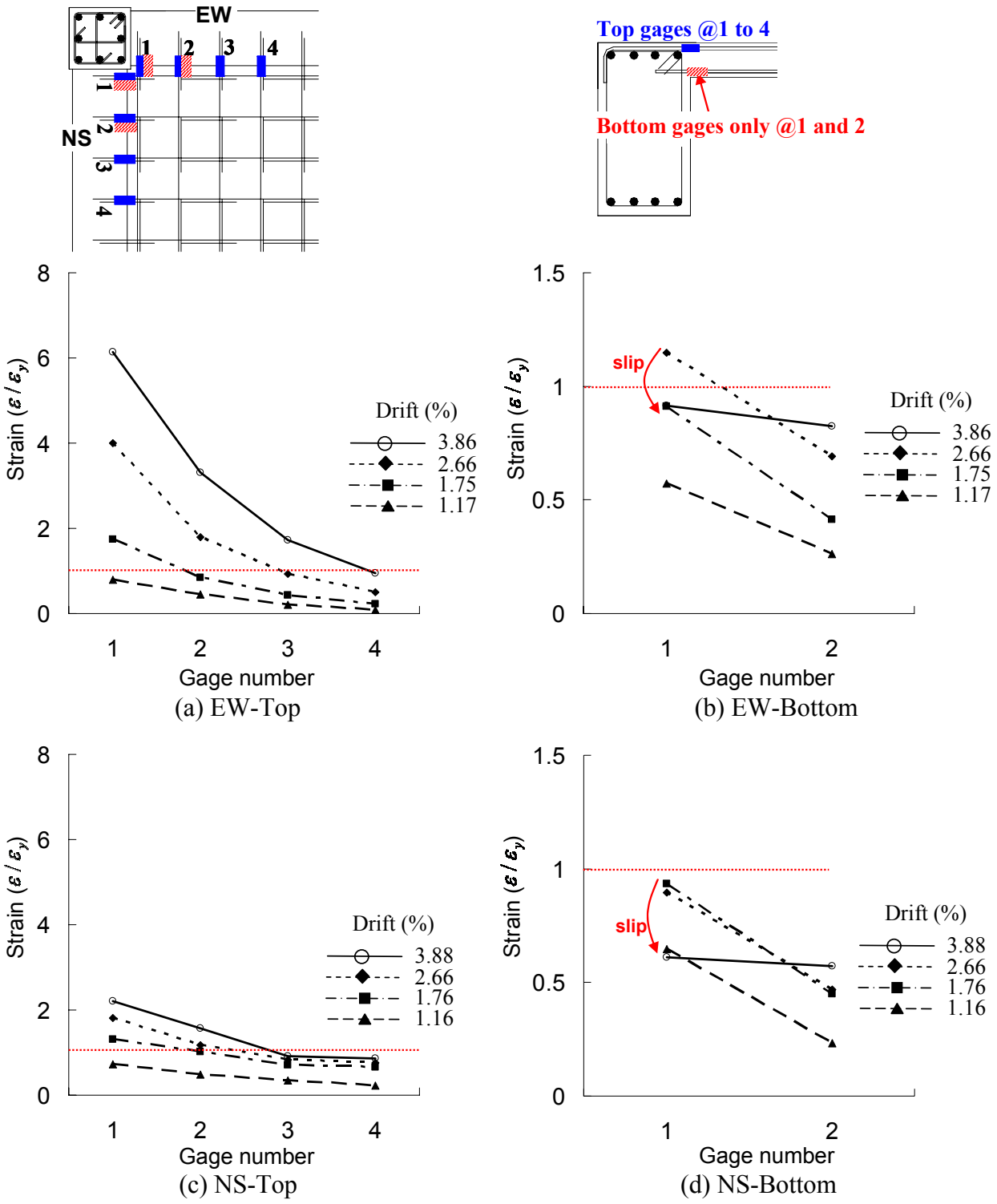

Figure V.28 Strains of the slab reinforcing bars of SP2.

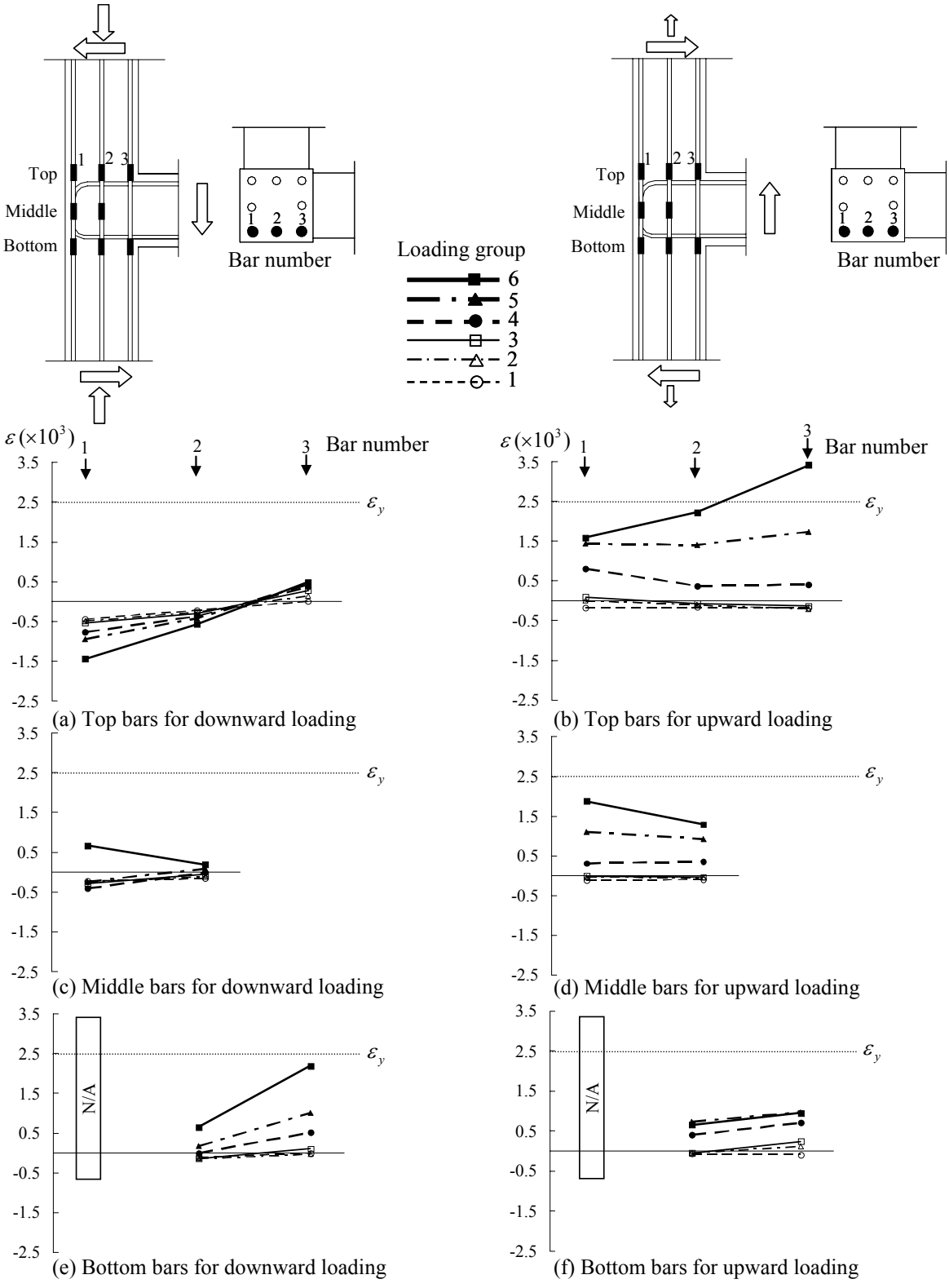

Figure V.29 Strains of the column reinforcing bars for the EW beam loading, SP2.

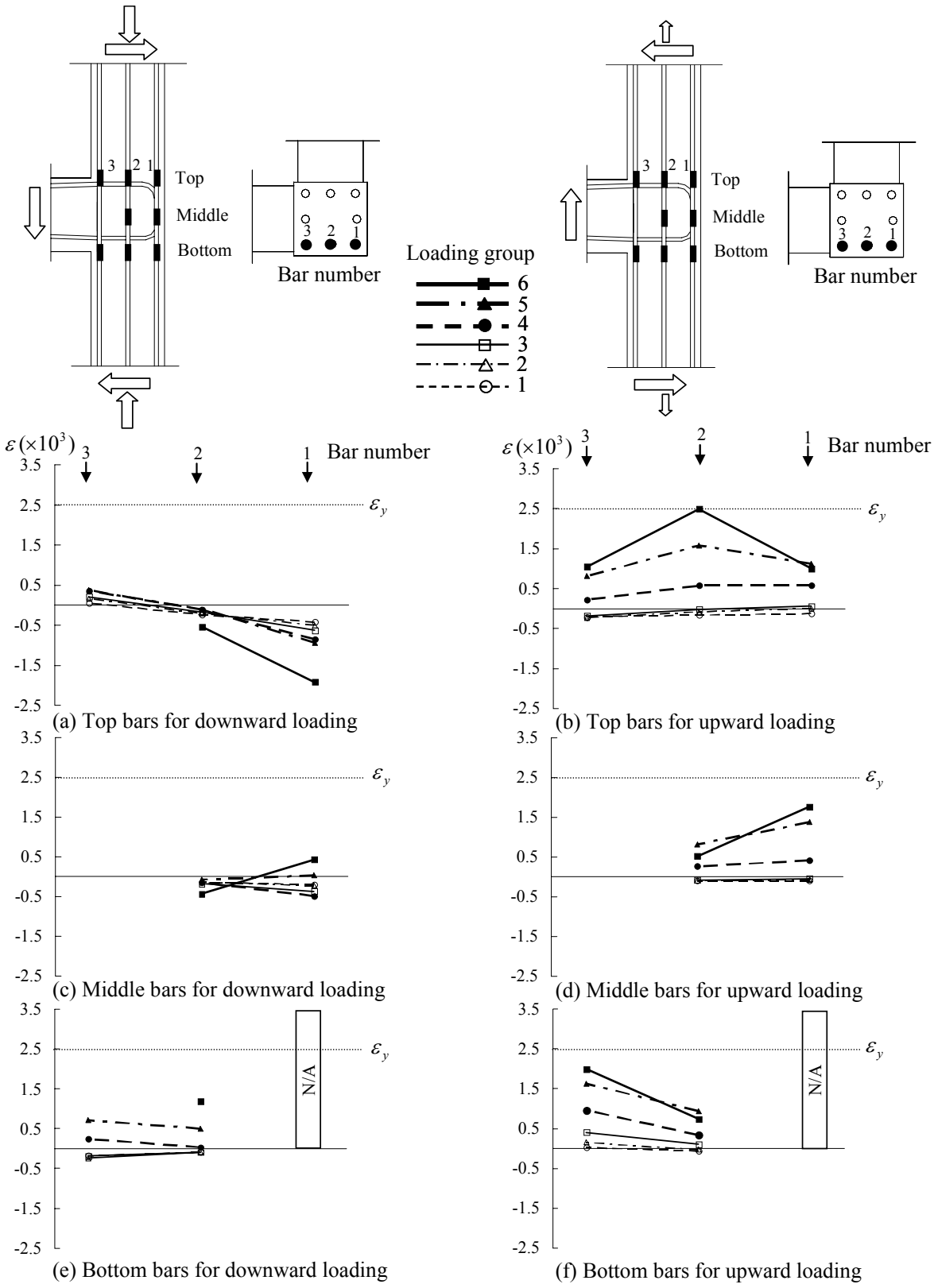

Figure V.30 Strains of the column reinforcing bars for the NS beam loading, SP2.

V-3 Specimen SP3

V-3.1 Load versus Drift Response

The hysteretic applied load versus drift responses of SP3 in the EW and NS directions are shown in Figure V.31 and their values at the peak of each cyclic loading group are given in Table V.7. For the downward loading of the EW beam, the first yielding of the top reinforcement occurred during the fourth group of loading ($\Delta_{EW} = -1.23\%$). In the subsequent fifth group of loading ($\Delta_{EW} = -1.89\%$), the peak load was achieved to be -40.4 kips (-179.7 kN). On the other hand, the bottom reinforcement in the EW beam yielded at the fifth group of loading ($\Delta_{EW} = 1.49\%$) for the upward loading, and at this loading group, the peak load was achieved to be 37.8 kips (168.1 kN).

In the NS beam, the top and bottom reinforcement yielded during the fifth group of loading for both downward and upward loading ($\Delta_{NS} = -1.94\%$; $\Delta_{NS} = 1.43\%$). At the same loading group, the peak loads of the NS beam were -35.8 kips (-159.3 kN) for the downward loading and 33.1 kips (147.2 kN) for the upward loading. Table V.7 shows that the applied loads in the NS beam were similar to those in the EW beam up to the third group of loading and thereafter less loads were applied to the NS beam for the same drift levels compared with the forces applied to the EW beam. This reduction of applied loads in the NS beam resulted from the damage of the joint panel during the EW beam loading.

The top and bottom reinforcement in the EW and NS beams yielded at the average drift level of 1.5%. Note that the estimated yield drift was 0.88% which corresponded to the drift at the third group of loading. The estimated yield drift was determined by conventional analysis for the beam-column subassemblies of the specimens using OpenSees (2010) without consideration of joint flexibility. This simplification in the computational model can explain the difference between the measured and estimated yield drift levels. In addition, the relatively earlier yielding of top reinforcement in the EW beam was caused by a larger cover concrete thickness at the top of beam cross-section which led to the reduction of the effective beam depth.

Based on the hysteretic load-drift responses plotted in Figure V.31, the applied loads increased up to the peak and thereafter sharply reduced without showing plateau as a distinction between SP3 and the previous two specimens, SP1 and SP2. The reduction of the applied beam loads after the peak was more significant than that observed in SP1 and SP2. Another remarkable observation was that the pinching behavior was not observed up to the peak and thereafter this behavior appeared due to the propagation of existing cracks in the joint panel instead of splitting cracks at the beam-joint interface, refer to Figure V.31. Finally, the applied beam loads reached their peak at the fifth group of loading in both directions when the beam reinforcement barely yielded.

The column response of SP3 is shown in Figure V.32. During testing, the column axial loads determined from Equation (IV.2b) were applied. In SP3, the column compressive axial load varied from 5 kips (22 kN) to 161 kips (716 kN). These column axial loads corresponded to the column axial load ratio of 0.4% and 13.8%, respectively. It is worth mentioning that the column axial load equations, i.e. Equations (IV.2a) and (IV.2b), intended that similar column axial loads were applied for SP1 and SP3 to investigate the effect of joint aspect ratio only. However, the column axial load ratios in SP3 were greater at the peak compression than that in SP1, i.e. $0.14 f_c' A_g$ for SP3 and $0.10 f_c' A_g$ for SP1, and no tension was applied to the column in SP3. For comparison with the results of SP1, the effect of 4% higher column axial load on the results of SP3 was expected to be negligible because the column axial load ratios did not vary beyond the value of $0.2 f_c' A_g$ shown in Figure II.5 of Chapter II. Finally, the peak vertical displacements were 0.073 in. (3.00 mm) in elongation and 0.102 in. (2.72 mm) in contraction, Figure V.32(b).

Table V.7 Load versus drift response of SP3.

Group No.	SP3							
	EW direction				NS direction			
	Downward (-)		Upward (+)		Downward (-)		Upward (+)	
	Δ (%)	V_b (kip)	Δ (%)	V_b (kip)	Δ (%)	V_b (kip)	Δ (%)	V_b (kip)
1	-0.40	-18.4	-0.02	6.8	-0.40	-17.5	-0.02	7.8
2	-0.58	-24.7	0.19	14.8	-0.62	-24.4	0.20	15.5
3	-0.82	-29.8	0.41	20.4	-0.84	-29.2	0.41	20.6
4	-1.23	-38.2[*1]	0.85	30.1	-1.27	-34.6	0.85	29.1
5	-1.89	-40.4[#2]	1.49	37.8[*1#2]	-1.94	-35.8[*1#2]	1.43	33.1[*1#2]
6	-2.82	-36.1	2.45	36.5	-2.91	-27.4	2.44	31.4
7	-4.39	-25.7	3.90	31.7	-4.44	-18.0	3.90	24.5
8	-6.58	-15.1	6.08	18.2	-6.59	-9.5	6.06	14.7

[*1] first yielding of beam reinforcement; [#2] peak loading.
Note: 1 kip = 4.45 kN.

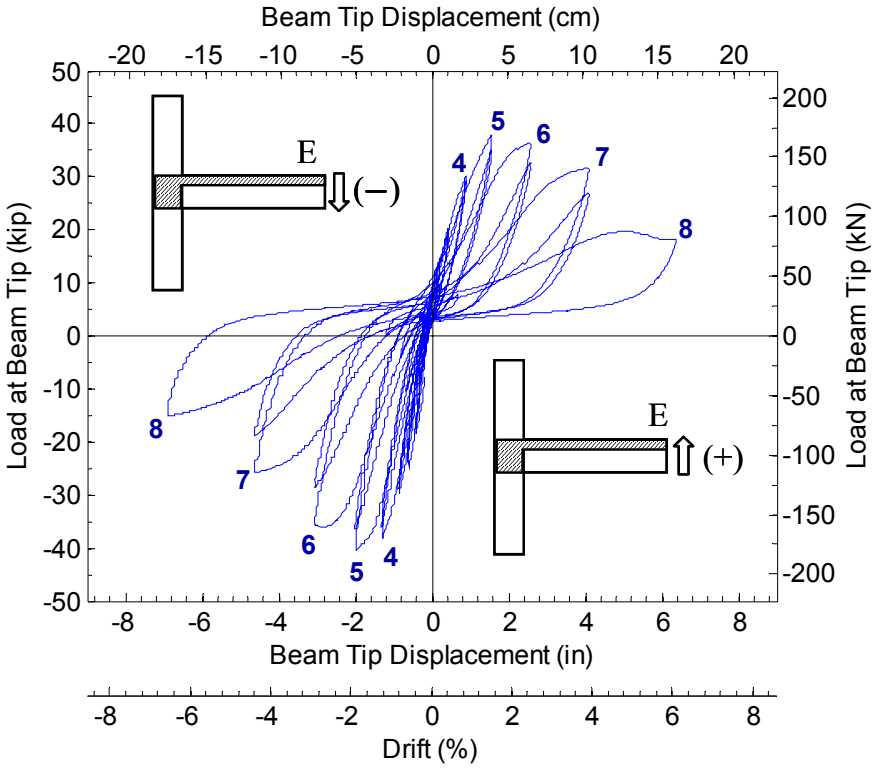

(a) EW direction

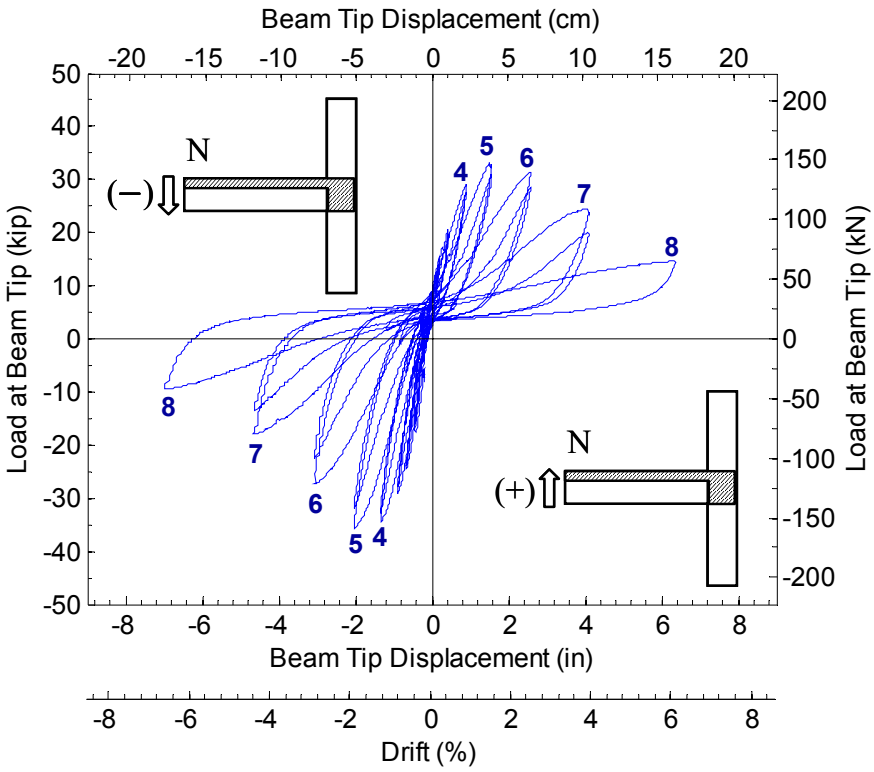

(b) NS direction

Figure V.31 Load versus drift response of SP3.

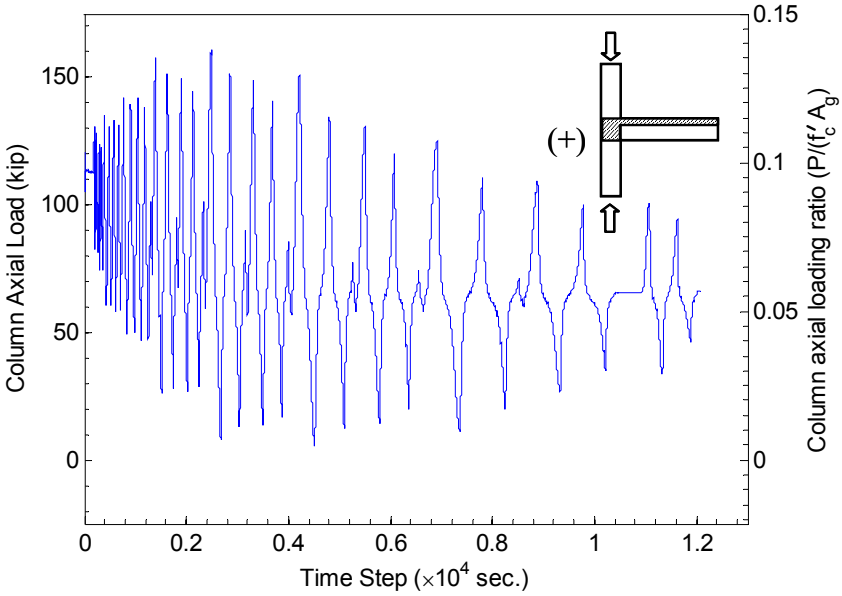

(a) Column Axial Load

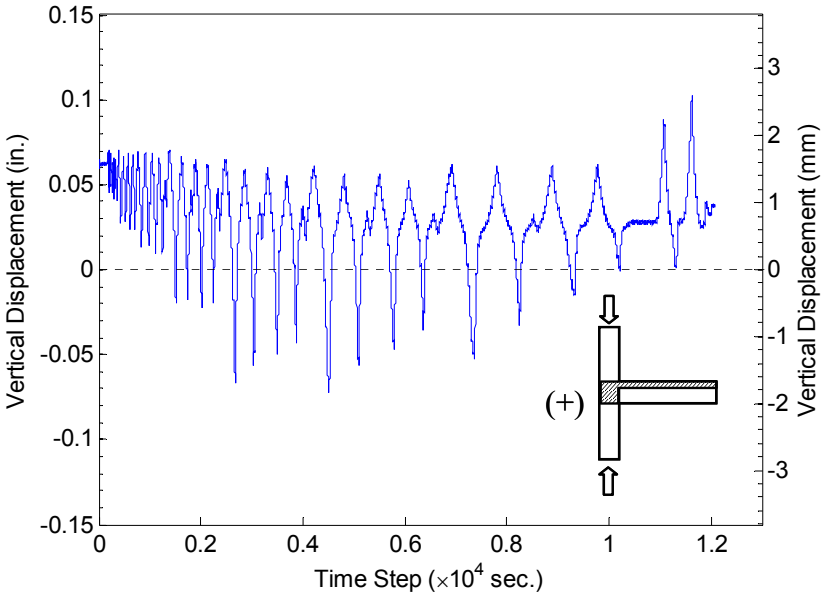

(b) Vertical Displacement

Figure V.32 Column response of SP3.

V-3.2 Observed Damage Progression

The qualitative damage progression of SP3 is summarized in Table V.8 and the photographs of the specimen taken during testing and at the end of the test are presented in Figures V.33 through V.35.

V-3.2.1 EW Direction

Joint Region

Multiple diagonal joint cracks with steep angle were observed during the test. Due to inappropriate camera installation, the onset of the first joint crack in the EW direction was not captured. The first photographs of EW joint were taken at the fourth group of loading ($\Delta_{EW} = -1.23\%$; $\Delta_{EW} = 0.85\%$), and they showed two downward (↘) diagonal cracks and an upward (↗) diagonal crack in the joint, Figure V.33(a). Based on the extent of the downward diagonal cracks propagation, it is obvious that the first downward diagonal crack developed prior to the fourth group. The opening of existing diagonal cracks was significant at the peak loading, $\Delta_{EW} = -1.89\%$ and $\Delta_{EW} = 1.49\%$, as shown in Figure V.33(b). Beyond the peak loading, joint cover concrete spalled and reinforcing bars of beam and column were exposed. Crushing of joint core concrete was observed through the exposed reinforcing bars at the end of test (Figure V.33(c)).

During the NS beam loading, a horizontal crack was observed at the top of the EW joint panel under upward loading as observed in specimens SP1 and SP2, and a horizontal crack also took place at the bottom of the joint panel for the downward loading. The location of the top horizontal crack was close to the layer of beam top reinforcement and the bottom horizontal crack was located in the layer of beam bottom reinforcement. Compared with the top horizontal cracks observed in SP1 and SP2, the crack propagation was moderate in SP3. The crack pattern is shown in Figure V.34(a). Generally, the damage of the joint and beam-joint interface due to the NS beam loading was negligible.

Beam and Slab

The first flexural crack initiated in the beam and slab during the first group of loading down to $\Delta_{EW} = -0.40\%$. In the subsequent loading, additional flexural cracks developed in the beam and slab, accompanied by splitting cracks at the beam-joint and beam-slab interfaces. When the EW beam drift was increasing up to the fourth group, there was no change in the crack pattern but the existing cracks became wider. At the fifth group of loading, which is the peak of EW beam, it was observed that the splitting cracks at both beam-joint top interface and NS beam-slab interface were opening wider than other flexural cracks in the beam and slab. The opening of the splitting cracks was confirmed by the instruments for rotation at the beam-joint interface. Beyond the peak load, flexural cracks did not propagate any more, but beam-joint interface was severely damaged. No plastic hinge occurred in the beam.

For the NS beam loading, multiple inclined cracks and splitting cracks occurred in the EW beam and beam-joint interface due to torsion (Figure V.34(a)). These cracks began to propagate at the peak of the NS beam loading. In particular, splitting cracks at the beam-joint interface widened and propagated down into the EW beam. Figure V.35 shows the existing cracks in the beam and slab after test.

V-3.2.2 NS Direction

Joint Region

The observed crack pattern in the NS joint was similar to that shown in the EW joint. A first downward (↙) joint crack was observed during the second group of downward loading, $\Delta_{NS} = -0.62\%$, while a first upward inclined crack (↖) appeared during the third group of upward loading ($\Delta_{NS} = 0.41\%$). Additional downward inclined cracks formed at the fourth group of loading. At the peak of NS beam loading, i.e. the fifth group of loading ($\Delta_{NS} = -1.94\%$; $\Delta_{NS} = 1.43\%$), there was a big opening of two downward diagonal cracks, but for the upward loading, only the early developed upward diagonal crack widened and additional minor upward inclined cracks newly formed in the joint. After the peak load, joint concrete suffered severe damage by cover concrete spalling, and corner quadrant concrete in the joint was separated from the joint. Beam and column bars were exposed and the crushing of joint core concrete was observed. Figure V.36 shows the progression of joint damages.

Under the EW beam loading, horizontal cracks developed at the top and bottom of the joint panel. The top horizontal crack continuously extended, while the bottom horizontal crack remained narrow without further propagation. The top horizontal crack was close to the top reinforcement of the NS beam, Figure V.34(b).

Beam and Slab

Splitting crack was observed at the beam-joint interface during the pre-loading. Flexural cracks appeared in the beam and slab from the first loading group ($\Delta_{NS} = 0.40\%$) and more flexural cracks took place in subsequent loading group. At the third group of downward loading, $\Delta_{NS} = -0.84\%$, a splitting crack at the beam-slab interface developed. Flexural cracks and splitting cracks in the beam and slab became wider up to the peak load and thereafter their width was slightly reduced because total drift was mostly attributed to the joint damage. By the EW beam downward loading, inclined cracks were induced in the beam. These cracks showed a big opening after the peak loading because heavy damage in the joint impaired its torsional rigidity. Cracks developed in the beam and slab during the test are shown in Figure V.35.

V-3.2.3 Summary

First joint cracks occurred at an average drift level of 0.5% , based on the observation of NS joint only. Until the fourth group of loading, the first developed diagonal crack for both downward and upward loadings propagated significantly. At the peak loading, i.e. the fifth group of loading ($\Delta = -1.92\%$; $\Delta = 1.46\%$), the later developed downward diagonal crack widened to have a

similar width of the early propagated diagonal crack, while the first upward diagonal crack continued to widen. Beyond the peak loading, joint cover concrete spalled and core concrete crushed.

For damage of the beam and slab, first flexural and splitting cracks developed during the first group of loading. Up to the fifth group of loading, additional flexural cracks occurred in the beam and slab and existing splitting cracks were widening further. By comparison with the first two specimens, the flexural and splitting cracks of SP3 showed minor propagation up to the peak loading since the peak loads were achieved right after beam reinforcement yielding. After the peak loading, the widths of flexural cracks were reduced but splitting cracks were widening continuously.

The orthogonal beam loading induced a horizontal crack at the top of joint and torsinal cracks in the transverse beam. However, these cracks remained minor until the EW and NS beam reached their peak loads. Therefore, it was expected that the joint responses for loading applied to the beam in the same direction were not affected by these cracks induced during the orthogonal beam loading. Figure V.37 shows that joint and column near the joint were severely damaged, while most damage of beams was imposed at the bottom close to the column by torsion.

Table V.8 Qualitative damage description of SP3.

Drift (%)	EW direction	NS direction
$\Delta_0 = -0.2$	-	- Splitting crack at beam-joint interface
$\Delta_{up} = -0.02$ $\Delta_{down} = -0.40$	- First flexural crack in beam and slab	- First flexural crack in beam and slab
$\Delta_{up} = 0.20$ $\Delta_{down} = -0.60$	- Additional flexural cracks in beam and slab - Splitting crack at beam-slab interface	- First downward diagonal crack in joint - Additional flexural cracks in beam and slab
$\Delta_{up} = 0.41$ $\Delta_{down} = -0.83$	-	- First upward diagonal crack in joint - Splitting crack at beam-slab interface
$\Delta_{up} = 0.85$ $\Delta_{down} = -1.25$	- Two downward diagonal cracks in joint - Upward inclined crack in joint - Splitting crack at beam-joint interface - First yielding of beam top bars	- Additional downward diagonal cracks in joint - First upward diagonal cracks in joint
$\Delta_{up} = 1.46$ $\Delta_{down} = -1.92$	- Large opening of downward and upward diagonal cracks - First yielding of beam bottom bars	- Additional upward inclined cracks in joint - Large opening of an upward diagonal crack - First yielding of beam top bars - First yielding of beam bottom bars
$\Delta_{up} = 2.45$ $\Delta_{down} = -2.87$	- Spalling of joint cover concrete	- Spalling of joint cover concrete
$\Delta_{up} = 3.90$ $\Delta_{down} = -4.42$	- Crushing of joint core concrete - Reduction of beam flexural cracks width	- Crushing of joint core concrete - Reduction of beam flexural cracks width
$\Delta_{up} = 6.07$ $\Delta_{down} = -6.59$	- Straightening of beam bars anchorage tail	-

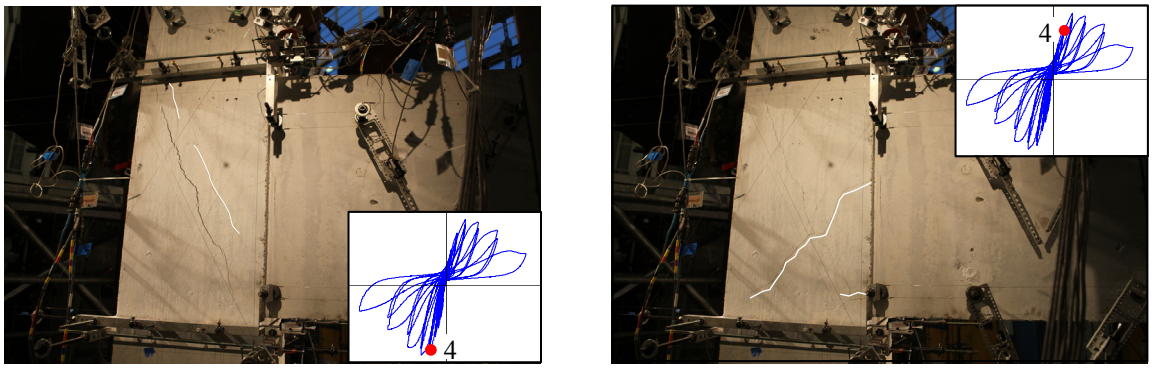

(a) Propagation of joint cracking

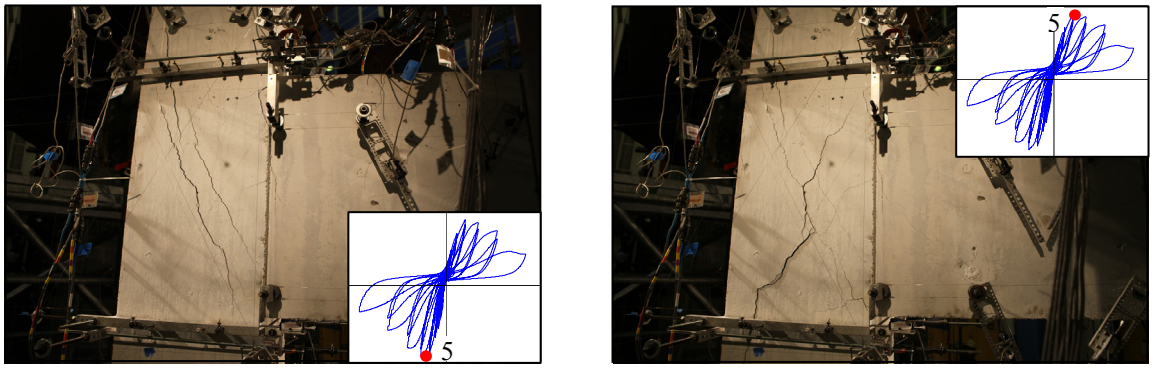

(b) Joint cracking before joint failure

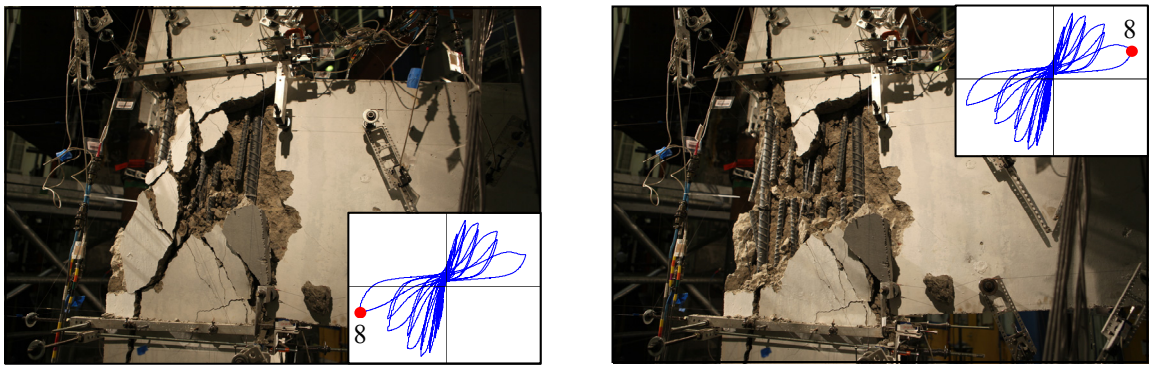

(c) Joint damage at the end of test

Figure V.33 Damage progression of joint in EW direction, SP3.

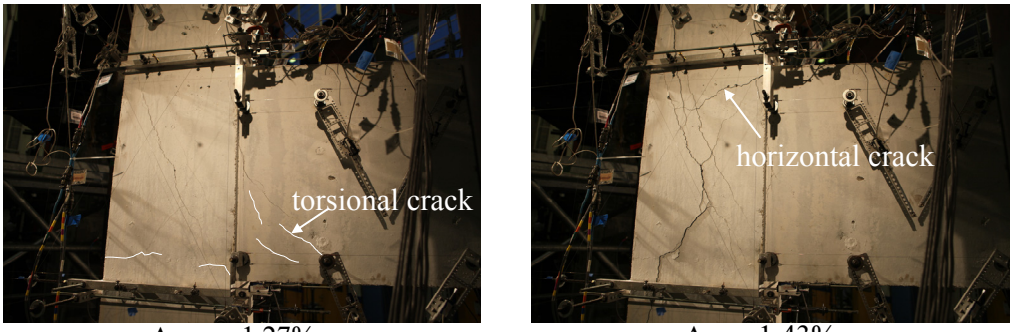

$\Delta_{NS} = -1.27\%$ $\Delta_{NS} = 1.43\%$

(a) Crack pattern in EW joint and beam by NS beam loading

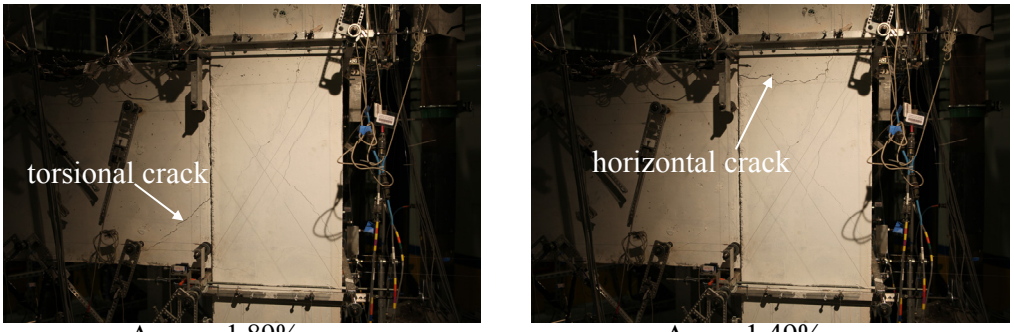

$\Delta_{EW} = -1.89\%$ $\Delta_{EW} = 1.49\%$

(b) Horizontal cracks in NS joint and beam by EW beam loading

Figure V.34 Crack patterns under the orthogonal beam loading, SP3.

(a) Cracks in EW beam

(b) Cracks in NS beam

(c) Cracks on slab

Figure V.35 Existing cracks after testing, SP3.

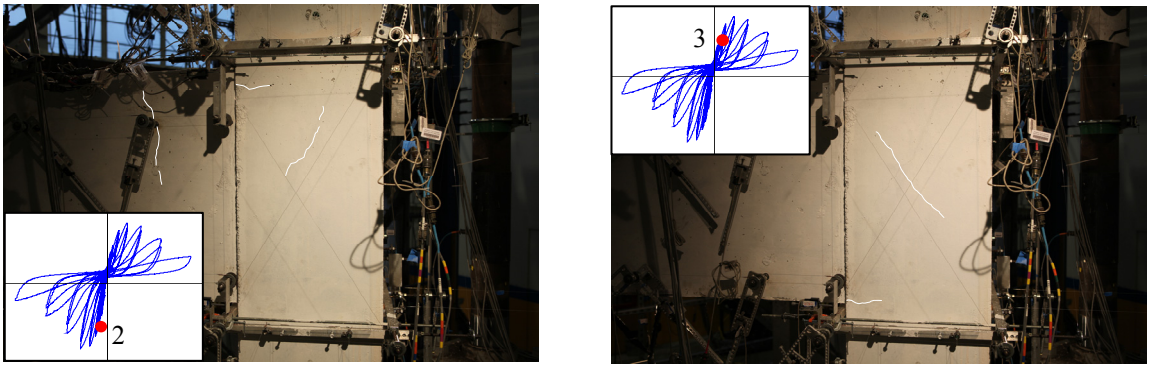

(a) First joint crack

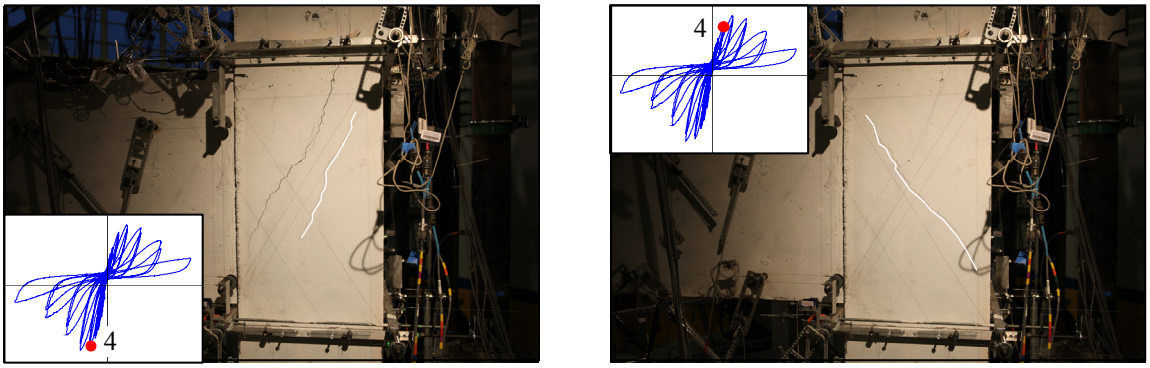

(b) Propagation of joint cracking

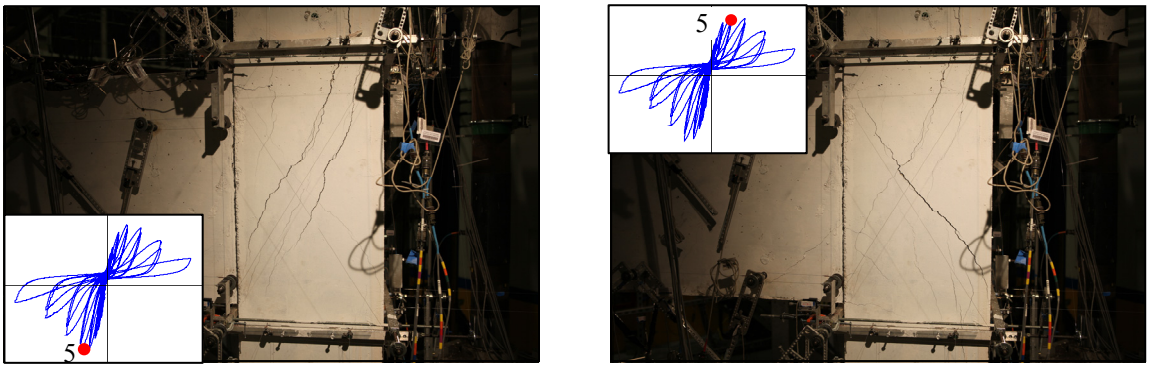

(c) Joint cracking before joint failure

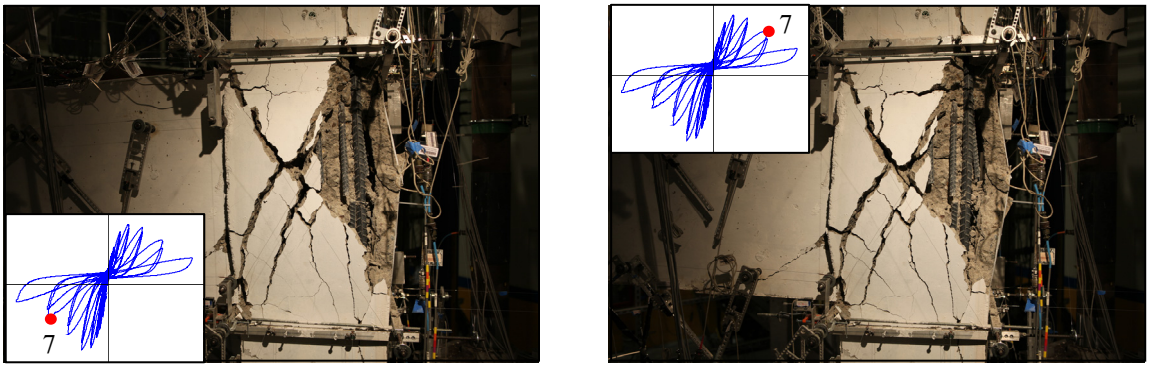

(d) Joint damage after failure

Figure V.36 Damage progression of joint in NS direction, SP3.

(a) Global view of specimen

(b) Inside corner joint

(c) NS beam

(d) EW beam

Figure V.37 Failure of SP3 after removing concrete fragments.

V-3.3 Joint Shear Stress versus Rotation Response

The hysteretic responses of joint shear stress versus strain up to the sixth group of loading are presented in Table V.9 and Figure V.38. For the calculation of joint shear stress, 0.9 times the beam effective depths were assumed as constant moment arms. To estimate the effective depth for the downward loading, top two slab reinforcing bars and one bottom bar were considered for the EW direction, while only top two bars were considered for the NS directions. The maximum joint shear stresses in the EW direction were 428 psi (2.95 MPa) for the downward loading and 379 psi (2.62 MPa) for the upward loading, and the corresponding normalized joint shear stresses were 7.1 $psi^{0.5}$ (0.59 $MPa^{0.5}$) and 6.3 $psi^{0.5}$ (0.52 $MPa^{0.5}$), respectively. In the NS direction, the maximum joint shear stresses were 375 psi (2.59 MPa) for the downward loading and 351 psi (2.42 MPa) for the upward loading, and the normalized values were 6.3 $psi^{0.5}$ (0.52 $MPa^{0.5}$) and 5.9 $psi^{0.5}$ (0.49 $MPa^{0.5}$), respectively. Given the maximum normalized joint stresses, the average of joint shear strengths were close to the shear strength by the ASCE41 as indicated by red dashed line in Figure V.38. It is noted that the maximum joint shear stresses of SP3 were less than those of SP1. Recalling both SP1 and SP3 had the same longitudinal reinforcement at the top and bottom of the beams, the strength reduction in SP3 can be explained by the effect of joint aspect ratio, as stated in Chapter II.

The joint shear strains at the peak load was 0.0060 rad. for the downward loading and 0.0073 rad. for the upward loading in the EW beam. In the NS direction, they were 0.0091 rad. for the downward and 0.0087 rad. for the upward loading. The joint shear strain response were more symmetric in both directions compared with the responses of SP1 and SP2. Joint shear strains gradually increased up to the peak and rapidly increased after the peak loading because joint cracks were widely opening. The rotations at the beam-joint interface are plotted in Figure V.39. The measured rotations at the beam-joint interface were less than those measured in SP1 and SP2. Combining the joint shear strain and rotation at the beam-joint interface, total joint rotations at the peak loading were 0.011 rad. for both downward and upward loadings in the EW direction. In the NS direction, they were 0.013 rad. for the downward loading and 0.012 rad. for the upward loading, Figure V.40.

According to Table V.9, the contribution of joint rotation to total drift was between 60% and 75% at the peak loading. It is noted that the joint rotation had more contribution to the total drift of SP3 compared with SP1 and SP2 results, because beam flexural deformation was smaller in SP3.

Table V.9 Joint response of SP3.

Dir.	EW											
Group No.	Downward						Upward					
	v_{jh} (psi)	γ (psi$^{0.5}$)	Δ (rad)	γ_{xy} (rad)	θ_j (rad)	θ_j/Δ	v_{jh} (psi)	γ (psi$^{0.5}$)	Δ (rad)	γ_{xy} (rad)	θ_j (rad)	θ_j/Δ
1	195	3.2	0.0040	-	-	-	68	1.1	0.00	-	-	-
2	261	4.4	0.0058	0.0011	0.0024	0.41	148	2.5	0.0019	0.00	0.0010	0.53
3	315	5.3	0.0082	0.0018	0.0035	0.43	205	3.4	0.0041	0.0004	0.0020	0.49
4	404[*1]	6.7	0.0123	0.0035	0.0061	0.50	302	5.0	0.0085	0.0023	0.0052	0.61
5	428[#2]	7.1	0.0189	0.0060	0.011	0.58	379[*1#2]	6.3	0.0149	0.0073	0.011	0.74
6	382	6.4	0.0282	0.010	0.016	0.57	366	6.1	0.0245	0.021	0.027	>1.0
7	272	4.5	0.0439	0.029	0.039	0.89	318	5.3	0.0390	0.032	0.042	>1.0
8	160	2.7	0.0658	-	-	-	183	3.0	0.0608	-	-	-
Dir.	NS											
Group No.	Downward						Upward					
	v_{jh} (psi)	γ (psi$^{0.5}$)	Δ (rad)	γ_{xy} (rad)	θ_j (rad)	θ_j/Δ	v_{jh} (psi)	γ (psi$^{0.5}$)	Δ (rad)	γ_{xy} (rad)	θ_j (rad)	θ_j/Δ
1	183	3.1	0.0040	-	-	-	83	1.4	0.00	-	-	-
2	256	4.3	0.0062	0.0005	0.0019	0.31	164	2.7	0.0020	0.0002	0.0005	0.25
3	306	5.1	0.0084	0.0014	0.0031	0.37	219	3.6	0.0041	0.0008	0.0015	0.37
4	363	6.0	0.0127	0.0038	0.0064	0.50	309	5.1	0.0085	0.0032	0.0047	0.55
5	375[*1#2]	6.3	0.0194	0.0090	0.013	0.67	351[*1#2]	5.9	0.0143	0.0091	0.012	0.84
6	287	4.8	0.0291	0.019	0.025	0.86	333	5.6	0.0244	0.022	0.024	0.98
7	189	3.1	0.0444	0.025	0.036	0.81	260	4.3	0.0390	0.045	0.046	>1.0
8	99	1.7	0.0659	-	-	-	156	2.6	0.0606	-	-	-

[*1] first yielding of beam reinforcement; [#2] peak loading.

Note: 1 psi = 0.0069 MPa; $1.0\sqrt{f_c'}$ psi$^{0.5}$ = $0.083\sqrt{f_c'}$ MPa$^{0.5}$.

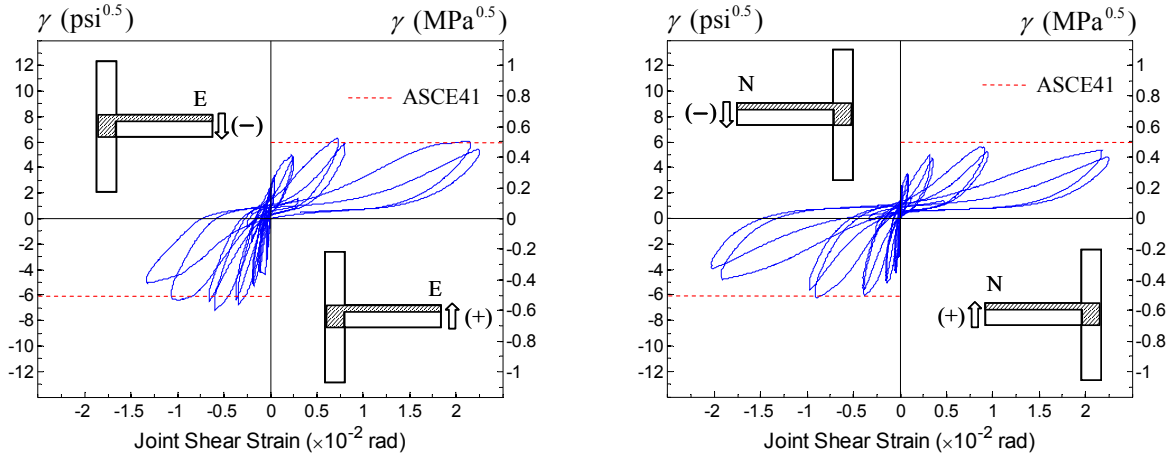

(a) EW direction (b) NS direction

Figure V.38 Joint shear stress versus strain response of SP3.

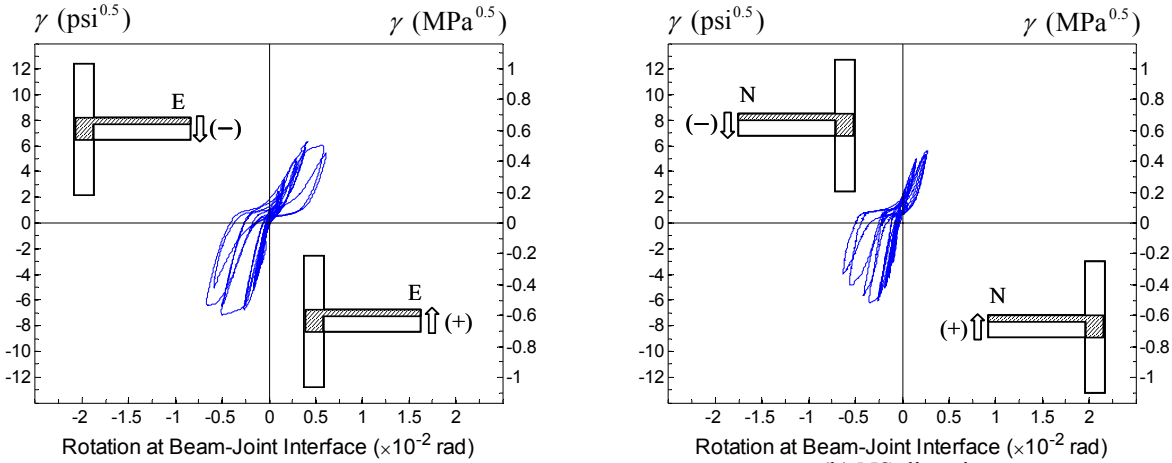

(a) EW direction (b) NS direction

Figure V.39 Joint shear stress versus rotation at beam-joint interface of SP3.

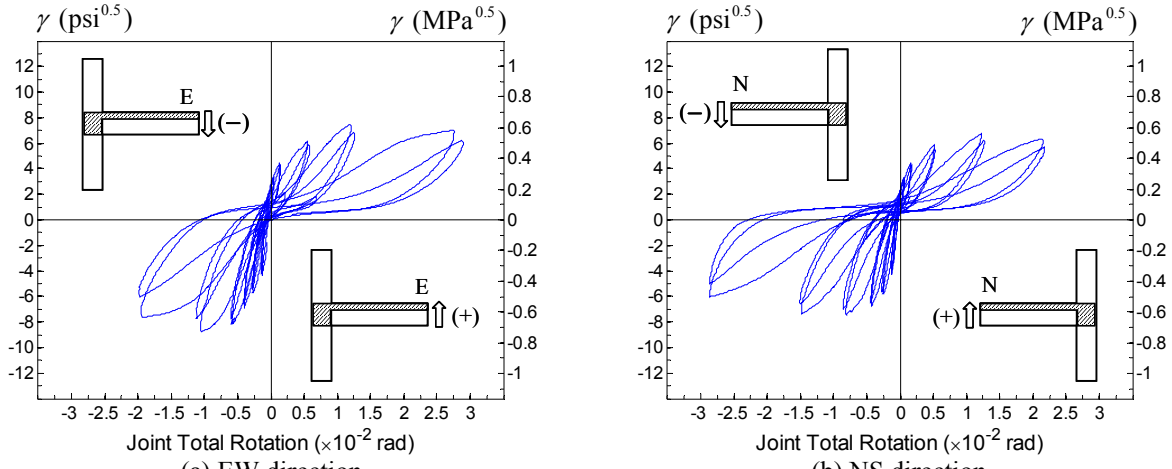

(a) EW direction (b) NS direction

Figure V.40 Joint shear stress versus total rotation of SP3.

V-3.4 Strain Measurements

V-3.4.1 Beam Reinforcement

The strain measurements of the beam reinforcing bars in the EW and NS directions are shown in Figures V.41 and V.42. It is noted that different drift levels from SP1 and SP2 were applied to SP3 even though the number of loading groups are the same for the labeled drift levels.

The first yielding of the EW beam top and bottom reinforcing bars occurred around the drift of 1.3%, while the NS beam reinforcing bars barely yielded during the fifth group of loading, $\Delta_{NS} = -1.94\%$ and 1.43%. The analytical yield drift without considering the joint flexibility was 0.88%. Compared with the strain gage data, the analytical yield drift was underestimated because joint flexibility was not taken into account. Coincidentally, the measured joint rotation was almost 1.1% radian which was close to the difference between the measured and estimated yield drift, i.e. $1.94 - 0.88 = 1.06\%$.

V-3.4.2 Slab Reinforcement

The strain variations of the slab reinforcing bars in the EW and NS directions are presented in Figure V.43. The figure shows that the strain values recorded in SP3 are less than those measured in specimens SP1 and SP2.

The first yielding of slab reinforcement in both directions took place when the beam top reinforcement yielded. In Figure V.43, top two and one bottom reinforcing bars in the EW slab yielded around the peak loading which corresponded to drift 1.89%, while only one top reinforcing bar yielded in the NS slab at the peak loading, i.e. drift 1.94%. As a result, top two and one bottom bars were included for estimating the effective depth of the EW beam. For the NS beam, top two bars were included because the second top bar was close enough to the yield strain.

V-3.4.3 Column Reinforcement

The strain results of the column longitudinal reinforcement are presented in Figures V.44 and V.45. For SP3 and SP4, column longitudinal reinforcement was designed with bar size of #10 (D32) to maintain the strong column/weak beam approach. The measured strains of all the column reinforcing bars were below the yield strain, i.e. 0.0023, up to the end of test, even though some damage was observed in the column. The strain distribution of the column intermediate reinforcing bars was measured over the height of the joint region. The tensile strain at the mid-height was less than the strain at either top or bottom in the EW joint, while it was greater than the strain at both of top and bottom in the NS joint. These results are insufficient to support that the column intermediate reinforcing bar acted as a tension tie in the joint panel.

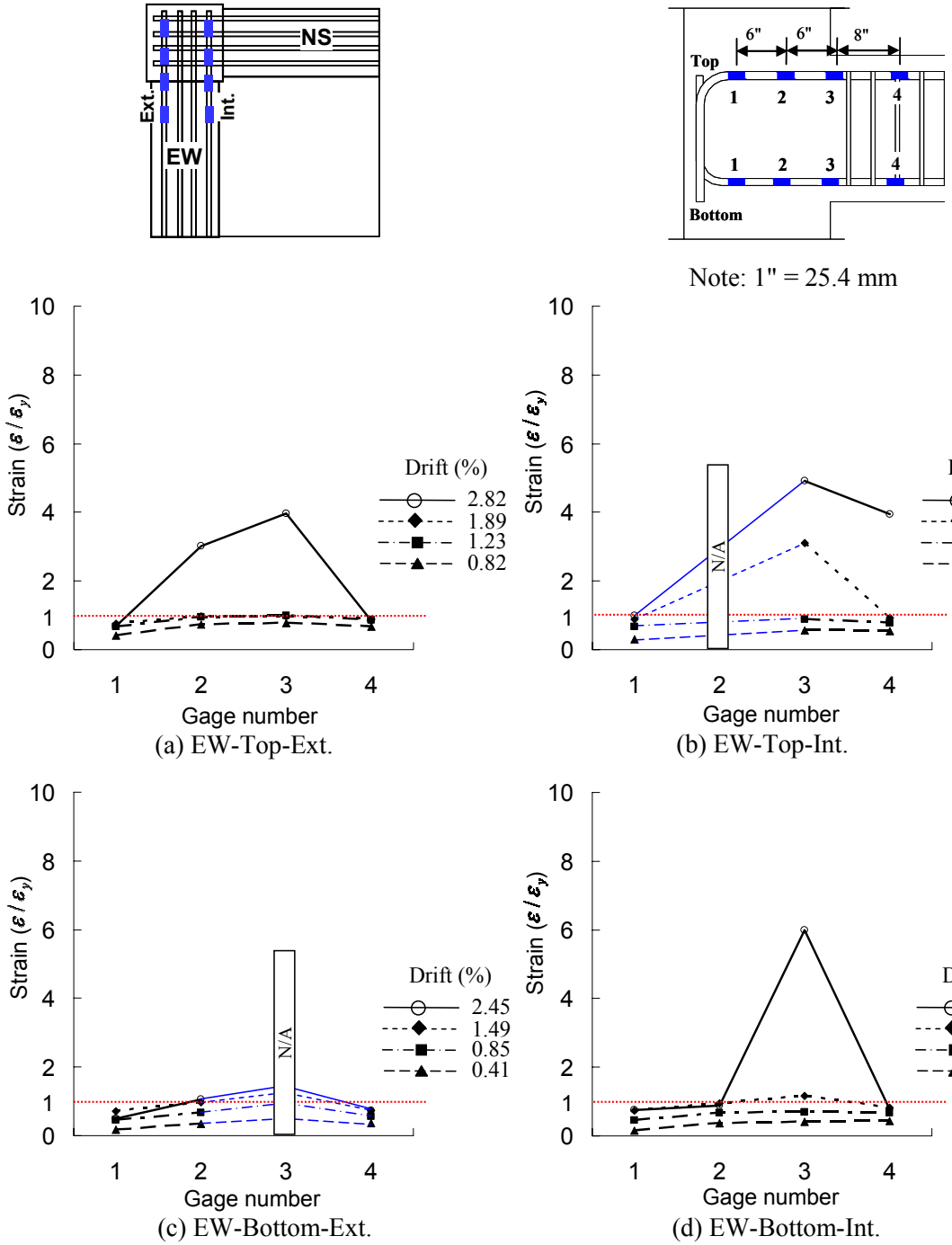

Figure V.41 Strains of the EW beam reinforcing bars of SP3.

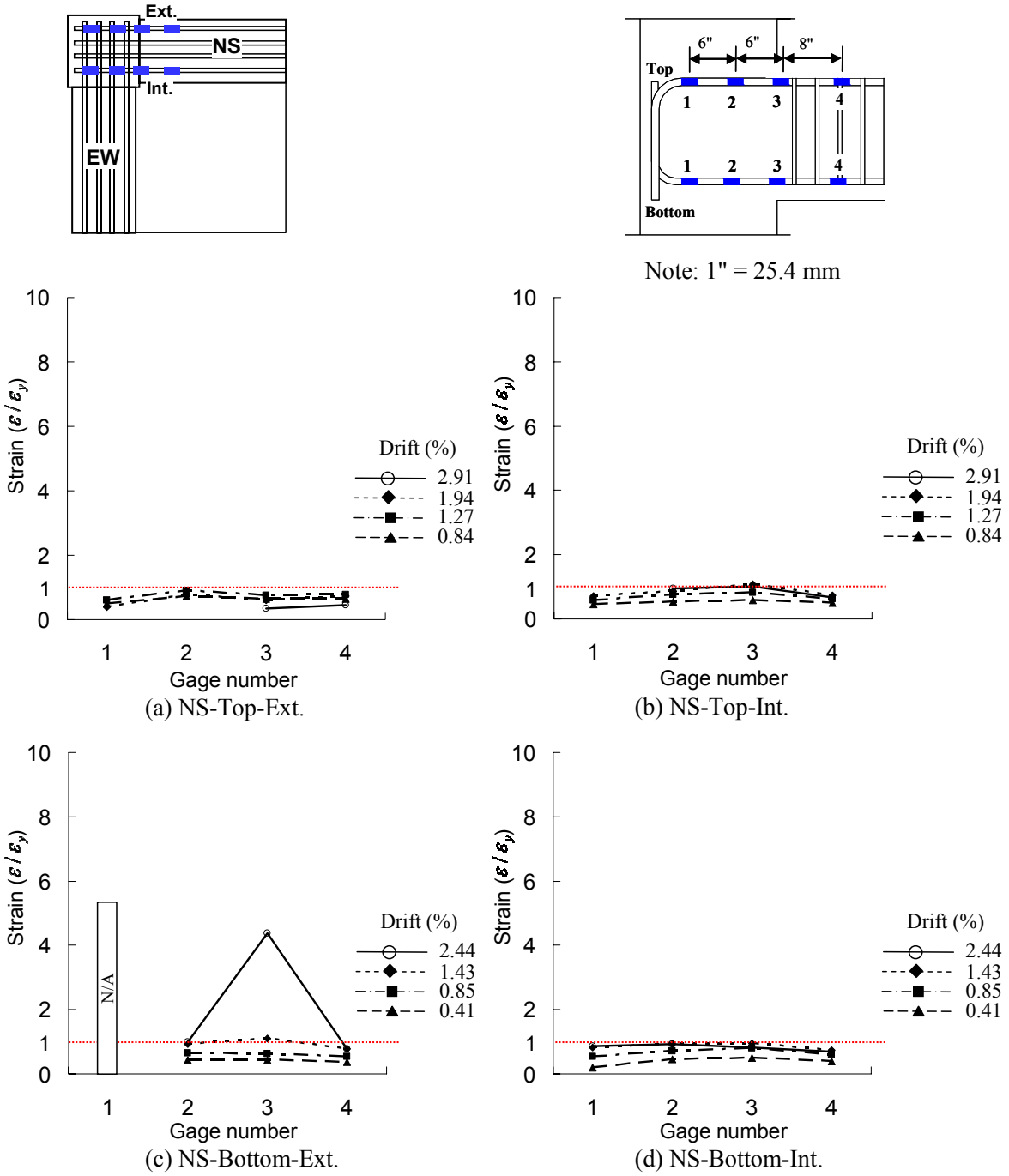

Figure V.42 Strains of the NS beam reinforcing bars of SP3.

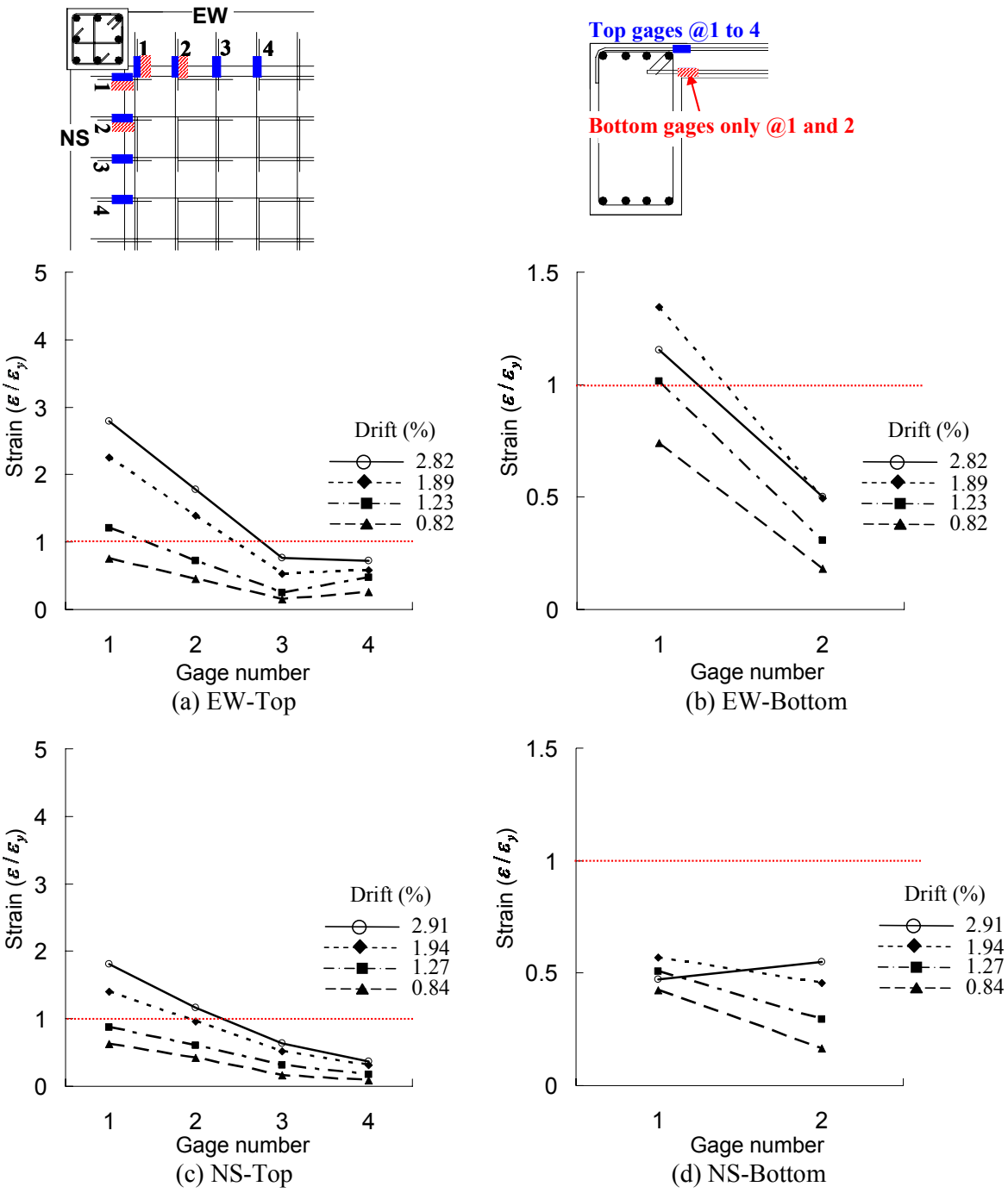

Figure V.43 Strains of the slab reinforcing bars of SP3.

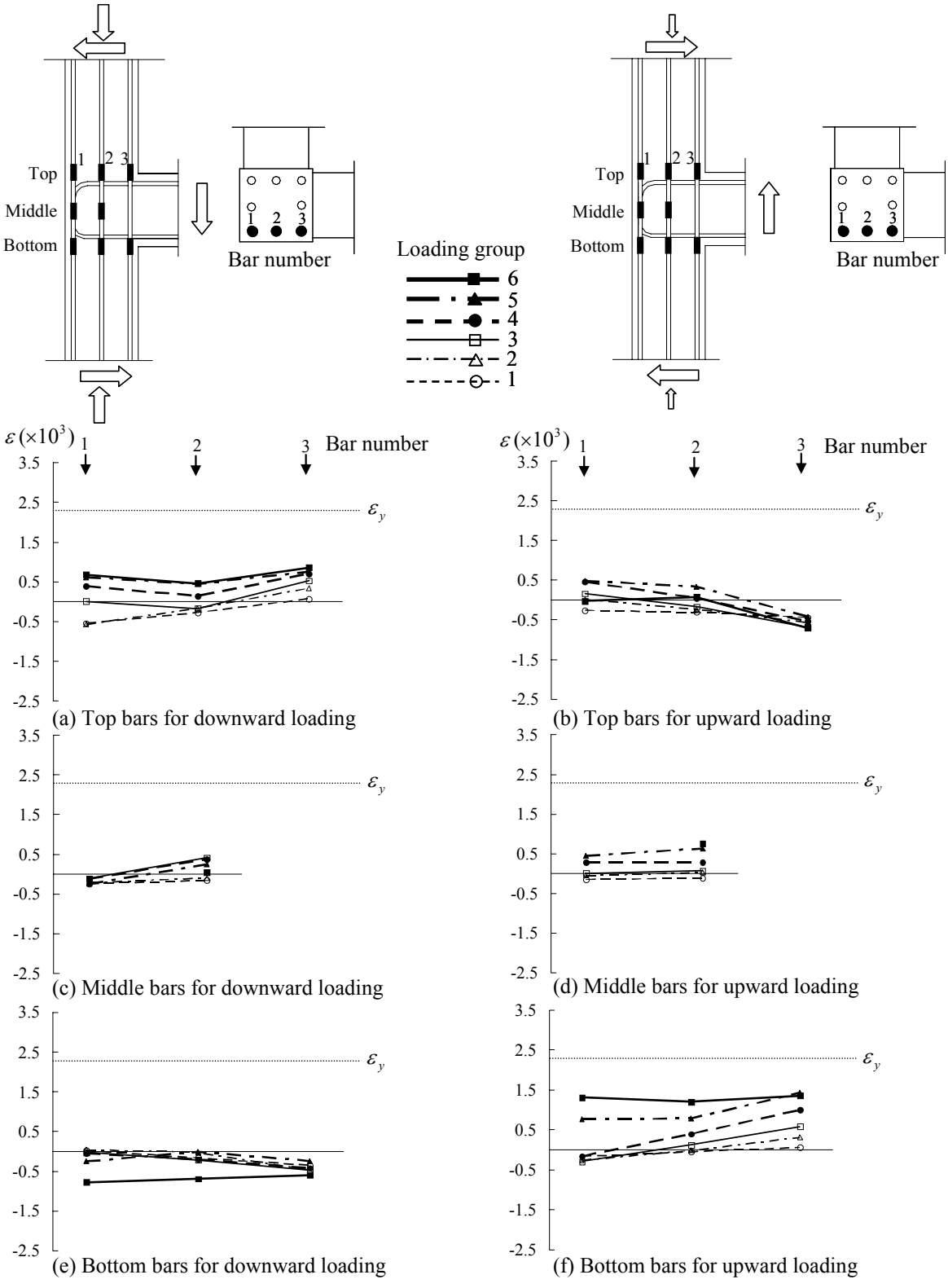

Figure V.44 Strains of the column reinforcing bars for the EW beam loading, SP3.

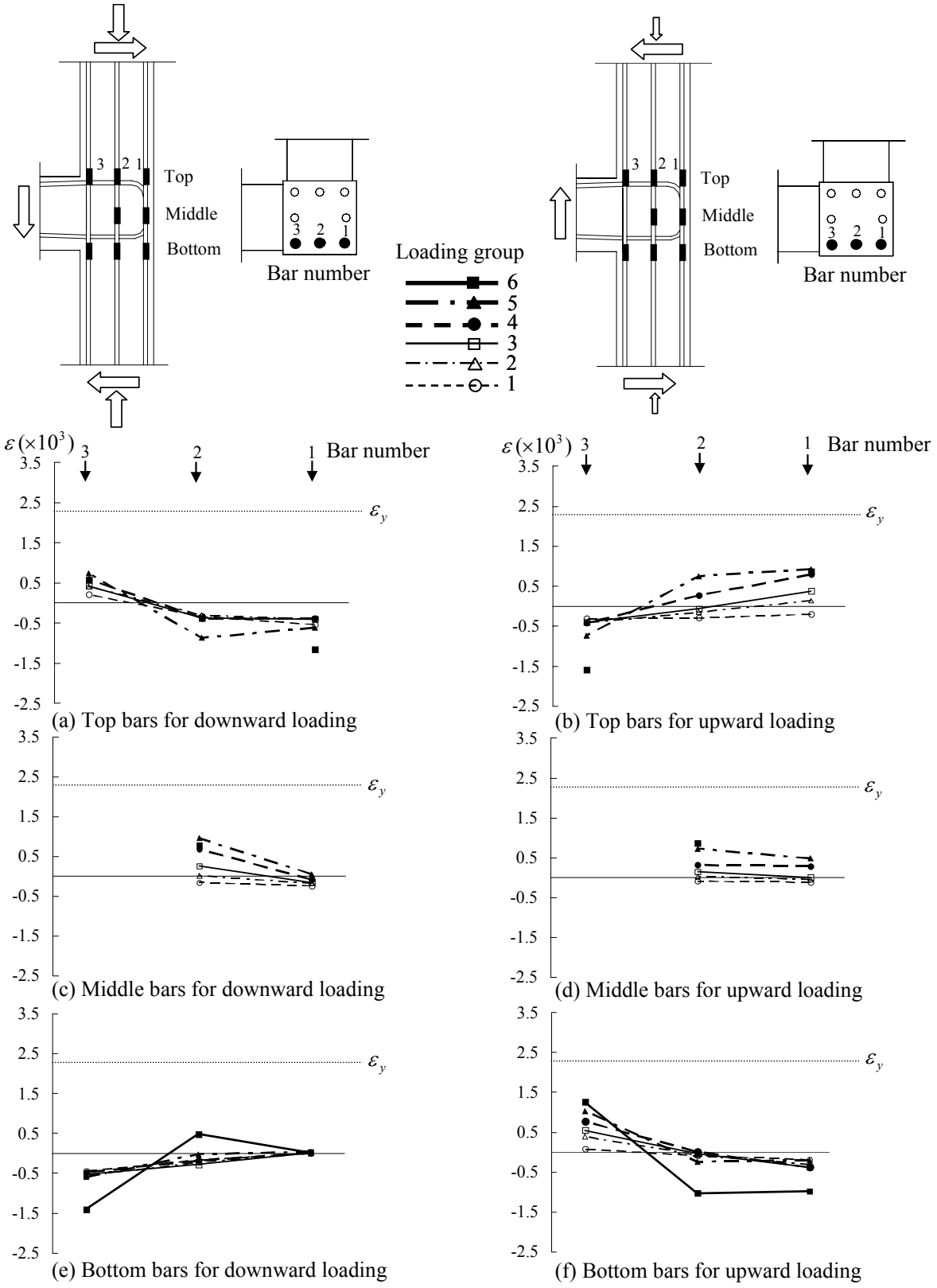

Figure V.45 Strains of the column reinforcing bars for the NS beam loading, SP3.

V-4 Specimen SP4

V-4.1 Load versus Drift Response

The hysteretic applied load versus drift responses of SP4 in the EW and NS directions are shown in Figure V.46 and their values at the peak of each cyclic loading group are given in Table V.10. The hysteretic load-drift responses showed that both EW and NS beams remained elastic up to the peak loading. The elastic responses were confirmed by the strains of the EW and NS beam longitudinal bars presented in Section V-4.4. Therefore, the failure of SP4 was designated as joint failure without beam reinforcement yielding, i.e. J failure mode, and the shear strength of this specimen could serve as a representative upper limit for the joint aspect ratio (h_b/h_c) of 1.67.

The peak loads of EW beam loading were achieved at the fifth loading group, $\Delta_{EW} = -1.94\%$ and $\Delta_{EW} = 1.52\%$, and the applied loads corresponded to -49.4 kips (-219.8 kN) for the downward loading and 45.6 kips (202.8 kN) for the upward loading. For the NS beam, the peak of the downward loading occurred at the fourth group, $\Delta_{NS} = -1.29\%$, and the applied load was -43.8 kips (-194.8 kN); for the upward loading, the peak occurred at the fifth loading group, $\Delta_{NS} = 1.53\%$, and the applied load was 39.2 kips (174.4 kN). It is noted that the one bottom reinforcement slightly yielded at the peak of upward loading of both EW and NS beams and its strain hysteretic responses remained elastic. The applied beam loads in the EW beam sharply reduced after the peak loads, while the peak load in the NS beam for the downward loading was maintained with 0.2 kips (0.9 kN) reduction during the subsequent loading group, i.e. the fifth loading group. Based on the hysteretic responses, it was postulated that the specimen began to lose its load-carrying capacity from the fifth group in both directions. The comparison of hysteretic responses between SP3 and SP4 showed that the peak loads were achieved at similar drift levels even though the peak loads were larger in SP4. The applied beam loads significantly reduced after the peak and the reduction was more significant than that observed in SP1 and SP2 as mentioned in Section V-3.1. Similar to SP3, the pinching behavior of SP4 began to appear after the peak loading due to the propagation of existing cracks in the joint panel, refer to Figure V.46.

The column response of SP4 is shown in Figure V.47. The column axial loads were controlled to follow Equation (IV.2b). As a result, the column compressive axial load varied from 2 kips (9 kN) to 187 kips (832 kN). These column axial loads corresponded to the column axial load ratio of 0.2% and 14.6%, respectively. It is noted that the column axial load equations, i.e. Equations (IV.2a) and (IV.2b), intended that similar column axial loads were applied for SP2 and SP4. However, the maximum column axial load ratio of SP4 was less than that of SP1, i.e. $0.15f_c'A_g$ for SP3 and $0.23f_c'A_g$ for SP2, and no tension was applied to the column in SP4. The reason of less column axial loads in SP4 was that the failure of SP4 occurred before beam reinforcement yielding, while SP2 experienced joint failure after beam reinforcement yielding. Nevertheless, the effect of less column axial loads on the results of SP4 was expected to be

negligible for comparison with the results SP2 because the column axial load ratios did not vary beyond the value of $0.2 f_c' A_g$ shown in Figure II.5 of Chapter II. Finally, the peak vertical displacements were 0.084 in. (2.13 mm) in elongation and 0.118 in. (3.00 mm) in contraction, Figure V.47(b).

Table V.10 Load versus drift response of SP4.

Group No.	SP4							
	EW direction				NS direction			
	Downward (-)		Upward (+)		Downward (-)		Upward (+)	
	Δ (%)	V_b (kip)	Δ (%)	V_b (kip)	Δ (%)	V_b (kip)	Δ (%)	V_b (kip)
1	-0.41	-24.5	-0.01	9.5	-0.41	-25.2	-0.02	8.9
2	-0.62	-32.2	0.21	20.3	-0.63	-34.3	0.20	19.3
3	-0.85	-38.9	0.42	27.1	-0.84	-39.8	0.43	26.2
4	-1.28	-45.9	0.86	37.6	-1.29	-43.8[#2]	0.86	34.3
5	-1.94	-49.4[#2]	1.52	45.6[*1#2]	-1.96	-43.6	1.53	39.2[*1#2]
6	-2.96	-43.0	2.51	43.0	-2.98	-35.5	2.52	37.1
7	-4.46	-31.6	4.01	37.9	-4.49	-24.3	4.00	28.9
8	-6.58	-20.4	6.23	23.7	-6.79	-9.5	6.20	17.2

[*1] first yielding of beam reinforcement; [#2] peak loading.
Note: 1 kip = 4.45 kN.

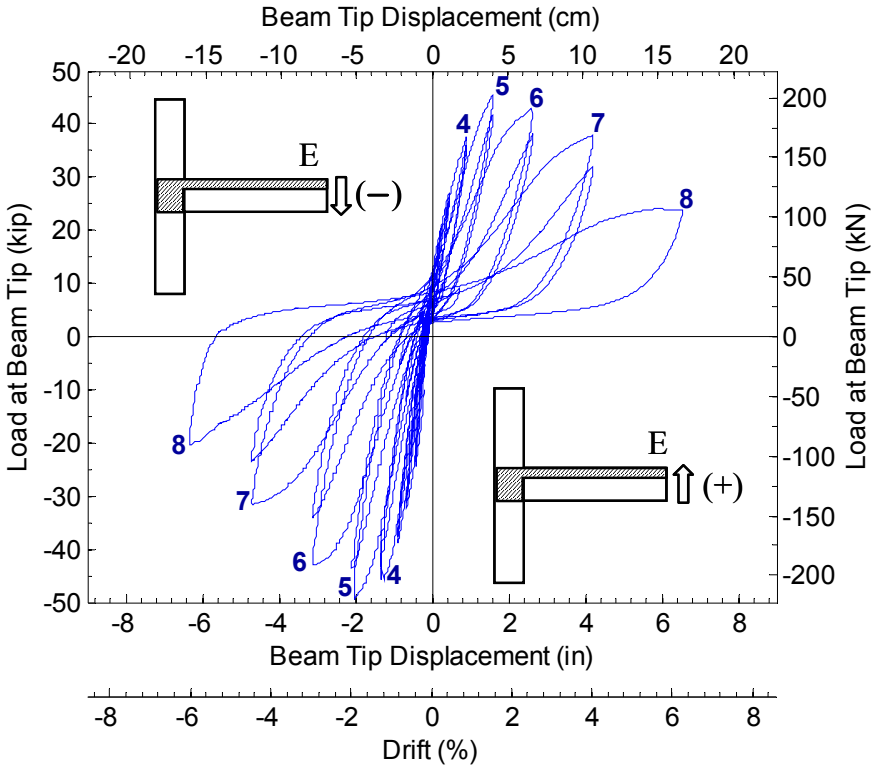

(a) EW direction

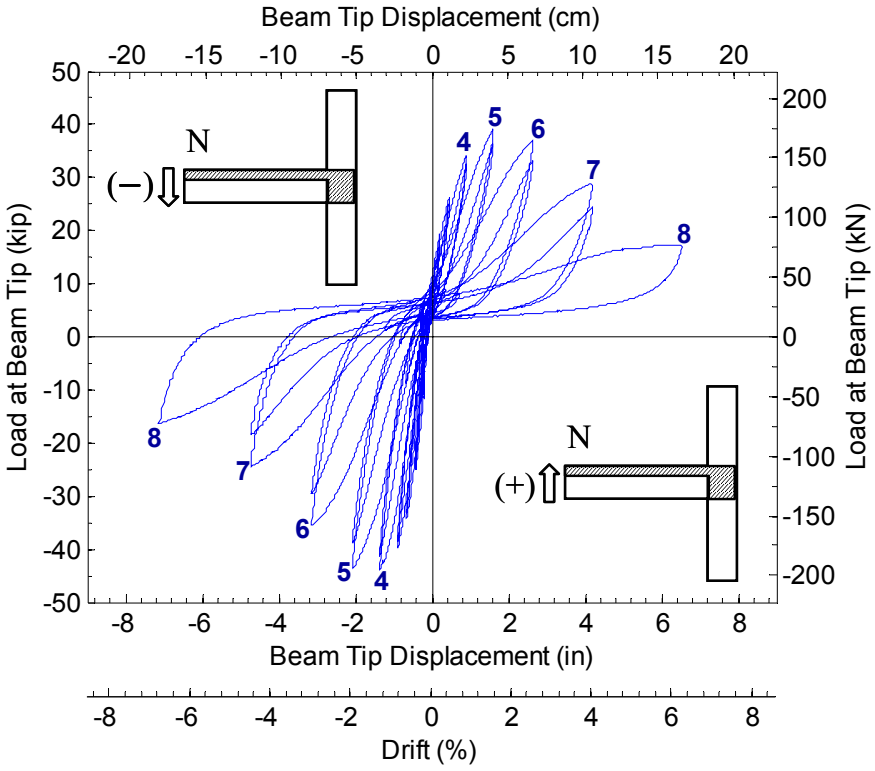

(b) NS direction

Figure V.46 Load versus drift response of SP4.

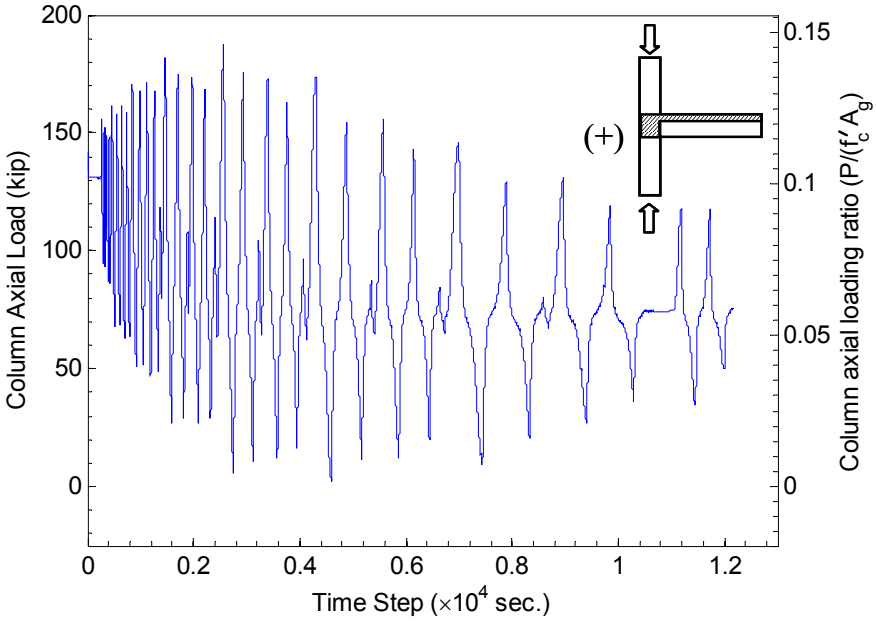

(a) Column Axial Load

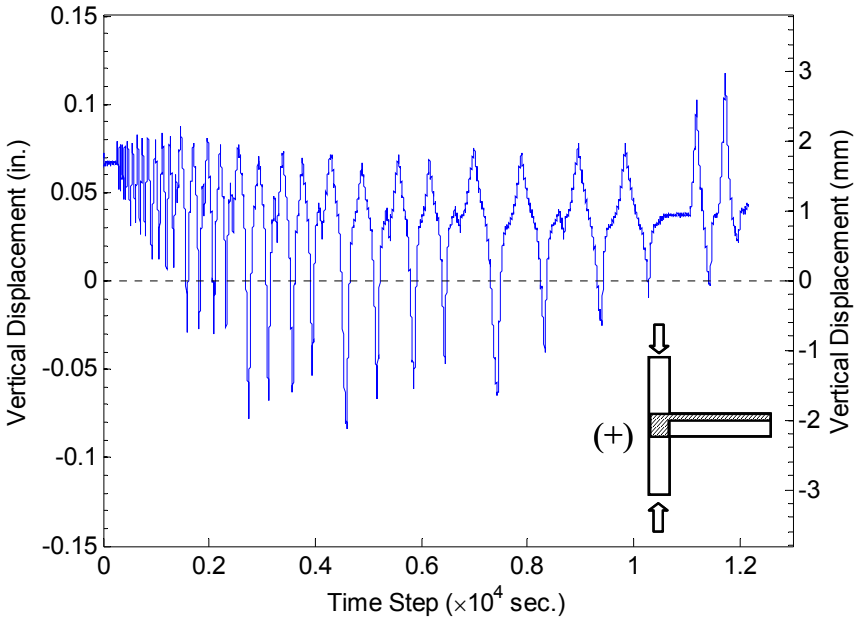

(b) Vertical Displacement

Figure V.47 Column response of SP4.

V-4.2 Observed Damage Progression

The qualitative damage progression of SP4 is summarized in Table V.11 and the photographs of the specimen taken during testing and at the end of the test are presented in Figures V.48 through V.52.

V-4.2.1 EW Direction

Joint Region

Multiple diagonal joint cracks developed and these cracks led to joint failure during the test. A first downward joint diagonal crack (↘) was observed at the first loading group, $\Delta_{EW} = -0.41\%$, and additional downward cracks appeared in the subsequent loading group. A first upward diagonal crack (↗) appeared at the middle of the joint width during the third loading group, $\Delta_{EW} = 0.42\%$, and thereafter additional upward cracks developed. Noticeable opening of the main downward diagonal crack was observed at the fourth loading group ($\Delta_{EW} = -1.28\%$), and other downward cracks widened showing similar width of main diagonal crack at the peak loading ($\Delta_{EW} = -1.94\%$). On the other hand, the existing upward diagonal crack exclusively widened up to the peak loading ($\Delta_{EW} = 1.52\%$), although additional minor upward cracks formed in the joint panel. It is worth mentioning that this pattern of crack propagations and width of cracks were remarkably similar to those observed in SP3, refer to Figures V.33(a) and (b) and Figures V.48(b) and (c). After the peak loading, the joint experienced severe damage by widening of the cracks and cover concrete spalling in the joint panel. Corner quadrant of joint concrete separated away and core concrete in the joint region crushed. Figure V.48 presents the progression of joint damage as the applied drift increased.

During the NS beam loading, the same observation was made that horizontal crack formed at the top of EW joint panel under the upward loading as observed in the other three specimens, Figure V.49(a). The top horizontal crack was located at the layer of beam top reinforcement. It was also found that concrete between existing joint cracks was bulging by the NS beam downward loading after the peak.

Beam and Slab

The first flexural crack initiated in the beam and slab during pre-loading, followed by splitting crack at the beam-joint interface under the downward loading at the first group. The beam and slab had more flexural cracks at top and bottom with the increase of applied beam tip displacement, but all these cracks were not quite visible, as shown in Figure V.48. There was no noticeable crack opening at the beam-joint interface up to the peak, which is confirmed by the instruments for rotation discussed in subsequent section. On the other hand, splitting crack along beam-slab interface continued to widen and dominated other flexural cracks in the slab. After the peak loading, the width of flexural cracks was reduced because of large opening of existing joint cracks, but the splitting crack at the beam-joint interface continued to widen. Based on the

damage of beams and slab, it was evident that the specimen lost its load-carrying capacity by joint failure without plastic hinge forming in the beam.

For the NS beam loading, it was observed that a pair of inclined cracks occurred in the beam, Figure V.49(a). Moreover, the beam-joint interface suffered significant splitting crack after the peak load. It is noted that this observations were similar to those observed in SP3. Figure V.50 shows the existing cracks in the beam and slab after test.

V-4.2.2 NS Direction

Joint Region

The joint panel in the NS direction followed similar crack pattern as shown in the EW direction. A first downward crack (↙) in the joint appeared in the second group, $\Delta_{NS} = -0.63\%$, while a first upward diagonal crack (↖) occurred during the fourth group, $\Delta_{NS} = 0.86\%$. Therefore, the first joint cracking in the NS direction took place at slightly larger drift level than in the EW direction. At the peak of downward loading, which was in the fourth loading group, $\Delta_{NS} = -1.29\%$, the existing downward diagonal crack width significantly increased with a new diagonal crack developing in parallel. At the fifth loading group ($\Delta_{NS} = -1.96\%$), the later developed downward diagonal crack showed a big opening. For the upward loading, a significant propagation of the existing upward diagonal crack took place at the peak loading, i.e. the fifth loading group where $\Delta_{NS} = 1.53\%$, accompanied by small additional inclined cracks. After the peak loading, joint diagonal cracks continued to widen further particularly around the location of the 90° hooks of the beam top and bottom bars. Joint cover concrete was finally splitting into several pieces along cracks and core concrete was also heavily damaged to the extent that the loose concrete pieces were detached by hand. Figure V.51 presents the progression of joint damage in the NS direction.

Under the EW beam loading, horizontal cracks developed at the top and bottom of the joint panel but top horizontal crack opening caused by the upward loading was more considerable than the bottom horizontal crack, Figure 49(b). After the peak, the EW beam loading caused further opening of the existing joint cracks.

Beam and Slab

The first flexural crack in the beam and slab was observed at the first loading group and beam-slab interface splitting crack initiated at the third loading group. Splitting crack at the beam-joint interface was not observed up to the peak load. Flexural cracks slightly propagated in the subsequent loading groups but the propagation was hard to recognize from the series of photographs. After the peak load, there was no further propagation of flexural and splitting cracks because joint crack propagation represented the main drift portion in the total responses. Torsional inclined cracks occurred during the EW beam downward loading and increase of their widths was observed after the peak load, Figure 49(b).

V-4.2.3 Summary

A first joint crack appeared in the EW joint panel around the drift level of 0.4%, while a first crack took place in the NS joint over the drift level of 0.6%. During the fourth group of loading ($\Delta_{down} = -1.29\%$; $\Delta_{up} = 0.86\%$), the first developed downward diagonal crack showed a significant propagation, but the upward diagonal crack remained minor. At the peak loading ($\Delta_{down} = -1.95\%$; $\Delta_{up} = 1.53\%$), the later developed downward cracks were opening as wide as the first downward diagonal crack propagated, while only the first upward diagonal crack showed a big opening, while minor multiple inclined cracks newly formed. Beyond the peak loading, the joint was severely damaged by spalling and crushing. Consequently, total drift was attributed to the joint rotation, which is shown in the subsequent section. The remarkable observation from the joint cracking was that the propagation pattern and width of the joint cracks were very similar for both SP3 and SP4 at the same drift level, compare Figures V.48 and V.51 with Figures V.33 and V.36.

For damage of the beam and slab, first flexural and splitting cracks developed during the pre-loading or the first group of loading, and these cracks continued to increase in widths up to the peak loading. However, these cracks were minor. In other words, the beam was intact at the end of test, except for a little damaged by torsion, Figure V.52.

During the orthogonal beam loading, typical crack pattern was observed. This crack pattern consisted of horizontal cracks in the joint panel and inclined cracks in the side of transverse beam. The horizontal cracks were induced during the orthogonal beam upward loading, while the inclined cracks were induced by the orthogonal beam downward loading. However, the joint shear strength and rotation in the longitudinal direction were not affected by these cracks.

Table V.11 Qualitative damage description of SP4.

Drift (%)	EW direction	NS direction
$\Delta_0 = -0.2$	- First flexural crack in beam	-
$\Delta_{up} = -0.02$ $\Delta_{down} = -0.41$	- First downward diagonal crack in joint - Splitting cracks at beam-joint and beam-slab interfaces	- First flexural crack in beam and slab
$\Delta_{up} = 0.21$ $\Delta_{down} = -0.63$	- Additional flexural cracks in beam and slab	- First downward diagonal crack in joint - Additional flexural cracks in beam and slab - Splitting cracks at beam-joint and beam-slab interfaces
$\Delta_{up} = 0.43$ $\Delta_{down} = -0.85$	- Second downward diagonal crack in joint - First upward diagonal crack in joint	- First upward diagonal crack in joint
$\Delta_{up} = 0.86$ $\Delta_{down} = -1.29$	- Large opening of the first downward diagonal crack in joint - Additional downward and upward diagonal cracks in joint	- Large opening of the first downward diagonal crack in joint - Additional downward and upward diagonal cracks in joint
$\Delta_{up} = 1.53$ $\Delta_{down} = -1.95$	- Large opening of the later developed downward diagonal cracks in joint - Large opening of the first upward diagonal crack in joint	- Large opening of the later developed downward diagonal cracks in joint - Large opening of the first upward diagonal crack in joint
$\Delta_{up} = 2.52$ $\Delta_{down} = -2.97$	- Spalling of joint cover concrete - Reduction of beam flexural cracks width	- Bulging of joint cover concrete with large opening of joint cracks - Reduction of beam flexural cracks width
$\Delta_{up} = 4.01$ $\Delta_{down} = -4.48$	- Crushing of joint core concrete	- Crushing of joint core concrete
$\Delta_{up} = 6.22$ $\Delta_{down} = -6.69$	- Straightening of beam bars anchorage tail	- Straightening of beam bars anchorage tail

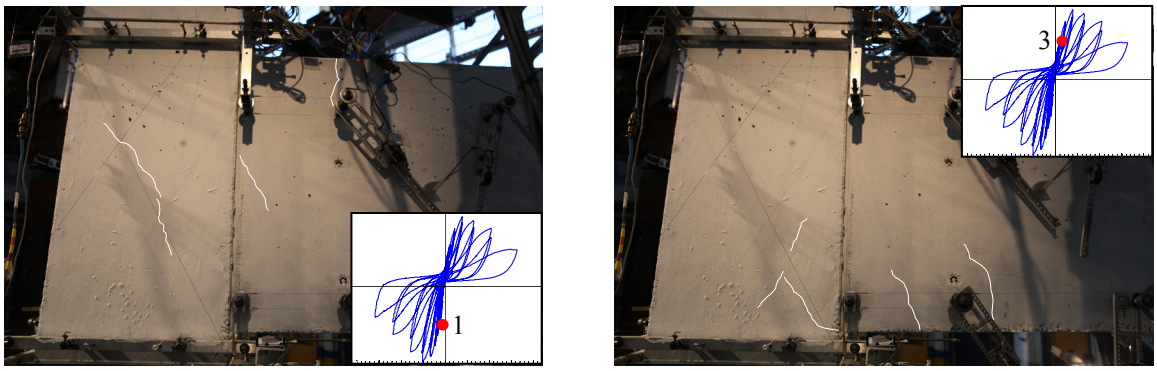

(a) First joint crack

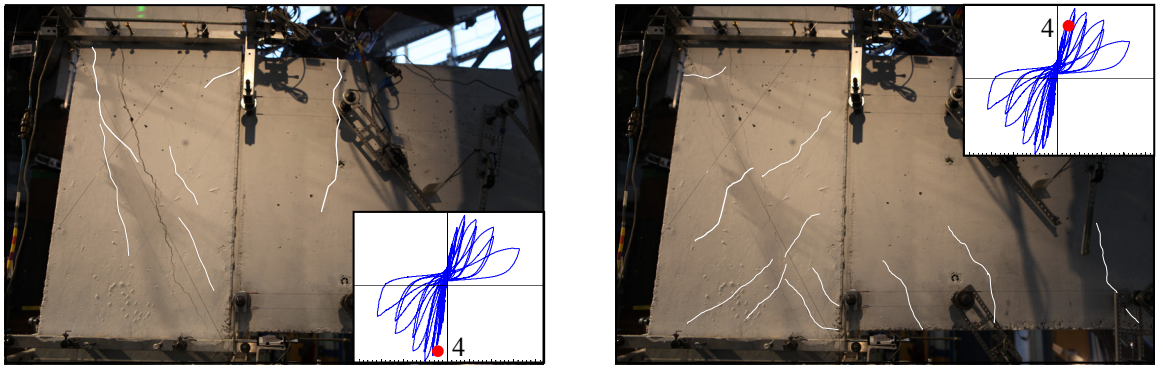

(b) Propagation of joint cracking

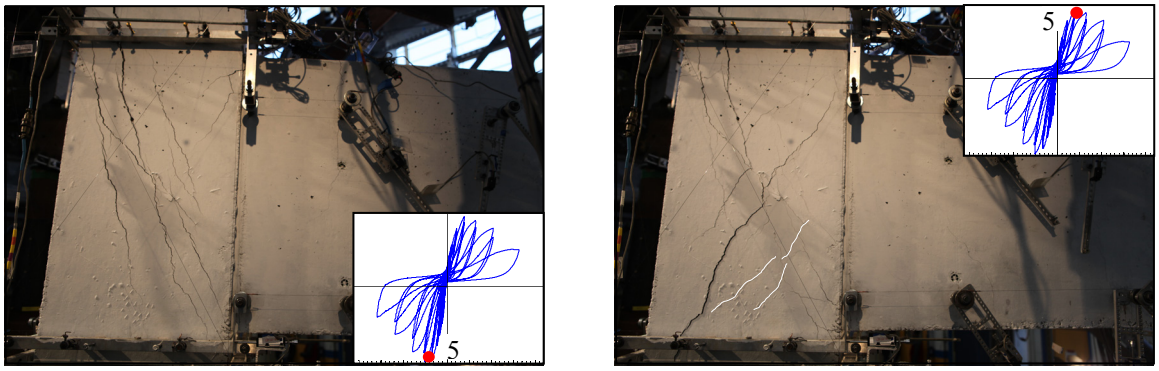

(c) Joint cracking before joint failure

(d) Joint damage at the end of test

Figure V.48 Damage progression of joint in EW direction, SP4.

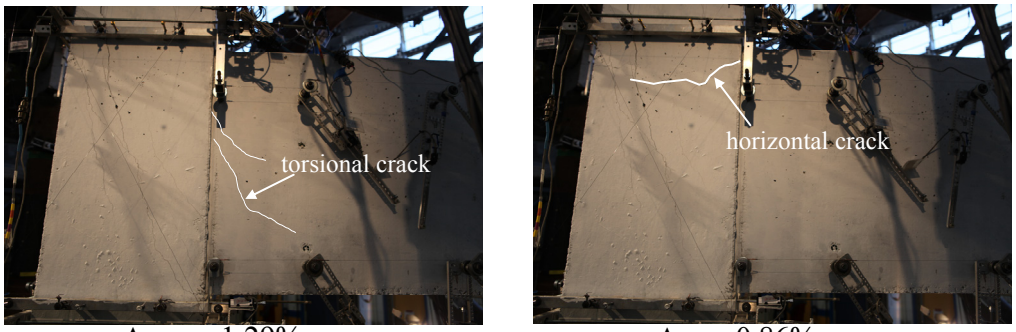

$\Delta_{NS} = -1.29\%$ $\Delta_{NS} = 0.86\%$

(a) Crack pattern in the EW joint and beam by NS beam loading

$\Delta_{EW} = -1.94\%$ $\Delta_{EW} = 1.52\%$

(b) Crack pattern in the NS joint and beam by EW beam loading

Figure V.49 Crack patterns under the orthogonal beam loading, SP4.

(a) Cracks in EW beam (b) Cracks in NS beam

(c) Cracks on slab

Figure V.50 Existing cracks after testing, SP4.

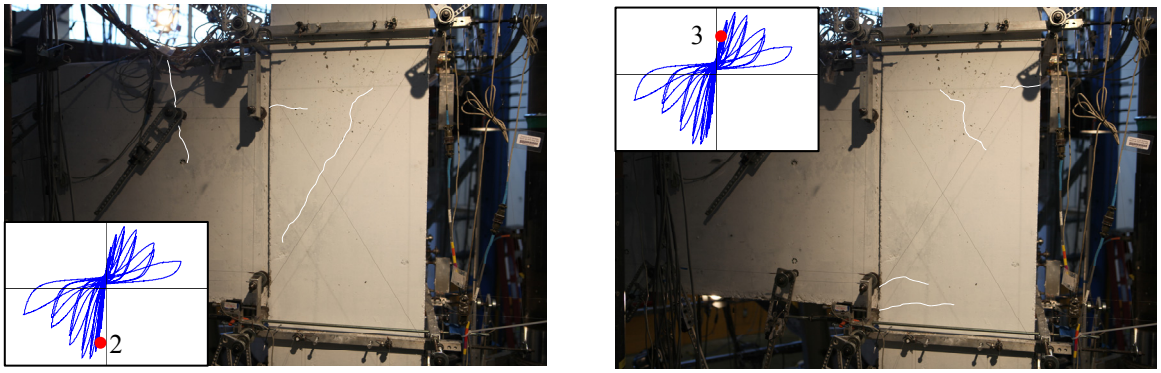

(a) First joint crack

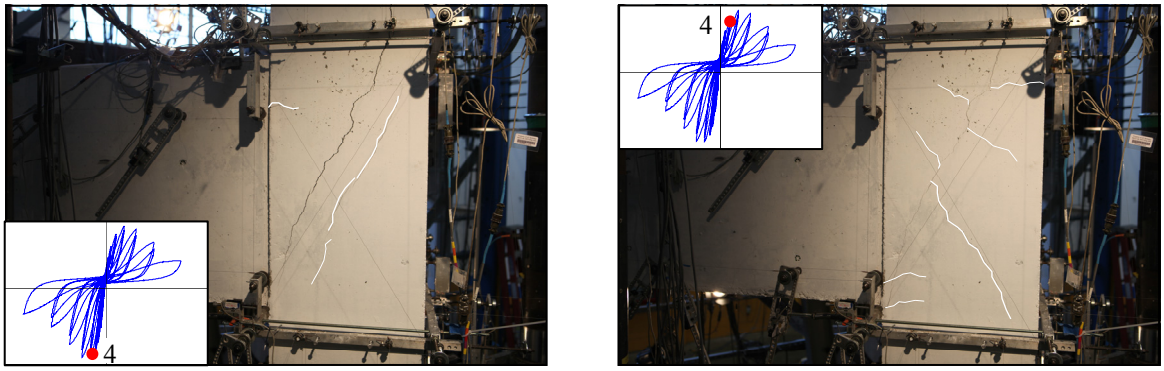

(b) Propagation of joint cracking

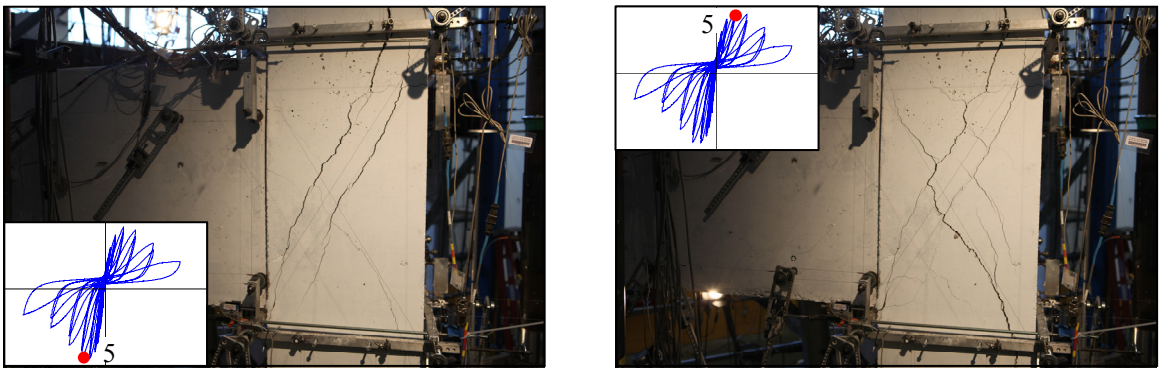

(c) Joint cracking before joint failure

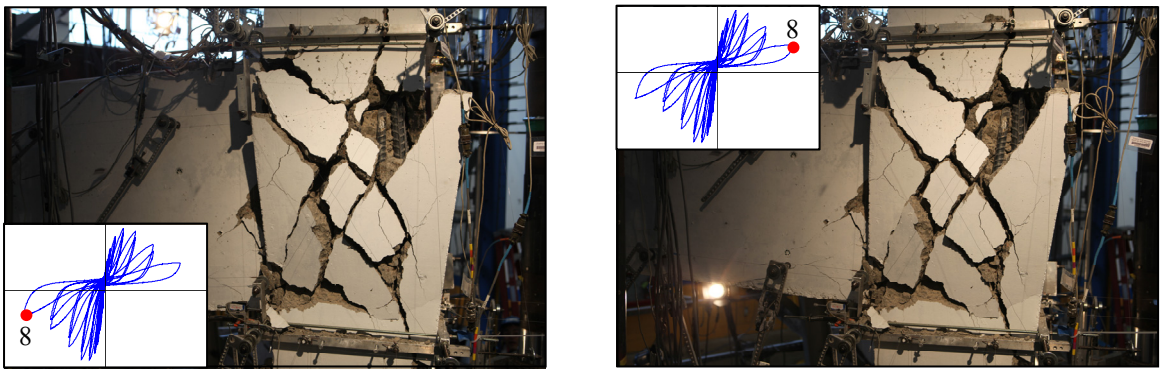

(d) Joint damage at the end of test

Figure V.51 Damage progression of joint in NS direction, SP4.

(a) Global view of specimen after testing

(b) Inside corner joint

(c) NS beam

(d) EW beam

Figure V.52 Failure of SP4 after removing concrete fragments.

V-4.3 Joint Shear Stress versus Rotation Response

The joint shear stress versus strain responses up to the sixth group of loading are shown in Table V.12 and Figure V.53. Since the yielding of beam top bars was not clearly observed from the strain data at the beam-joint interface, 0.875 times the beam effective depth was assumed to be a constant moment arm. Furthermore, it was assumed that there was no slab contribution to flexural strength based on the strain data of slab reinforcement. Accordingly, the effective depth was estimated from the beam cross-section only. The maximum joint shear stresses in the EW direction were 551 psi (3.80 MPa) for the downward loading and 471 psi (3.25 MPa) for upward loading; in the NS direction, they were 467 psi (3.22 MPa) for downward loading and 423 psi (2.92 MPa) for upward loading. The corresponding normalized joint shear stresses were 8.8 $psi^{0.5}$ (0.73 $MPa^{0.5}$) for the downward loading and 7.5 $psi^{0.5}$ (0.62 $MPa^{0.5}$) for the upward loading in the EW direction; 7.4 $psi^{0.5}$ (0.61 $MPa^{0.5}$) for the downward loading and 6.7 $psi^{0.5}$ (0.56 $MPa^{0.5}$) for the upward loading in the NS direction. These maximum normalized joint shear stresses were greater than the ASCE41 recommendation as indicated by dashed line in Figure V.53. To sum up the strength comparison between ASCE41 and the tested four specimens, the ASCE41 provisions is expected to underestimate the shear strength of unreinforced exterior and corner joints particularly having low ratio of beam depth to column depth.

The joint shear strains at the peak load were 0.0063 rad. for the downward loading and 0.0089 rad. for the upward loading in the EW beam. They were 0.0045 rad. for the downward loading and 0.0098 rad. for the upward loading in the NS beam. The rotations at the beam-joint interface and total joint rotations are presented in Figures V.54 and V.55, respectively. The total joint rotations at the peak load were 0.011 rad. for the downward loading and 0.012 rad. for the upward loading in the EW direction and they were 0.0081 rad. for the downward loading and 0.012 for the upward loading in the NS direction.

Comparison of the joint deformation between SP3 and SP4 shows that at the same drift levels, the two specimens had very similar joint shear strain and beam-joint interface rotation even after the peak, regardless of the different level of the joint shear stresses. It should be also emphasized that joint shear strains represented a significant portion of the joint total rotation in SP3 and SP4, while the joint total rotations were mostly due to the rotation at the beam-joint interface in the low aspect ratio specimens, SP1 and SP2. Table V.12 indicates that joint rotation had a significant contribution to the total drift in SP4 and this contribution increased by more than about 50% from the fourth group of loading.

Table V.12 Joint response of SP4.

Dir.	EW											
Group No.	Downward						Upward					
	v_{jh} (psi)	γ (psi$^{0.5}$)	Δ (rad)	γ_{xy} (rad)	θ_j (rad)	θ_j/Δ	v_{jh} (psi)	γ (psi$^{0.5}$)	Δ (rad)	γ_{xy} (rad)	θ_j (rad)	θ_j/Δ
1	274	4.3	0.0041	-	-	-	98	1.6	0.00	-	-	-
2	359	5.7	0.0062	0.0013	0.0027	0.44	210	3.3	0.0021	0.00	0.0003	0.14
3	434	6.9	0.0085	0.0019	0.0040	0.47	280	4.4	0.0042	0.0007	0.0013	0.31
4	512	8.1	0.0128	0.0029	0.0059	0.46	388	6.2	0.0086	0.0034	0.0055	0.64
5	551[#2]	8.8	0.0194	0.0063	0.011	0.57	471[*1#2]	7.5	0.0152	0.0089	0.012	0.79
6	480	7.6	0.0296	0.012	0.019	0.64	444	7.1	0.0251	0.023	0.028	>1.0
7	353	5.6	0.0446	0.024	0.035	0.78	391	6.2	0.0401	0.036	0.043	>1.0
8	228	3.6	0.0658	-	-	-	245	3.9	0.0623	-	-	-
Dir.	NS											
Group No.	Downward						Upward					
	v_{jh} (psi)	γ (psi$^{0.5}$)	Δ (rad)	γ_{xy} (rad)	θ_j (rad)	θ_j/Δ	v_{jh} (psi)	γ (psi$^{0.5}$)	Δ (rad)	γ_{xy} (rad)	θ_j (rad)	θ_j/Δ
1	269	4.3	0.0041	-	-	-	96	1.5	0.00	-	-	-
2	366	5.8	0.0063	0.0008	0.0025	0.40	208	3.3	0.0020	0.0005	0.0006	0.30
3	425	6.7	0.0084	0.0015	0.0043	0.51	283	4.5	0.0043	0.0013	0.0017	0.40
4	467[#2]	7.4	0.0129	0.0045	0.0081	0.63	370	5.9	0.0086	0.0038	0.0051	0.59
5	465	7.4	0.0196	0.0010	0.015	0.77	423[*1#2]	6.7	0.0153	0.0098	0.012	0.78
6	379	6.0	0.0298	0.022	0.029	0.97	400	6.4	0.0252	0.018	0.022	0.87
7	259	4.1	0.0449	0.043	0.054	>1.0	312	5.0	0.0400	0.028	0.031	0.78
8	101	1.6	0.0679	-	-	-	186	2.9	0.0620	-	-	-

[*1] first yielding of beam reinforcement; [#2] peak loading.

Note: 1 psi = 0.0069 MPa; $1.0\sqrt{f_c'}$ psi$^{0.5}$ = $0.083\sqrt{f_c'}$ MPa$^{0.5}$.

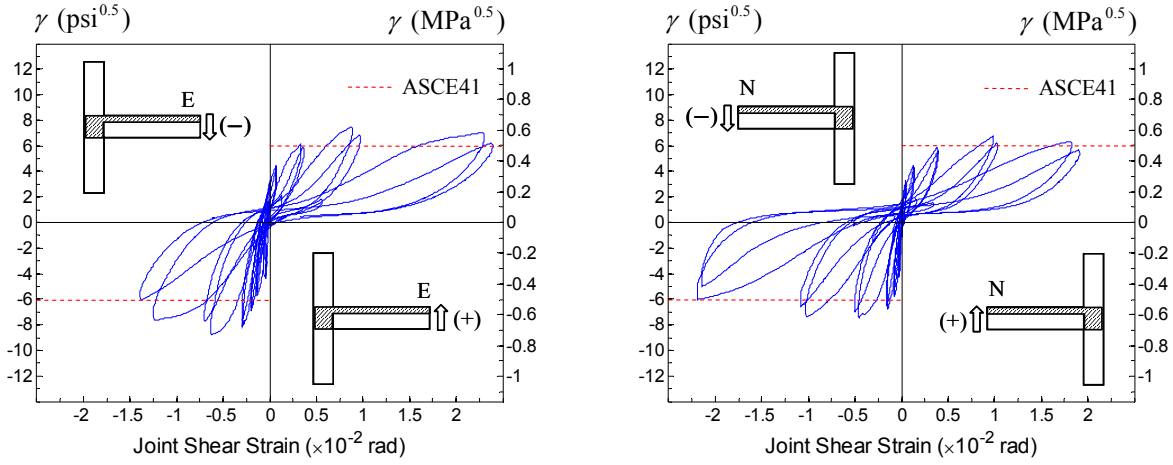

(a) EW direction (b) NS direction

Figure V.53 Joint shear stress versus strain response of SP4.

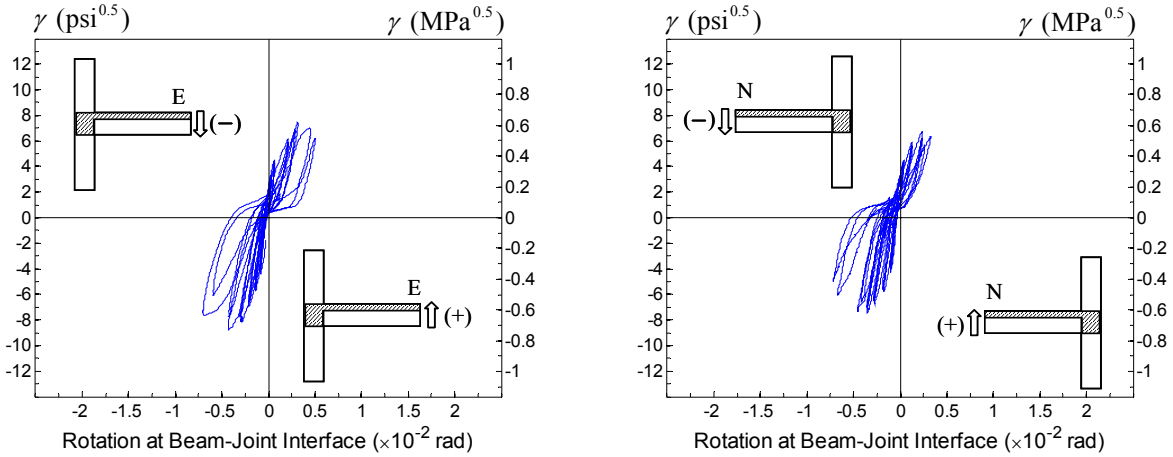

(a) EW direction (b) NS direction

Figure V.54 Joint shear stress versus rotation at beam-joint interface of SP4.

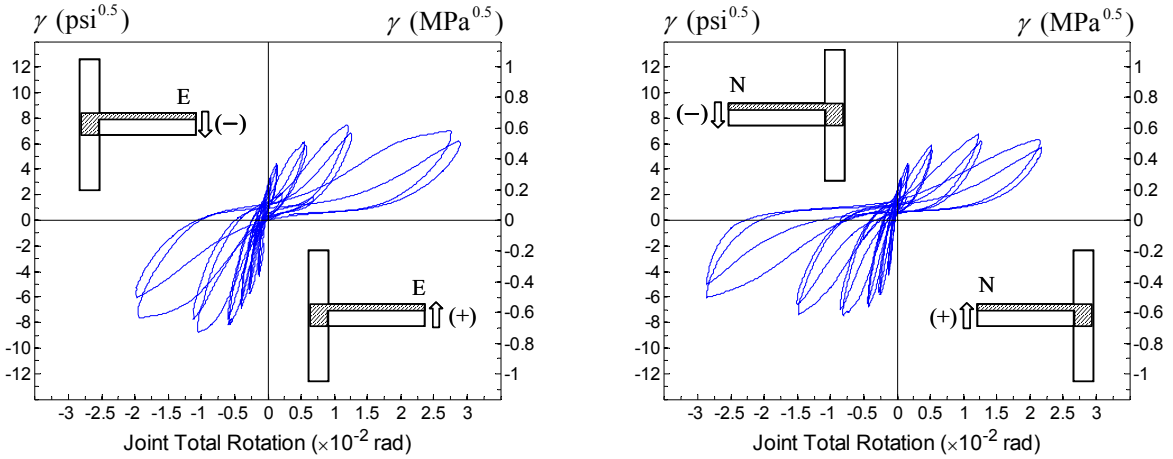

(a) EW direction (b) NS direction

Figure V.55 Joint shear stress versus total rotation of SP4.

V-4.4 Strain Measurements

V-4.4.1 Beam Reinforcement

The strain measurements of the beam longitudinal bars in the EW and NS directions are shown in Figures V.56 and V.57. The strain data of both EW and NS beam longitudinal bars measured at the beam-joint interface using gages number 3 were slightly less than the yield strain until the peak loading, i.e. fifth group of loading, except for the internal layer of the EW and NS beam bottom bars which barely reached the yield strain. In some cases, the beam longitudinal bars yielded at the inner side of the joint, i.e. at gages number 2. However, this yielding did not represent the beams flexural yielding because it occurred at the sixth loading group which was after the peak loading. Instead, the damage of joint panel and the consequent bond deterioration might have caused this yielding.

V-4.4.2 Slab Reinforcement

The strain variations of the slab reinforcing bars at the beam-slab interface in the EW and NS directions are presented in Figure V.58. The measured strain data of slab reinforcement showed that these bars did not yield during testing of SP4. The first gage on the EW slab top reinforcement did not function and the second gage was also damaged at the fifth loading group which was the peak of the EW beam loading and thus no strain data were available around the peak load. However, their strains were expected to be less or conservatively close to the yield strain considering the strain value of the internal layer of the beam top reinforcement, Figure V.56(b), which was closest to the first gage of slab top reinforcement. Since the strains of slab reinforcement were less than its yield strain, no slab reinforcement was taken into account for estimating the effective beam depth.

V-4.4.3 Column Reinforcement

The strain results of the column longitudinal reinforcement are presented from Figures V.59 and V.60. As the column was designed to be elastic, the strains of all the column reinforcing bars were less than the yield strain until the peak loading. The strain distribution of longitudinal column intermediate bars was measured over the height in the joint region. The tensile strain at the mid-height was greater than the strains at the top and bottom gages in the joint panel but this strain remained at small value, i.e. less than half the yield strain. Therefore, it was expected that the column intermediate reinforcing bars did not act as a tension tie in the joint.

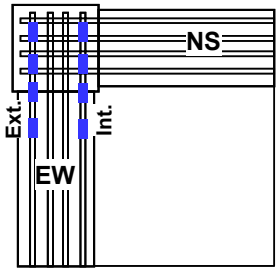

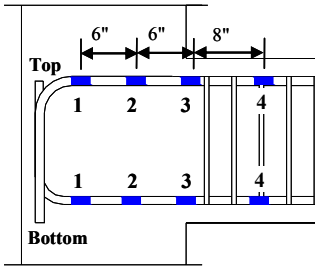

Note: 1" = 25.4 mm

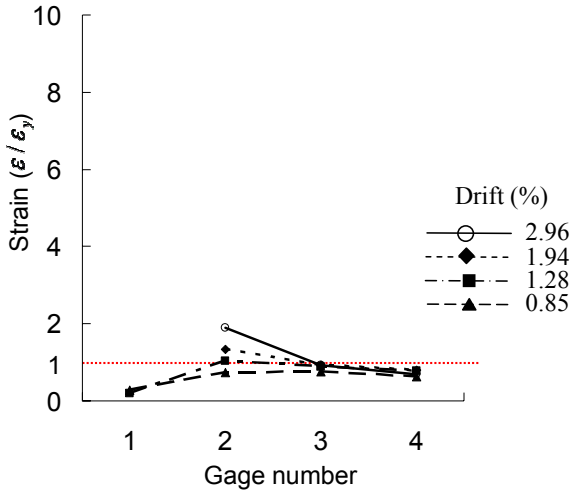

(a) EW-Top-Ext.

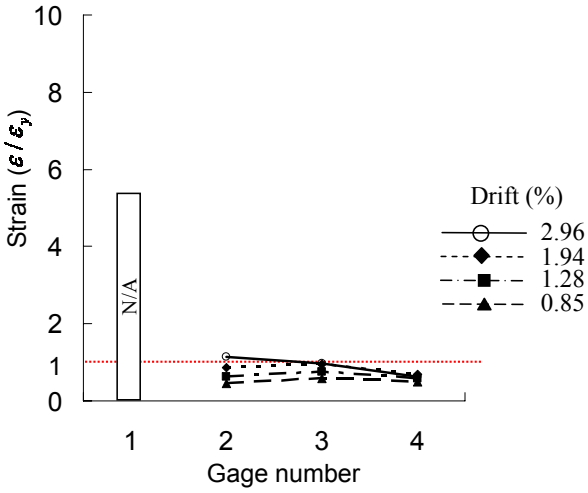

(b) EW-Top-Int.

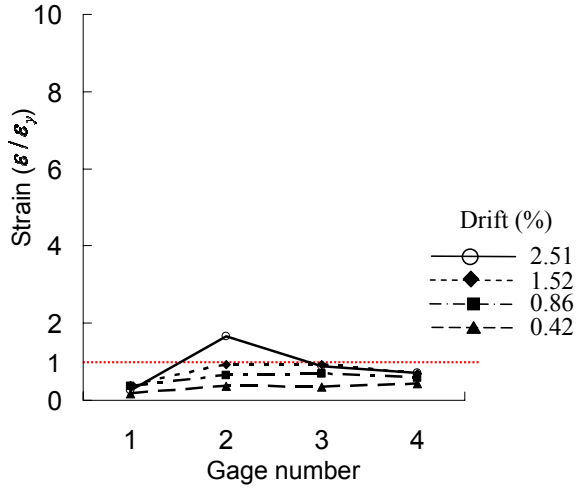

(c) EW-Bottom-Ext.

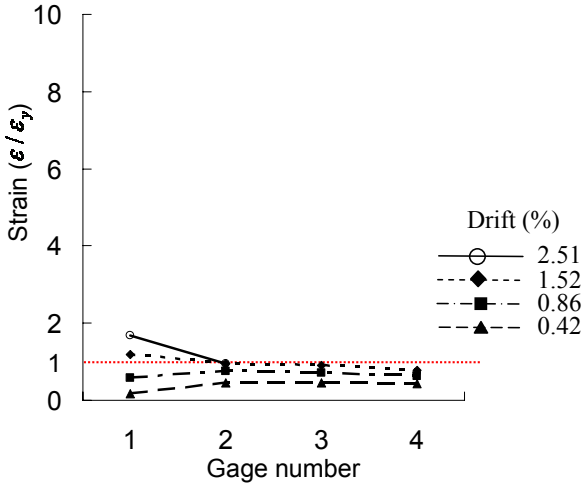

(d) EW-Bottom-Int.

Figure V.56 Strains of the EW beam reinforcing bars of SP4.

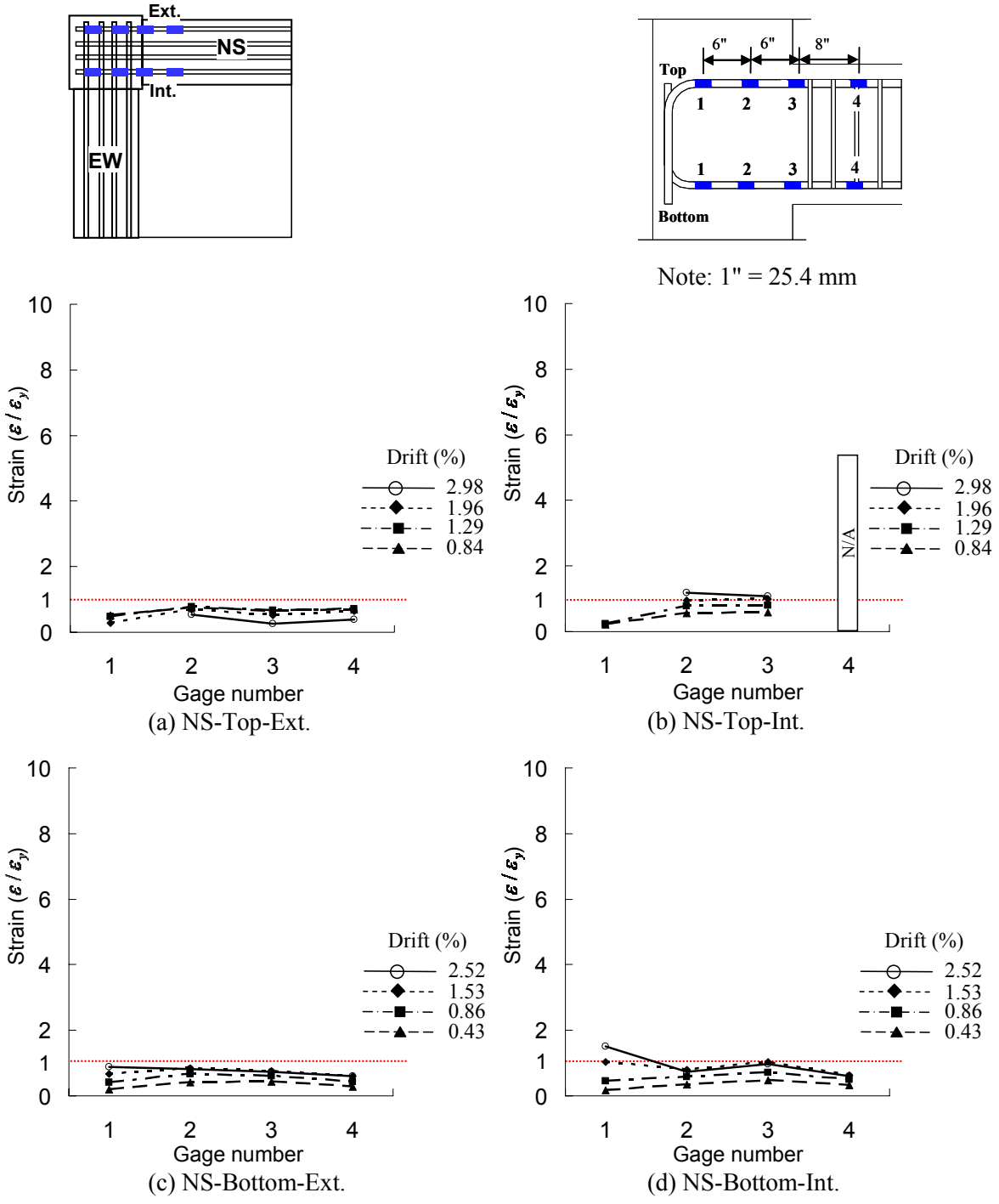

Figure V.57 Strains of the NS beam reinforcing bars of SP4.

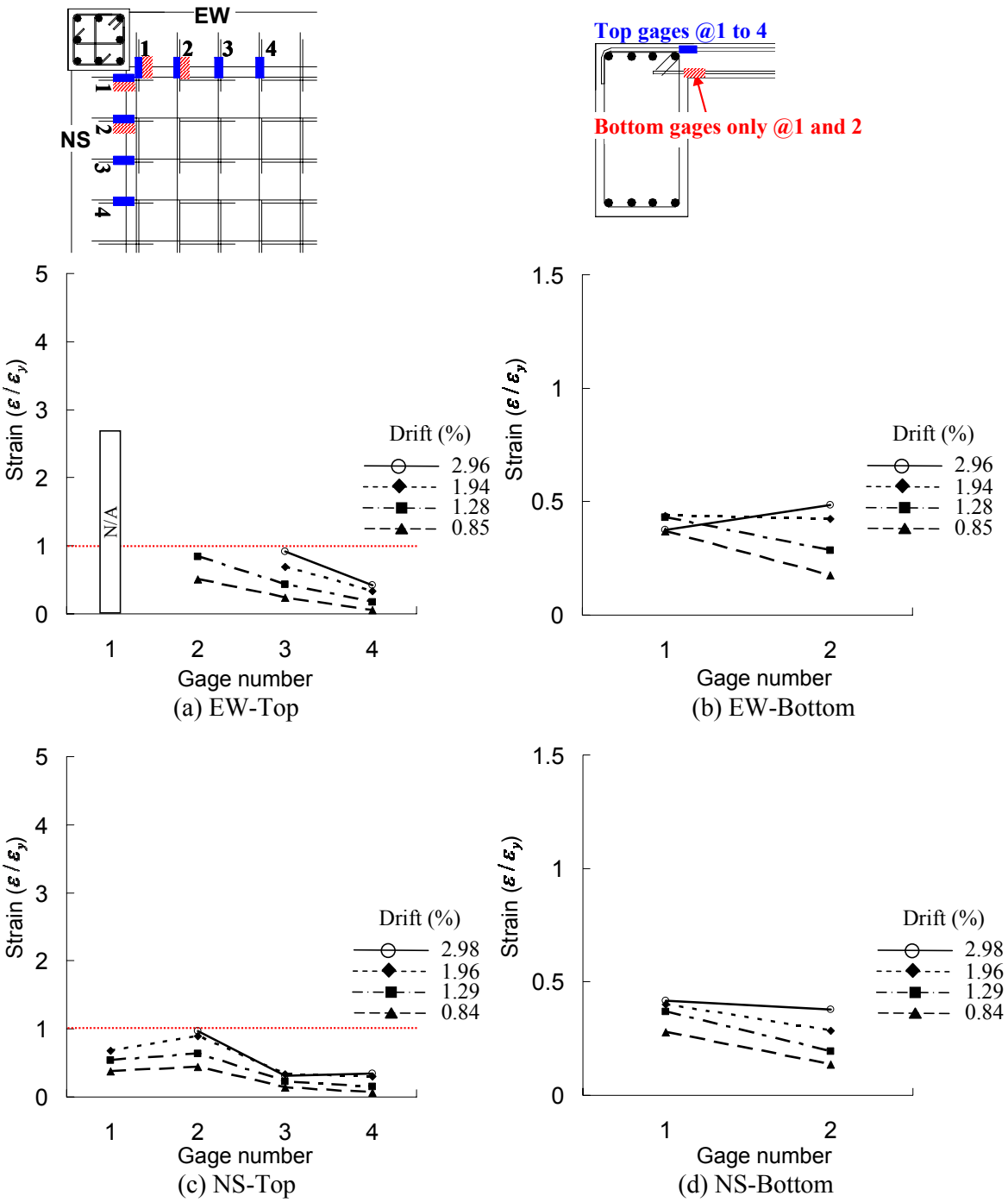

Figure V.58 Strains of the slab reinforcing bars of SP4.

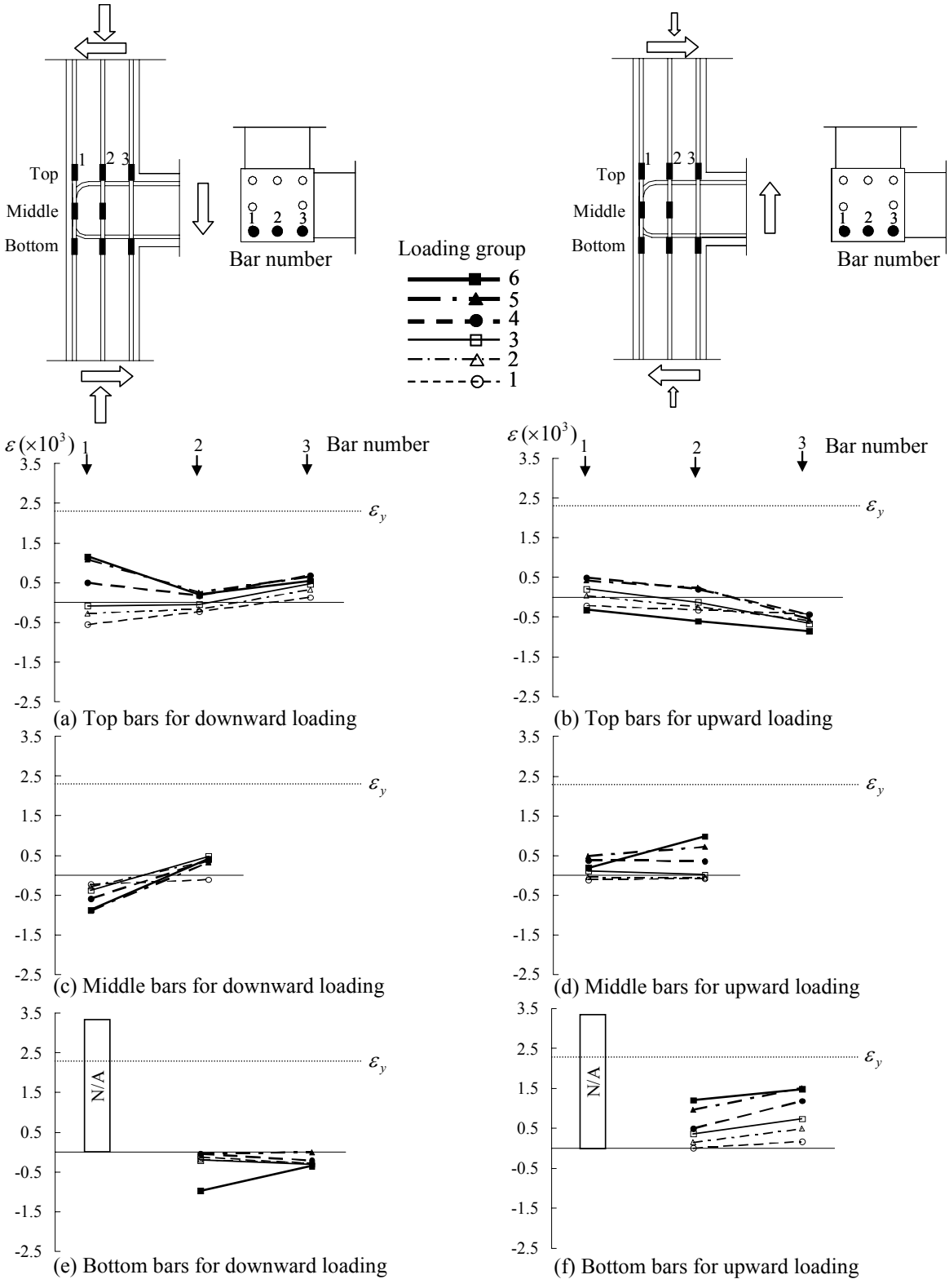

Figure V.59 Strains of the column reinforcing bars for the EW beam loading, SP4.

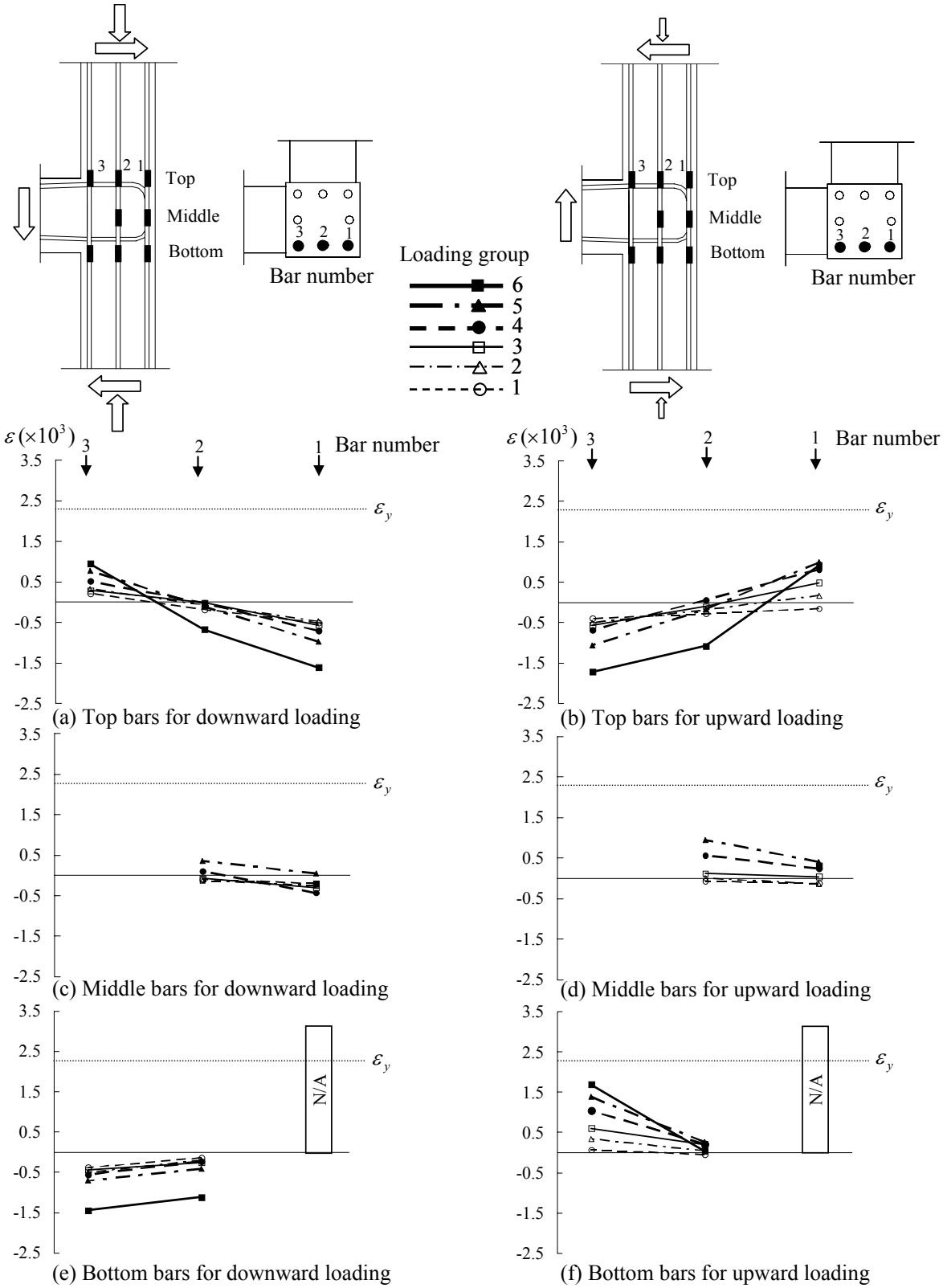

Figure V.60 Strains of the column reinforcing bars for the NS beam loading, SP4.

VI Discussion of Experimental Results

VI-1 Evaluation of Joint Shear Strength

For comparison of the test results among the four specimens, joint shear strength of each specimen is evaluated at three following critical events of the response. First, the peak load is important to represent the joint shear strength of each specimen. In this study, joint shear strength is defined as the maximum joint shear force, i.e. $V_{jh,\max} = \gamma_{\max} b_j h_c \sqrt{f_c'}$. As the second and third critical events, it is valuable to assess the joint shear stress at the onset of first cracking in the joint and at yielding of the beam longitudinal bars, if these bars yielded, for developing a backbone relationship for joint macro-model. The normalized joint shear stresses for those three events are presented in Table VI.1. For each specimen, the normalized joint shear stresses are separately evaluated for each of the EW and NS beam downward and upward loading. It is noted that the reported values for first cracking in the joint and peak loading in the beams corresponds the first peak of the cyclic loading group when these events were observed, while the values for first beam reinforcement yielding are determined from the beam loads when the strain of beam longitudinal bars reached their yield strain by tracing the strain gage data.

According to the results presented in Table VI.1, the joint shear stresses of first joint cracking and beam reinforcement yielding are similar for both EW and NS directions but those at the peak loads are generally greater in EW direction because the EW beam loading preceded the NS beam loading. Therefore, special attention is given to the joint shear stresses in EW direction.

Table VI.1 Evaluation of normalized joint shear stress, γ (psi$^{0.5}$).

Observation	SP1				SP2			
	EW		NS		EW		NS	
	Down	Up	Down	Up	Down	Up	Down	Up
First crack	5.6	6.6	7.2	6.9	8.0	7.9	10.4	7.8
First yield	6.7	7.5		7.5	12.2	9.1	**12.4**	9.4
Peak	**8.5**	**8.5**	**7.9**	**8.1**	**12.7**	**10.0**		**9.7**
Observation	SP3				SP4			
	EW		NS		EW		NS	
	Down	Up	Down	Up	Down	Up	Down	Up
First crack	-*	-*	4.3	3.5	4.3	4.4	5.8	4.5
First yield	6.7	6.2	6.0	No yield	No yield	**7.5**	No yield	**6.7**
Peak	**7.1**	**6.3**	**6.3**	**5.9**	**8.8**		**7.4**	

* A cracking was not detected because of inappropriate camera installation.

VI-2 Comparison of Test Results with Model Predictions

The shear strengths of the four specimens are compared with predictions using the semi-empirical and analytical models proposed in Chapter III. As summarized in Table VI.2, the two proposed models accurately predict the shear strengths with 2% and 8% errors, respectively. If the joint shear strengths are compared only for the EW direction because lower strengths are generally obtained in the NS direction due to the loading sequence, the accuracy of the semi-empirical model is maintained but the analytical model underestimates the joint shear strength by 12%. This underestimation comes from the predictions of SP2 and SP4 where relatively larger diameter bars were used.

The analytical model is improved by the subsequent modifications to resolve its underestimation for the case of beams having longitudinal bars with large diameters. The fraction factor derived in Chapter III is dependent on the diameter of beam longitudinal bar such that a large diameter of bar increases the values of fraction factor α_1 and α_2 without limitation. To limit the effect of the bar diameter in the fraction factor, each of the values α_1 and α_2 is bounded by an upper limit determined with the aid of the semi-empirical model. In the semi-empirical model, the maximum and minimum of the joint shear strength are proposed as $a_2 \cos\theta / [1.31 + 0.085 h_b / h_c]$ with a_2= 23 for maximum and a_2= 10 for minimum in psi units, refer to Equation III.7. On the other hand, the capacity of the diagonal strut ST1 is estimated as a_2= 8.3 (Equation III.27) in the analytical model. The fraction factor α_1 represents the maximum fraction factor for the case of joint failure at the onset of beam longitudinal bars yielding and the fraction factor α_2 is the fraction factor corresponding to the case of joint failure with significant strain hardening of beam longitudinal bars after yielding. Therefore, the fraction factor α_1 can be limited to 0.36 which is the ratio of ST1 capacity to the maximum joint shear strength, i.e. 8.3/23, while the fraction factor α_2 can be limited to 0.83 which is the ratio of ST1 capacity to the minimum joint shear strength, i.e. 8.3/10. Adopting this modification, Equations (VI.1) and (VI.2) for fraction factors α_1 and α_2 are rewritten as follows:

$$\alpha_1 = \frac{H}{H - 0.85h_b}\left(1 - \frac{4}{\phi_b}\frac{\mu_E}{f_y} l_h\right) \le 0.36 \qquad \text{(VI.1)}$$

$$\alpha_2 = \frac{H}{H - 0.85h_b}\left(1 - \frac{4}{\phi_b}\frac{\mu_Y}{f_y + \frac{4}{\phi_b}\mu_Y l_h} l_h\right) \le 0.83 \qquad \text{(VI.2)}$$

The joint shear strengths for the four specimens using the modified analytical model are re-evaluated in Table VI.3. The accuracy of the analytical model is improved from 8% underestimation error to 1% overestimation error by applying these limits to the fraction factors.

Table VI.2 Comparison of test results with predictions by the proposed models.

Specimen	Joint Face	Loading direction	γ_{test} (psi$^{0.5}$)	Semi-Empirical		Analytical	
				$\gamma_{emp.}$ (psi$^{0.5}$)	$\gamma_{test}/\gamma_{emp.}$	$\gamma_{anal.}$ (psi$^{0.5}$)	$\gamma_{test}/\gamma_{anal.}$
SP1	EW	Down	8.5	8.6	0.99	8.5	1.00
		Up	8.5	7.8	1.08	7.3	1.18
	NS	Down	7.9	8.6	0.92	8.5	0.93
		Up	8.1	7.8	1.03	7.3	1.11
SP2	EW	Down	12.7	11.7	1.10	10.0	1.28
		Up	10.0	9.5	1.06	8.4	1.20
	NS	Down	12.4	11.7	1.10	10.0	1.28
		Up	9.7	9.5	1.06	8.4	1.16
SP3	EW	Down	7.1	7.3	0.97	6.5	1.09
		Up	6.3	6.8	0.93	6.0	1.05
	NS	Down	6.3	7.3	0.85	6.5	0.95
		Up	5.9	6.8	0.86	6.0	0.97
SP4	EW	Down	8.8	8.2	1.08	7.8	1.12
		Up	7.5	7.7	0.97	6.8	1.10
	NS	Down	7.4	8.2	0.91	7.8	0.95
		Up	6.7	7.7	0.87	6.8	0.99
Both EW and NS directions				Mean	0.98	Mean	1.08
				COV	0.08	COV	0.13
Only for EW direction				Mean	1.02	Mean	1.12
				COV	0.07	COV	0.14

Table VI.3 Shear strength predictions of tested specimens by modified analytical model.

Specimen	Joint Face	Loading direction	γ_{test} (psi$^{0.5}$)	$\gamma_{mod.}$ (psi$^{0.5}$)	$\gamma_{test}/\gamma_{mod.}$
SP1	EW	Down	8.5	8.9	0.95
		Up	8.5	7.6	1.12
	NS	Down	7.9	8.9	0.89
		Up	8.1	7.6	1.07
SP2	EW	Down	12.8	12.0	1.07
		Up	10.0	9.1	1.10
	NS	Down	12.8	12.0	1.07
		Up	9.7	9.1	1.07
SP3	EW	Down	7.2	7.2	1.00
		Up	6.3	6.5	0.96
	NS	Down	6.3	7.2	0.87
		Up	5.7	6.5	0.89
SP4	EW	Down	8.8	8.4	1.04
		Up	7.5	7.6	0.98
	NS	Down	7.4	8.4	0.88
		Up	6.7	7.6	0.88
Both EW and NS directions				Mean	0.99
				COV	0.08
Only for EW direction				Mean	1.03
				COV	0.07

VI-3 Effect of Joint Aspect Ratio

The joint shear strengths of the tested specimens are plotted against the corresponding joint aspect ratio together with the literature test data points to further investigate the consistency of the joint aspect ratio effect, as shown in Figure VI.1. The joint aspect ratio, h_b/h_c , of specimens SP1 and SP2 correspond to 1.00 on the horizontal axis the abscissa, while that of specimens SP3 and SP4 correspond to 1.67.

For specimens SP1 and SP2 having joint aspect ratio of $h_b/h_c = 1.00$, the joint shear strength ranges from 12.8 $\text{psi}^{0.5}$ (1.06 $\text{MPa}^{0.5}$) to 7.9 $\text{psi}^{0.5}$ (0.66 $\text{MPa}^{0.5}$). The maximum shear strength is achieved for downward loading in SP2 and the minimum shear strength is achieved during upward loading in SP1. For specimens SP3 and SP4 of $h_b/h_c = 1.67$, the joint shear strength ranges from 8.8 $\text{psi}^{0.5}$ (0.73 $\text{MPa}^{0.5}$) to 5.7 $\text{psi}^{0.5}$ (0.47 $\text{MPa}^{0.5}$). The maximum shear strength is achieved for downward loading in SP4 and the minimum shear strength is achieved for upward loading in SP3.

Recalling the beam reinforcement details illustrated in Chapter IV, specimens SP1 and SP3 have 4-#6 (D19) bars in their beams, while SP2 and SP4 have 4-#8 (D25) bars at top and 4-#7 (D22) bars at bottom of the beams. Slab reinforcements are identical in all the tested four specimens. Considering the beam and slab reinforcement details for the two pairs of specimens, i.e. SP1 & SP3 and SP2 & SP4, it is obvious that the reduction of joint shear strength form SP1 to SP3 and from SP2 to SP4 is attributed to the increase of the joint aspect ratio from 1.00 to 1.67. In addition, the maximum values of test results are slightly exceeding the proposed upper limit which is also drawn in Figure VI.1 where the upper limits are 11.7 $\text{psi}^{0.5}$ (0.97 $\text{MPa}^{0.5}$) for $h_b/h_c = 1.00$ and 8.2 $\text{psi}^{0.5}$ (0.68 $\text{MPa}^{0.5}$) for $h_b/h_c = 1.67$.

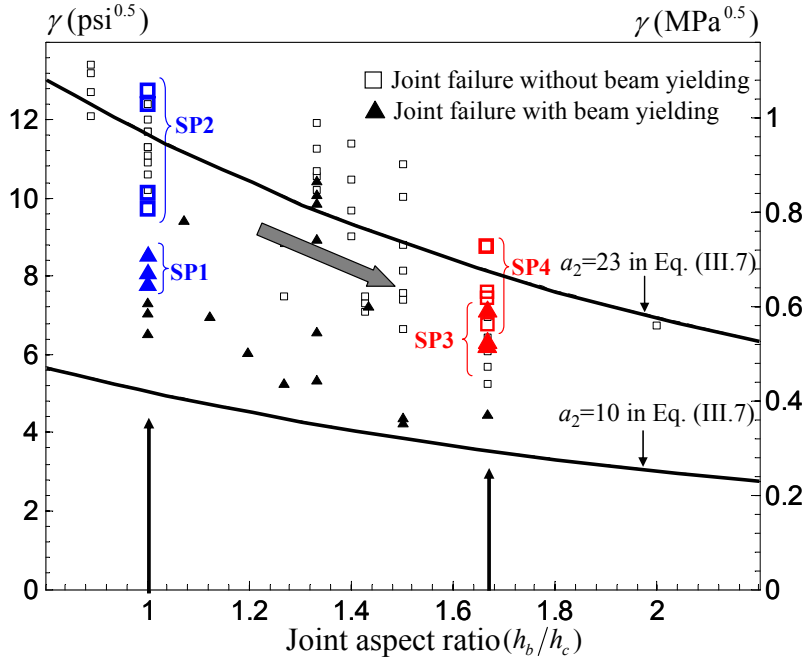

Figure VI.1 Test results of normalized joint shear strength versus the joint aspect ratio.

VI-4 Effect of Beam Longitudinal Reinforcement

The effect of beam longitudinal reinforcement is investigated focusing on the change of joint shear strength and the level of yield propagation into the joint. The joint shear strengths for the four tested specimens are plotted in Figure VI.2 against the corresponding beam reinforcement index which is presented in Chapter III. As shown in Figure VI.2, the joint shear strengths clearly increased from lower reinforcement ratio specimens to higher reinforcement ratio specimens, i.e. from SP1 to SP2 for the joint aspect ratio of $h_b/h_c = 1.00$ and from SP3 to SP4 for the joint aspect ratio of $h_b/h_c = 1.67$. This result can provide strong evidence that the joint shear strength is proportional to the beam reinforcement index up to a certain limit. The upper limit is proposed in the Chapter III and it will be clarified by the ongoing tests having larger beam longitudinal reinforcement ratio than that provided in SP2 and SP4.

The calculated beam reinforcement indices are compared with the joint shear stresses measured at yielding of the beam longitudinal bars in Table VI.4. The beam reinforcement indices for negative bending, i.e. slab in tension, are separately calculated with and without consideration of slab reinforcement contribution. The amount of slab reinforcement is determined based on the strain data when the beam longitudinal bars were yielding. As a result, slab top two reinforcing bars are included to calculate the beam reinforcement indices of SP1, SP2 and SP3 but no slab reinforcing bar is used for SP4. It is noted that the beam reinforcement index equation, $\left(A_s f_y / b_j h_c \sqrt{f_c'}\right)\left(1 - 0.85\, h_b/H\right)$, is independent of the shape of beam cross-section such as T-shape and L-shape because the cross-sectional height, h_b, is the same for rectangular and other two shapes of beam cross-section. Therefore, when the slab reinforcement is considered, total sectional area of the considered slab reinforcement is added to those of beam longitudinal bars in tension, A_s, while the sectional area of the bottom longitudinal bars only is included in A_s in the beam reinforcement index for positive bending, i.e. slab in compression. The beam reinforcement indices are shown to strongly correlate to the prediction of the normalized joint shear stress at yielding of beam longitudinal bars ($\gamma_{test@yield}$) during testing, as shown in Table VI.4, particularly if the contribution of slab reinforcement is taken into consideration except for SP1. It is noted that the presented normalized joint shear stresses correspond to the values for the EW direction in each of the four tested specimens. Due to the accurate prediction of joint shear stresses using the beam reinforcement index at the onset of beam reinforcement yielding, the semi-empirical model previously shows good correlation with the shear strengths of the four tested specimens.

The strain values of the beam longitudinal bars in the specimens having relatively less beam reinforcement, i.e. SP1 and SP3, are greater than those of the counterpart specimens, i.e. SP2 and SP4. Thus, the yielding of the beam longitudinal bars propagated further into the joint in specimens SP1 and SP3. The strain values of SP1 and SP2 are compared in Figure VI.3. The yield propagation of the beam longitudinal bars lead to slippage at the beam-joint interface due to bond strength deterioration. Consequently, it is expected that the contribution of the diagonal strut ST1 to joint shear resistance is greater in SP1 and SP3 than that of ST1 in SP2 and SP4, respectively. This behavior can be confirmed by significant opening of beam-joint interface

crack and joint diagonal crack in SP1 and SP3. Figure VI.4 shows significant opening of splitting crack at the beam-joint interface and diagonal crack in the joint panel in SP1.

Table VI.4 Beam reinforcement index (RI_b).

Specimen	SP1			SP2			SP3			SP4		
Tension region	Top		Bot.	Top		Bot.	Top		Bot.	Top		Bot.
	without slab bars	with slab bars		without slab bars	with slab bars		without slab bars	with slab bars		without slab bars	with slab bars	
RI_b	6.8	7.6	6.8	11.2	12.0	8.7	6.2	6.9	6.2	9.8	10.5	7.5
$\gamma_{test@yield}$	6.7		7.5	12.2		9.1	6.7		6.2	-		7.5

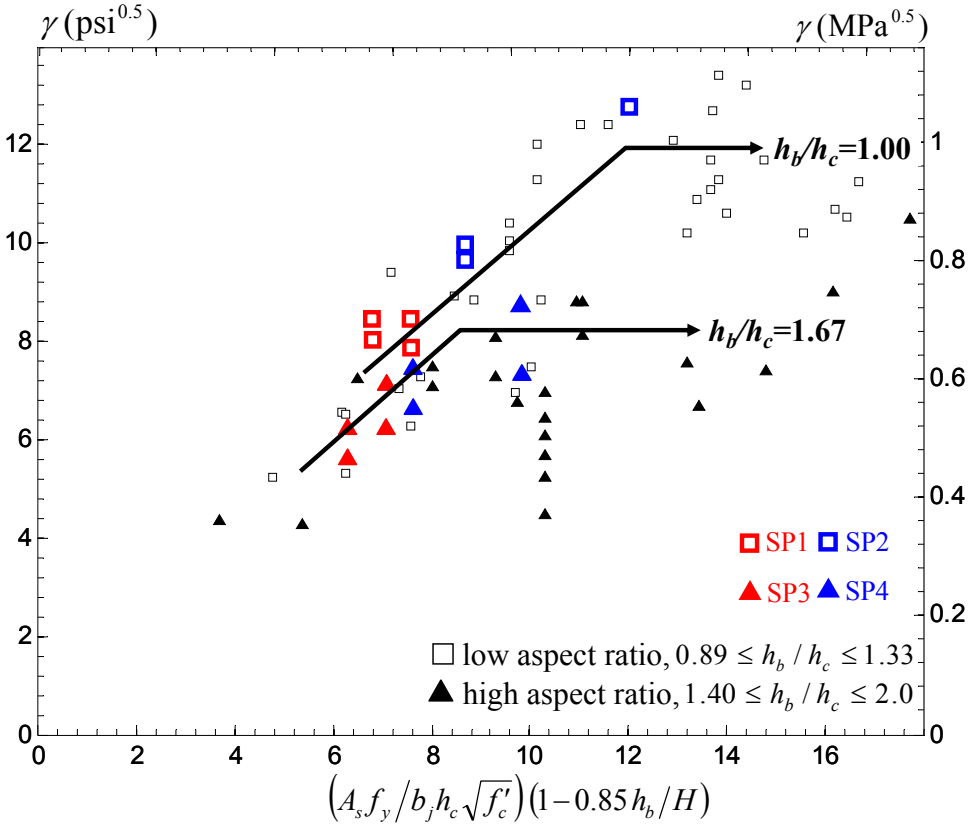

Figure VI.2 Test results of normalized joint shear strength versus the beam longitudinal reinforcement ratio.

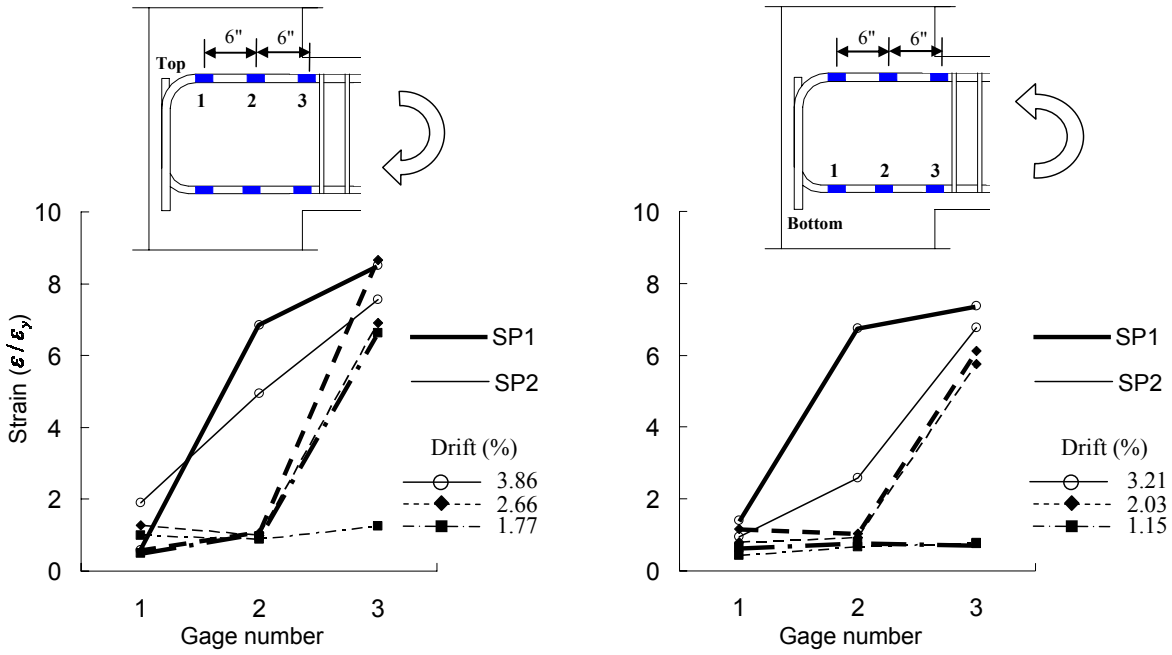

(a) EW-Top-Ext. (b) EW-Bottom-Ext.

Note: 1" = 25.4 mm

Figure VI.3 Comparison of beam longitudinal bar strains for specimens SP1 and SP2.

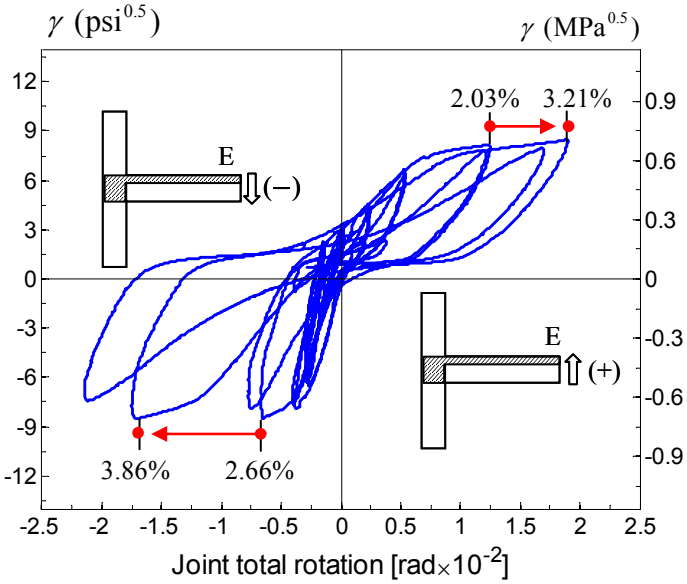

(a) EW direction

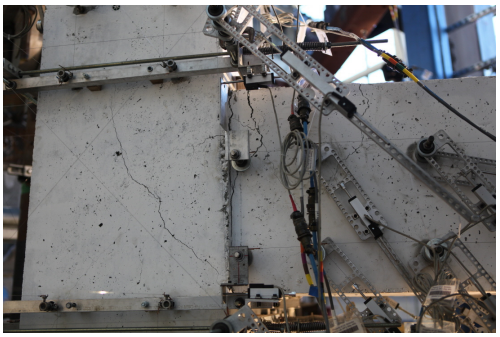

(b) EW beam down to 2.66%

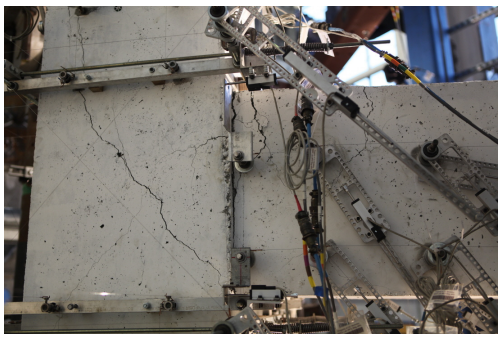

(c) EW beam down to 3.86%

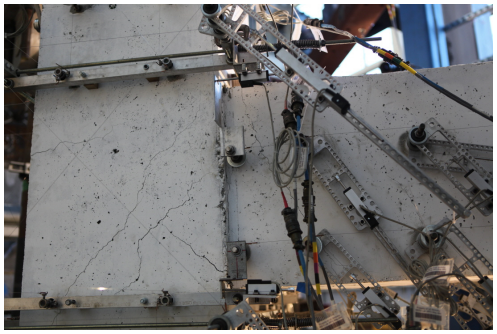

(d) EW beam up to 2.03%

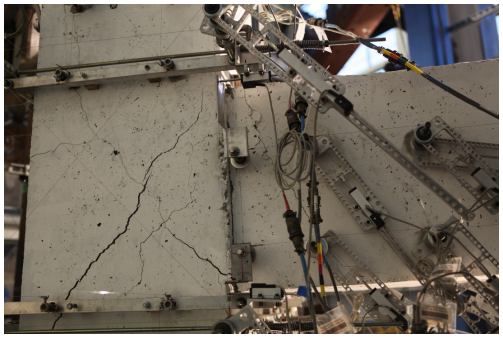

(e) EW beam up to 3.21%

Figure VI.4 Opening of diagonal and beam-joint interface cracks after deterioration of bond in specimen SP1.

VI-5 Effect of Slab

VI-5.1 Contribution of Slab Reinforcement

The strain and stress distributions of the slab reinforcement along the interface between the slab and beam orthogonal to the loading direction are presented in Figure VI.5 where the strain and stress values of the top reinforcement in the beams are also included for better understanding of the behavior of the L-shape beam cross-section. A typical approach to estimate the effective width of the slab is to compare the measured flexural moment with the calculated value including slab reinforcement within a certain overhanging portion at a fixed level of drift, usually 2% (French et al, 1991). However, the fixed drift level of 2% is generally selected to represent an upper limit for a seismically well-designed building where beam-column joints are sufficiently reinforced. Hence, this approach is not applicable to the evaluation of slab contribution for the four tested specimens because the joint deformation had a significant contribution to the total drift.

In this study, the contribution of the slab reinforcement is estimated using the comparison of the measured flexural moment with the calculated moment at the peak loading in the beams instead of 2% drift. First, the measured flexural moments are determined as the applied beam shear force times the distance between the loading point and the beam-joint interface, and this moment is considered as a reference moment. Alternatively, the moment can be calculated using the stresses of the beam longitudinal bars in the beam cross-section without consideration of slab reinforcement in this calculation. At the peak loading, these two moment values can be evaluated according to the aforementioned calculation and compared with each other. From this comparison, the effective slab width is estimated as follow. If the reference moment is greater than the calculated moments using the stress values of beam longitudinal bars only, some of slab top reinforcing bars are now taken to re-calculate the moment of the cross-section. Then, the effective slab width is defined as the distance from the beam-joint interface to the location of the last slab top bars considered along the direction orthogonal to the loading beam. The estimated effective slab width is indicated in Figure VI.5. It is noted that the contribution of slab bottom reinforcing bars is ignored based on the observation of their low strain and slippage because of insufficient anchorage detail and development, as discussed in Chapter V.

According to ASCE 41, the combined stiffness and strength for flexural and axial loading shall be calculated considering a width of effective flange on each side of the web equal to the smaller of: (1) the provided flange width, (2) eight times the flange thickness, (3) half the distance to the next web, or (4) one-fifth of the span for beams. When the flange is in compression, both the concrete and reinforcement within the effective width shall be considered effective in resisting flexure and axial loads. In the New Zealand seismic assessment guideline (NZSEE, 2006), at each side of the beam centerline a value corresponding to the lesser of (1) one-fourth of the beam span, (2) half the span of the slab transverse to the beam under consideration, and (3) one-fourth of the span of the transverse edge beam, must be considered. Two code provisions are compared with the estimated effective slab width in Figure VI.5. In

most cases including the four tested specimens, the last criterion for both ASCE 41 and NZSEE controlled the effective width. According to Figure VI.5, The effective width per ASCE 41 is suitable for SP1 only and it overestimates the effective slab width for other three specimens because joint shear failure is not considered in the criteria of ASCE 41. To generalize the contribution of the slab reinforcement for the four test specimens, a different approach is required to account for the joint shear failure.

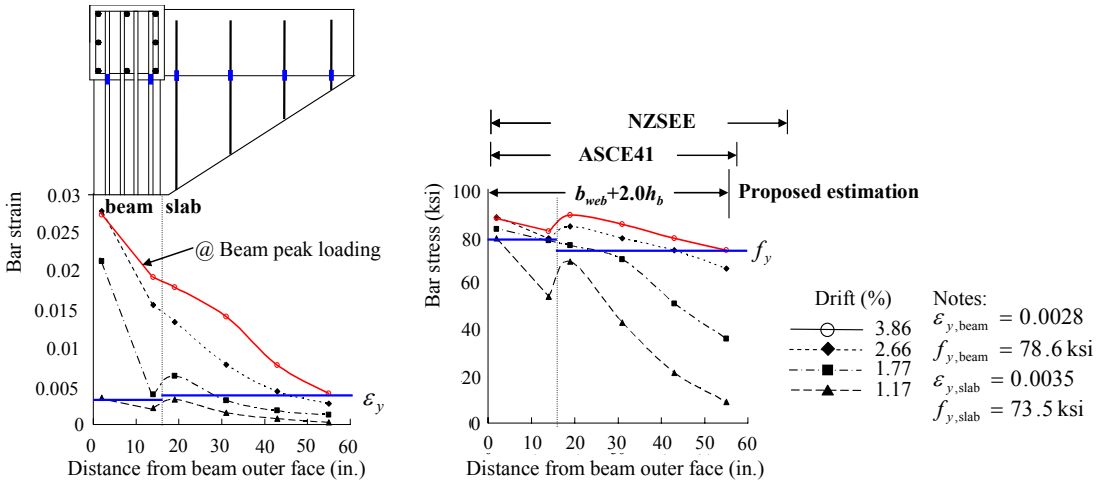

(a) SP1-EW direction

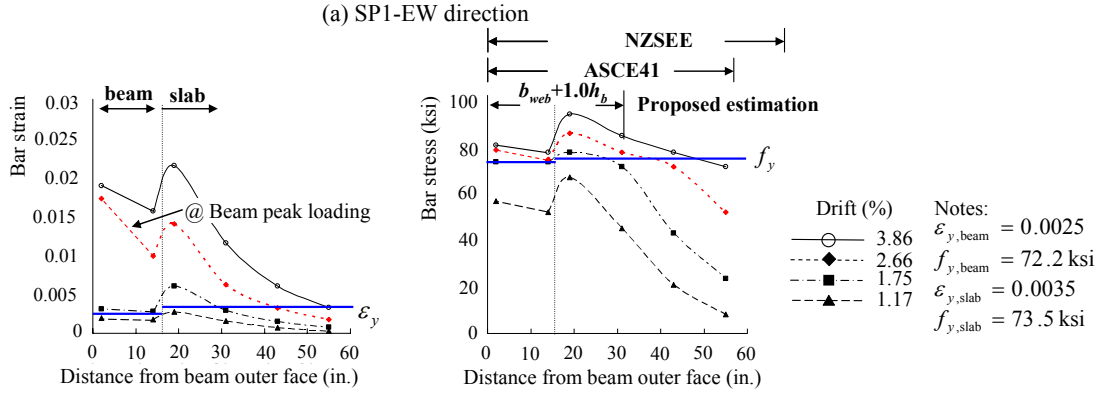

(b) SP2-EW direction

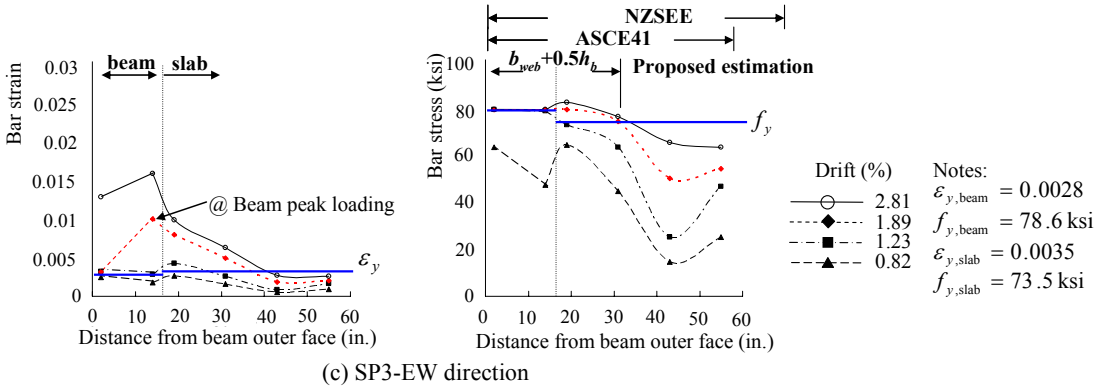

(c) SP3-EW direction

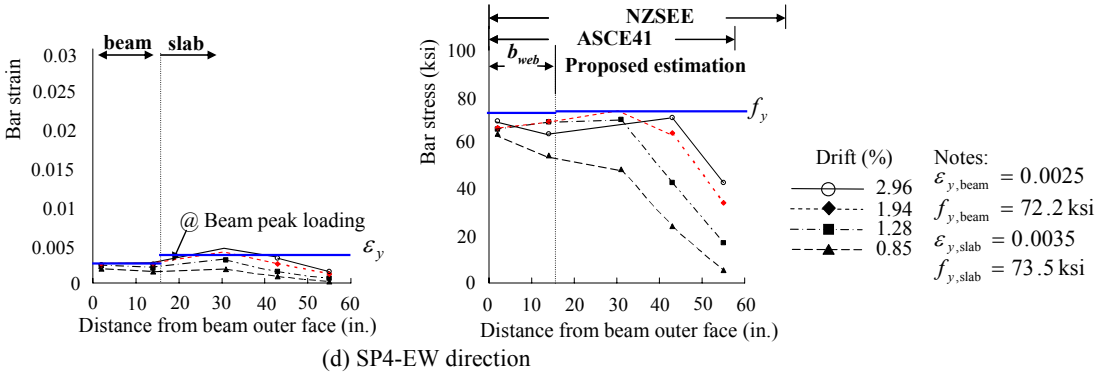

(d) SP4-EW direction

Figure VI.5 Strain and stress distributions of slab reinforcement.

VI-5.2 Consideration of Slab Reinforcement in Joint Shear Calculation

From the strain data of the slab reinforcement, it is observed that the strain began to significantly increase after beam longitudinal bars yielding and thus the contribution of the slab reinforcement to flexural strength changes depending on the type of joint failure, i.e. joint shear failure with or without beam reinforcement yielding. Based on this observation, it is postulated that the slab reinforcement contribution to the joint shear stress calculation can be estimated by the stress level of beam longitudinal bars when joint failure occurs. For example, the top two slab reinforcing bars were included to calculate the joint shear stress in SP3 where the beam longitudinal bars slightly yielded, while no slab reinforcing bars were included in the joint shear stress calculation for SP4 where beam longitudinal bars were not yielding.

To estimate the contribution of slab reinforcement depending on the beam longitudinal bar stress, the beam reinforcement index without slab contribution, $V_{jh,beam}$, and the maximum shear strength for a given joint aspect ratio, $V_{jh,\max}$, are utilized as proposed in Chapter III,

$$V_{jh,beam} = \frac{A_{s,beam} f_y}{b_j h_c \sqrt{f_c'}} \left(1 - 0.85 \frac{h_b}{H}\right) \tag{VI.3a}$$

$$V_{jh,\max} = 23 \frac{\cos\theta}{1.31 + 0.085\left(\frac{h_b}{h_c}\right)} \tag{VI.3b}$$

The effective slab width is proposed as

$$\text{For } V_{jh,beam} \geq V_{jh,\max}, \qquad b_{eff} = b_{web} \tag{VI.4a}$$

$$\text{For } V_{jh,beam} < V_{jh,\max}, \qquad b_{eff} = b_{web} + \kappa\left(\frac{V_{jh,\max}}{V_{jh,beam}} - 1\right) h_b \tag{VI.4b}$$

where κ is determined based on test results and an effective slab width proposed in the literature. Pantazopoulou et al. (1988) proposed that the effective slab width for exterior joints having two transverse beams, i.e. T-shape beam, is equal to the web width plus six times the depth of longitudinal beam at large drifts. Extending this estimation to a corner joint which has a transverse beam on one side only, i.e. L-shape beam, the overhanging slab width is taken as the half of the value for T-shape beam which is three times the depth of longitudinal beam. A large drift is achieved at a lower value of $V_{jh,\max}/V_{jh,beam}$ because ductile response is accompanied by beam reinforcement yielding and strain hardening. Consequently, κ is selected to be 3.0, assuming large drifts are achieved around the ratio of $V_{jh,\max}/V_{jh,beam} = 2.0$. The concept of the proposed effective slab estimation is as follow. If $V_{jh,beam}$ is greater than $V_{jh,\max}$ at the given joint aspect ratio, no slab reinforcement is taken into calculation. Otherwise, the slab contribution can be estimated based on the ratio of $V_{jh,\max}/V_{jh,beam}$. Obviously, further investigation of the coefficient κ is needed to refine the proposed value.

VI-6 Effect of Loading Sequence

The lateral loading was applied in the EW beam prior to the NS beam in each cyclic loading group. As a result of this loading sequence, the overall peak loads are generally greater in EW direction than in NS direction. Figure VI.6 shows that the ratio of the applied EW beam loads to the NS beam loads is around 1.0 until the drift level for beam yielding in each specimen, which means the peak loads are not affected by the loading sequence until the beams yield. After beam yielding, the ratios decrease as the drift levels increase and more significantly decrease after the overall peak loading where the joint failure occurred in the tests. Based on these observations, the joint responses obtained in the EW direction are taken as representative results for developing backbone relationships in Chapter VII.

During the longitudinal beam loading, the transverse beam was subjected to torsion due to the slab connecting the two orthogonal beams. Note that the definitions of longitudinal and transverse beams in Chapter I where the former is the beam in the direction of loading and the latter is the one in the direction perpendicular to the loaded beam. Two different types of cracks were observed in the transverse beam during the longitudinal beam downward and upward loading. Inclined cracks took place in the transverse beam when the longitudinal beam was loaded down, as shown in Figure VI.7(a). Horizontal cracks developed at the top of the joint panel in the transverse direction when the longitudinal beam was loaded up, as shown in Figure VI.7(b). The mechanisms of these cracks are depicted using free body diagrams in Figure VI.7. These two types of cracks closed when the beam loading was switched to the orthogonal beam. For example, the horizontal and inclined cracks formed in the joint and beam in the EW direction during the NS beam loading, as shown in Figure VI.7, but these cracks closed during the subsequent EW beam loading.

Twisting angles were measured as the difference of vertical displacement between two sides of the beam at locations A, B, and C, as shown in Figures VI.8 through VI.11. A considerable increase of twisting angle is observed between locations A and B in the transverse direction during the longitudinal beam downward loading, while the variation of twisting angle from A to C was relatively small during the upward loading. Considering the aforementioned crack pattern and the different variation of twisting angles in the transverse direction for the downward and upward loadings of the longitudinal beam, it can be concluded that twisting was localized around the inclined crack of the transverse beam when the beam was loaded down but the entire transverse beam was twisted during the beam upward loading causing a horizontal crack at the top of the joint panel in the transverse direction.

Some existing joint cracks and splitting crack at the beam-joint interface in the transverse direction were affected by the longitudinal beam loading. In general, this influence is, however, negligible because the cracks closed during the beam loading in the same direction. Therefore, it is concluded that the damage of the joint and beam in one direction induced by the orthogonal beam loading makes little difference in the joint responses for subsequent longitudinal beam loading.

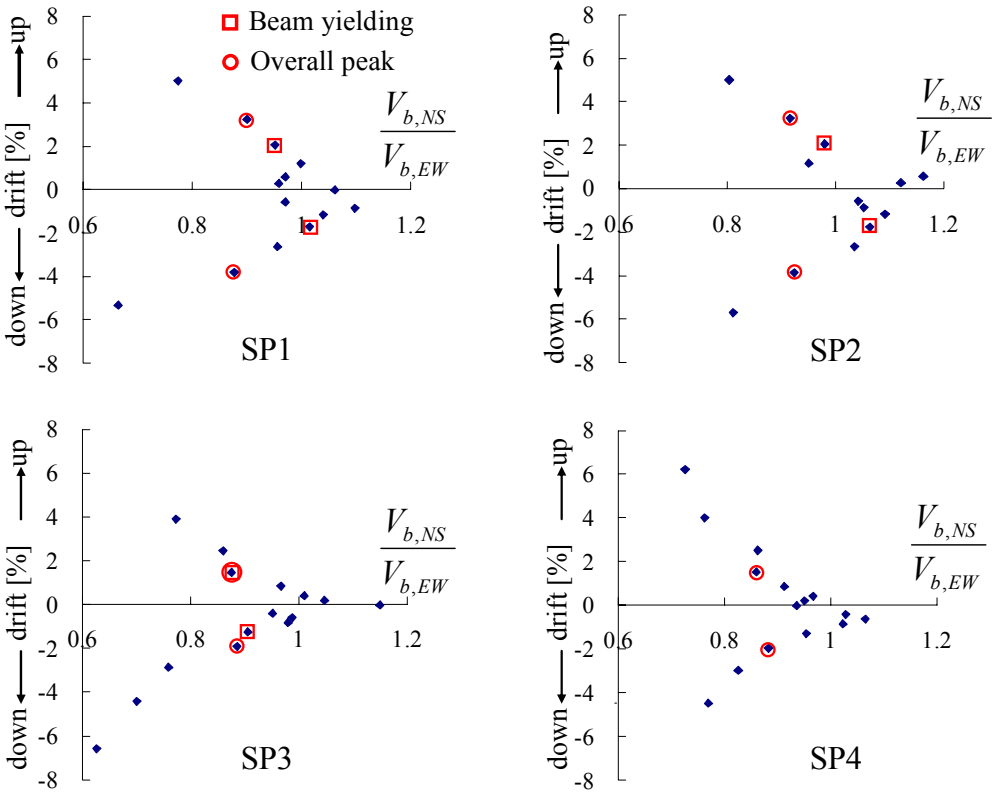

Figure VI.6 Comparison of peak load ratios for the EW and NS beams.

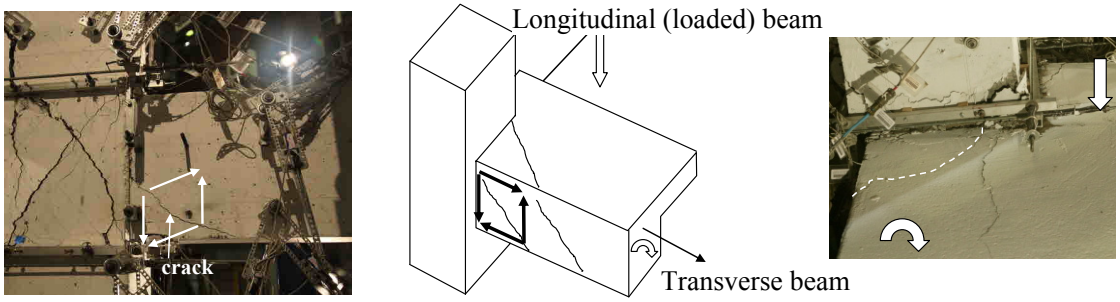

(a) Inclined cracks in the EW beam during the NS beam downward loading

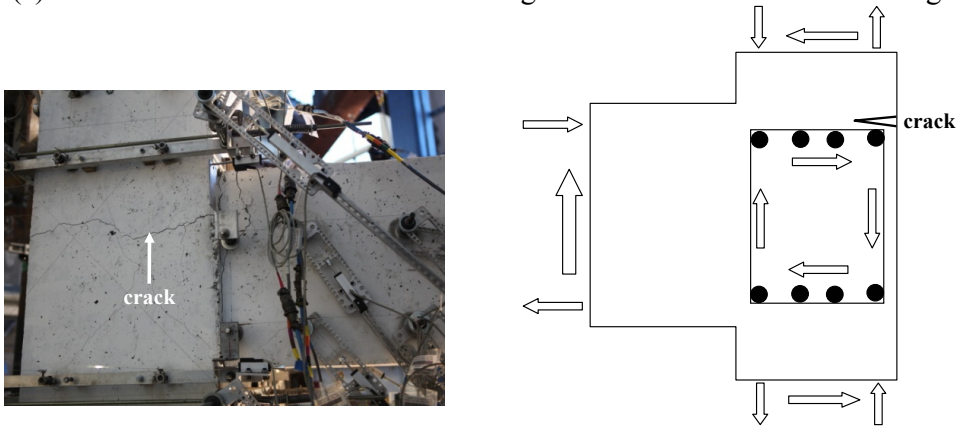

(b) Horizontal crack in the EW joint during the NS beam upward loading

Figure VI.7 Cracking by the orthogonal beam loading.

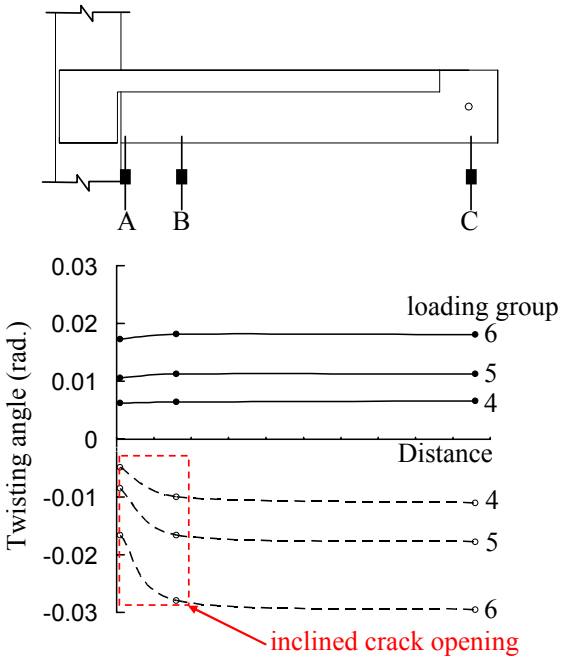

(a) Twisting of EW beam during NS beam loading

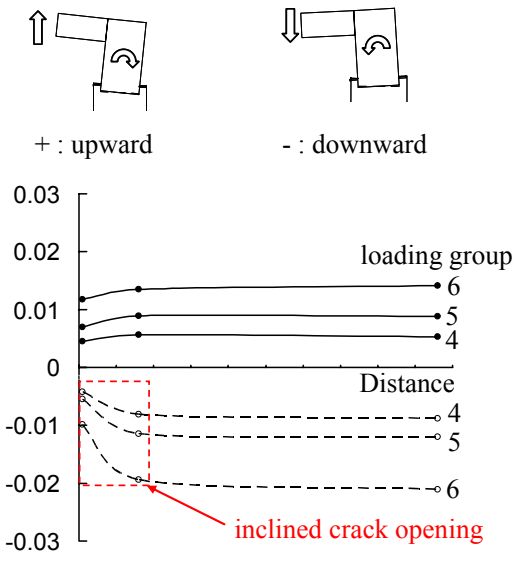

(b) Twisting of NS beam during EW beam loading

Figure VI.8 Twisting by the orthogonal beam loading in SP1.

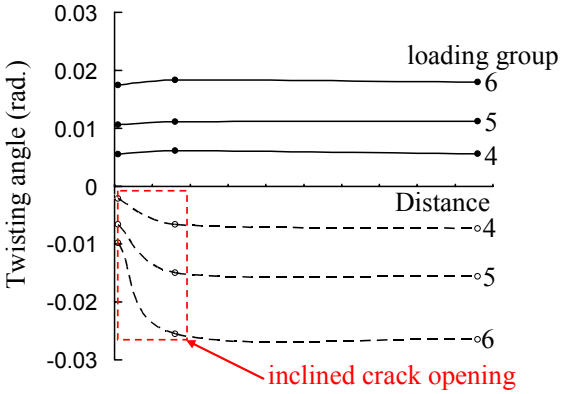

(a) Twisting of EW beam during NS beam loading

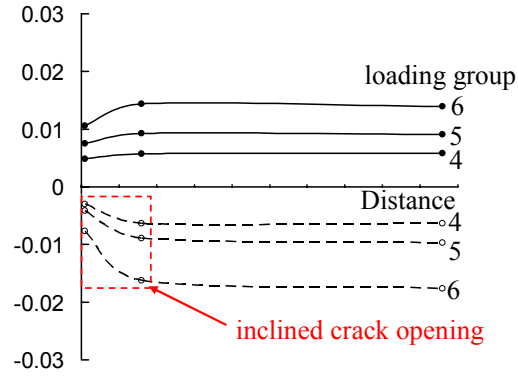

(b) Twisting of NS beam during EW beam loading

Figure VI.9 Twisting by the orthogonal beam loading in SP2.

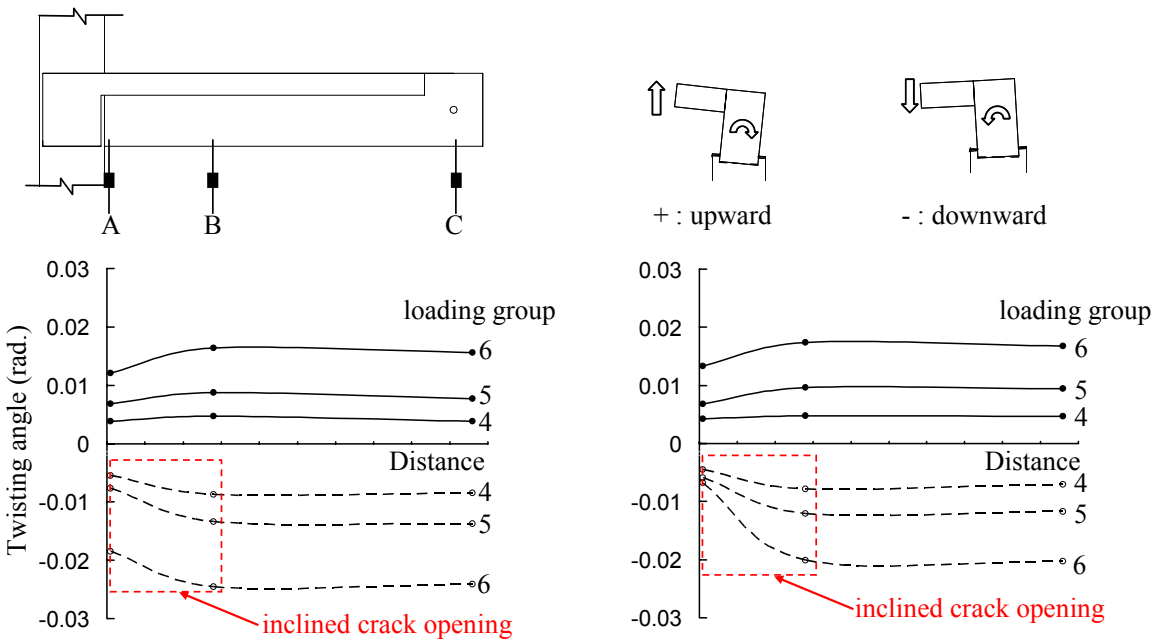

(a) Twisting of EW beam during NS beam loading (b) Twisting of NS beam during EW beam loading

Figure VI.10 Twisting by the orthogonal beam loading in SP3.

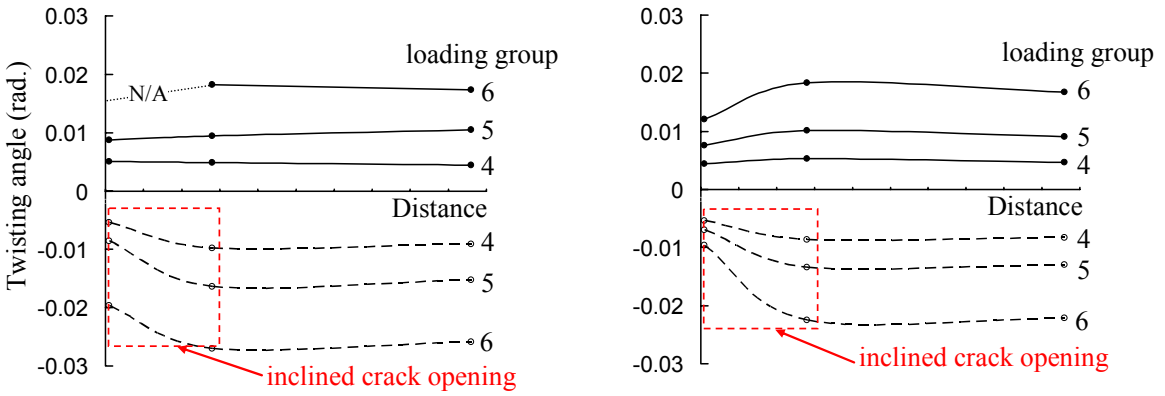

(a) Twisting of EW beam during NS beam loading (b) Twisting of NS beam during EW beam loading

Figure VI.11 Twisting by the orthogonal beam loading in SP4.

VI-7 Role of Column Intermediate Bars

Hwang et al. (2005) claimed that column intermediate bar(s) can carry vertical tension force F_v, as shown in Figure VI.12, if the bond capacity between the column longitudinal bars and surrounding concrete is maintained. To investigate the role of the column intermediate bars, the strain variation of these bars along the joint cross section height was measured and the results are presented in Figures VI.13 and VI.14. In specimens SP1 and SP2 having 8-#8 column longitudinal bars, the tensile strain at the joint mid-height location is less than either the strain at the joint top or the strain at the joint bottom. In specimens SP3 and SP4 having 8-#10 column longitudinal bars, the tensile strain at the joint mid-height location is greater than the strains at the joint top or the strain at the joint bottom for some beam loadings but this is not clear evidence that an column intermediate bar acted as a tension tie in joint shear resisting mechanism. Unlike reinforced joints, it appears that two inclined struts indicated in Figure VI.12 are hardly developed simultaneously because of the steep angle and the bond deterioration around the column longitudinal bars.

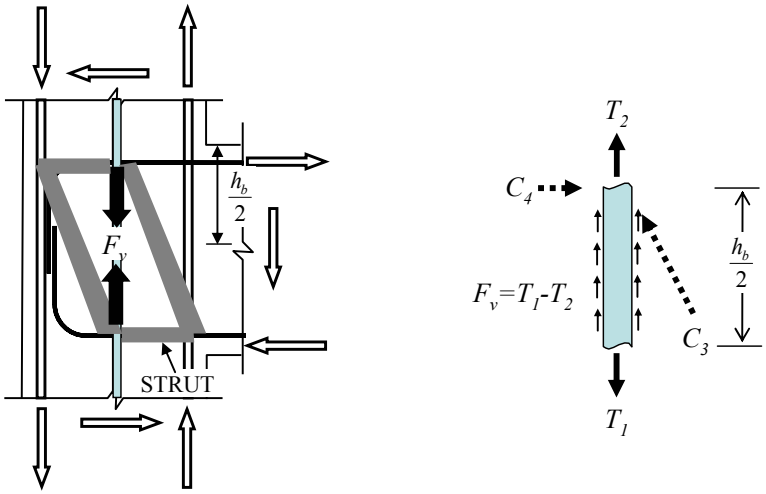

Figure VI.12 Role of column intermediate bars as a tension tie (Hwang et al., 2005).

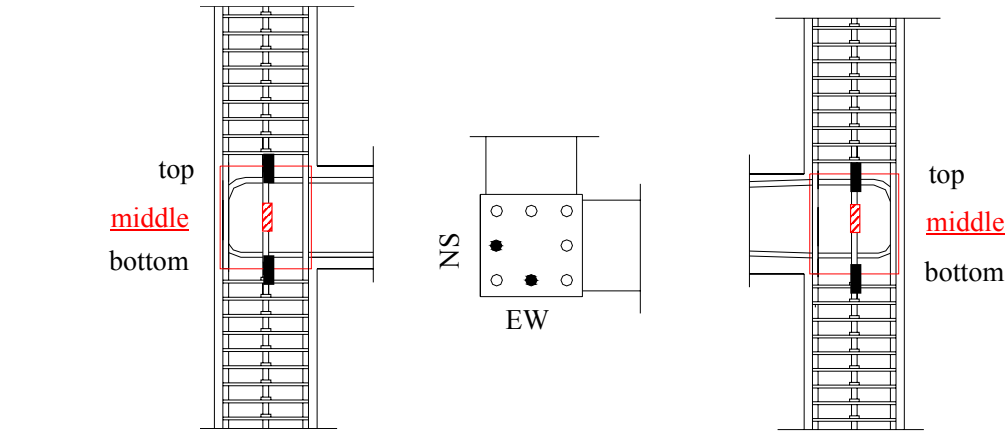

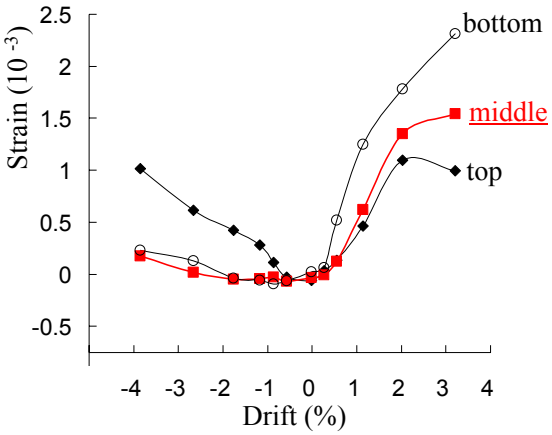

(a) SP1-EW direction

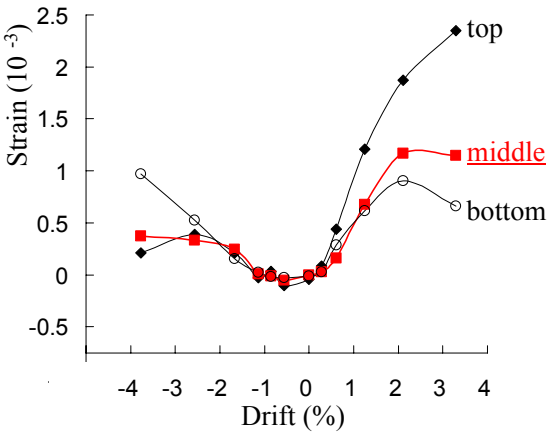

(b) SP1-NS direction

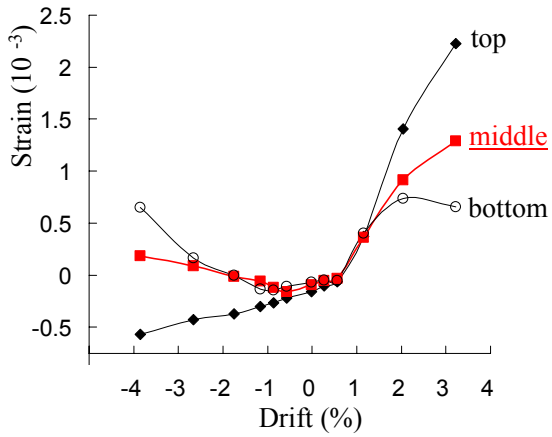

(c) SP2-EW direction

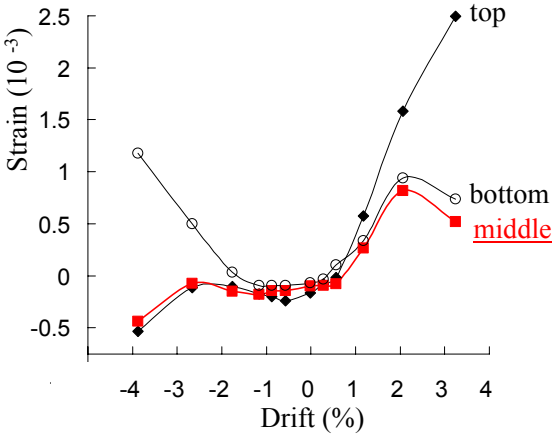

(d) SP2-NS direction

Figure VI.13 Strain distributions of column intermediate bars in SP1 and SP2.

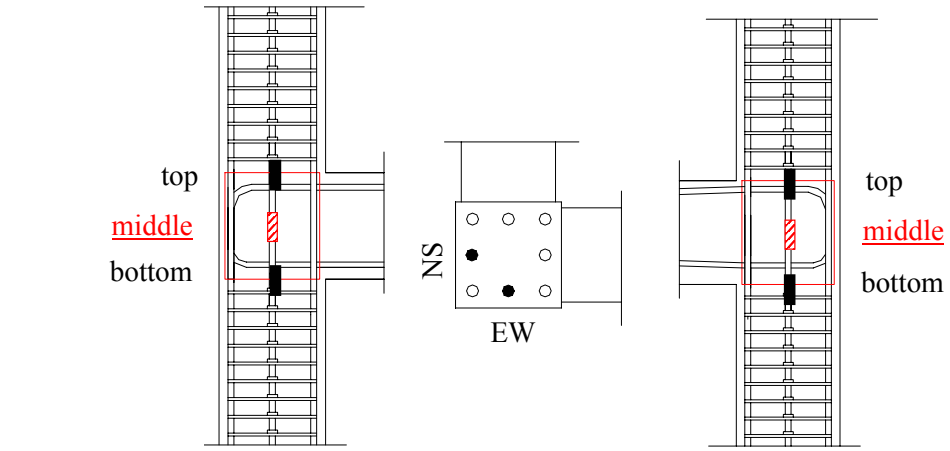

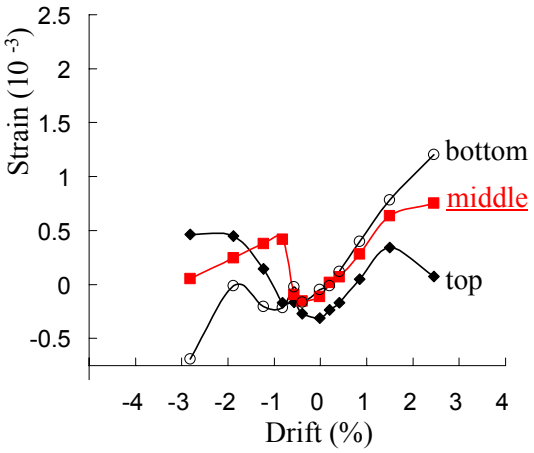

(a) SP3-EW direction

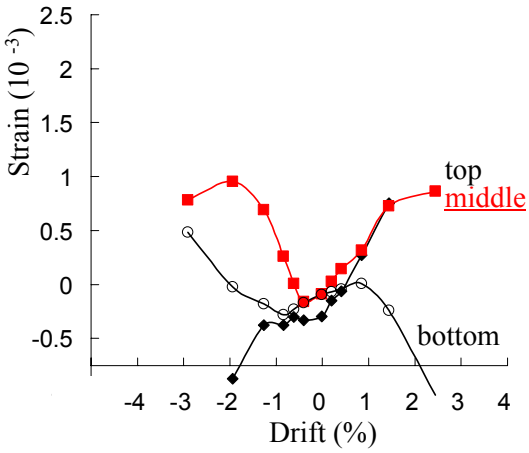

(b) SP3-NS direction

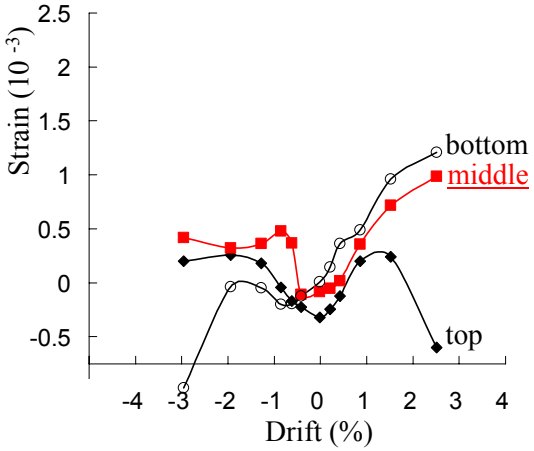

(c) SP4- EW direction

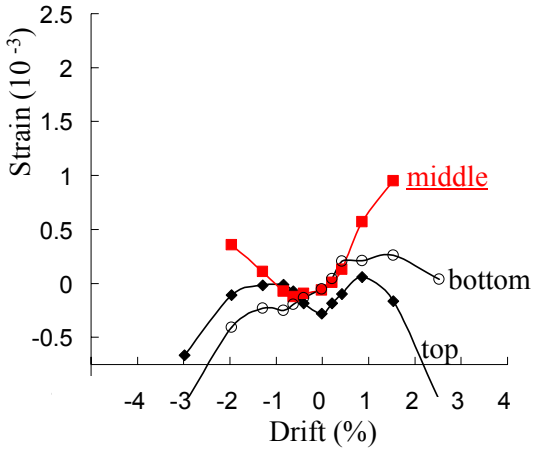

(d) SP4-NS direction

Figure VI.14 Strain distributions of column intermediate bars in SP3 and SP4.

VII Simulation with Joint Flexibility

VII-1 Development of Backbone Relationships

For nonlinear analysis, ASCE 41 classifies modeling parameters for exterior beam-column joints and other types of joints, i.e. interior and knee joint. The backbone curve for each type of joint is differently defined according to column axial load ratio, $P/f_c' A_g$, transverse reinforcement spacing, and the ratio of the design shear force, V, to the shear strength for the joint, V_n. The parameters corresponding to unreinforced joints under low column axial load are illustrated in Figure VII.1. According to the definition of ASCE 41, the four test specimens correspond to "Exterior joints with nonconforming transverse reinforcement", where joint shear strength, V_n, is equal to $6\sqrt{f_c'}b_j h_c$ (psi$^{0.5}$). In this type of beam-column joints, the backbone curve is independent of the column axial load ratio and the V/V_n ratio.

For an implicit joint macro-modeling adopted in the subsequent simulation, joint shear strain and relative deformation at the beam-joint interface were measured during the four tested specimens, as explained in Chapter IV. Joint rotation is defined earlier in Chapter V as the sum of the joint shear strain and the relative deformation at the beam-joint interface. The measured joint rotations for the four specimens are plotted in Figure VII.2. For the results, joint rotation values are affected by the joint aspect ratio rather than the beam flexural strength. For example, the joint rotation of SP1 is similar to that of SP2 but considerably different from that of SP3. According to the data, the joint shear strain is proportional to the joint shear stress level, and the relative deformation is different depending on both the occurrence of beam yielding and beam cross-section height. Hence, for the specimens having low beam reinforcement ratio, lower joint shear demand induces small joint shear strain, while the occurrence of beam yielding results in larger relative deformation at the beam-joint interface. The responses are the opposite for the specimens having high beam reinforcement ratio. Consequently, these two factors balance each other, and the results of the high and low beam reinforcement specimens become similar. On the other hand, beam cross-section depth serves as a denominator in the calculation of the relative deformation (Figure VII.2(a)) and thus the relative deformation must be less for larger beam cross-section depth.

Based on the measured joint shear stress-rotation and visual observations of the corner joint tests, a multi-linear backbone relationship is proposed in Figure VII.3. Modeling parameters are defined at the following responses: (1) λ_1 and θ_a represent initial joint cracking, (2) λ_2 and θ_b represent either beam reinforcement yielding or significant opening of existing joint crack, (3) θ_c represents either existing joint crack further propagation or additional joint crack opening at

the peak loading, and (4) λ_3 and θ_d represent the residual joint shear stress ratio and rotation when the damage of joint is severe. It is noted that the joint shear strength corresponding to V_n can be predicted by the proposed joint shear strength models. Each modeling parameter is evaluated in Table VII.1. From the four test specimens, the parameters λ_1, λ_2, θ_a and θ_b are shown to be not sensitive to the joint aspect ratio and the beam longitudinal reinforcement ratio so that they are selected as listed in Table VII.1. These parameters are selected as the quinary (5-based) numbers rounding off the mean values of these parameters measured from the four test specimens. It is noted that the parameter θ_b is selected as 0.0050 instead of 0.0055 in this study to compare the subsequent simulation results using the proposed backbone relationship with those using ASCE 41 at the same joint rotation point, i.e. 0.005, refer to Figure VII.1. The parameter θ_c, i.e. joint rotation at the peak loading, is affected by the joint aspect ratio in the way that the value of θ_c is larger for low aspect ratio specimens than for high aspect ratio specimens. On the other hand, changing the beam reinforcement ratio for the specimens with the same aspect ratio makes little difference in the value of θ_c. Therefore, θ_c is intended to reflect the effect of the joint aspect ratio and its equation is proposed as follows,

$$\theta_c = 0.0325 - 0.0125\frac{h_b}{h_c} \tag{VII.1}$$

The Equation (VII.1) gives 0.0200 and 0.0116 for the joint aspect ratios (h_b/h_c) of 1.00 and 1.67, respectively, and these values are close to 0.0196 and 0.0113, respectively: the former value is the mean value of θ_c from SP1 and SP2, and the latter value is the mean value of θ_c from SP3 and SP4. The parameters λ_3 and θ_d are selected to match the responses at the end of the four test specimens because the instrumented data are not reliable after severe joint damage. These selections are

$$\lambda_3 = 0.5\,, \quad \theta_d = \theta_c + 0.03 \tag{VII.2}$$

Knowing the dimensions of the RC frame and its joints, the moment at the center of joint, M_j, is obtained from the joint shear stress using Equation (II.28a). Thus, the vertical axis values of the backbone curve are transformed into the joint moment to be used in a moment-rotation relationship in the implicit joint macro-modeling.

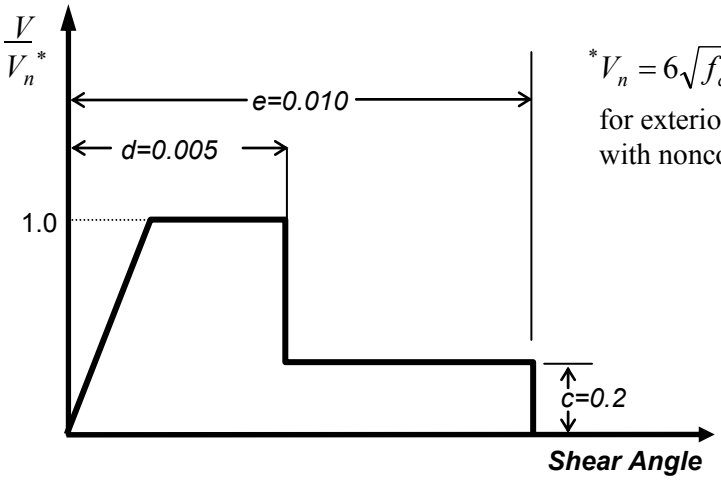

Figure VII.1 Backbone curve of exterior nonconforming beam-column joint (ASCE 41).

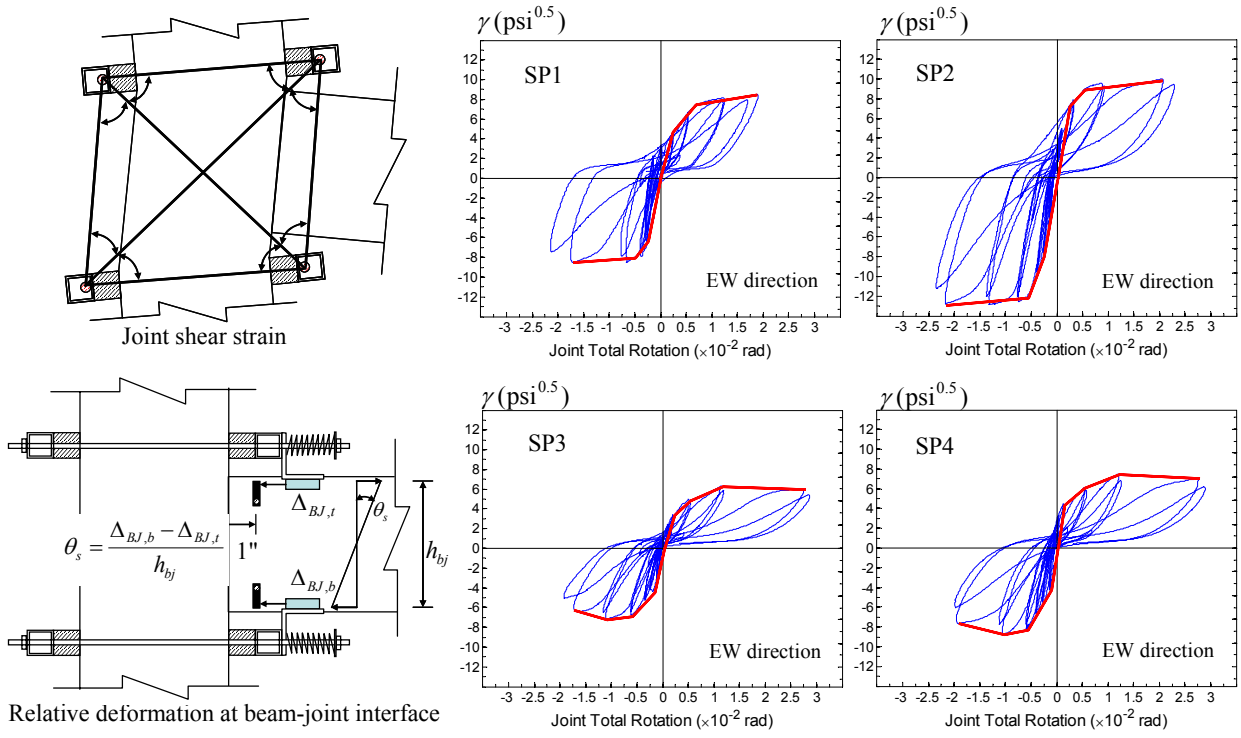

(a) Instrumentation of joint rotation (b) Measured joint shear stress and total rotation

Figure VII.2 Comparison of joint shear stress versus rotation responses for the four test specimens.

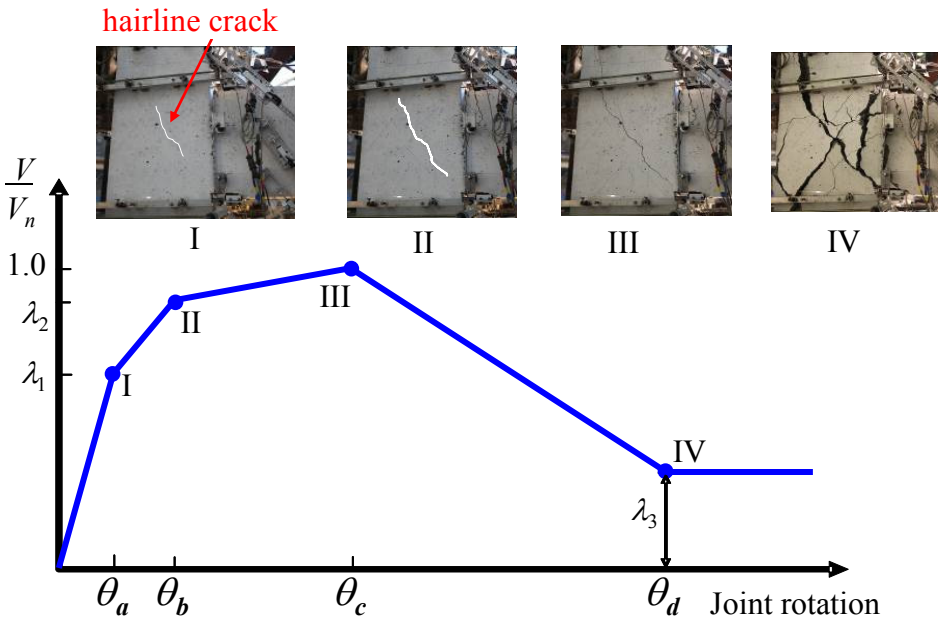

Figure VII.3 Proposed backbone relationship from the test specimens.

Table VII.1 Evaluation of backbone curve parameters.

	SP1		SP2		SP3		SP4		Mean	Proposed Model
	Down*1	Up*2	Down*1	Up*2	Down*1	Up*2	Down*1	Up*2		
λ_1	0.66	0.54	0.63	0.78	0.61	0.54	0.65	0.59	0.63	0.65
λ_2	0.94	0.87	0.92	0.90	0.95	0.80	0.93	0.82	0.88	0.90
θ_a	0.0025	0.0024	0.0027	0.0032	0.0019	0.0020	0.0027	0.0013	0.0023	0.0025
θ_b	0.0050	0.0068	0.0054	0.0057	0.0061	0.0052	0.0059	0.0055	0.0057	0.0050
θ_c	0.0170	0.0189	0.0218	0.0207	0.0111	0.0114	0.0105	0.0121	-	Eq. VII.1
	Mean of SP1 and SP2 = 0.0196				Mean of SP3 and SP4 = 0.0113					

*1: Beam loaded downward;
*2: Beam loaded upward.

VII-2 Simulation of Tested Four Corner Joint Specimens

VII-2.1 Simulation Assumptions

Simulations are performed for the tested four specimens under the following assumptions. First, it is assumed that two dimensional analysis is representative enough to simulate the response of the EW and NS directions independently. This assumption is justified because the applied lateral loading alternated between the two orthogonal beams instead of simultaneous bi-directional loading, and the responses of the joint, beam and slab were observed to be little affected by the orthogoanl beam loading.

Second, the variable column axial load is not taken into account. Instead, the initial column axial load is imposed and kept constant during the cyclic lateral beam loading in this analysis. This assumption is justified because the change of column flexural deformation due to the variable axial load is not significant in the total response, considering that columns in the four specimens remained elastic during testing as discussed in Chapter V.

Third, the beam cross-sections are modeled with effective slab width estimated based on the strain measurements of slab reinforcement. Actual slab effect as a plate-bending element is not included in the model. For negative bending, only top reinforcing bars are included in the model within the width of effective slab proposed in Chapter VI. For positive bending, the beam cross-section is taken as rectangular section without consideration of the slab.

Fourth, the cover concrete thicknesses measured after the tests are accounted for in the beam cross-sections. The strength and ultimate strain of core concrete confined by hoops for column and stirrups for beam are calculated using the models by Mander et al. (1988), Qi and Moehle (1991), and Saatçioğlu and Razvi (1992).

Last, the backbone curve developed in the preceding section is utilized and implemented as a rotational spring for modeling beam-column joints implicitly.

VII-2.2 Comparison of Simulations with Experimental Responses

The simulations are performed for two different types of specimen idealizations using OpenSees (2010). The first idealization considers the one-dimensional beam and column elements intersecting at the joint where the orthogonality between beam and column is maintained, as depicted in Figure VII.4(a). The second idealization is similar to the first but the joint region is modeled with a rotational spring and joint offsets, Figure VII.4(b). Hereafter, the first and second idealizations are referred to as “conventional center-to-center model” and “model with joint rotational spring”, respectively.

The beam and column materials are modeled using the following uniaxial materials available in OpenSees (2010):

1. Cover concrete of beam and column, and slab concrete: *Concrete01*;
2. Confined core concrete of beam and column: *Concrete04*; and
3. Reinforcing bars of beam and column: *ReinforcingSteel*.

The parameters of each material are designated to be identical with the material test results presented in Appendix B. The beam and column elements are modeled using *nonlinearBeamColumn* element utilizing the advantage of force method formulation, e.g. no need to define the plastic hinge length. Five integration points are assigned in each element. The cross-sections of beam and column are discretized along the depth using layers with thickness of 0.5 in. (12.7 mm) for each layer, where each layer is divided into three fibers to represent the concrete cover and the core material, as shown in Figure VII.5.

In the model with-joint-rotational-spring, the backbone relationship for the joint rotational spring is implemented using *Pinching4* uniaxial material and the finite size of the joint panel represented by the rigid links in Figure VII.4(b). The following parameters are used for unloading and reloading of hysteretic curves:

$$rDispP = rDispN = 0.5,\ rForceP = rForceN = 0.25,\ uForceP = uForceN = 0.05$$

Other stiffness and strength degradation parameters are set to be zero.

The simulated load-displacement responses for the tested four specimens are compared with the test results in Figure VII.6 through VII.9. Here, it is noted that the joint shear strength (V_n) of the backbone curve is adjusted to match the peak load of the tested specimens. For all the specimens, the simulation using the proposed backbone relationship shows good agreement with test results, while the conventional center-to-center model analysis predicts ductile response of specimens because hoops and stirrups are sufficiently provided in the column and beams. From the comparison of the simulated results and the test results, the inclusion of joint flexibility is essential for simulating older-type RC buildings having unreinforced exterior joints. The discrepancies between the simulations using the proposed model and the test results for the positive loading excursions, i.e. slab in compression, is attributed to the RC slab contribution which is not properly modeled as a plate-bending element in the current simulations.

For a blind prediction of the response, the simulations are re-performed with the predicted joint shear strengths, i.e. V_n in the backbone curve in Figure VII.3, for the four tested specimens using the semi-empirical strength model developed in Chapter III. Furthermore, the simulations are compared with those using the ASCE41 joint shear strength prediction, i.e. $V_n = 6\sqrt{f_c'}b_j h_c$ (psi$^{0.5}$), and the backbone curve shown in Figure VII.1. In Figure VII.10 through VII.13, the simulation using the proposed shear strength prediction and backbone relationship shows good agreement with test results, while the ASCE 41 generally underestimates the shear strength and deformability of the tested specimens. It is noted that the discrepancy of the peak loads in the simulations using the proposed model are attributed to the small errors of joint shear strength predictions by the semi-empirical model.

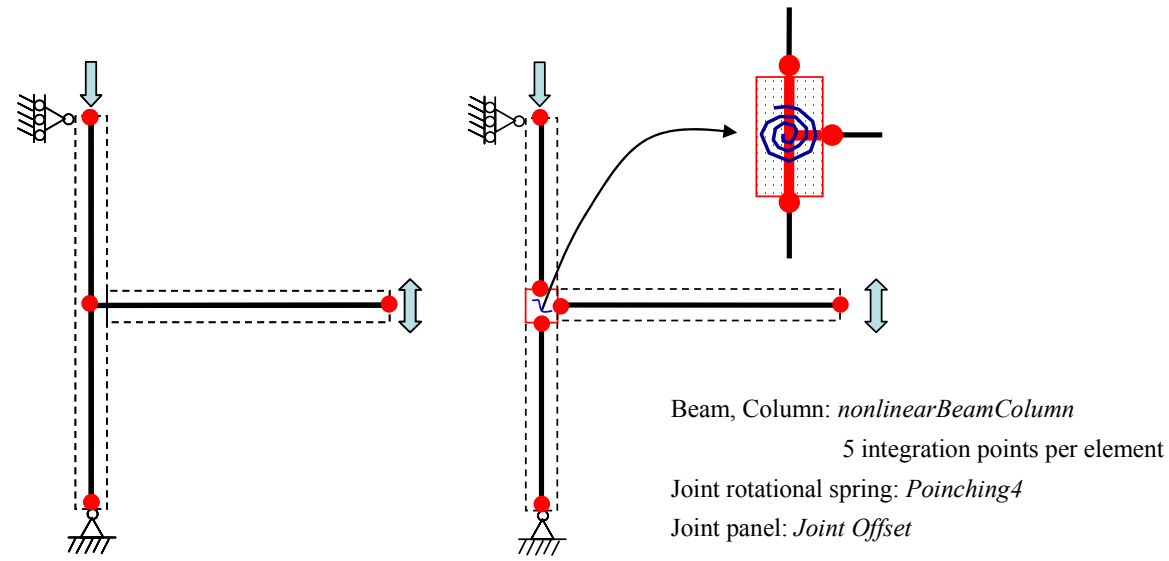

(a) Conventional center-to-center model (b) Model with joint rotational spring

Figure VII.4 Two dimensional modeling of test specimens.

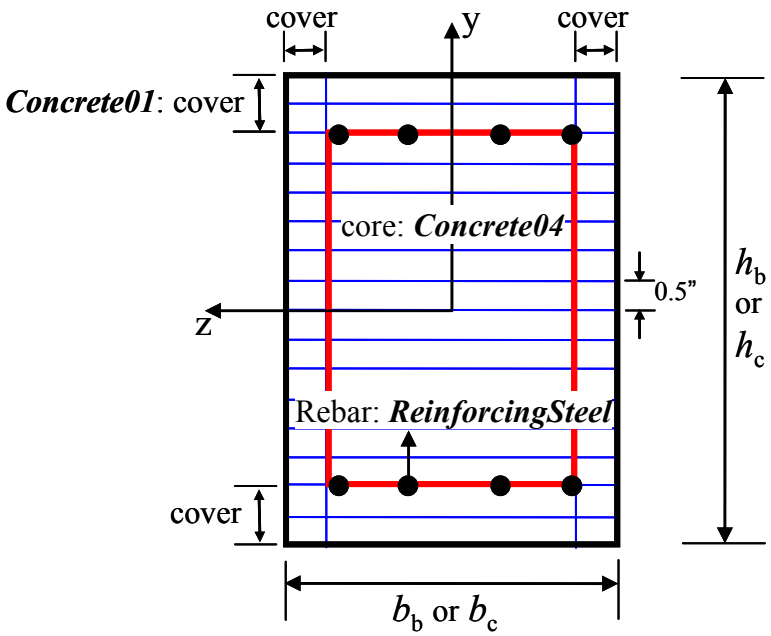

Figure VII.5 Adopted materials and discretization of beam and column cross-sections.

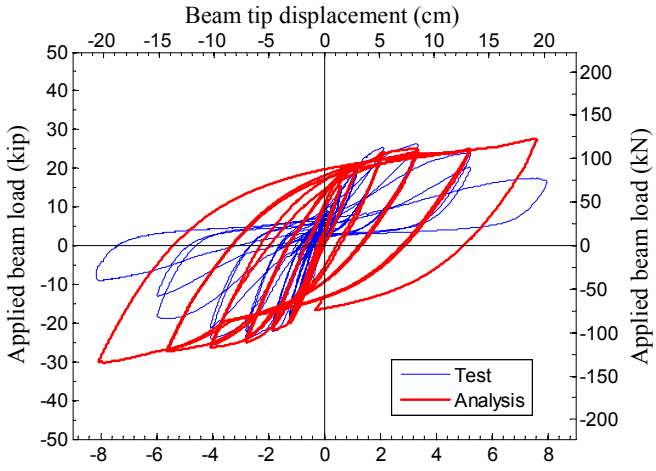

(a) Conventional center-to-center

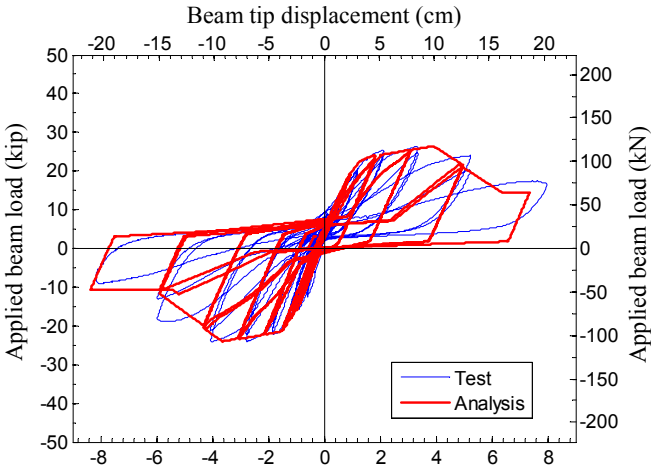

(b) Model with joint rotational spring, EW direction

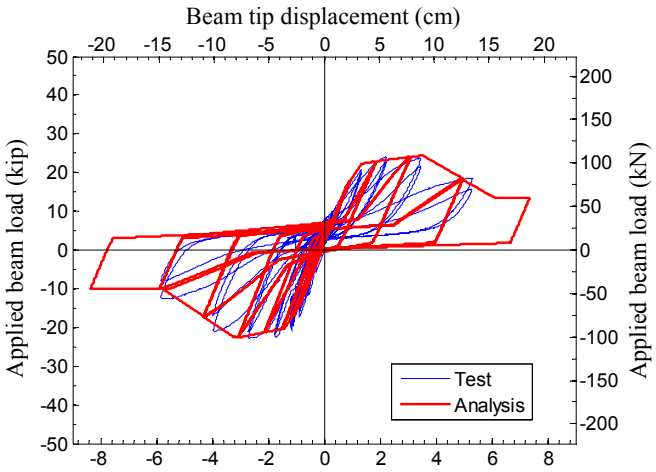

(c) Model with joint rotational spring, NS direction

Figure VII.6 Comparison of simulations with test results, SP1.

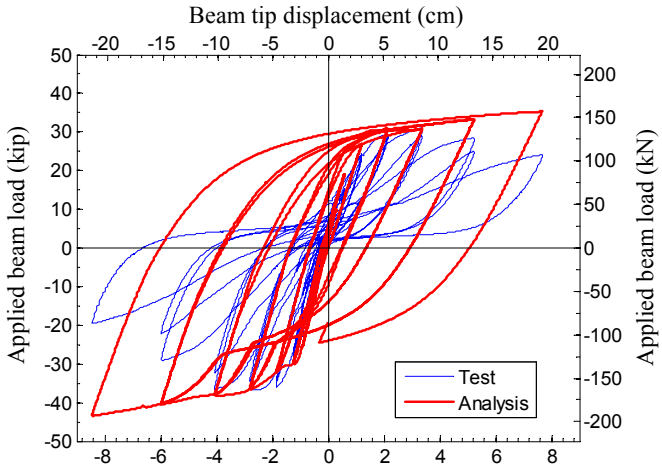

(a) Conventional center-to-center

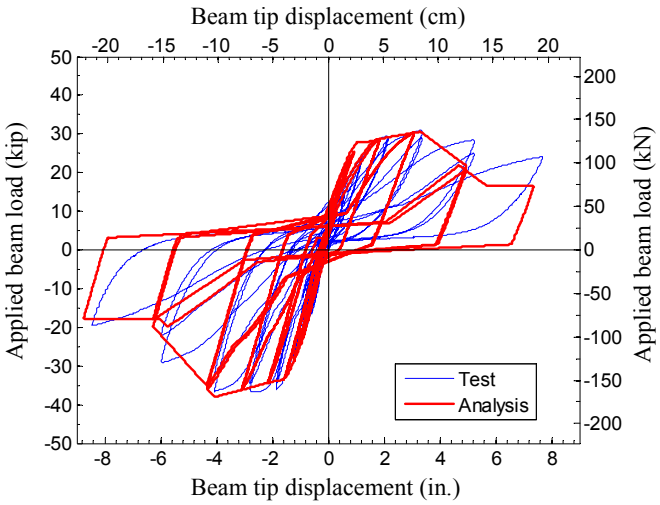

(b) Model with joint rotational spring, EW direction

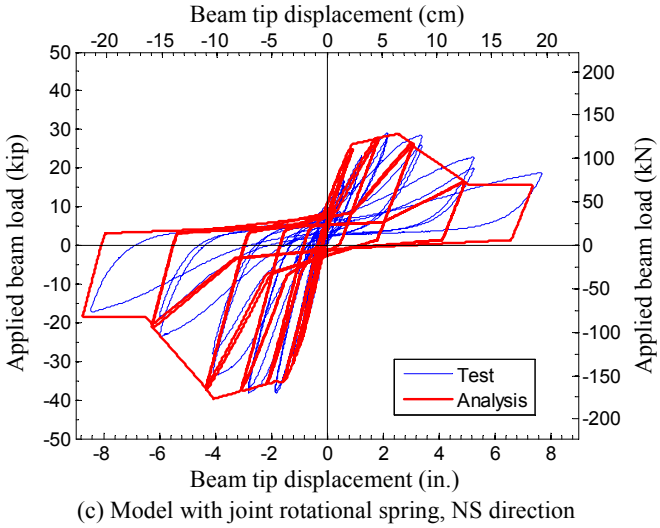

(c) Model with joint rotational spring, NS direction

Figure VII.7 Comparison of simulations with test results, SP2.

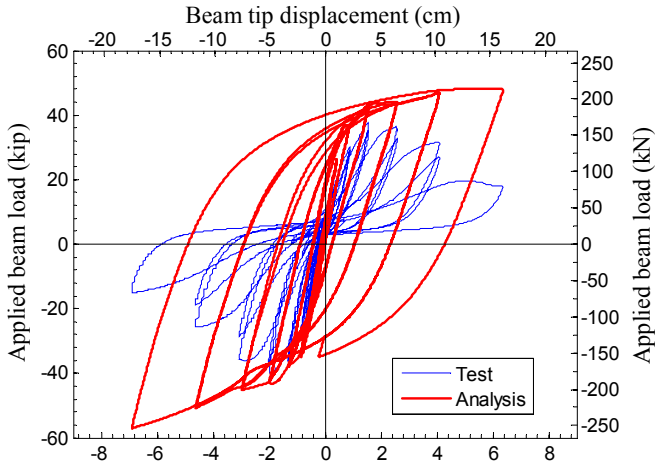

(a) Conventional center-to-center

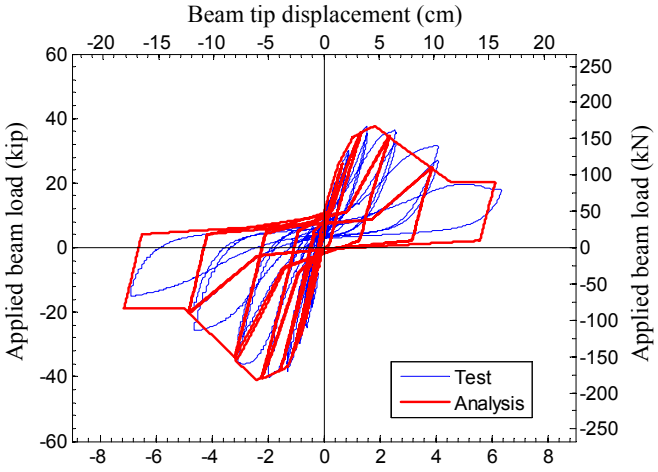

(b) Model with joint rotational spring, EW direction

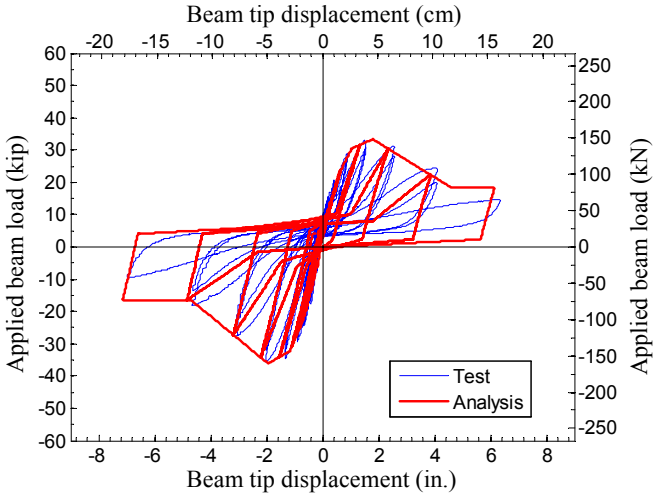

(c) Model with joint rotational spring, NS direction

Figure VII.8 Comparison of simulations with test results, SP3.

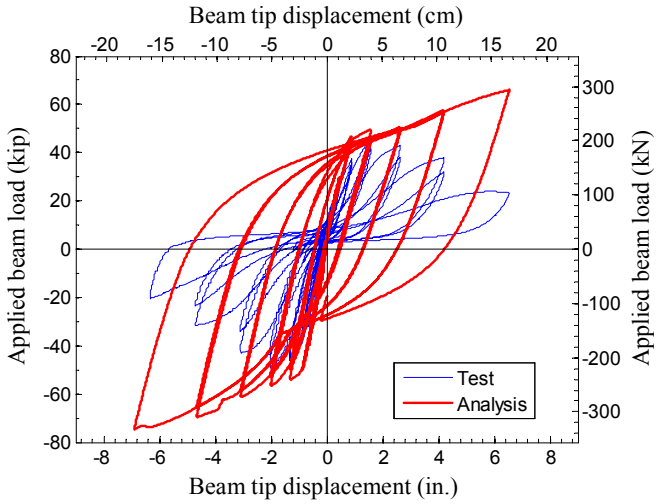

(a) Conventional center-to-center

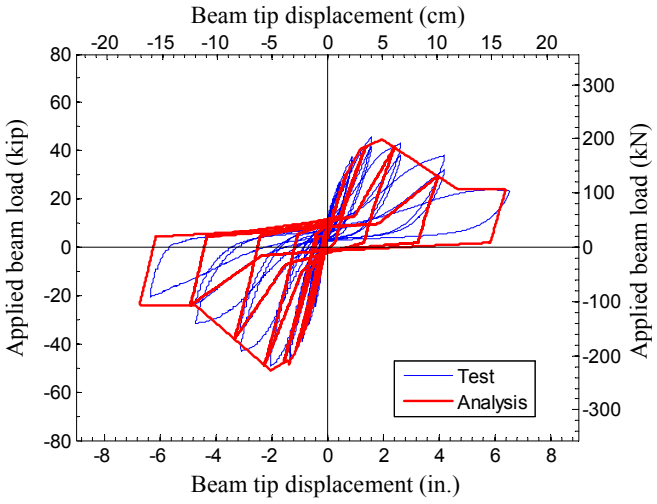

(b) Model with joint rotational spring, EW direction

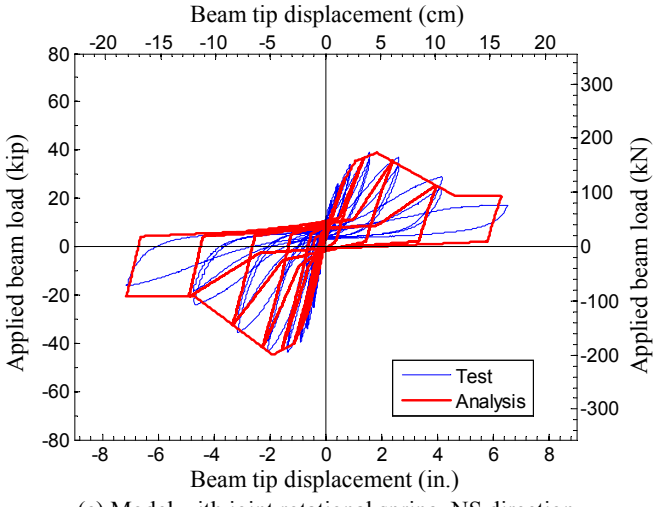

(c) Model with joint rotational spring, NS direction

Figure VII.9 Comparison of simulations with test results, SP4.

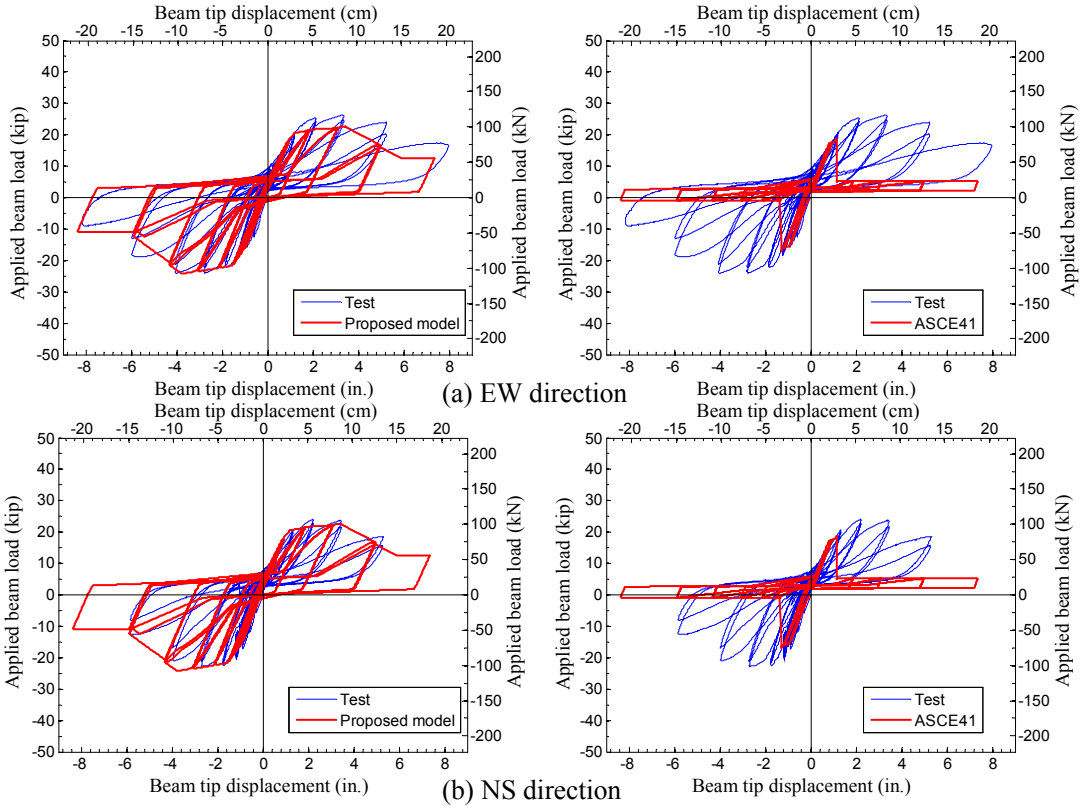

Figure VII.10 Comparison of proposed model with ASCE41, SP1.

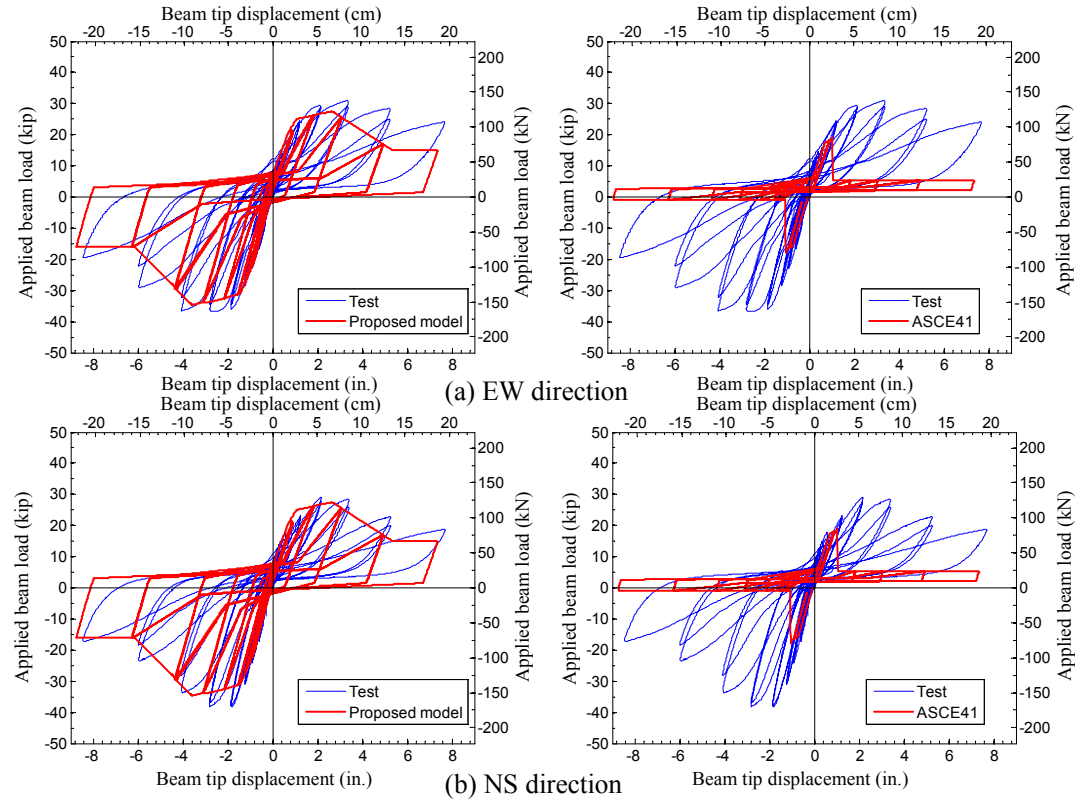

Figure VII.11 Comparison of proposed model with ASCE41, SP2.

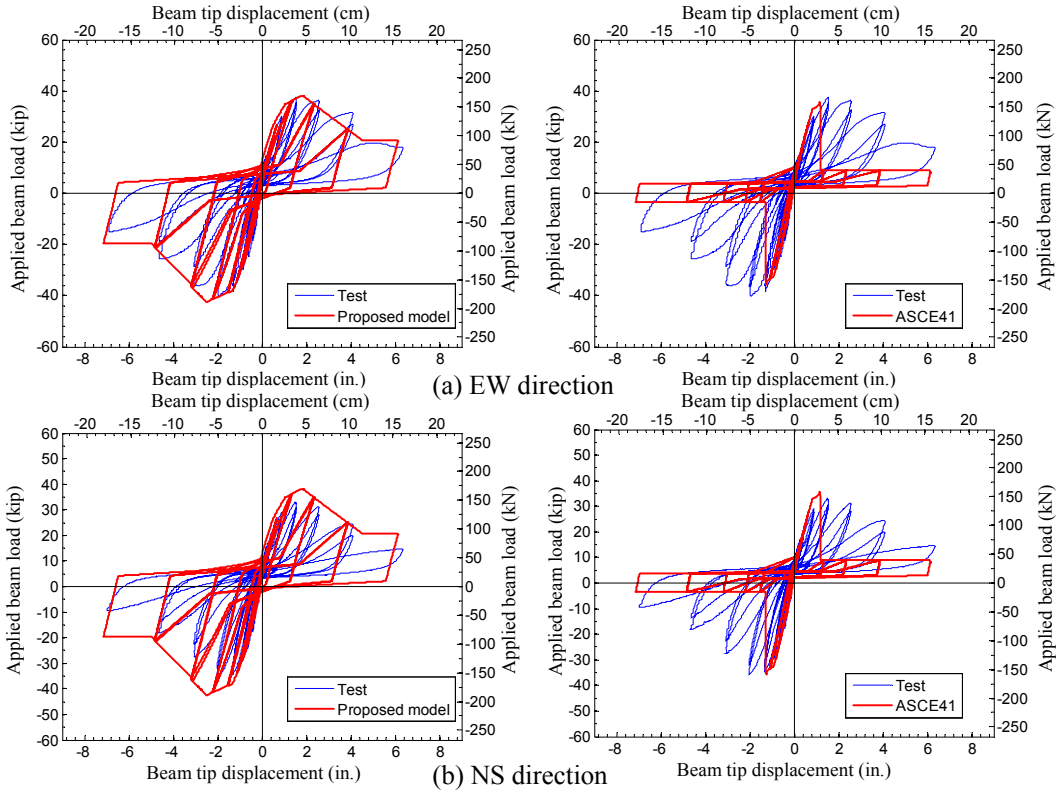

Figure VII.12 Comparison of proposed model with ASCE41, SP3.

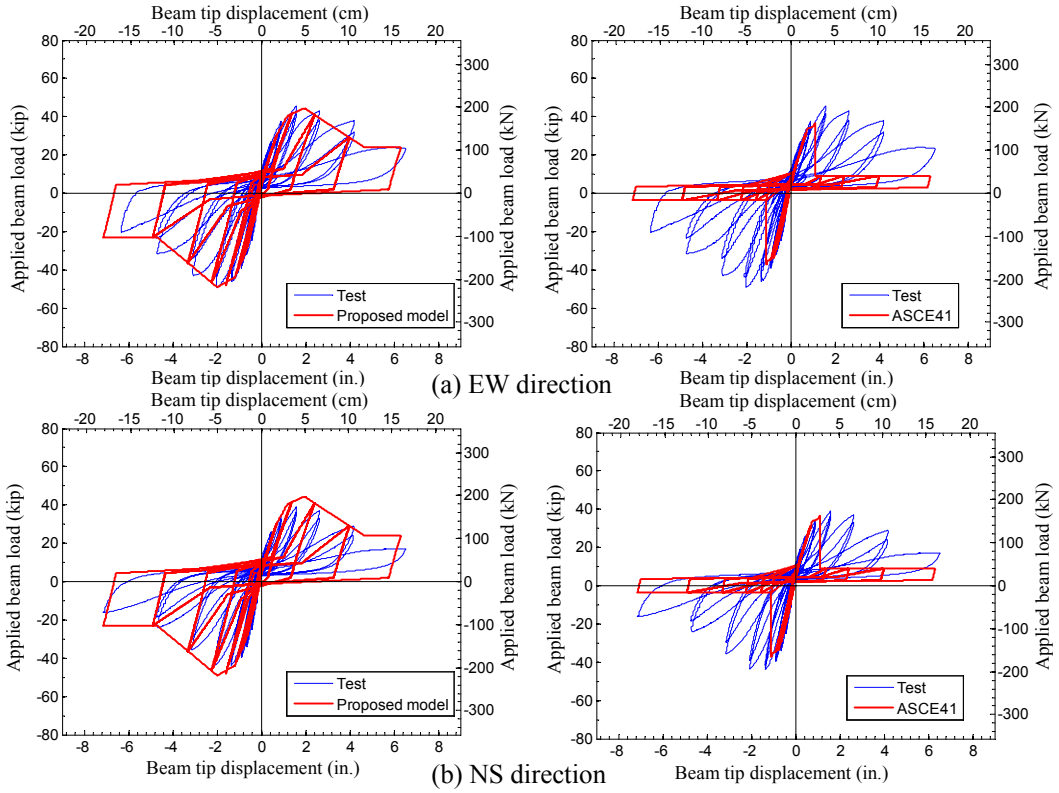

Figure VII.13 Comparison of proposed model with ASCE41, SP4.

VII-3 Simulation of Four Planar Exterior Joint Specimens

Four planar unreinforced exterior joint tests are selected from Wong (2005) to investigate the joint response for various aspect ratios from 1.0 to 2.0. Material properties, test setup and details of the selected four specimens are presented in Table VII.2 and Figure VII.14. The joint aspect ratios of BS-L-300, JA-NN03, BS-L-450, and BS-L-600 correspond to 1.00, 1.33, 1.50 and 2.00, respectively. It is noted that these specimens used metric sizes of steel reinforcing bars. Specimens JA-NN03 and BS-L-450 were tested through load control up to the beam yielding followed by displacement control, while specimens BS-L-300 and BS-L-600 were fully tested under displacement control. The column axial loads were kept constant at $0.03f_c'A_g$ for JA-NN03 and $0.15f_c'A_g$ for the other three specimens. Specimens JA-NN03 and BS-L-450 were previously simulated using the proposed analytical model in Chapter III but the joint rotational spring did not properly account for the initial stiffness and post-failure behavior in the analysis.

The selected four planar exterior joint specimens from Wong (2005) are simulated with joint rotational spring to investigate the applicability of the proposed backbone relationship. Displacement history for the simulation is obtained from the published load-displacement plots in Wong (2005). The shear strengths are predicted using the proposed semi-empirical model. Figure VII.15 compares the simulated response in dashed lines with the test result as solid lines. For each specimen, the proposed backbone curve is symmetric for both loading directions because longitudinal bars are identically placed at the top and bottom of the beam without overhanging slab. On the other hand, the experimental responses are not symmetric because the joint strength is not retained for one loading direction if the joint is previously damaged during the loading in the other direction. The simulations using the proposed model are successful in obtaining good agreement with the experimental responses such as the displacement at the peak force and post failure behavior. However, the peak forces have small discrepancies between predictions by the proposed shear strength model and the test results. These discrepancies result from insufficient detailed information about the material properties and in particular the strength of BS-L-300 (Figure VII.15(a)) is questionable because its yielding for positive loading occurred beyond the estimated beam capacity, represented by the thick horizontal dashed line in Figures VII.15(a) and (b). From the simulations of the four test specimens by Wong (2005), the proposed backbone curve is shown to be adequate for simulating the seismic response of older-type RC buildings having unreinforced exterior beam-column joints.

Table VII.2 Material properties of specimens by Wong (2005).

	Concrete [ksi (MPa)]		Yield strength of reinforcing bars [ksi (MPa)]
	Cube strength	Cylinder strength	
BS-L-300	6.17 (42.6)	4.94 (34.1)	75.4 (520)
JA-NN-03	8.12 (56.0)	6.49 (44.8)	
BS-L-450	5.59 (38.6)	4.48 (30.9)	
BS-L-600	6.59 (45.5)	5.28 (36.4)	

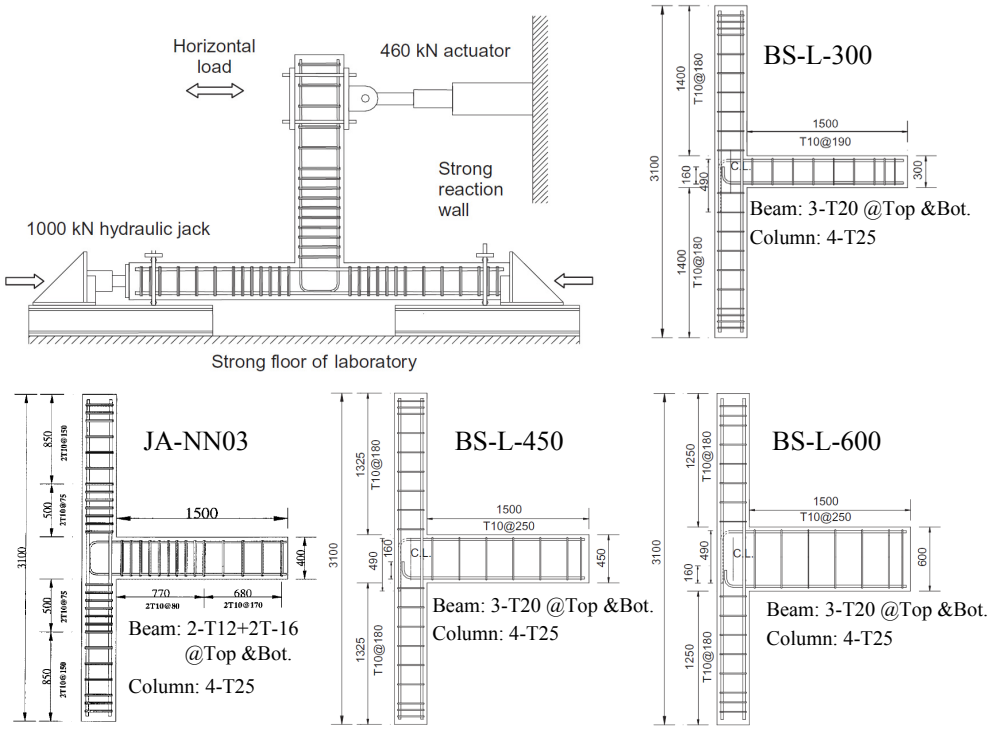

Note: dimensions are in mm and SI units are used

Figure VII.14 Details of planar unreinforced exterior joint specimens (Wong, 2005).

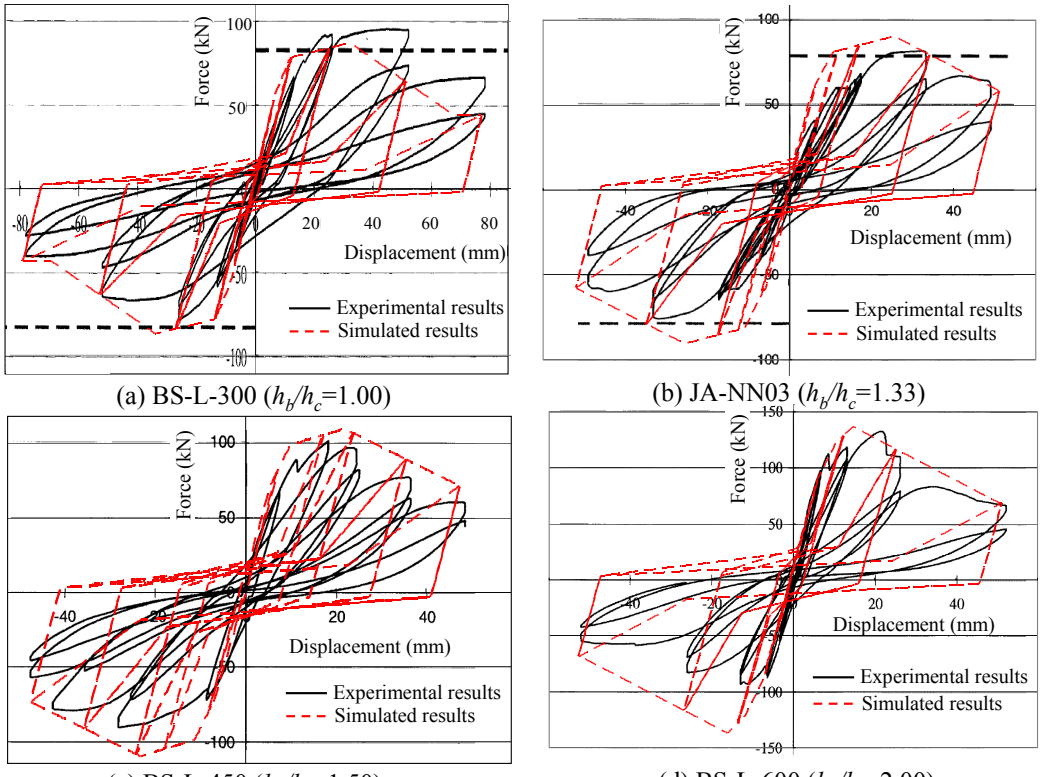

(a) BS-L-300 (h_b/h_c=1.00)

(b) JA-NN03 (h_b/h_c=1.33)

(c) BS-L-450 (h_b/h_c=1.50)

(d) BS-L-600 (h_b/h_c=2.00)

Figure VII.15 Simulations of four specimens tested by Wong (2005) using the proposed model.

VII-4 Simulation of Prototype Buildings

VII-4.1 Description

Two hypothetical prototype buildings are designed with guidelines from the design details of the Van Nuys Holiday Inn Hotel used as the prototype of the test matrix, as discussed in Chapter IV. The transverse frame of the structure, which has three bays, is considered in this simulation. The lateral resisting system of this building is RC moment resisting frame. The building was designed per Los Angeles City Building Code 64 (1964) and was built in 1966. Therefore, the design details of the Van Nuys Holiday Inn can be considered to represent non-ductile old-type existing RC buildings.

One prototype building is designed to be identical with the original details of the Van Nuys Holiday Inn structure, except for the shear reinforcement in the columns and beams as discussed below, and this prototype building is referred to hereafter as "reference building". The material properties, beam and column schedule, and layout are presented in Table VII.3 and Figure VII.16. From the shear strength prediction of the beam-column joints in the reference building, it is expected that the failure of all the beam-column joints is accompanied by beam yielding. To observe the change of the lateral response for the case of joint failure without beam yielding, an additional prototype building is designed with increasing flexural strength of the beams and columns of the original Van Nuys Holiday Inn structure, referred to hereafter as "strengthened building". The modifications of the strengthened building from the original Van Nuys Holiday Inn are presented in Table VII.4. To focus on the effect of the beam-column joints on the lateral response, beams and columns for both buildings are assumed to have enough shear reinforcement to prevent their shear failures. Furthermore, floor slabs are not included for simplicity. It is worth mentioning that shear-critical columns will be included in the progressive collapse analysis which will be pursued as a future extension of this study. For example of a shear-critical column model, the shear friction-based model developed by Elwood (2002) and recently updated in (Elwood and Moehle, 2005) to account for shear-axial interaction is implemented in OpenSees (2010) and it is utilized for progressive collapse analysis by Talaat and Mosalam (2007).

Table VII.3 Details of the reference building.

	Dimension ($b_c \times h_c$, in.)	Rebars (f_y, ksi)	Concrete (f'_c, psi)	Floor	C-9	C-18	C-27	C-36
Column	14×20	60	5,000	1st	8-#9	12-#9	12-#9	8-#9
			4,000	2nd	6-#7	8-#9	8-#9	6-#7
		60	3,000	3rd	6-#7	8-#9	8-#9	6-#7
				4th	6-#7	6-#9	6-#9	6-#7
				5th	6-#7	6-#7	6-#7	6-#7
				6th	6-#7	6-#7	6-#7	6-#7
				7th	6-#7	6-#7	6-#7	6-#7
	$b_b \times h_b$	f_y	f'_c	Floor	Location	B4	B5	B6
Beam	14×30	40	4,000	2nd (2FS-)	Top	3-#9	3-#9	2-#9
					Bot.	2-#9	2-#8	2-#9
	14×22.5	40	3,000	3rd (FS-)	Top	3-#10	3-#10	3-#10
					Bot.	2-#8	2-#8	2-#8
				4th (FS-)	Top	3-#10	3-#10	3-#10
					Bot.	2-#8	2-#8	2-#8
				5th (FS-)	Top	3-#9	3-#9	3-#9
					Bot.	2-#8	2-#8	2-#8
				6th (FS-)	Top	3-#9	3-#9	3-#9
					Bot.	2-#8	2-#8	2-#8
				7th (FS-)	Top	2-#9	3-#8	2-#9
					Bot.	2-#8	2-#8	2-#8
	14×22	40	3,000	Roof (RS-)	Top	2-#8	3-#7	2-#8
					Bot.	2-#7	2-#7	2-#7

Table VII.4 Modification of the strengthened building.

	Dimension ($b_c \times h_c$, in.)	Rebars (f_y, ksi)	Concrete (f'_c, psi)	Floor	C-9	C-18	C-27	C-36
Column	14×20	80	5,000	1st	10-#10	12-#10	12-#10	10-#10
			4,000	2nd	8-#9	10-#9	10-#9	8-#9
			3,000	3rd-6th	8-#9	10-#9	10-#9	8-#9
				7th	8-#8	10-#8	10-#8	8-#8
	$b_b \times h_b$	f_y	f'_c	Floor	Location	B4	B5	B6
Beam	14×30	80	4,000	2nd (2FS-)	Top	3-#9	3-#9	3-#9
					Bot.	3-#9	3-#9	3-#9
	14×22.5		3,000	3rd -7th (FS-)	Top	3-#9	3-#9	3-#9
					Bot.	3-#9	3-#9	3-#9
	14×22		3,000	Roof (RS-)	Top	3-#8	3-#8	3-#8
					Bot.	3-#8	3-#8	3-#8

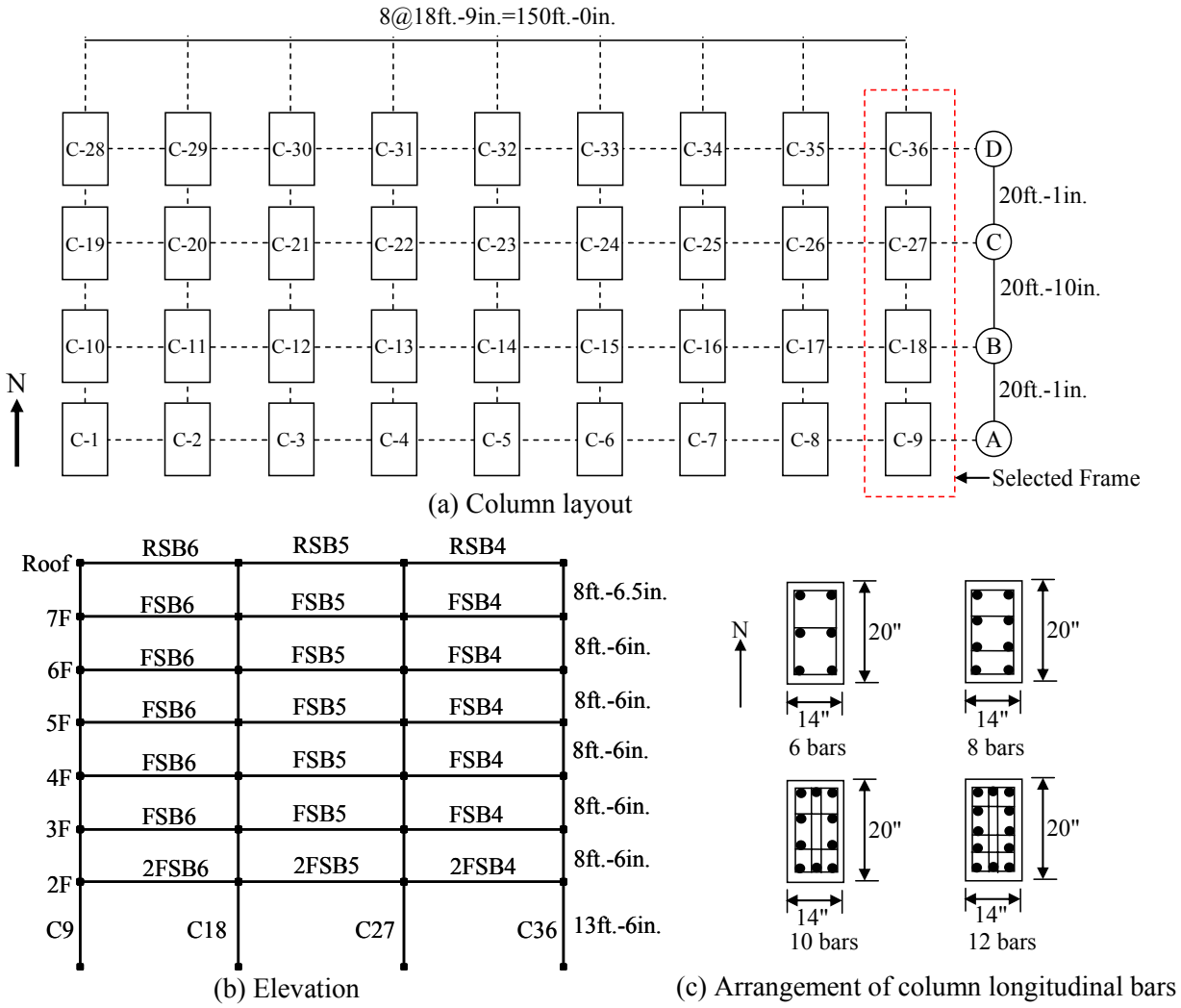

Figure VII.16 Layout of Van Nuys Holiday Inn building (Krawinkler, 2005).

VII-4.2 Modeling

The prototype building frame is modeled using the following uniaxial materials in OpenSees (2010):

1. Cover concrete of beam and column: *Concrete01*;
2. Confined core concrete of beam and column: *Concrete01*; and
3. Reinforcing bars of beam and column: *Steel02*.

It is noted that *Concrete01* is adopted for modeling both cover and core concrete in the beams and columns cross-section for numerical stability, especially in dynamic analysis. In this modeling, slabs are not considered in the prototype frame. Moreover, *nonlinearBeamColumn* is used for modeling the beam and column elements and five integration points are assigned in each element as considered in the previous simulations of the beam-column subassemblies. The cross-sections of beam and column are discretized along the depth using layers with thickness of 0.5 in. (12.7 mm) for each layer, where each layer is divided into three fibers to represent the concrete cover and the core material as discussed for the simulations of the beam-column subassemblies.

For modeling of the joint rotational springs, the developed backbone relationship is applied to the exterior joints and further extended to the interior joints and joints in the roof. The ACI 352 and ASCE 41 provisions for joint shear strength give an idea for the extension of the proposed backbone curve to other types of joints. According to ACI 352 and ASCE 41, joint shear strengths are differently defined depending on the number of beams and columns framing into joints, as shown in Figure VII.17. The concept of these two code provisions is that joint shear strength is changed by the joint confinement condition which is provided by the surrounding beams and columns, and there exist certain ratios among those different joint shear strengths. The ratios of shear strengths of three other types of joints with respect to the exterior joint shear strength are calculated and selected values are presented in Table VII.5. The joint shear strengths for interior joints, roof interior joints and roof exterior joints are estimated using the proposed semi-empirical model considering the following modifications and assumptions:

1. Upper and lower limits for a given joint aspect ratio are modified as follows:

$$\Gamma \times 10 \frac{\cos\theta}{1.31 + 0.085\left(h_b / h_c\right)} \le \frac{V_{jh}}{b_j h_c \sqrt{f_c'}} \le \Gamma \times 23 \frac{\cos\theta}{1.31 + 0.085\left(h_b / h_c\right)} \qquad \text{(VII.3)}$$

   where Γ is a coefficient to represent the shear strength ratio of other joint types with respect to the exterior joint, e.g. $\Gamma = 1.67$ for interior joints, $\Gamma = 1.00$ for roof interior joints, and $\Gamma = 0.67$ for roof exterior joints, as selected in Table VII.5.
2. The same equation of beam reinforcement index is also applicable to the three other joint types because this index is derived based on the global equilibrium. For interior joints, the total sectional area of beam longitudinal reinforcement in tension becomes the sum of the cross-sectional area of top bars in one side of the joint and bottom bars in the other side of the joint, refer to Figure VII.18. For roof joints, the height between upper and lower column inflection points used in defining the beam reinforcement index (Equation III.12), can be taken as half of the last story height.
3. The same over-strength factor for exterior joints is used to determine the shear strengths of the three other joint types.

4. The parameters of the joint rotation for the three other types of joints are assumed to be identical with those of the exterior joints.

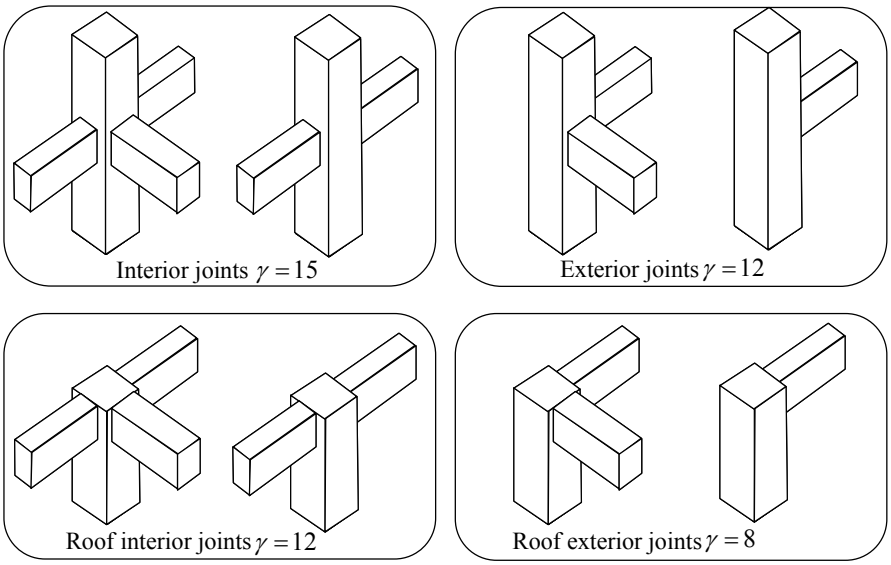

(a) Joint shear strengths in ACI 352

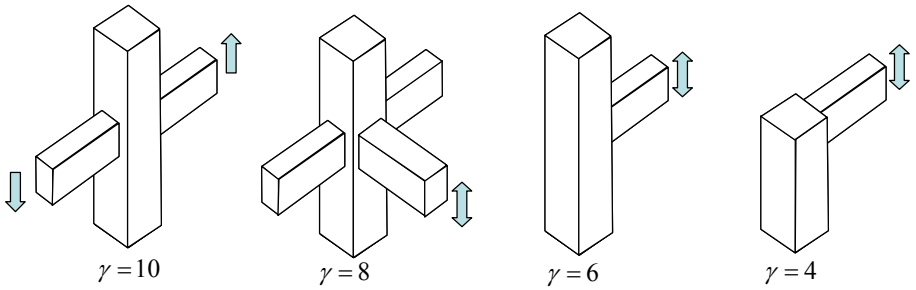

(b) Joint shear strengths in ASCE 41

Figure VII.17 Joint shear strengths in ACI 352 and ASCE 41.

Table VII.5 Joint shear strength comparison for different joint types.

Type	ACI 352		ASCE 41		Selected Γ
	γ	Γ [*1]	γ	Γ	
Exterior joints	12	1.00	6	1.00	1.00
Interior joints	15	1.67	10	1.67	1.67
Roof interior joints	12	1.00	6[*2]	1.00	1.00
Roof exterior joints	8	0.66	4	0.66	0.66

[*1]: $\Gamma = \gamma / \gamma_{exterior}$

[*2]: This value is not explicitly specified but it can be postulated that this joint type has the same strength as the exterior joint because these two joints are geometrically identical with a 90^o turn.

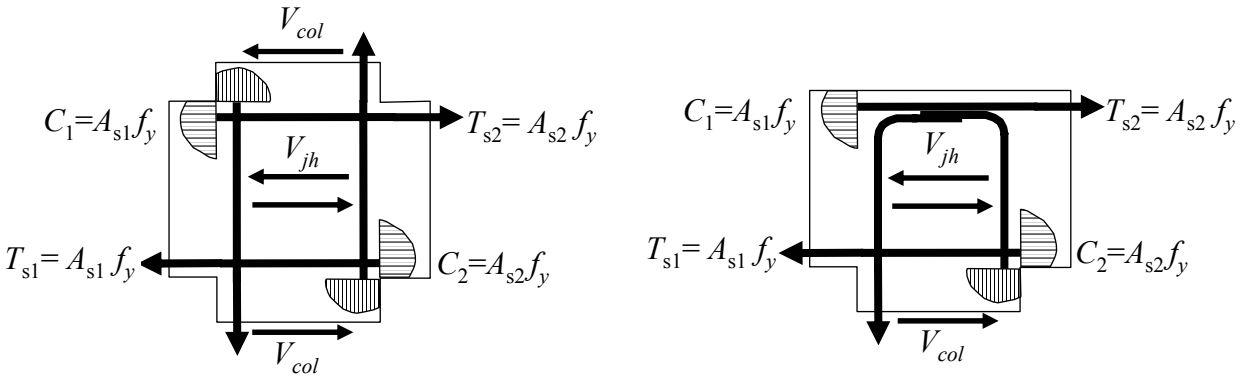

$$V_{jh} = C_1 + T_{s2} - V_{col} = T_{s1} + T_{s2} - V_{col} = (A_{s1} + A_{s2}) f_y - V_{col}$$

Figure VII.18 Equilibrium in interior beam-column joints.

VII-4.3 Nonlinear Static Analysis

Nonlinear static (push-over) analysis is performed to investigate how the response changes depending on the inclusion of joint flexibility. The lateral load pattern is selected as follows,

$$F_i = \omega_i W_{total}, \qquad \omega_i = \frac{W_i h_i}{\sum_{j=1}^{n} W_j h_j} \tag{VII.4}$$

where F_i is the reference lateral load at the i^{th} story, W_{total} is the total weight of the frame, ω_i is vertical distribution factor at the i^{th} story, and h_i is the height from the ground to the i^{th} story. The total weight of the frame is taken as the total building weight divided by the number of frames in the transverse direction assuming that lateral displacement of each frame is identical in the same story due to the floor slab, i.e. diaphragm action. The determined values are shown in Figure VII.19.

Figures VII.20 and VII.21 show the response in terms of the base shear versus the critical story and roof drifts for the two prototype buildings. For each prototype building, the lateral responses are compared between the model with joint rotational springs and the model with rigid joints. The drift is defined as the story displacement divided by the height from the ground to the corresponding story beam level. For instance, the roof drift is equal to the roof displacement divided by the total height of the building. The critical story in each analysis is selected as the one showing the largest story drift at the peak base shear among the six stories except for the roof, based on the lateral deformed shape shown in Figure VII.22. In this regard, the second story is the critical story in the reference building, while the third story is the critical story in the strengthened building, as shown from the drift profiles in Figure VII.22.

For the reference building, at 75% of the peak base shear obtained from the rigid joints model, the second story displacement of the model with joint rotational spring reaches 2.26 inch which is 1.65 times more than that of the model with rigid joints, i.e. 1.37 inch. At 2% of second story drift, the base shear of the model with joint rotational spring is equal to 125 kips, while it is equal to 143 kips in the rigid joint model. Consequently, the lateral load carrying capacity of the reference building including joint flexibility is estimated to be 13% less than that obtained from the analysis with the conventional rigid joints model. This reduction is not significant because the shear strengths of all the beam-column joints are obtained after beams yielding. More reduction of the base shear is expected in the strengthened building where joints are expected to fail before beam yielding.

For the strengthened building, at 2% of roof drift, the base shear for the model with joint rotational springs reaches 190 kips which is about 83% of the base shear for the rigid joint model, i.e. 230 kips. Furthermore, the base shear begins to decrease drastically beyond the roof drift of 1.5% in the model with joint rotational springs, while the base shear for the rigid joints model keeps increasing due to strain hardening of the reinforcing bars. In conclusion, the response of the structure having unreinforced joints is strongly affected by whether joint flexibility is included or not, and the difference is more considerable if joints are subjected to shear failure before beam yielding.

From the push-over curves presented in Figure VII.20 and VII.21, it is found that the initial stiffness is reduced as joint rotational springs are included in the computational model because the rotational springs increase the flexibility of the building. Therefore, fundamental period of the building is also affected by the inclusion of the joint flexibility, which provides a motivation for conducting the dynamic analysis in the subsequent section.

Although the push-over analysis does not consider shear failure of columns, the shear demands of columns in the reference building are compared with their shear strengths by ACI 318-08 in Figure VII.23(a). For this purpose the following equations are used.

$$V_u = \phi(V_c + V_s), \qquad V_c = 2\left(1 + \frac{P}{2000 A_g}\right)\sqrt{f_c'} b_c d_c \text{ and } V_s = \frac{A_v f_{yt} d_c}{s} \tag{VII.5}$$

where the strength reduction factor is 0.75, A_v and f_{yt} are the cross-sectional area and yield strength of column hoop, d_c is the effective cross-sectional depth of the column, and s is column hoop spacing. From the results in Figure VII.23(a) for the first three story exterior columns (labeled C9 and C36 in Figure VII.16), the first story columns (1C36 in VII.23(a) and also 1C9 if load direction is reversed) can be subjected to shear failure around the peak base shear but other columns are not likely to fail in shear. It is worth mentioning that the shear strengths of all the columns are Figure VII.23(b) shows that the column loading equation applied to specimens SP3 and SP4, which is similar to the exterior joint of the first story frame of the reference prototype building, is close to the analysis results.

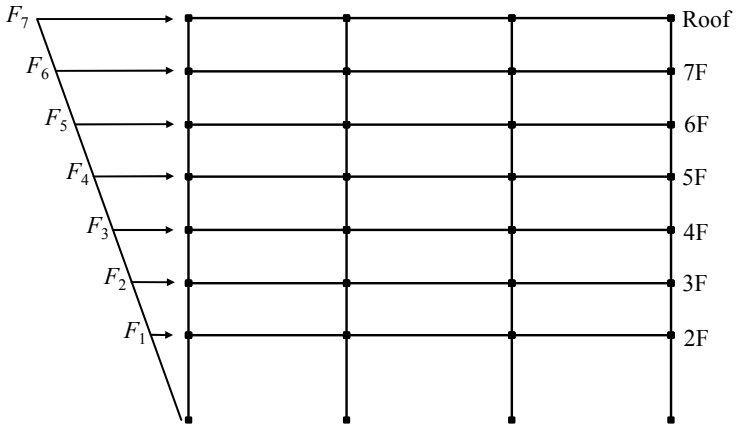

Story	F_i (kip)	ω_i	$W_i h_i$ (kip-in.)
7	262	0.234	120741
6	227	0.203	104762
5	192	0.172	88860
4	158	0.141	72959
3	123	0.110	57058
2	90	0.080	41156
1	67	0.060	30929
$\sum$	1119	1.000	516465

Figure VII.19 Reference lateral load distribution in push-over analysis.

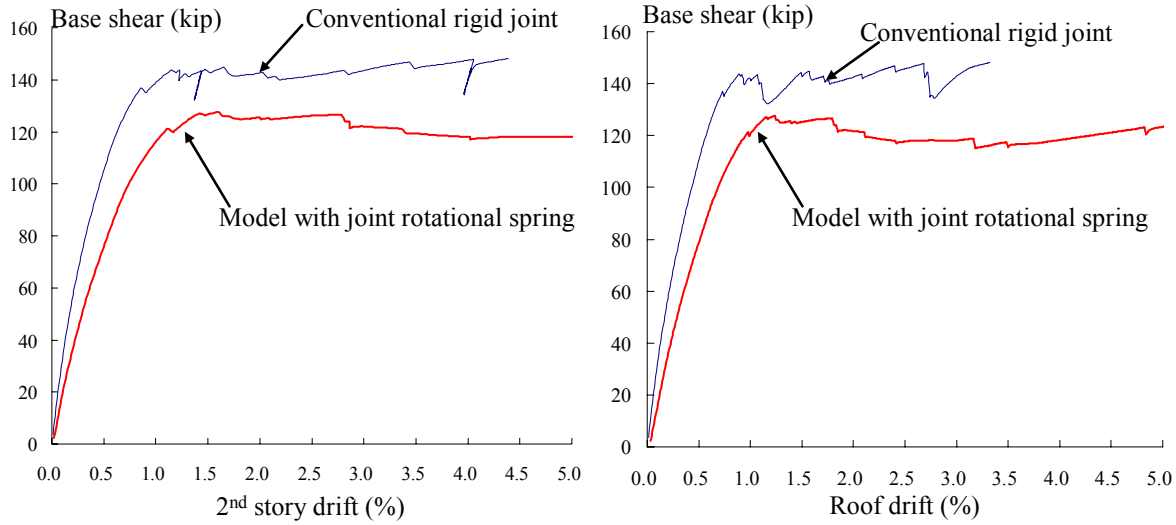

(a) Base shear versus 2nd story drift (b) Base shear versus roof drift

Figure VII.20 Response of base shear versus drift for the reference building.

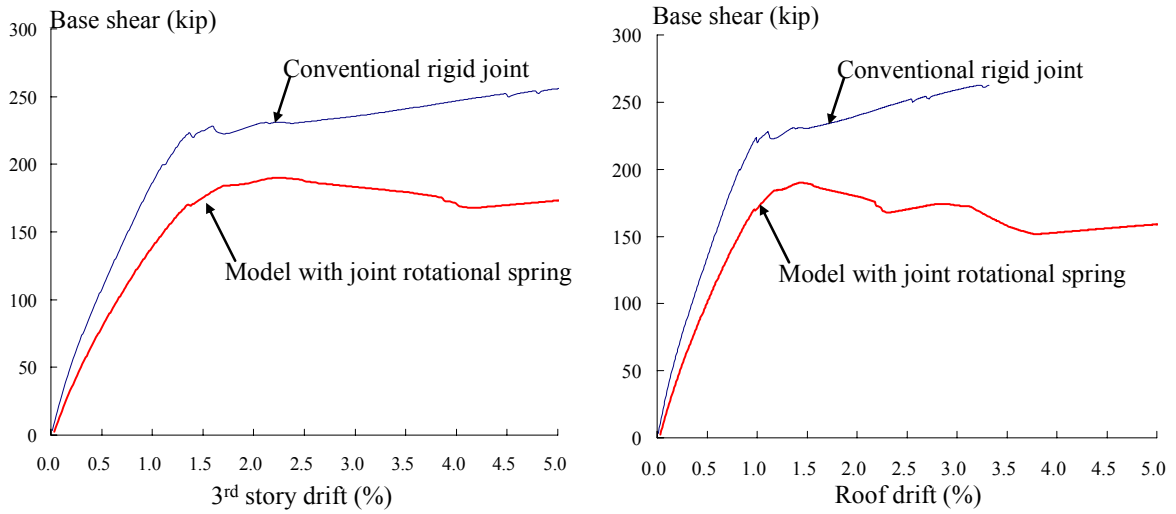

(a) Base shear versus 3rd story drift (b) Base shear versus roof drift

Figure VII.21 Response of base shear versus drift for the strengthened building.

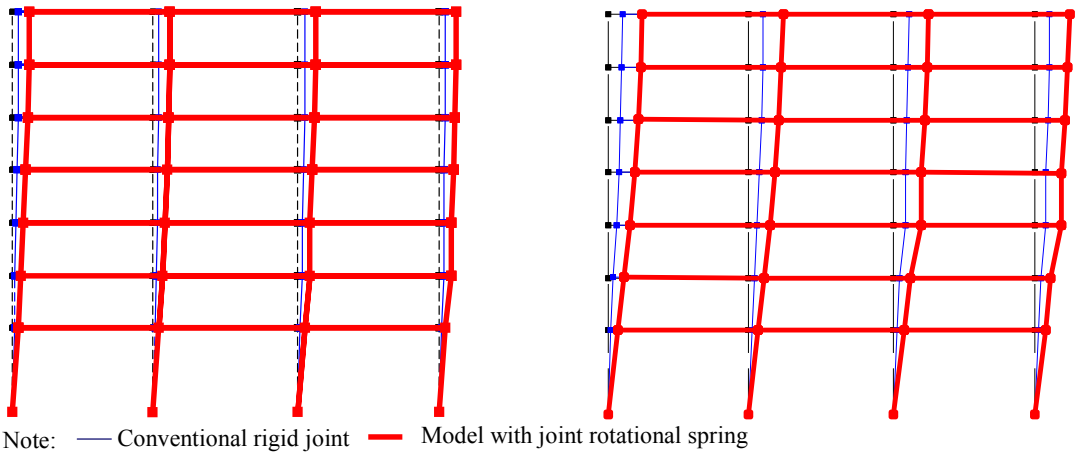

(a) Deformed shape of the reference building (b) Deformed shape of the strengthened building

Figure VII.22 Deformed shape of the two prototype buildings.

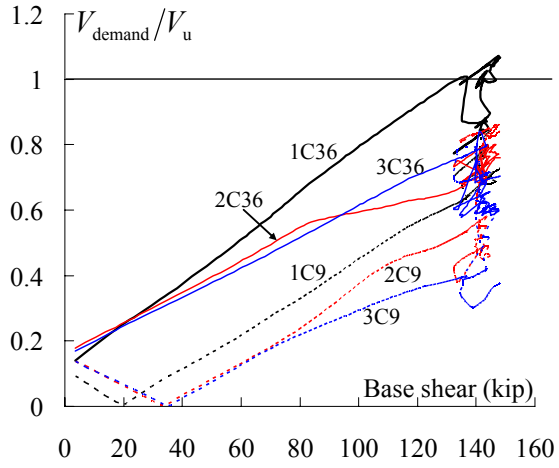

(a) Ratio of column shear demand to strength

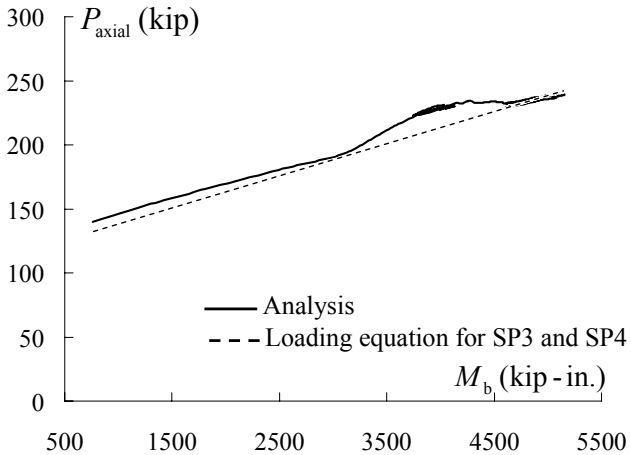

(b) Relationship of column (1C36) axial load and beam (2FSB4) moment

Figure VII.23 Column shear and axial load response.

VII-4.4 Nonlinear Dynamic Analysis

The previous static analysis shows that the initial stiffness of the prototype building is different between the model with joint rotational springs and that with rigid joints. The change of the initial stiffness results in change of the fundamental period of the frame. This observation stimulates the need to perform dynamic analysis of the frame. The input ground motion used for this dynamic analysis was recorded during Northridge (1994) earthquake (Tarzana station in the 90° direction) and scaled to peak ground acceleration PGA = 1.04g approximately corresponding to 2% probability of being exceeded in 50 years (hereafter referred to as 2/50 hazard level) and peak ground PGA = 0.62g corresponding to 10% probability of being exceeded in 50 years (hereafter referred to as 10/50 hazard level) at the location of Van Nuys Holiday Inn building. For reference, 10/50 and 2/50 hazard levels are defined as Basic Safety Earthquake 1 and 2, respectively, in FEMA 356. The ground motion and pseudo-spectral acceleration (PSa) are presented in Figure VII.24.

The fundamental periods of the two prototype buildings are presented in Table VII.6. It is obvious that the fundamental period increases for the model with joint rotational springs in both prototype buildings. Time history responses of the two prototype buildings are presented in Figures VII.25 through VII.27. It is shown that the peak drift is greater in the model with joint rotational spring even though its peak base shear is less than the model with rigid joints. The residual displacement is also observed in post-failure response for the model with joint rational springs, which is quite different from the response for the model with rigid joints.

When the reference building is subjected to the 10/50 hazard level ground motion, the peak critical story drift is 0.9% if modeling the joints as rigid connection but this drift increases up to 1.8% by including the joint flexibility which can be acceptable value. However, the drift value of 1.8% should not be interpreted as a ductile response of the building because this drift is significantly attributed to the damage of the joints in the building as the residual displacement is observed in the post-failure response. For the 2/50 hazard level, the critical story drift in the reference building is equal to 2.3% for the model with rigid joints and 2.9% for the model with joint rotational springs. These drift values represent the significant damage of beams and columns as well as joints in the building which can lead to collapse of the building if the shear and axial failure model for the columns are modeled in this analysis.

For the strengthened building responses under the 10/50 hazard level ground motion, the peak critical story drift is 0.7% in the model with rigid joints and 1.2% in the model with joint flexibility. This building remains elastic even with including the joint flexibility because there is no residual displacement at the end of excitation. If the 2/50 hazard level ground motion is applied to the strengthened building, the lateral responses of this building are significantly changed by including the joint flexibility. The peak critical story drift increases from 1.6% in the model with rigid joints to 3.3% in the model with the joint flexibility. The residual displacement is observed only in the model with joint flexibility. From these observations in the strengthened building, the lateral responses are significantly changed by considering joint flexibility, in particular, if the building includes unreinforced joints with flexural beams such that the failure of joints occur before beam yielding.

In conclusion, dynamic responses of the two prototype buildings are strongly affected by the modeling of the beam-column joint flexibility using joint rotational springs and thus the inclusion of joint flexibility is essential for simulating the earthquake response of older-type RC buildings having unreinforced beam-column joints.

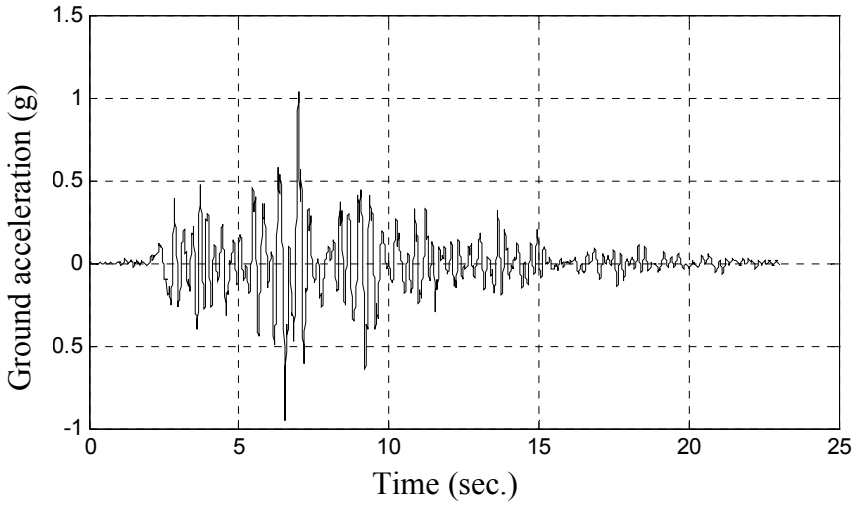

(a) Ground motion (PGA = 1.04g)

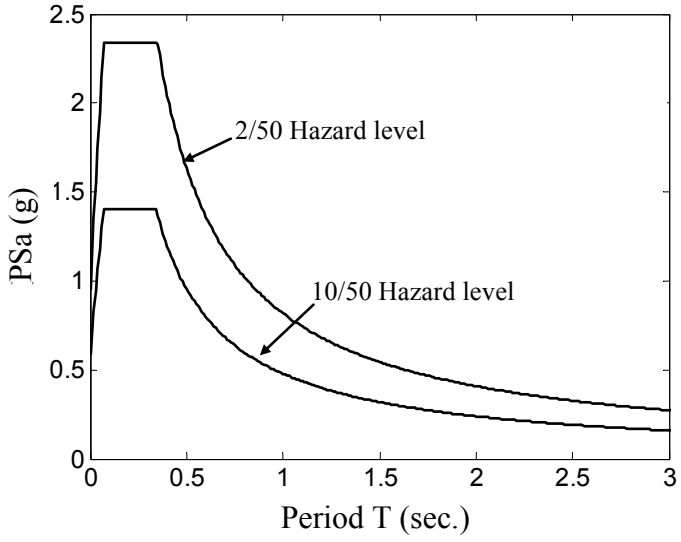

(b) Spectral acceleration

Figure VII.24 Selected ground motion and spectral acceleration.

Table VII.6 Fundamental period of the two prototype buildings.

Building	Reference building		Strengthened building	
	Model with joint rotational springs	Model with rigid joints	Model with joint rotational springs	Model with rigid joints
Period (sec.)	1.63	1.29	1.53	1.28

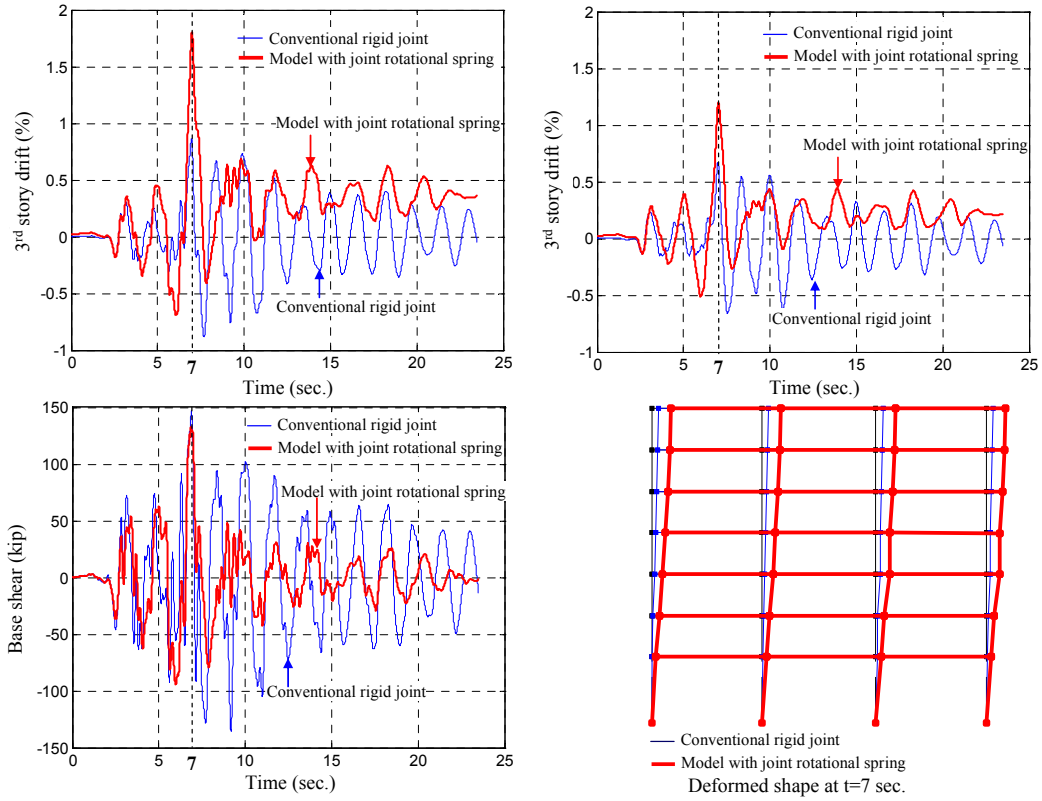

Figure VII.25 Dynamic response of the reference building for 10/50 hazard level.

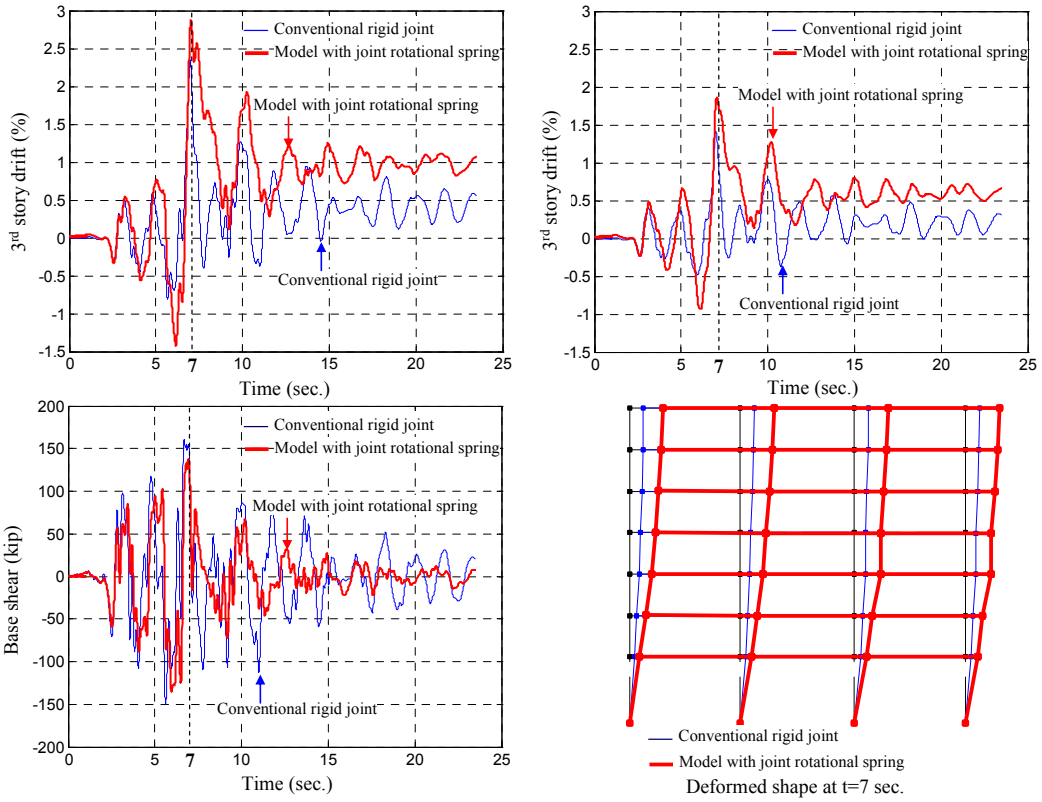

Figure VII.26 Dynamic response of the reference building for 2/50 hazard level.

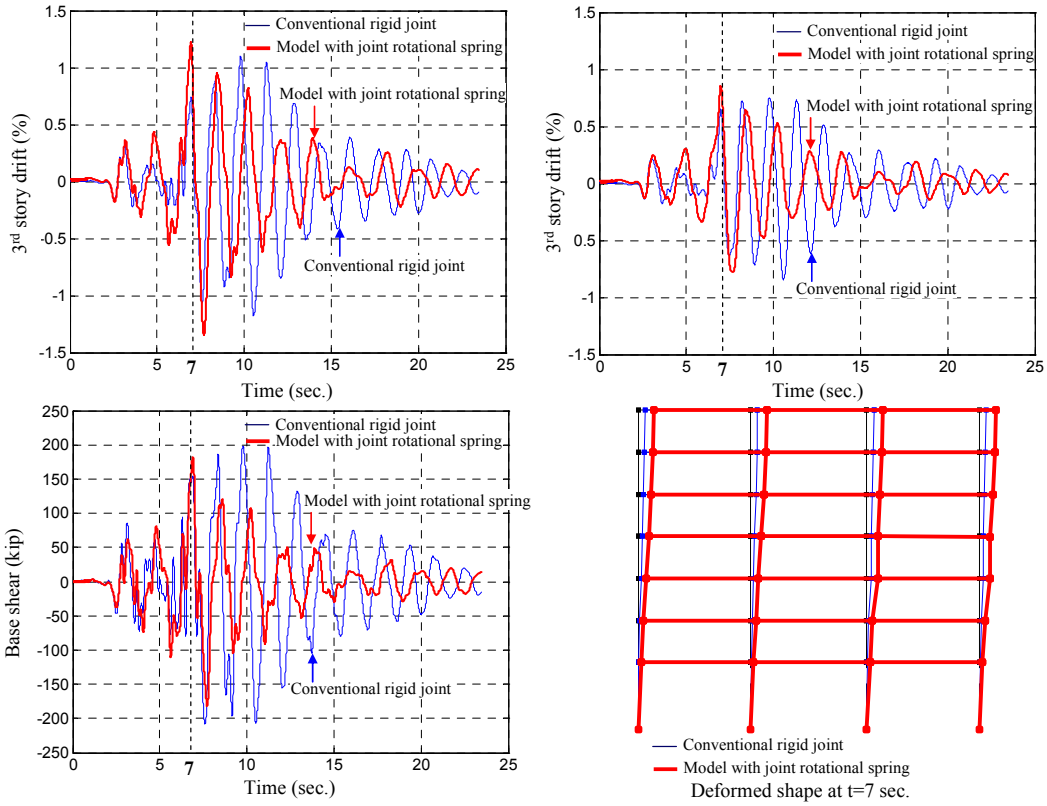

Figure VII.27 Dynamic response of the strengthened building for 10/50 hazard level.

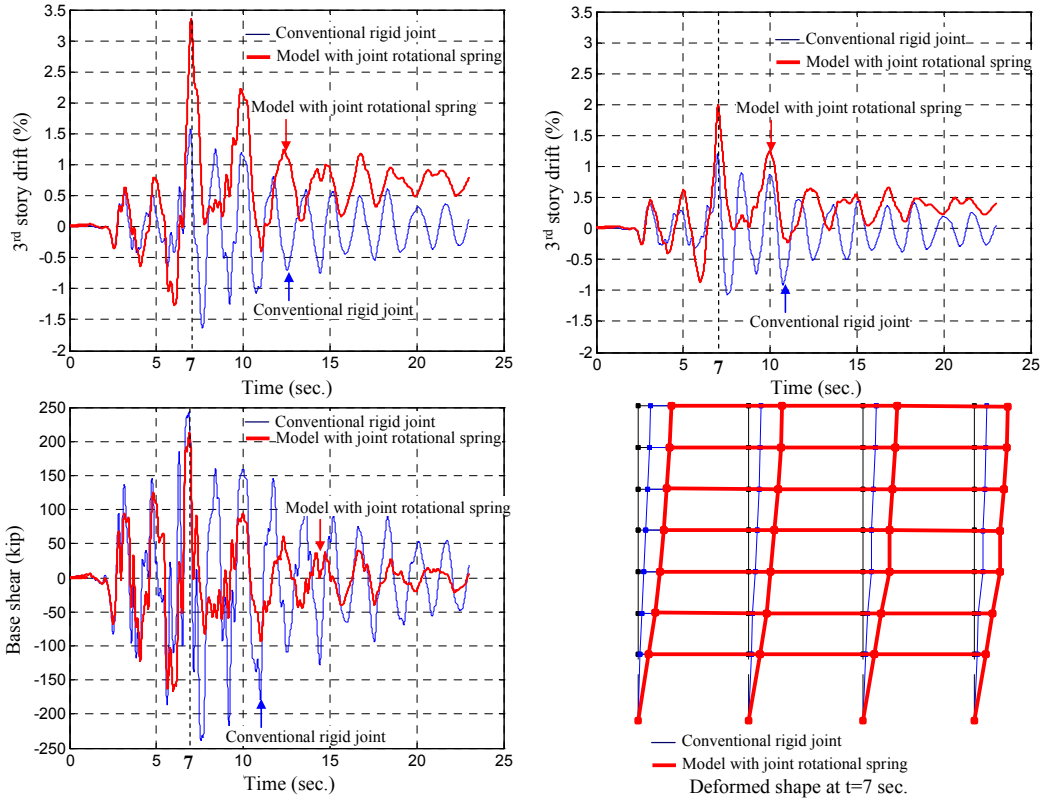

Figure VII.28 Dynamic response of the strengthened building for 2/50 hazard level.

VIII Summary, Conclusions and Future Extensions

VIII-1 Summary and Conclusions

Understanding and modeling the behavior of unreinforced exterior joints under earthquake loading is of interest in this study. To achieve the study goals, an analytical and experimental research program is performed.

The first stage of this study is to collect a large amount of unreinforced exterior and corner beam-column joint test data from literature with consistent criteria for data selection. From the parametric study using the collected experimental test database, shear strength of unreinforced exterior joints is strongly affected by two parameters: (1) joint aspect ratio and (2) beam flexural strength. In parallel with the parametric study, existing joint shear strength models and joint macro-modeling methods for structural simulation are reviewed to develop an accurate strength model and backbone relationships for unreinforced exterior joints. From the first stage of this study, the following conclusions are drawn:

1. Shear strength of unreinforced exterior beam-column joints decreases as the joint aspect ratio increases. This is because a steeper diagonal strut is developed for high joint aspect ratio and therefore such strut is less effective to equilibrate the horizontal joint shear force. This conclusion is consistent with the trend observed in the experimental database.
2. From the experimental database, it is found that the scatter in the joint shear strengths for a given joint aspect ratio is bounded between upper and lower limits. Between the upper and lower limit of the joint shear strength for a given joint aspect ratio, the joint shear strength is linearly proportional to the beam reinforcement index. This finding is explained by the two shear strength models developed in this study.
3. The column axial load has little influence on the joint shear strength of unreinforced beam-column joints for column axial load less than $0.2f_c'A_g$ because the column axial load produces both beneficial and detrimental effects to the joint shear strength and the combined effect becomes insignificant compared with the above mentioned two influential parameters.
4. The average principal stress and strain compatibility equations, which are the basic concept of most existing models, are not able to reflect realistic behavior of unreinforced exterior beam-column joints because the joint shear failure is localized in these unreinforced joints. In particular, the tensile strains of the beam and column longitudinal reinforcements cannot represent average strains for the horizontal and vertical directions in the joint panel. Moreover, the strut-and-tie (SAT) approach in such joints faces the critical issue of estimating the diagonal strut area because the joint shear strength is shown to be sensitive to this estimated area.
5. In the existing models, three modification methods are adopted to obtain the reduced shear strength for joint shear failure following beam reinforcement yielding: (1) directly

reducing the joint shear strength, (2) reducing the area of diagonal strut by a ductility factor, and (3) reducing the applied joint shear force in the average joint stress equilibrium equation by a ductility factor. These modifications are not practical because the ductility factor needs to be monitored during the analysis of the structural systems. Moreover, the relationship between the reduction of the joint shear strength and the ductility factor is proposed empirically in each model.

For the second stage of this study, two shear strength models to reflect the effect of the aforementioned two parameters are developed by semi-empirical and analytical approaches. The equation to represent the effect of joint aspect ratio is derived based on a SAT concept using equilibrium in the joint region and a softening concrete model, while another equation for the beam reinforcement index to represent the effect of beam flexural strength is derived using global equilibrium in a beam-column subassembly and approximations of some variables. The semi-empirical model is developed based on a single strut mechanism using two derived parametric equations. The basic concept of the semi-empirical model is that for a certain joint aspect ratio, the upper and lower limit of the joint shear strength are determined by the equation reflecting the joint aspect ratio effect and then between the upper and lower limits, the joint shear strength is linearly proportional to the beam reinforcement index. In the analytical model, two inclined struts are assumed to resist the horizontal joint shear in parallel, where the horizontal joint shear force is resisted by the sum of the two horizontal components of the two struts but the shear distortion is uniformly distributed. The contribution of each strut to the total joint shear is formulated using the bond resistance of the beam longitudinal tension reinforcement. The joint shear failure is defined when the demand of the diagonal strut reaches its capacity. In the second stage of this study, the following conclusions are drawn:

6. Two derived equations are proven to adequately represent the effects of the joint aspect ratio and the beam reinforcement index by the comparison with the experimental database.
7. Using the parametric equation of the joint aspect ratio, the upper and lower limits of the joint shear strength are empirically defined based on the comparison with the experimental database.
8. The upper and lower limits of the joint shear strength are also obtained analytically as follows:
    a. The parametric equation of the joint aspect ratio gives the upper limit by choosing the coefficients to represent the J failure mode which corresponds to the upper limit.
    b. The analytical model shows that the fraction factor for the upper limit specimens from the database is close to 0.35. This fraction factor can be considered as the ratio of the lower limit to the upper limit.

    These analytical upper and lower limits are coincident with the empirically determined ones.
9. Despite of simplicity, the proposed semi-empirical model predicts the shear strength of the experimental database specimens with high accuracy compared with several existing models.
10. The analytical model accurately predicts the shear strength of unreinforced exterior beam-column joints for both types of joint failure, i.e. joint shear failure with (BJ) and without (J) beam reinforcement yielding, through a consistent procedure.

11. The occurrence of beam longitudinal reinforcement yielding at joint failure is accurately captured by the analytical model without the need for the complexity of ductility consideration.
12. The relationship of moment versus rotation in the joint region is derived from the analytical model and implemented as a joint rotational spring. The preliminary simulations using this joint rotational spring successfully reproduce the force-displacement responses of four published tests, which were intended to show different types of joint failure.

Thirdly, an experimental test program is conducted. Four full-scale corner beam-column joint specimens are constructed with RC slabs. The test matrix addresses two parameters: (1) the joint aspect ratio, and (2) the beam longitudinal reinforcement ratio. Two values of the joint aspect ratio and two values of the beam longitudinal reinforcement are presented in the test matrix. The lateral load is quasi-statically applied through controlled displacement at the end of each beam. The applied displacement alternates between the two beams, i.e. one beam remains at a reference point during the loading of the other orthogonal beam. Column axial load varies in real time following a predefined equation which is a function of the shear forces applied to the beams. The joint shear strengths of the test specimens are evaluated and compared with the predictions by the proposed joint shear strength models. The test results are discussed focusing on the effects of the joint aspect ratio, the beam reinforcement index, the slab contribution, the transverse beam loading, and the column intermediate bars. The joint shear strain and relative deformation at the beam-joint interface are measured in order to convey key information to the next stage of this research. In the third stage of this study, the following conclusions are drawn:

13. The two proposed models accurately predict the shear strengths of four specimens with 2% and 8% errors, respectively. If the joint shear strengths are compared for the EW direction only because of the lower strength of NS direction due to the loading sequence, the accuracy of semi-empirical model is retained but the analytical model shows the underestimation of the joint shear strength by 13%. Alternatively, the analytical model is modified to prevent its underestimation for the specimens having large bar diameters and its prediction is accordingly improved to have only 1% error for both directions and 3% error for the EW direction only.
14. For the effect of joint aspect ratio, the joint shear strengths for specimens SP1 and SP2 having $h_b/h_c = 1.00$ are greater than that for specimens SP3 and SP4 having $h_b/h_c = 1.67$. The joint shear strength reduction is fit into the trend shown in the experimental database for specimens ranging from $h_b/h_c = 1.00$ to $h_b/h_c = 1.67$.
15. With increase of beam longitudinal reinforcement ratio, the joint shear strengths also increased. This result can be an evidence that the joint shear strength is proportional to the beam reinforcement index up to a certain limit. This upper limit is proposed in Chapter III and it will be clarified by ongoing tests having larger beam longitudinal reinforcement ratios than that in specimens SP2 and SP4.
16. The contribution of slab reinforcement to the horizontal joint shear stress is different depending on the type of joint failure, i.e. joint shear failure with or without beam reinforcement yielding. Based on the measured strain data of the slab reinforcement, the effective slab width under lateral loading is proposed to be related to the ratio of the beam reinforcement index to the upper limit of the joint shear strength for a given joint aspect ratio. Further investigation is needed to validate the proposed estimation.

17. The joints in the longitudinal direction undergo cracking and twisting by the transverse beam loading but the damage appears to be negligible. In general, the damage induced by the transverse beam loading have little influence on the behavior of the joint for the subsequent longitudinal loading.
18. There is no strong evidence that the column intermediate longitudinal bars act as tension ties in joint shear resisting mechanism. This is attributed to the fact that inclined struts between the column intermediate and outer bars are hardly developed because of the steep angle of these struts and the bond deterioration of these bars.

Lastly, backbone relationships for the unreinforced exterior joints are developed. Based on the measured joint shear stress-rotation and visual observation of the corner joint tests, multi-linear backbone relationships are proposed to reflect the following aspects: (1) initial joint cracking, (2) either beam reinforcement yielding or significant opening of existing joint cracks, (3) either existing joint cracks further propagation or additional joint cracks opening at the peak, and (4) residual joint shear stress and rotation at unacceptable joint performance. Modeling parameters to represent these aspects are defined from the comparison with test results. For verification of the proposed backbone relationships, analytical simulations are performed with the subassemblies of the tested four corner joint specimens and additional four planar exterior joint specimens from literature. Furthermore, two prototype buildings are designed with changing the flexural strength of beams and columns in order to achieve different types of joint failure. One is for joint failure without beam yielding and the other is for joint failure followed by beam yielding. Nonlinear static and dynamic analyses are performed with the two prototype buildings to investigate how the structural responses are changed by including joint flexibility in the building model. In the last stage of this study, the following conclusions are drawn:

19. The proposed backbone relationships are validated by accurate reproduction of the load-displacement responses for the tested four corner joint specimens and another four planar joint specimens from literature, while the ASCE 41 provisions are conservative for predicting the shear strength and deformation.
20. The proposed backbone relationships are adequate for simulation of older-type RC buildings having unreinforced exterior joints.
21. Building responses are strongly affected by whether joint flexibility is included or not. By modeling joint flexibility, the lateral load carrying capacity of the building is reduced, and also the fundamental period of the building is increased. The changes of responses are more considerable for the building whose joints are subjected to shear failure before beam yielding.
22. Joint flexibility is essential for simulating beam-column subassemblies and older-type RC buildings containing unreinforced joints. Conventional analyses, where joints are assumed to maintain the orthogonality between beams and columns, may not reflect the realistic responses of those types of RC structures under earthquake loading.

VIII-2 Future Extensions

This study should ultimately culminate to progressive collapse analysis of older-type RC buildings to generate the partial and complete collapse fragility functions for this class buildings under earthquake loads. To reach this ultimate goal, the following tasks should be considered in the future:

1. More test data are required to refine the proposed joint shear strength models and the proposed estimation of the effective slab width.
2. More test data are required to evaluate the proposed backbone relationships for unreinforced exterior joints. In particular, the influence of high column axial load on the backbone relationship is to be investigated with focusing on the axial failure of the joint.
3. Shaking table tests on RC buildings designed with unreinforced joints are needed for further verification of the backbone relationships.
4. Further investigation about simultaneous bi-directional loading effects on shear strength and deformability of unreinforced joints is necessary for three dimensional analyses of older-type RC buildings.
5. Further study is required to accurately modify the developed shear strength models and backbone relationships for interior joints, knee joints and others. Preliminary extension of the proposed semi-empirical model to interior and roof story joints is made for simulating the prototype buildings in this study.
6. For the case of weak column/strong beam, the behavior of unreinforced exterior joints is to be investigated.
7. The progressive collapse analysis necessitates the development of element removal criteria (Talaat and Mosalam, 2008) for unreinforced joints. Furthermore, this requires procedures to be developed to re-define the connectivity and type or internal degrees-of-freedom of beams and columns associated to the removed beam-column joints.
8. Several prototypes of older-type RC buildings are necessary to be identified and idealized for fragility analysis.
9. The joint modeling with a rotational spring and rigid links to beams and columns can be implemented as a standalone element in OpenSees, BuildingTcl (Mazzoni, 2010) for easy adoption in modeling RC structural systems.

REFERENCES

AASHTO (1996). Standard specifications for highway bridges. American Association State and Highway Transportation Officials, Washington DC.

ACI Committee 318 (2008). Building Code Requirements for Structural Concrete (ACI 318-08) and Commentary (318R-08). American Concrete Institute, Farmington Hills, Mich.

ACI-ASCE Commmittee 352 (2002). Recommendations for design of beam-column connections in monolithic reinforced concrete structures (ACI 352R-02). American Concrete Institute, Farmington Hills, Michigan.

ASCE/SEI Seismic Rehabilitation Standards Committee, (2007). Seismic Rehabilitation of Existing Buildings (ASCE/SEI 41-06). American Society of Civil Engineers, Reston, VA.

Alath, S., and Kunnath, S.K. (1995). Modeling Inelastic Shear Deformation in RC Beam-Column Joints. *Engineering Mechanics: Proceedings of Tenth Conference,* University of Colorado at Boulder, ASCE, Vol.2, pp822-825.

Alire, D. A. (2002). Seismic Evaluation of Existing Unconfined RC Beam–Column Joints. *MSCE thesis,* University of Washington.

Altoontash, A., and Deierlein, G.G. (2003). A Versatile Model for Beam-Column Joints. *ASCE Structures Congress Proceedings*, Seattle, Washington.

Anderson, M., Lehman, D., and Stanton, J. (2008). A Cyclic Shear Stress-Strain Model for Joints without Transverse Reinforcement. *Engineering Structures*, No. 30, pp. 941-954.

Antonopoulos, C.P., and Triantafillou, T.C. (2003). Experimental Investigation of FRP-Strengthened RC Beam-Column Joints. *ACSE Journal of Composites for Construction*, V. 7, No. 1, pp 39-49.

Bakir, P.G., and Boduroğlu, H.M. (2002). A new design equation for predicting the joint shear strength of monotonically loaded exterior beam-column joints. *Engineering Structures*, No. 24, pp. 1105-1117.

Bažant, Z. P., and Yu, Q. (2005). Designing Against Size Effect on Shear Strength of RC Beams without Stirrups: II. Verification and Calibration. *ACSE Journal of Structural Engineering*, V. 131, No. 12, pp. 1886-1897.

Beres, A., White, R. N., and Gergely, P. (1992). Seismic Performance of Interior and Exterior Beam-to-Column Joints Related to Lightly RC Frame Buildings: Detailed Experimental Results. *Structural Engineering Report* 92-7, School of Civil and Environmental Engineering, Cornell University.

Biddah, A., and Ghobarah, A. (1999). Modelling of Shear Deformation and Bond Slip in Reinforced Concrete Joints. *Structural Engineering and Mechanics*, V.**7**, No. 4, pp. 413–432.

Booth, E. and Fenwick, R. (1994). Concrete Structures in Earthquake Regions: Design and Analysis. Longman Scientific and Technical, Essex, UK.

Canadian Standard Association. (1994). Design of Concrete Structures. Structural Design, Roxdale, Canada.

Celik, O.C., and Ellingwood, B.R. (2008). Modeling beam-column joints in fragility assessment of gravity load designed reinforced concrete frames. *Journal of Earthquake Engineering*, V.12, No. 3, pp. 357-381.

Clyde, C., Pantelides, C.P., and Reaveley, L.D. (2000). Performance-Based Evaluation of Exterior Reinforced Concrete Building Joints for Seismic Excitation. *PEER Report* 2000/05, University of California, Berkeley.

Collins, M.P, and Mitchell, D. (1986). A Rational Approach to Shear Design-1984 Canadian Code Provisions. *ACI Structural Journal*, V. 83, No. 6, pp. 925-933.

Comité Euro-International du Béton (1993). Bulletin d'Information No. 213/214 CEB-FIP Model Code 1990. Thomas Telford, London, UK.

El-Amoury, T., and Ghobarah, A. (2002). Seismic Rehabilitation of Beam-Column Joints Using GFRP Sheets. *Engineering Structures*, V. 24, No. 11, pp. 1397-1407.

El-Attar, A.G., White, R.N., and Gergely, P. (1992). Shake Table Test of a 1/6 Scale 2-Story Lightly Reinforced Concrete Building. *NCEER-91-0017*, National Center for Earthquake Engineering Research, State University of New York at Buffalo.

Engindeniz, M. (2008). Repair and Strengthening of Pre-1970 Reinforced Concrete Corner Beam-Column Joints Using CFRP Composites. *PhD Dissertation*, Georgia Institute of Technology.

Elwood, K.J., and Moehle, J.P. (2003). Shake Table Tests and Analytical Studies on the Gravity Load Collapse of Reinforced Concrete Frames. *PEER Report 2003/01,* University of California, Berkeley.

Eurocode 2. (1992). Design of concrete structures, Part 1: General rules and rules for buildings (DD ENV 1992-1-1: 1992). Commission of the European Communities.

FEMA Publication 356 (2000). NEHRP Guidelines for the Seismic Rehabilitation of Buildings. Federal Emergency Management Agency, Washington.

Ghannoum, W.M. (2007). Experimental and Analytical Dynamic Collapse Study of a Reinforced Concrete Frame with Light Transverse Reinforcement. *PhD Dissertation*, University of California, Berkeley.

Gencoğlu, M., and Eren I. (2002). An Experimental Study on the Effect of Steel Fiber Reinforced Concrete on the Behavior of the Exterior Beam-Column Joints Subjected to Reversal Cyclic Loading. *Turkish Journal of Engineering & Environmental Science*, V. 26, pp 493-502.

Ghobarah, A., and Said, A. (2001). Seismic Rehabilitation of Beam-Column Joints using FRP Laminates. *Journal of Earthquake Engineering*, V. 5, No. 1, pp 113-129.

Günay, S.M., and Mosalam, K.M. (2010). Structural Engineering Reconnaissance of the April 6, 2009, Abruzzo, Italy, Earthquake and Lessons Learned. *PEER Report 2010/105,* University of California, Berkeley.

Hakuto, S., Park, R., and Tanaka, H. (2000). Seismic Load Tests on Interior and Exterior Beam-Column Joints with Substandard Reinforcing Details. *ACI Structural Journal*, V. 97, No. 1, pp. 11-25.

Hanson, N.W., and Conner, H.W. (1967). Seismic Resistance of Reinforced Concrete Beam-Column Joints. *ACSE Journal of Structural Division*, V. 93, No. ST5, pp 533-560.

Hanson, N.W., and Conner, H.W. (1972). Tests of Reinforced Concrete Beam-Column Joints under Simulated Seismic Loading. *Portland Cement Association Research and Development Bulletin*.

Hegger, J., Sherif, A., and Roeser, W. (2003). Nonseismic Design of Beam-Column Joints. *ACI Structural Journal*, V. 100, No. 5, pp. 654-664.

Hertanto, E. (2005). Seismic Assessments of Pre-1970s Reinforced Concrete Structure. *MSCE thesis,* University of Canterbury.

Hwang, S.J., and Lee, H.J. (1999). Analytical Model for Predicting Shear Strength of Exterior Reinforced Concrete Beam-Column Joints for Seismic Resistance. *ACI Structural Journal*, V. 96, No. 5, pp. 846-858.

Hwang, S.J., Wang, K.C., and Lee, H.J. (2001). Designing and Retrofitting Strategy of Reinforced Concrete Beam-Column Joints. *Proceedings of SINO-UK Joint Workshop on Deep Excavations and Earthquake Resistance Design of Structures*, Taiwan.

Hwang, S.J., and Lee, H.J. (2002). Strength Prediction for Discontinuity Regions by Softened Strut-and-Tie Model. *ASCE Journal of Structural Engineering*, V. 128, No. 12, pp. 1519-1526.

Hwang, S.J., Lee, H.J., Liao, T.F., Wang, K.C., and Tsai, H.H. (2005). Role of Hoops on Shear Strength of Reinforced Concrete Beam-Column Joints. *ACI Structural Journal*, V. 102, No. 3, pp. 445-453.

Jirsa, J.O., Breen, J.E., Bergmeister, K., Barton, D., Anderson, R., and Bouadi, H. (1991). Experimental studies of nodes in strut-and-tie models. Report of the IABSE Colloquium on Structural Concrete. Stuttgart, Germany.

Kanada, K., Kondo, G., and Fujii, S. (1984). and Morita, S., Relation Between Beam Bar Anchorage and Shear Resistance at Exterior Beam-Column Joints. *Transaction of the Japan Concrete Institute*, V. 6, pp. 433-440.

Karayannis, C.G., Chalioris, C.E., and Sirkelis, G.M. (2008). Local Retrofit of Exterior RC Beam-Column Joints Using Thin RC Jackets- An Experimental Study. *Earthquake Engineering and Structural Dynamics*, V. 37, pp. 727-746.

Kim, J., and LaFave, J.M. (2007). Key Influence Parameters for the Joint Shear Behavior of Reinforced Concrete (RC) Beam-Column Connections. *Engineering Structures*, No. 29, pp. 2523-2539.

Kurose, Y. (1987). Recent Studies on RC Beam-Column Joints in Japan. *PMFSEL Report* No. 87-8, University of Texas at Austin.

Kurose, Y., Guimaraes, G., Liu, Z., Kreger, M., and Jirsa, J. O. (1988). Study of Reinforced Concrete Beam-Column Joints Under Uniaxial and Biaxial Loading. *PMFSEL Report* No. 88-2, University of Texas at Austin.

Lehman, D.E., and Moehle, J.P. (1998). Seismic Performance of Well-Confined Concrete Bridge Columns. *PEER Report* 1998/01, University of California, Berkeley.

Li, B., Wang, Z., Mosalam, K.M., and Xie, H. (2008). Wenchuan Earthquake Field Reconnaissance on Reinforced Concrete Framed Buildings With and Without Masonry Infill Walls. The 14th World Conference on Earthquake Engineering, Beijing, China.

Liu, C. (2006). Seismic Behavior of Beam-Column Joint Assemblies Reinforced with Steel Fibers. *MSCE thesis,* University of Canterbury.

Lowes, L.N., and Altoontash, A. (2003). Modeling Reinforced-Concrete Beam-Column Joints Subjected to Cyclic Loading. *ASCE Journal of Structural Engineering*, V. 129, No. 12, pp. 1686-1697.

Lowes, L.N., Mitra, N., and Altoontash, A. (2004). A Beam-Column Joint Model for Simulating the Earthquake Response of Reinforced Concrete Frames. *PEER Report* 2003/10, University of California, Berkeley.

Lynn, A.C. (2001). Seismic Behavior of Existing Reinforced Concrete Building Columns. *PhD Dissertation*, University of California, Berkeley.

MacGregor, J.G. (1997). Reinforced concrete mechanics and design. Prentice-Hall, New Jersey.

Mander, J.B., Priestley, M.J.N., and Park, R. (1988). Theoretical Stress-Strain Model for Confined Concrete. *ACSE Journal of Structural Engineering*, V. 114, No. 8, pp. 1804-1826.

Meinheit, D.F., and Jirsa, J.O. (1977). The Shear Strength of Reinforced Concrete Beam-Column Joints. *CESRL Report* No. 77-1, University of Texas at Austin.

Mitra, N., and Lowes, L.N. (2007). Evaluation, Calibration, and Verification of a Reinforced Concrete Beam-Column Joint Model. *ACSE Journal of Structural Engineering*, V. 133, No. 1, pp. 105-120.

Moehle, J.P. (2008). Private communication.

NZS 3101:1995 (1995). Concrete structures standard (NZS 3101). Standard Association of New Zealand, Wellington, New Zealand.

Ohwada, Y. (1976). A Study on Effect of Lateral Beams on RC Beam-Column Joints (1). *Transaction of AIJ*, Extra, No. 2510.

Ohwada, Y. (1977). A Study on Effect of Lateral Beams on RC Beam-Column Joints (2). *Conference of AIJ*, No. 61.

OpenSees, 2010. Open System for Earthquake Simulation. PEER, University of California, Berkeley. http://opensees.berkeley.edu.

Ortiz, I.R. (1993). Strut-and-Tie Modeling of Reinforce Concrete Short Beams and Beam-Column Joints. *PhD Dissertation*, University of Westerminster.

Pampanin, S., Magenes, G., and Carr, A. (2003). Modeling of Shear Hinge Mechanism in Poorly Detailed RC Beam Column Joints. FIB Symposium, *Concrete Structures in Seismic Regions*, Athens.

Pantazopoulou, S., and Bonacci, J. (1992). Consideration of Questions about beam-column joints. *ACI Structural Journal*, V. 89, No. 1pp. 27-37.

Pantelides, C.P., Hansen, J., Nadauld, J., and Reaveley, L.D. (2002). Assessment of Reinforced Concrete Building Exterior Joints with Substandard Details. *PEER Report* 2002/18, University of California, Berkeley.

Park, R. (1997). A Static Force-Based Procedure for the Seismic Assessment of Existing Reinforced Concrete Moment Resisting Frames. *Bulletin of the New Zealand National Society for Earthquake Engineering*, V. 30, No. 3, pp. 213-226.

Park, S., and Mosalam, K.M. (2009). Shear Strength Models of Exterior Beam-Column Joints without Transverse Reinforcement. *PEER Report 2009/106,* University of California, Berkeley.

Parker, D.E., and Bullman, P.J.M. (1997). Shear Strength within Reinforced Concrete Beam-Column Joints. *The Structural Engineer*, V. 75, No. 4, pp. 53-57.

Pessiki, S.P., Conley, C., Gergely, P., and White, R.N. (1990). Seismic Behavior of Lightly-Reinforced Concrete Column and Beam Column Joint Details. *NCEER-90-0014*, National Center for Earthquake Engineering Research, State University of New York at Buffalo.

Priestley, M.J.N. (1997). Displacement-Based Seismic Assessment of Reinforced Concrete Buildings. *Journal of Earthquake Engineering*, V. 1, No. 1, pp. 157-192.

Sagbas, G. (2007). Nonlinear Finite Element Analysis of Beam-Column Subassemblies. *Master of Applied Science thesis,* University of Toronto.

Sarsam, K.F., and Phipps, M.E. (1985). The Shear Design of In-situ Reinforced Beam-Column Joints Subjected to Monotonic Loading. *Magazine of Concrete Research*, V. 37, No. 130, pp. 16-28.

Scott, R.H. (1992). The effects of detailing on RC beam/column connection behaviour. *The Structural Engineer*, V. 70, No. 18, pp. 318-324.

Scott, R.H., and Hamil, S.J. (1998). Connection Zone Strain in the Reinforced Concrete Beam Column Connections. *Proceedings of the 11th International Conference on Experimental Mechanics*, Oxford, UK, pp. 65-69.

Sezen, H. (2002). Seismic Behavior and Modeling of Reinforced Concrete Building Columns. *PhD Dissertation*, University of California, Berkeley.

Sezen, H., Elwood, K.J., Whittaker, A.S., Mosalam, K.M., Wallace, J.W., and Stanton, J.F. (2000). Structural Engineering Reconnaissance of the August 17, 1999 Earthquake: Kocaeli (Izmit), Turkey. *PEER Report 2000/09,* University of California, Berkeley.

Shin, Y.B. (2007). Shaking Table Tests on Reinforced Concrete Columns. *PhD Dissertation*, University of California, Berkeley.

Shin, M., and LaFave, J.M. (2004). Testing and Modeling for Cyclic Joint Shear Deformations in RC Beam-Column Connections. Proceeding of the Thirteenth World Conference on Earthquake Engineering, Vancouver, B.C., Canada.

Schlaich, J., and Schäfer, K. (1991). Design and detailing of structural concrete using strut-and-tie models. *The Structural Engineer*, V. 69, No. 6, pp. 113-125.

Theiss, A.G. (2005). Modeling the Earthquake Response of Older Reinforced Concrete Beam-Column Building Joints. *MSCE thesis,* University of Washington.

Tsonos, A.G. (2007). Cyclic Load Behavior of Reinforced Concrete Beam-Column Subassemblages of Modern Structures. *ACI Structural Journal*, V. 104, No. 4, pp. 468-478.

Uang, C.M., Elgamal, A., Li, W.S., and Chou, C.C. (1999). Ji-Ji Taiwan Earthquake of September 21, 1999: Brief Reconnaissance Report. University of California, San Diego.

Ueda, T., Lin, I., and Hawkins, N.M. (1986). Beam Bar Anchorage in Exterior Column-Beam Connections. *ACI Journal Proceedings*, V. 83, No. 3, pp. 412-422.

Uzumeri, S.M. (1977). Strength and Ductility of Cast-In-Place Beam-Column Joints. *ACI Structural Journal*, SP53, pp. 293-350.

Vecchio, F.J., and Collins, M.P. (1986). The Modified Compression-Field Theory of Reinforced Concrete Elements Subjected to Shear. *ACI Structural Journal*, V. 83, No. 2, pp. 219-231.

Vollum, R.L. (1998). Design and Analysis of Exterior Beam Column Connections. *PhD Dissertation*, Imperial College of Science Technology and Medicine-University of London.

Walker, S.G. (2001). Seismic Performance of Existing RC Beam–Column Joints. *MSCE thesis,* University of Washington.

Wong, H.F. (2005). Shear Strength and Seismic Performance of Non-Seismically Designed Reinforced Concrete Beam-Column Joints. *PhD Dissertation*, Hong Kong University of Science and Technology.

Woo, S.W. (2003). Seismic Performance of RC Frames in a Low to Moderate Seismicity Region. *PhD Dissertation*, Korea University.

Youssef, M., and Ghobarah, A. (2001). Modelling of RC Beam-Column Joints and Structural Walls. *Journal of Earthquake Engineering*, V.5, No. 1, pp. 93-111.

Zhang, L.X., and Hsu, T.C. (1998). Behavior and Analysis of 100MPa Concrete Membrane Elements. *ASCE Journal of Structural Engineering*, V. 124, No. 1, pp. 24-34.

Zhang, L., and Jirsa, J.O. (1982). A Study of Shear Behavior of RC Beam-Column Joints. *PMFSEL Report* No. 82-1, University of Texas at Austin.

APPENDIX A: DRAWINGS OF SPECIMENS AND TEST SETUP

A.1 SPECIMEN DRAWINGS

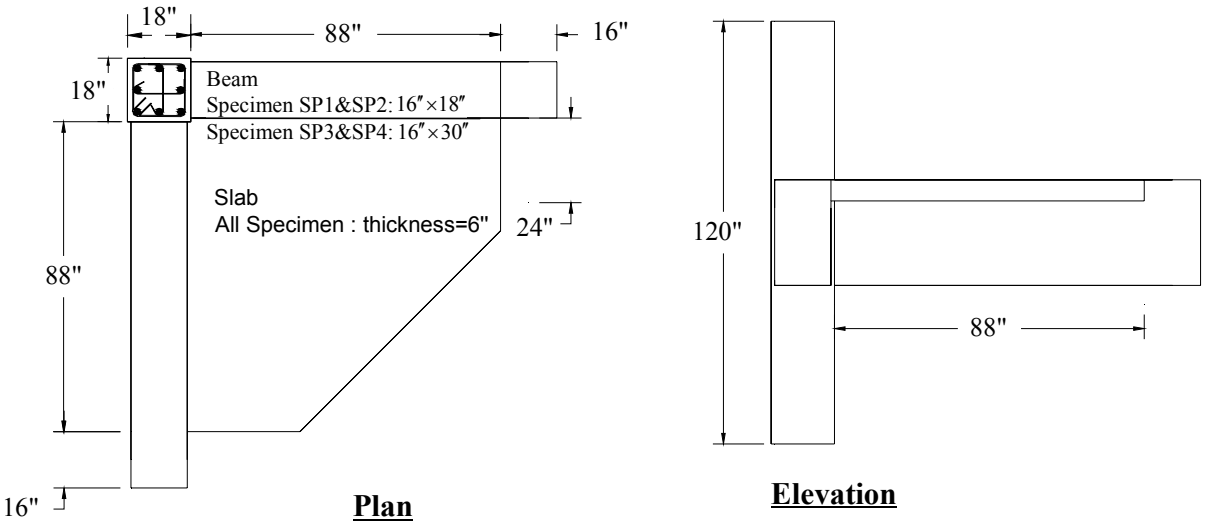

Plan **Elevation**

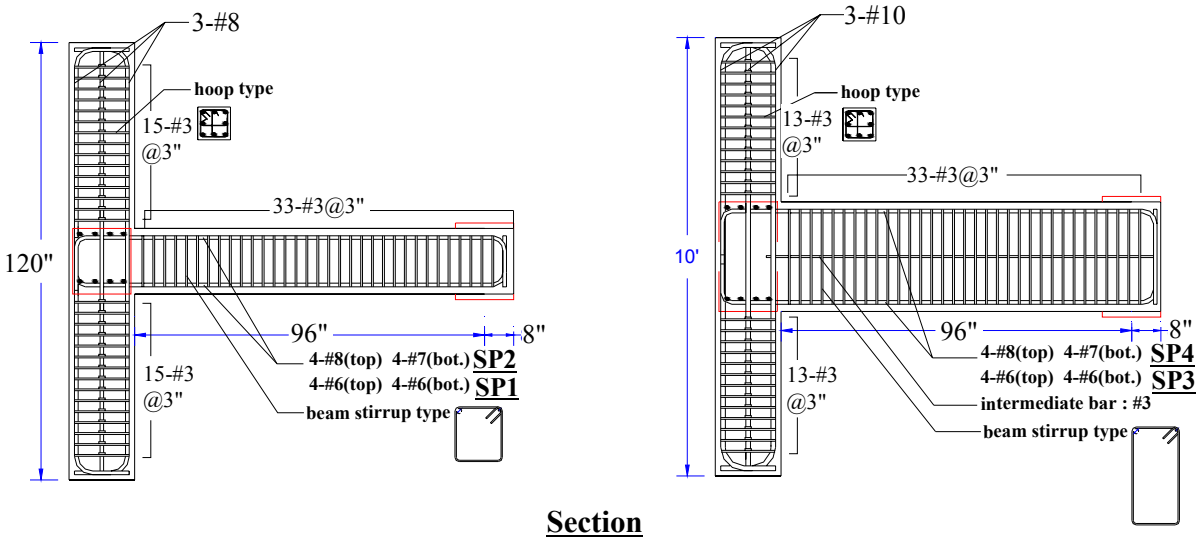

Section

Column Details

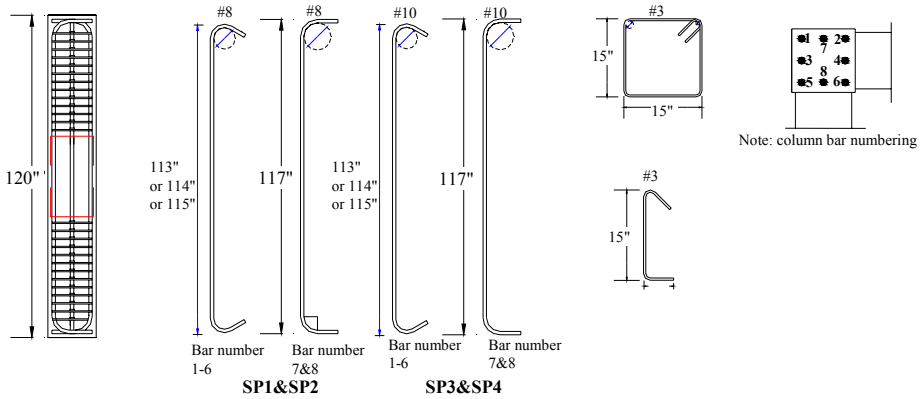

Beam Details

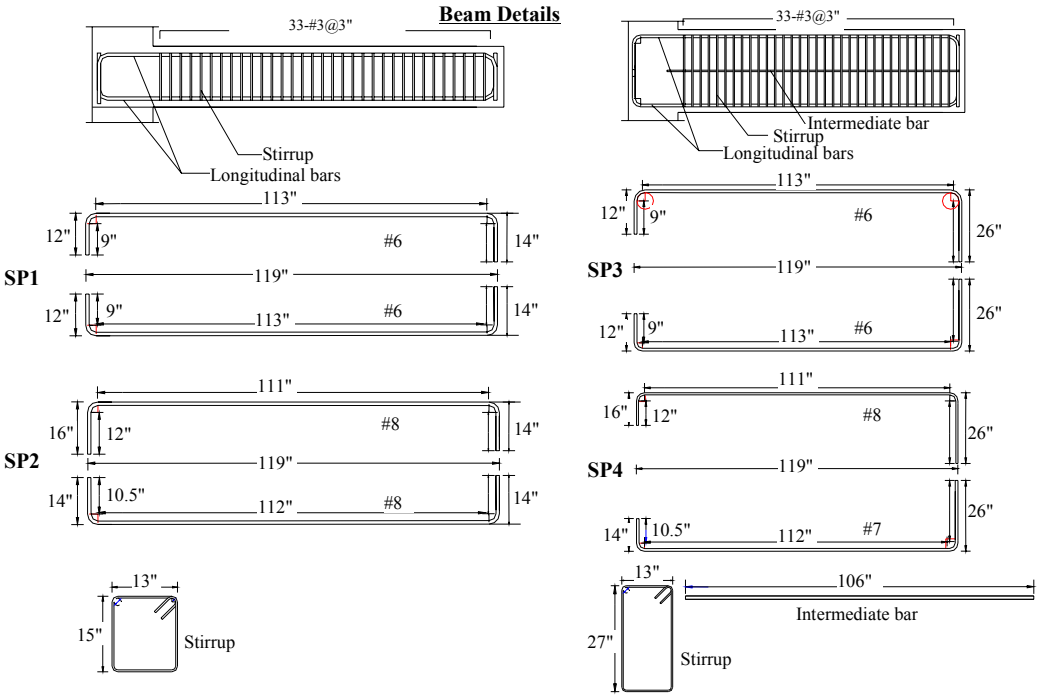

Slab Details

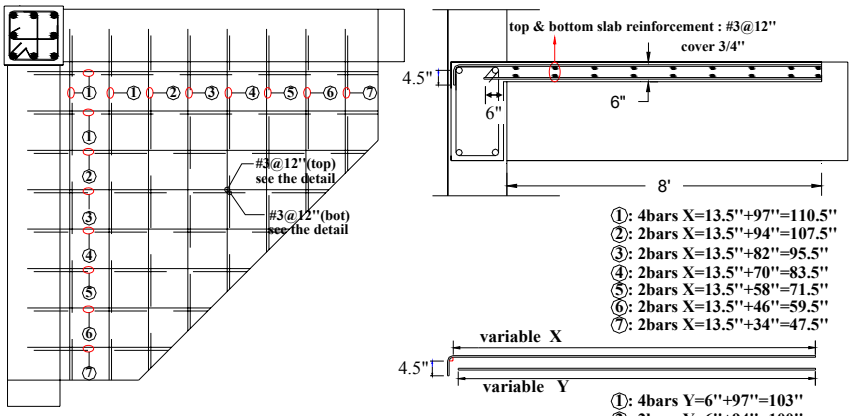

A.2 TEST SETUP DRAWINGS

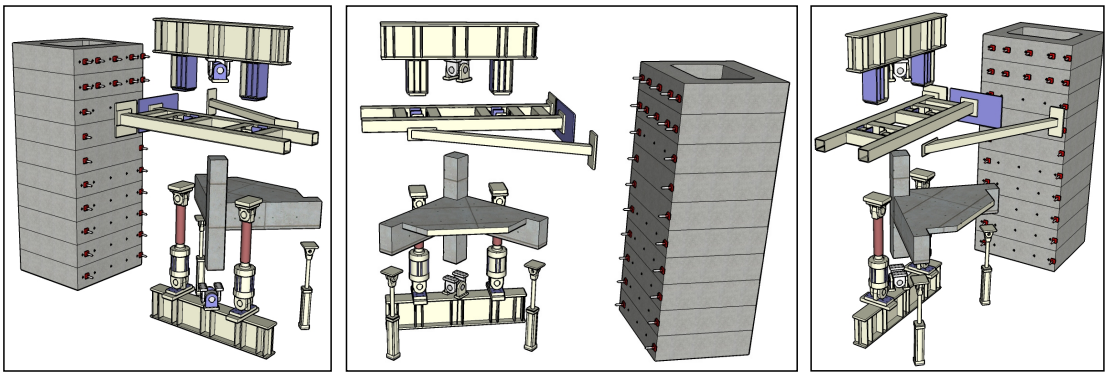

Global view

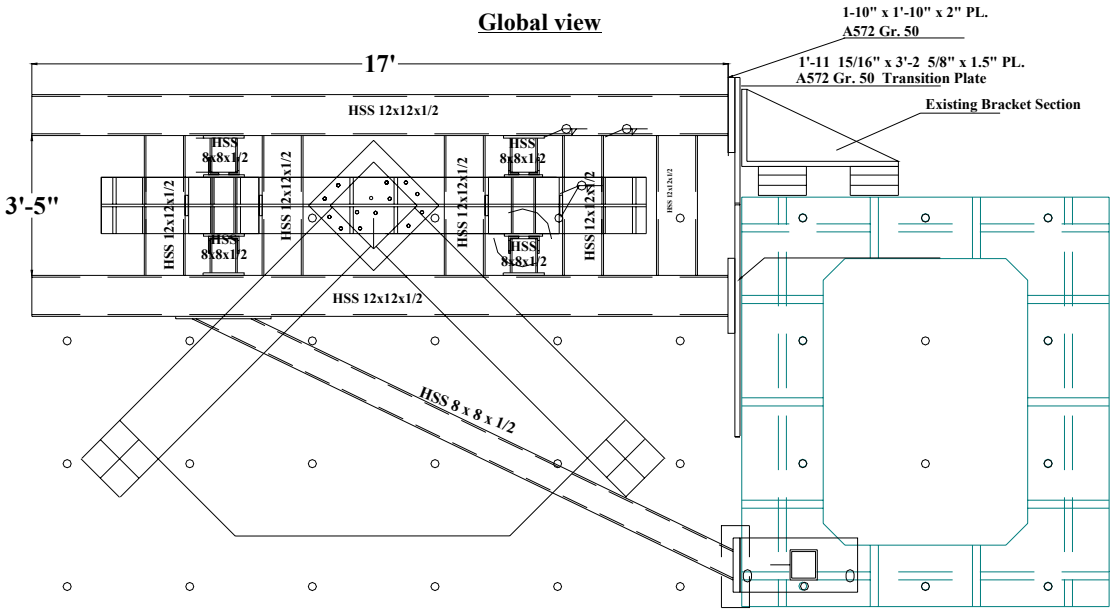

Plan

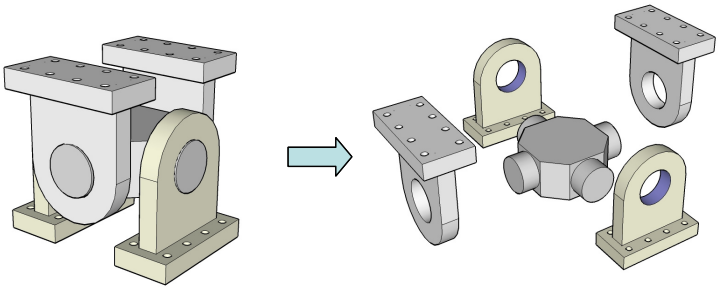

Bidirectional Clevis

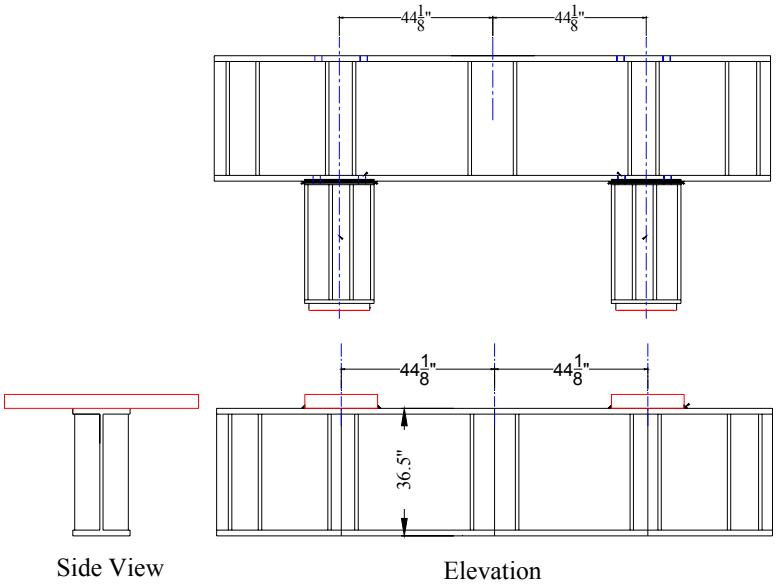

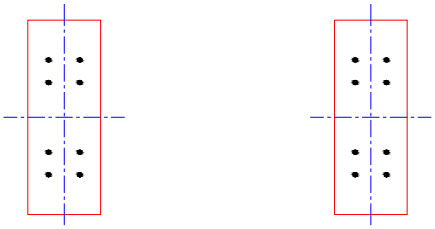

Vertical Frame

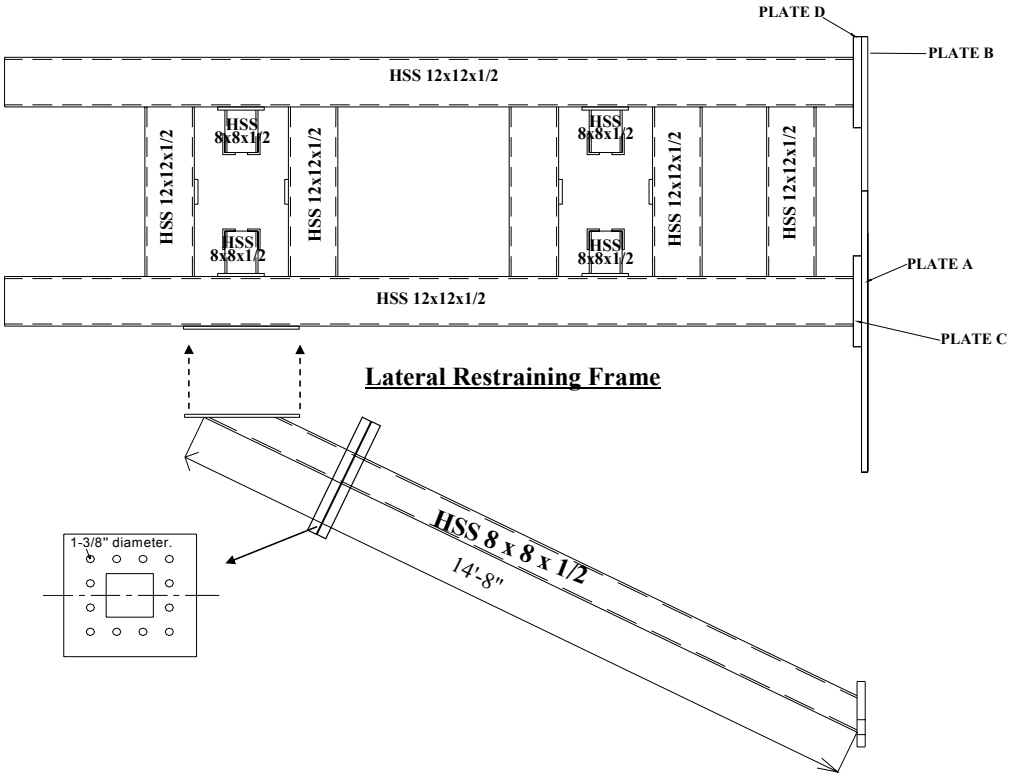

Lateral Restraining Frame

Brace of Lateral Restraining Frame

APPENDIX B: MATERIAL PROPERTIES

B.1 CONCRETE PROPERTIES

B.1.1 Mix Design

The relevant concrete mixes were selected to test the four full-scale test specimens designed according to typical older type reinforced concrete buildings. Specimens SP1 and SP2 concrete were cast using one mix truck from a single batch (referred to as "Mix1"), and the other two specimens SP3 and SP4 were cast using two mix trucks having the same concrete mix (referred to as "Mix2") due to the capacity of a mix truck. Maximum aggregate size was equal to 1 in. (25.4 mm) for both two mixes.

For the Mix1, the concrete compressive strength was quite lower than its targeted strength at 28th day. Accordingly, the water/cement ratio increased for the Mix2. The two mix designs are summarized in Tables B.1 and B.2.

Table B.1 SP1 and SP2 concrete mix design (Mix1).

Material	Saturated Surface Dry Weight (lb)	Absolute Volume (ft^3)
Cement ASTM C-150 Type II-V	323.0	1.64
Fly Ash ASTM C-618 Class F	57.0	0.39
Fine Aggregate ASTM C-33	1714.7	9.88
Aggregate ASTM C-33 1″×#4	1750.0	9.73
Water reducer ASTM C-494 Type A	13.0 fl. Oz.	
Water ASTM C-94	283.7	4.55
Air	-	0.81
Total	4128	27.00
Water/Cement Ratio = 0.75 Slump = 4 ± 1(in) Anticipated Strength @28th day = 3500 ± 500 psi		

Table B.2 SP3 and SP4 concrete mix design (Mix2).

Material	Saturated Surface Dry Weight (lb)	Absolute Volume (ft^3)
Cement ASTM C-150 Type II-V	470.0	2.39
Aggregate 1″×#4	1500.0	8.94
Regular top sand	1235.0	7.41
SR blend sand	514.0	3.17
Water reducer ASTM C-494 Type A	23.5 fl. Oz.	0.41
Water	292.0	4.68
Total	4001	27.00
Water/Cement Ratio = 0.621 Slump = 4 ± 1(in) Anticipated Strength @28th day = 3500 ± 500 psi		

B.1.2 Concrete Test Results

To test the compressive and tensile strength of the cast concrete, standard 6 in.×12 in. (152 ×305 mm) cylinders were made and cured in the same condition of the specimens except for 7 and 14 days testing cylinders of Mix1, refer to Figure B.1. The plastic forms of the cylinders were stripped on the same day when the specimen forms were removed. The six cylinders of Mix1 for 7 and 14 days testing were stripped at 4days to be capped with high-strength sulfur.

Due to the low compressive strength of Mix1 until 21st day after casting, the form of SP1 and SP2 was maintained until 60 days after casting. To improve the compressive strength, the exposed surface was watered three times a day and after watering, this surface was covered by blanket and plastic until stripping the forms. The compressive strength of Mix2 showed acceptable values at 14 days testing and thus the forms of SP3 and SP4 were stripped.

According to ASTM C39-05(ASTM 2005), the cylinders were capped with a sulfur compound and were tested in a Universal Testing Machine at a rate of 35 psi/min (0.241 MPa/min). At the day of test, another three cylinders were used for split test to measure the tensile strength according to ASTM C496. The concrete cylinder test results are summarized in Tables B.3 and B.4. Concrete stress-strain curves are given in Figure B.2 for the results of compressive tests conducted at the testing day.

Table B.3 Concrete cylinder test results of SP1 and SP2 (Mix1).

Specimen	SP1 and SP2							
Test	Compressive Strength (ksi)							Tensile Strength
after casting	7	15	21	26	50	295 (SP1[*1])	358 (SP2[*2])	359
Cylinder 1	1.44	1.91	2.07	2.16	2.84	3.66	3.56	0.37
Cylinder 2	1.38	1.87	1.90	-	2.74	3.76	3.48	0.32
Cylinder 3	1.37	1.80	1.83	-	-	3.31[*]	3.54	0.33
Avg.	1.39	1.86	1.93	2.16	2.8	3.58	3.53	0.34

[*1]: day of testing SP1.
[*2]: day of testing SP2.

Table B.4 Concrete cylinder test results of SP3 (Mix2).

Specimen	SP3							
Test	Compressive Strength (ksi)							Tensile Strength
after casting	7	14	21	28	63	324	378	378
Cylinder 1	2.08	3.25	3.15	3.70	3.86	3.82	3.59	0.32
Cylinder 2	2.14	3.09	3.30	3.06	3.68	3.82	3.57	0.34
Cylinder 3	2.25	3.29	3.24	3.23	3.77	3.95	3.66	0.31
Avg.	2.16	3.21	3.23	3.33	3.77	3.86	3.60	0.32
Specimen	SP4							
Test	Compressive Strength (ksi)							Tensile Strength
after casting	7	14	21	28	63	324	421	421
Cylinder 1	2.11	3.07	3.32	3.82	3.97	4.07	4.06	0.48
Cylinder 2	2.13	3.00	3.36	3.61	4.23	3.80	3.73	0.42
Cylinder 3	2.14	3.02	3.26	3.60	4.32	4.01	4.09	0.43
Avg.	2.13	3.03	3.32	3.68	4.17	3.96	3.96	0.44

Figure B.1. Slump test and curing.

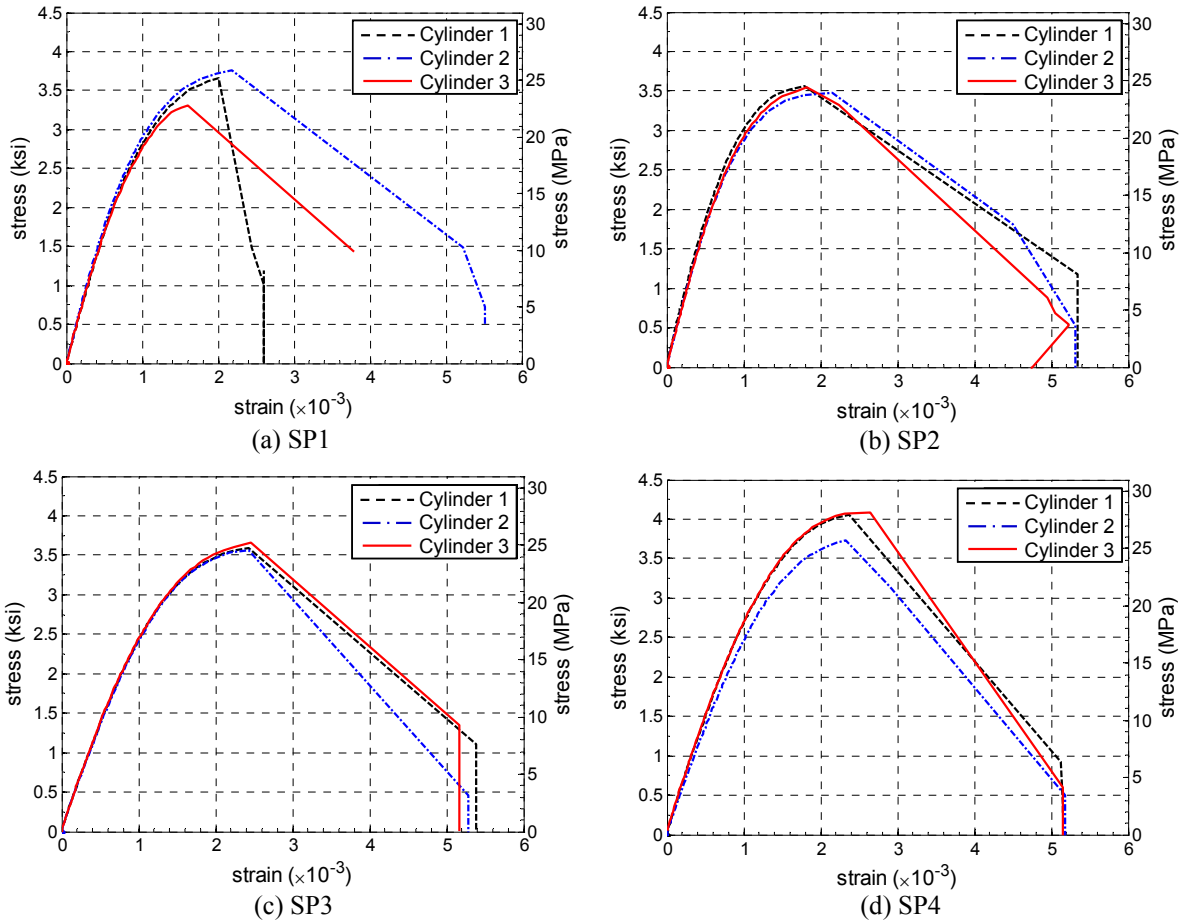

(a) SP1 (b) SP2

(c) SP3 (d) SP4

Figure B.2 Concrete stress versus strain curves.

B.2 REINFORCING BAR PROPERTIES

Five different bar sizes (#3, #6, #7, #8, and #10) were used in the four test specimens. The local contractor provided the metric bar sizes, D10, D19, D22, D25, and D32, which correspond to the above US standard bars, respectively. The column longitudinal bars were designed with #8 bars in SP1 and SP2, #10 bars in SP3 and SP4. The beam longitudinal bars of SP1 and SP3 were designed with #6 bars at the top and bottom of the beams and those of SP2 and SP4 were designed with #8 and #7 bars at the top and bottom of the beams, respectively. The #3 bars were used for the slab reinforcement, column hoops and beam stirrups of the four test specimens.

All reinforcing bars used in the four test specimens were tested to confirm that the material properties corresponded to the ASTM A 706. For each bar size, three coupons were tested in tension according to ASTM A370. The selected reinforcing bars were cut by 24 in. (609.6 mm) length and the cross-section within the middle of 6 in. (152.4 mm) length was machined to reduce sectional area. The measured data are summarized in Table B.5. For the #3 bars, the yield stress and strain were defined using 0.1% offset method. For other bars, the yield stress was defined as the stress at the plateau, and the yield strain was taken as the strain corresponding to the yield stress. The stress-strain curve of the coupon tests are shown in Figure B.3.

Table B.5 Reinforcing bars material properties.

Bar size	#3 (D10)	#6 (D19)	#7 (D22)	#8 (D25)	#10 (D32)
Yield stress(ksi)	73.5*	78.6	73.3	72.2	68.3
Ultimate stress	115	104.5	103.1	102.6	100.5
Yield strain	0.0035*	0.0028	0.0027	0.0025	0.0023
Plateau strain	-	0.0195	0.0127	0.0133	0.0124
Ultimate strain	0.105	0.12	0.12	0.12	0.12
Fracture strain	0.157	0.223	0.225	0.226	0.222
Elastic Modulus	28200	27900	26700	28900	29600

*: determined by 0.1% offset method

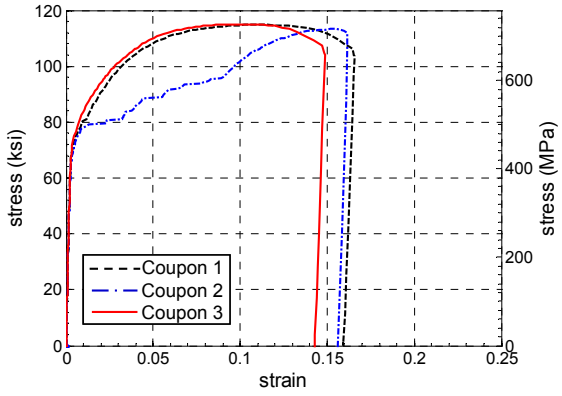

(a) #3 (D10) Bar

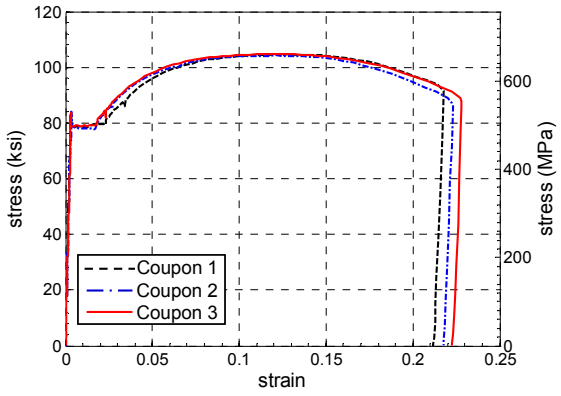

(b) #6 (D19) Bar

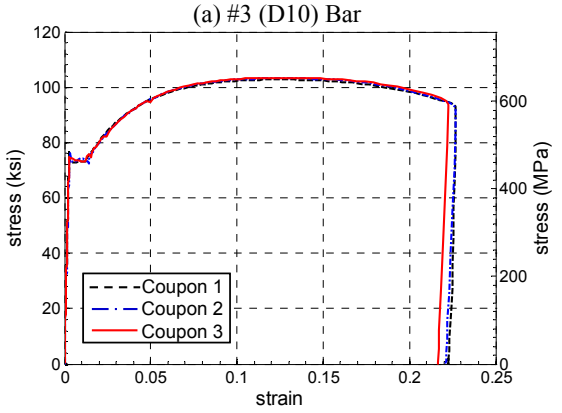

(c) #7 (D22) Bar

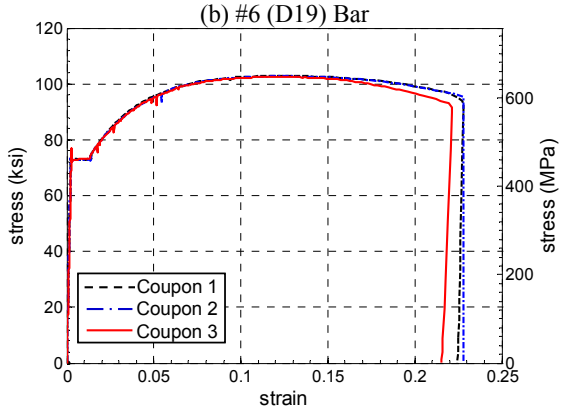

(d) #8 (D25) Bar

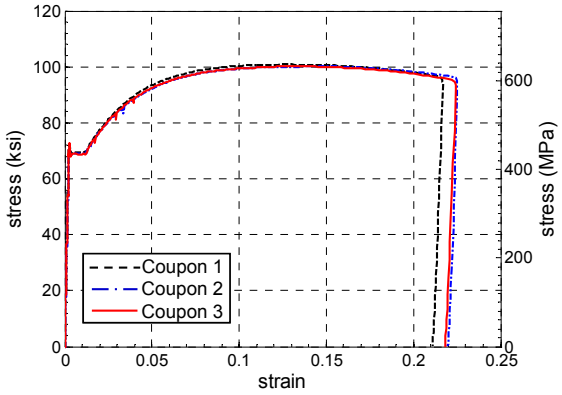

(e) #10 (D32) Bar

Figure B.3 Reinforcing bars stress versus strain curves.